Green Energy and Technology

Wallace C. H. Choy *Editor*

Organic Solar Cells

Materials and Device Physics

Springer

Green Energy and Technology

For further volumes:
http://www.springer.com/series/8059

Wallace C. H. Choy
Editor

Organic Solar Cells

Materials and Device Physics

Springer

Editor
Wallace C. H. Choy
Department of Electrical and Electronic Engineering
The University of Hong Kong
Hong Kong
People's Republic of China

ISSN 1865-3529 ISSN 1865-3537 (electronic)
ISBN 978-1-4471-4822-7 ISBN 978-1-4471-4823-4 (eBook)
DOI 10.1007/978-1-4471-4823-4
Springer London Heidelberg New York Dordrecht

Library of Congress Control Number: 2012953251

Printed on acid-free paper

Springer is part of Springer Science+Business Media (www.springer.com)

Contents

Chapter 1
Introduction to Organic Solar Cells

Dixon D. S. Fung and Wallace C. H. Choy

Abstract Organic solar cells (OSCs) have attracted strong attention in recent years, due to the advantages of flexibility, thinness, and simple manufacturing process. In this chapter, we overview the basics of OSCs. The basics of organic semiconductors are first described. We then provide details of the four steps in the operation principles of OSCs, including exciton generation, exciton diffusion, exciton dissociation, and charge collection. The basic architecture of OSC and the methods of characterization of OSCs are also explained. This chapter provides the fundamentals of OSCs to facilitate understanding of more advanced topics.

1.1 Introduction

Since the discovery of high conductivity in perylene-iodine complex in 1954, organic semiconductors have been under intense research [1]. Potential applications of organic semiconductors emerged when Tang et al. demonstrated the first OLED in the 1970s [2]. With the unique properties of organic semiconductors of flexibility, thinness, and simple fabrication process, OLEDs have spawned a unique industry of flexible and ultra-thin displays. OLEDs have already been adopted in commercial applications such as small OLED displays on mobile appliances, and large area displays such as televisions are receiving more attention. Other than OLEDs, another important application of organic semiconductors is organic solar cells (OSCs). In contrast to OLEDs, OSCs make use of organic

D. D. S. Fung · W. C. H. Choy (✉)
Department of Electrical and Electronic Engineering, The University of Hong Kong, Pokfulam, Hong Kong
e-mail: chchoy@eee.hku.hk

W. C. H. Choy (ed.), *Organic Solar Cells*, Green Energy and Technology,
DOI: 10.1007/978-1-4471-4823-4_1,

semiconductors to absorb light and convert it to electrical energy. With the inorganic solar cells technology running into cost bottlenecks for large area applications, the simple and cheap fabrication process of OSCs provides a huge potential for large area applications. Also, OSCs have the unique properties of flexibility and lightweight that may also result in new applications such as portable solar panels. The properties of OSCs are very interesting for understanding organic devices. Their basic principles are described in this chapter.

1.2 Overview of Organic Semiconductors

Organic semiconductors are carbon-based materials possessing semiconductor characteristics. Atoms within an organic semiconductor molecule are bonded by conjugated **π-**bonds, while molecules are bonded to each other by weak van der Waal's force, as opposed to the giant covalent structure exhibited by inorganic semiconductors. The bonding structure gives organic semiconductors its unique flexibility, light weight, and low sublimation point which allow easy processing.

From the macroscopic point of view, the band structure of organic semiconductors can be treated similarly as inorganic semiconductors. The valence band is normally filled with electrons and conduction band is normally free of electrons. In organic semiconductors, the Highest Occupied Molecular Orbital (HOMO) and the Lowest Unoccupied Molecular Orbital (LUMO) are analogs to the valence band and conduction band respectively. The HOMO and LUMO of organic semiconductors represent the hybridization between bonding and antibonding of the conjugated π-electrons [3, 4].

Organic semiconductors are composed of organic molecules which are formed by a π-conjugated system. Carbon atoms are sp^2 hybridized and the sp^2 bonds form three strong σ-bonds with neighboring atoms [4]. The remaining p-orbitals of the C atoms form a delocalized cloud of electrons through the formation of weaker π-bonds. This bond structure forms a quasi-one-dimensional structure for the conjugated organic semiconductors. The π-bond system can have different bonding configurations according to the electron wavefunction overlap of neighboring atoms. For example, in Fig. 1.1, we can see two different states of the π-bonds, with the bonding and antibonding states corresponding to different energy levels.

The HOMO and LUMO of organic semiconductors refer to energy bands that correspond to different hybridization states of the π-bonds which will result in

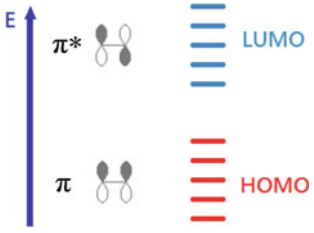

Fig. 1.1 Illustration of bonding–antibonding interactions between the HOMO/LUMO levels of an organic semiconductor

different energy levels of an organic semiconductor. When an electron is excited from the HOMO to the LUMO of an organic semiconductor, the molecule itself is excited into a higher energy state, as opposed to the actual excitation of a free electron from the valence band to the conduction band in inorganic semiconductors.

The carrier transport mechanism in organic semiconductors is also different from that of inorganic semiconductors. In organic semiconductors, thermally activated 'hopping' of carriers occurs to overcome the energy barriers within the disordered conjugated polymer structure, thus allowing carrier transport within the semiconductor. [5]. This is highly different for charge transport in inorganic semiconductors, which can be described by movement of free carriers in the valence or conduction band. The hopping transport mechanism gives organic semiconductors a rather low mobility when compared to their inorganic counterparts. Up to $\sim 1.5 \times 10^{-3}$ m^2 V^{-1} s^{-1} hole mobility is achieved for small molecule organic semiconductors [6, 7], while silicon has a mobility of up to $\sim 4.5 \times 10^{-2}$ m^2 V^{-1} s^{-1} [8]. On the other hand, electron mobility for some small molecule materials reaches $\sim 1 \times 10^{-5}$ m^2 V^{-1} s^{-1} [9, 10], while silicon has a much higher electron mobility of 0.1 m^2 $V^{-1}s^{-1}$. In solar cell applications, the commonly studied P3HT:PCBM blend has hole and electron mobilities of the order of $\sim 10^{-7}$–10^{-8} m^2 V^{-1} s^{-1} in the mixed blend film [11]. The low mobility, when compared to inorganic semiconductors, is a major disadvantage for organic semiconductors and consequently, different devices were proposed to overcome this weakness.

1.3 Operational Principles of OSCs

1.3.1 Exciton Generation

Upon the absorption of a photon, an electron in the organic semiconductor is excited from the HOMO to the LUMO. This is analogous to exciting an electron from the valence band to the conduction band of inorganic semiconductors. However, due to the low dielectric constant and localized electron and hole wavefunctions in organic semiconductors [12, 13], strong Coulombic attraction exists between the electron–hole pair. The resulting bound electron–hole pair is called an exciton, with a binding energy of 0.1–1.4 eV [13], as opposed to a much lower binding energy of a few meV in inorganic semiconductors. Hence, it is relatively higher possibility to generate free charge carriers after absorption of photons in an inorganic semiconductor as the electron–hole pairs easily dissociate by absorbing thermal energy; while strongly bound excitons are generated in organic semiconductors.

The absorption coefficient of organic materials is commonly high at $\sim 10^5$ cm^{-1} [14]. Hence, although the thickness of the active layer of OSCs are limited by electrical conduction, a few hundreds of nanometers of the active layer is thick enough to absorb an adequate amount of light and show significant solar cell characteristics [15]. To further improve absorption, particularly in the

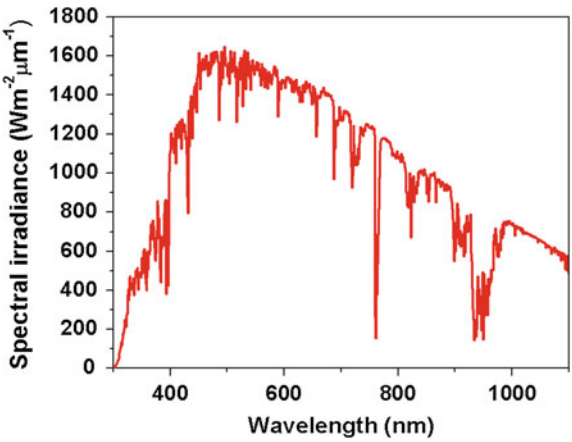

Fig. 1.2 AM1.5G reference solar spectrum

wavelength range where the inherent absorption of the material is weak, various light trapping techniques such as gratings [16, 17], folded cells [18], and lens concentrators [19] have been suggested. A main concern for organic materials is the commonly large band gap and small absorption range which lead to low absorption efficiency of photons in the long wavelength region. With a LUMO–HOMO difference of 1.1 eV, it is reported that ~77 % of solar light is absorbed [20]. In contrast, the benchmark material for OSCs, P3HT, has a band gap of ~1.9 eV, while most organic materials have band gaps of ~2 eV [21]. Figure 1.2 shows the AM1.5G reference solar spectrum. Compared to common materials which do not absorb in the region >700 nm, it is evident that a large portion of energy can be harvested in the long wavelength regions (>700 nm) and the absorption efficiency can be enhanced by using low band gap materials.

1.3.2 Exciton Diffusion and Dissociation

With an exciton generated, the next question is how to separate the bound electron–hole pair to generate free charges which eventually leads to electricity generation. An ingenious solution was provided by Tang et al., who demonstrated that using two different organic materials with correctly aligned band levels can result in efficient solar cells [22]. The junction between the two materials is called the heterojunction. Ever since that discovery, the heterojunction has become the basis of OSC design. To achieve exciton dissociation, two organic materials with band alignment shown in Fig. 1.3 are placed adjacent to each other. The difference between the HOMO of material A and the LUMO of material B has to be lower than the potential difference between the bound electron–hole pair, i.e., the band gap of either material A or B minus the exciton binding energy. When an exciton is generated in, for instance material A, it migrates toward the heterojunction. As the potential difference between $LUMO_B$ and $HOMO_A$ is lower than that of the energy of the exciton, the transfer of an

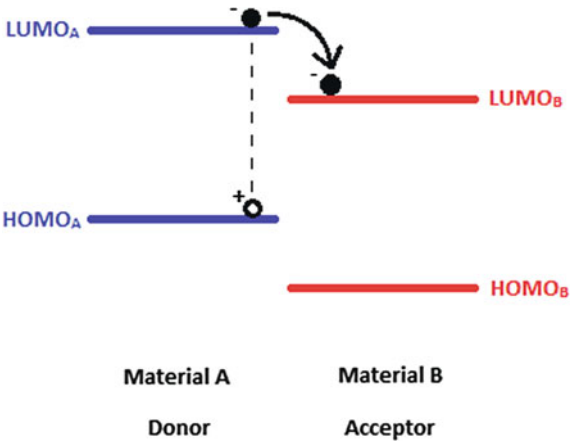

Fig. 1.3 Band alignment of donor and acceptor materials for a heterojunction

electron from the exciton to $LUMO_B$ is an energetically favorable process. An electron is hence transferred from the exciton to $HOMO_B$, while a hole remains in $HOMO_A$. As a result of this charge transfer process, materials A and B are called a *donor* and *acceptor* respectively. The competing process of luminescence, which involves the radiative recombination of excitons, occurs at a timescale of $\sim$1 ns [23]. In contrast, the charge transfer process occurs at a much shorter timescale of $\sim$45 fs [24], allowing efficient exciton dissociation at the heterojunction. After dissociation, electron–hole pairs form a charge pair called a *geminate pair*, which are charges still Coulombically bound and have to be separated by an internal field.

The distance that excitons can diffuse before recombination is called the *exciton diffusion length*. Common exciton diffusion lengths in organic semiconductors are very short, at a few tens of nanometers [7, 20]. Excitons generated at a distance from the heterojunction longer than this length will recombine before reaching the heterojunction, resulting in lower exciton dissociation efficiency. Hence, the active layers have to be kept thin in order to ensure that phase separation between the donor and acceptor is within the exciton dissociation length. However, a thin active layer results in a serious tradeoff of low absorption efficiency. Therefore, it is important to have a large interface area for exciton dissociation and adequate phase separation to ensure efficient exciton dissociation. To achieve this, innovative device architectures such as the bulk heterojunction and nanostructured active layers have been suggested.

1.3.3 Carrier Transport

The geminate pairs generated after exciton dissociation have to travel to electrodes for collection within their lifetimes. The main driving forces for the transport of holes to the anode and electrons to the cathode are drift and diffusion currents [25]. The drift current corresponds to carrier movement along the potential gradient within the solar cell. This potential gradient is mainly determined by the choice of

electrodes in a solar cell. Commonly, a high work function anode and low work function cathode are used and this difference creates a built-in electric field within the solar cell that determines the open circuit voltage (V_{oc}) of the cell. When an external bias is applied, the internal electric field is modified and the drift current changes. The carriers drift along the resultant internal electric field of the solar cell toward the respective electrodes for collection. Another mechanism of carrier transport is the diffusion current, which is the diffusion of carriers along the carrier concentration gradient within a solar cell. As the geminate pairs are generated around the solar cell heterojunction, the concentration of electrons and holes are commonly higher around the heterojunction. Carriers hence diffuse along the concentration gradient away from the heterojunction, leading to the diffusion current. The diffusion current mainly dominates when the applied bias modifies the internal electric field to nearly zero, while drift current dominates when the internal electric field is large.

The main limitation of carrier transport is the mobility in the active layer. As hole and electron mobilities in organic materials are commonly low, the active layer has to be kept relatively thin to allow carriers to reach the electrodes within their lifetimes. The mobility difference is also a critical factor in determining charge transport characteristics, as a difference of more than a factor of 10 will lead to space charge limited current (SCLC) [26–28]. In short, SCLC arises when one type of carrier, say electrons (electron commonly has higher mobility in OSC materials [29]) is transported much more efficiently to the cathode. As the rate of electrons reaching the cathode is higher than that of holes to the anode, electrons may accumulate in the active layer near the cathode interface and creates the space charge effect, which modifies the charge transport characteristics of the active layer and creates an upper limit for the current output of a solar cell. Hence, to achieve efficient carrier transport in the active layer of solar cell, balanced hole and electron mobilities is desired.

1.3.4 Charge Extraction at Electrodes

After the charge carriers transport to the active layer/electrode interface, they are extracted from the active layer to the electrodes. To achieve high efficiency in charge extraction, the potential barrier at the active layer/electrode interfaces have to be minimized. Thus, the work function of the anode is ideally expected to match the donor HOMO, while the work function of the cathode is expected to match the acceptor LUMO. When these occur, the contacts are called *ohmic contacts* and V_{oc} correlates positively with the difference between the acceptor LUMO and donor HOMO [30]. On the other hand, if the work functions of anode and cathode materials are not near the donor HOMO or acceptor LUMO, correspondingly an ohmic contact cannot be formed. In this case, the carrier extraction behavior is governed by the metal-insulator-metal (MIM) model [31].

A method to improve the work function matching at the electrodes is to utilize different types of materials as electrodes. Commonly, indium tin oxide (ITO) is

used as an anode contact as its work function of ~4.7 eV [31] matches well with the HOMO of P3HT [32]. High work function metals, e.g., Au (5.1 eV) can also be used as the anode contact [33]. On the cathode side, low work function metals such as Al (4.2 eV) are commonly used to match the LUMO of PCBM. Besides changing materials to achieve work function matching, interlayers can also be inserted between the electrodes and the active layer to better align the electrode work function and the active layer LUMO or HOMO. For instance, a very thin layer of LiF is usually evaporated on the active layer before fabricating the cathode to form an ohmic contact [33, 34]. Solution processed materials such as TiO_2 [35–37] and ZnO [38, 39] have also been shown to effectively enhance electron collection. On the anode side, transition metal oxides, such as MoO_3 or WO_3, have been used as an interlayer to form ohmic contacts [39–42]. When transition metal oxides are used as the interlayer, it was demonstrated that even low work function metals such as Al can be evaporated on top to form an anode in an inverted configuration [43]. Other than changing the work function of the electrodes, increasing the roughness or interface area of the electrodes can also provide a larger area for more efficient charge collection [44, 45].

1.3.5 Summary of the Operation

The overall operation of solar cells is summarized in four steps as follows: (1) Photon absorption leading to exciton generation; (2) Exciton diffusion to a donor/acceptor heterojunction; (3) Exciton dissociation at a heterojunction to form geminate pairs; (4) Carrier transport and carrier extraction at the electrodes. The four steps are illustrated in Fig. 1.4.

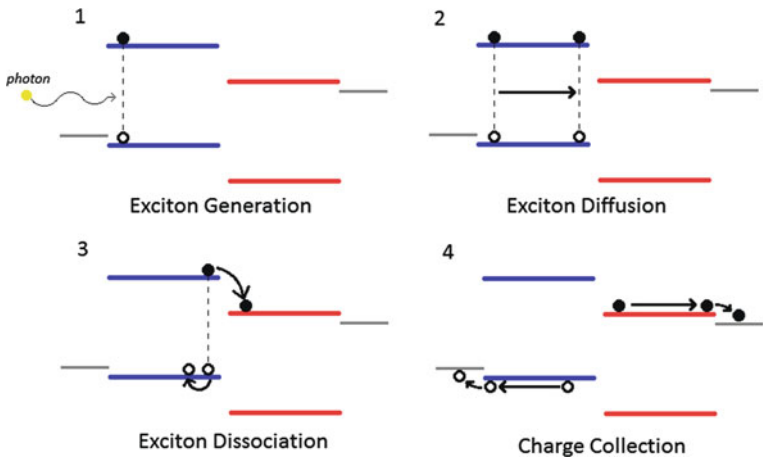

Fig. 1.4 Illustration of the principle of charge separation in solar cell

The efficiency of the four steps is represented by η_A, η_{diff}, η_{diss}, and η_C respectively. The external quantum efficiency (EQE) is defined as

$$\eta_{eqe} = \eta_A \cdot \eta_{diff} \cdot \eta_{diss} \cdot \eta_C \tag{1.1}$$

The EQE represents the percentage of photons that are eventually converted to charge carriers collected at the electrodes. Generally, there are two major factors which limit the EQE. (1) Incomplete absorption of the solar spectrum, either due to narrow absorption band or a thin active layer, leads to a reduction in η_A. (2) Recombination of excitons due to various reasons such as quenching at metal electrodes and limited phase separation in active layer lead to a loss of photo-generated excitons and a lower EQE. To reduce these losses, different solar cell architectures have been proposed and they will be discussed in the next section.

1.4 Solar Cell Architectures

1.4.1 Bilayer Solar Cell

The formation of the heterojunction by Tang et al. [22] in 1986 was first demonstrated in the form of a bilayer solar cell. As shown in Fig. 1.5, the common structure of a bilayer solar cell consists of an anode, hole collection layer, active layer composed of donor and acceptor, electron collection layer, and cathode fabricated sequentially. The hole collection layer and electron collection layer are used to modify the work function of the electrodes to form an ohmic contact. A single, well-defined interface exists between the donor and acceptor at which excitons dissociate. With this structure, the bilayer solar cell is the simplest structure described by the basic operating principle of the solar cell.

A significant drawback for bilayer solar cell is that the short exciton diffusion length of organic materials limits the thickness of the donor and acceptor layers. If the donor or acceptor layer is too thick, the excitons generated far away from the

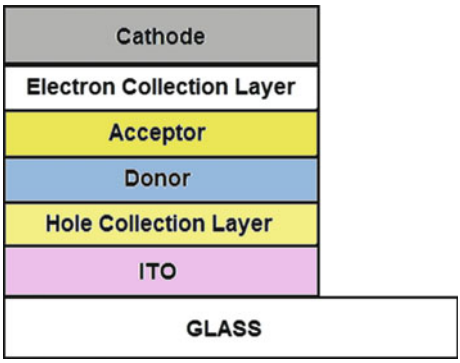

Fig. 1.5 Structure of a bilayer solar cell

heterojunction may recombine before reaching the heterojunction. Also, the donor and acceptor layers are limited to tens of nanometers which lead to weak absorption. To ensure that excitons are generated near the heterojunction, interference effects have to be considered fully during the design of bilayer solar cells. These mutual tradeoff factors lead to low EQE and impose challenges in the design of bilayer OSCs.

1.4.2 Bulk Heterojunction Solar Cells

One of the most important breakthroughs in the field of OSCs is arguably the discovery of the bulk heterojunction (BHJ) in the mid 1990s [46]. The BHJ structure is shown in Fig. 1.6. Although thermal co-deposition methods can be used to fabricate a BHJ [47], the junction is commonly formed by intermixing donor and acceptor materials in a solution, then forming the active layer by spin-coating of the mixed solution on a substrate. The resulting film is an interpenetrating nanoscale network of donor and acceptor materials. The phase separation within the film is commonly 10–20 nm, which is within the exciton diffusion length of many organic semiconductors. Consequently, nearly unity internal quantum efficiency have been achieved for BHJ solar cell [48], which means that nearly all photogenerated excitons are dissociated. Carriers are then transported through percolated pathways within the active layer toward the respective contacts for collection.

Due to the small nanoscale phase separation in BHJs, a thicker active layer can be fabricated in these cells when compared to bilayer solar cells. However, as the spin-coating process is inherently less controlled than the vapor deposition process commonly used in bilayer solar cells, the performance of BHJ solar cells is susceptible to various parameter changes. The efficiency of solar cells is strongly dependent on the morphology of the BHJ and various methods such as thermal annealing [49], solvent annealing [50], and modifying polymer functional groups [51] have been studied to optimize the performance of OSCs.

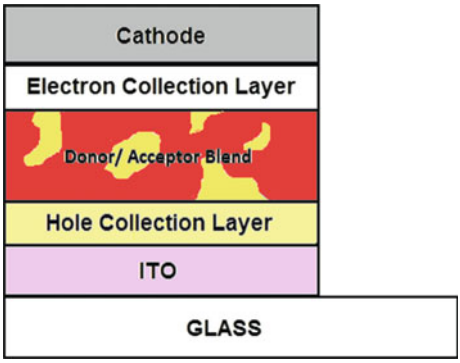

Fig. 1.6 Structure of a bulk heterojunction solar cell

Amongst various materials, P3HT:PCBM BHJ is the most commonly used and well-optimized active layer used in OSCs. Using these blend materials, Schilinsky et al. demonstrated a short-circuit current of 8.7 mA/cm^2, which was the highest current at that time [52]. Within a year, the efficiency of P3HT:PCBM solar cells was pushed up to 3.5 % efficiency [53] and the P3HT:PCBM came under intense research. Thermal annealing of P3HT:PCBM BHJ was found to improve carrier mobility and cause the crystallization of P3HT in the BHJ [54]. The effect of the regioregularity of P3HT was studied, with improving regioregularity showing improved performance due to better stacking of P3HT chains [55]. Studies such as optimization P3HT:PCBM ratio [56] and using additives in solution [57] were also conducted to optimize the performance. Eventually, over 5 % efficiency was reported by Yang et al. using a solvent annealing approach which improved the morphology of the P3HT:PCBM layer [58]. Due to the consistency and simple fabrication process of this material, P3HT:PCBM OSC has become a benchmark solar cell for investigating various device mechanisms in solar cells.

1.4.3 Tandem Solar Cells

To overcome the limitation of weak absorption strength and absorption range of the active layer of OSCs, fabricating solar cells in tandem has been proposed (see Fig. 1.7). Stacking the solar cells in series (a 2-terminal structure) will produce a large V_{oc} and active layers with different absorption regions in the tandem structure can allow the cell to absorb light over a wide wavelength range. For instance, this was demonstrated in a P3HT:PCBM and ZnPc:C60 tandem solar cell which showed improved V_{oc} and wide absorption range [59]. A thin layer of Au or Ag as the intermediate layer fabricated by thermal evaporation was also successfully used in tandem cells [60, 61]. It has also been demonstrated that tandem cells can be entirely solution processed, by using polymer: small molecule active layers and titanium oxide/PEDOT:PSS as the interlayer between subcells [62]. Other interlayers such as ZnO/PEDOT:PSS were also demonstrated successfully to

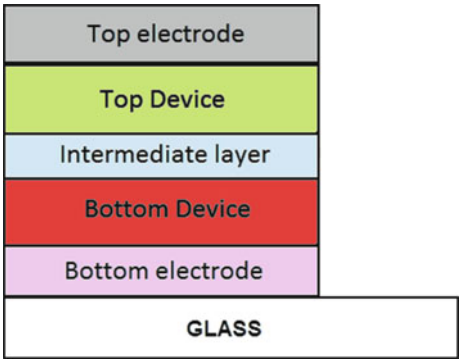

Fig. 1.7 Structure of a tandem cell

produce efficient tandem solar cells [63]. Apart from connecting the subcells in series, it has been demonstrated that connecting the cells in parallel (a 3-terminal structure) can also result in improved efficiency. When the cells are connected in parallel, the short-circuit current is ideally the sum of the current outputs from the two subcells. Sista et al. have demonstrated a large short-circuit current of 15.1 mA/cm^2 and a power conversion efficiency of 4.8 % using a 3-terminal configuration and also showed that both the common-anode and common-cathode configurations are possible by using PEDOT:PSS/Au/V_2O_5 and TiO_2:Cs/Al/Au as the intermediate layer respectively [64].

Despite the advantages, tandem solar cells suffer from difficulties in matching subcells. As carriers from the top and bottom subcells recombine at the interlayer, a good interlayer has to be chosen to allow efficient recombination and has to be transparent to reduce optical losses. Also, current matching between subcells has to be achieved in order to prevent charge accumulation on one of the subcells which deteriorates in efficiency. During fabrication, it is also important that newly fabricated layers will not damage the layers below as more layers are fabricated. These factors present engineering challenges for tandem solar cell design.

1.5 Characterization of Organic Solar Cells

1.5.1 J–V Characteristics

OSCs are typically characterized under 1000 W/m^2 light of AM 1.5 solar spectrum [65]. The operation of a solar cell at difference bases is illustrated in Fig. 1.8.

At (i) reverse bias, the applied bias reinforces the built-in electric field, enhancing exciton dissociation and charge transport and results in a large photocurrent. Drift current is dominant due to the presence of a strong electric field. When (ii) the applied bias is close to zero, mainly the built-in field exists in the device and the built-in field drives the carriers to the corresponding electrodes for collection. When the applied bias is increased in positive direction, the positive bias opposes the built-in field. As the resultant field inside the device reduces, drift current becomes smaller and the magnitude of current decreases. Eventually the field reaches a point where (iii) the applied field is equal to the built-in field. Around this point, diffusion current dominates the current, as the electric field is very small inside the device. When (iv) the external bias is further increased, the applied field is larger than the built-in field and the potential gradient in the device is reversed. As the barrier is now triangular, carrier injection occurs through the tunneling mechanism and positive current results.

When the applied bias and current are opposite in direction, power is outputted from the solar cell. The point where the magnitude of the product of J and V is maximum is the maximum power output point. A number of the parameters that are commonly used to evaluate solar cell performance are described below.

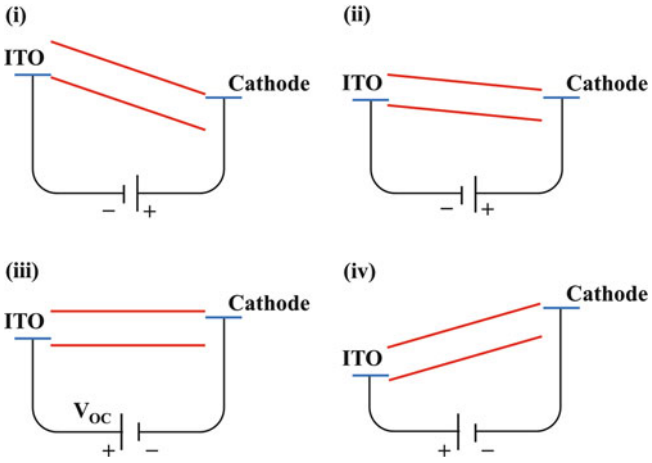

Fig. 1.8 Operation of a solar cell at different biases: **a** large reverse bias; **b** small reverse bias; **c** positive bias, zero resultant internal field, and corresponding to open circuit condition; **d** positive bias, carrier injection

Short circuit current (J_{sc}). The short-circuit current is defined as the current at which the externally applied voltage is 0. J_{sc} represents the number of charge carriers that are generated and eventually collected at the electrodes at short circuit condition. Enhanced optical/electrical parameters such as a small band gap, high absorption coefficient, smaller phase separation, and high carrier mobility improve J_{sc}.

Open circuit voltage (V_{oc}).The open circuit voltage defined as the voltage at which the current density output is 0. V_{oc} has been reported to be mainly dependent on the work function difference of metal contacts. If an ohmic contact is formed at the electrodes, V_{oc} is dependent on the HOMO–LUMO difference between the donor and the acceptor.

Fill Factor (*FF*). The fill factor defines the shape of the *J*–*V* curve and is defined as

$$FF = \frac{J_{mpp} V_{mpp}}{J_{sc} V_{oc}} \tag{1.2}$$

where J_{mpp} and V_{mpp} are the current density and the voltage at the point of maximum output power respectively. As shown above, FF is the ratio between the maximum power output point and the maximum attainable power output, i.e., J_{sc} times V_{oc}. FF represents dependence of current output on the internal field of the device and is quantified by the series resistance and shunt resistance. For instance, low carrier mobility will cause carriers to recombine before reaching a heterojunction. In this case, increasing the external bias will sweep the carriers, which otherwise may recombine at lower field strength, to the heterojunction for dissociation, resulting in an increase in current output. This leads to a strong dependence of current on the applied bias, which is shown by a lower FF.

Power conversion efficiency (*PCE*). Finally, the PCE represents the efficiency of the solar cell and can be calculated as follows:

$$PCE = \frac{V_{oc} J_{sc} FF}{P_{in}}, \tag{1.3}$$

where P_{in} is the input power density.

1.5.2 Incident Photon to Electron Conversion Efficiency

J–V characteristics alone are not sufficient to fully characterize a solar cell, as they do not illustrate optical factors in detail. To further study the efficiency of our solar cell at each wavelength, the measure of incident photon to electron conversion efficiency (IPCE) is important. IPCE represents the percentage of incident photons that are converted to carriers that are finally collected at the electrodes under short circuit conditions and is equivalent to EQE. Hence, the integration of an IPCE spectrum is proportional to the short circuit current.

The shape of IPCE curve is highly dependent on the absorption curve of the active layer. In particular, IPCE is useful evidence when applying techniques to improve absorption in particular wavelength positions (e.g. using plasmonic structures) can be reflected as improvements in IPCE at the corresponding wavelengths. Other than optical effects, electrical effects such as enhanced charge collection is reflected as shifts of an entire IPCE curve as electrical characteristics are largely wavelength independent.

1.6 Conclusions

In this chapter, we have briefly described the basics of OSCs. An overview of organic semiconductors was first provided. The four essential steps of the operation of solar cells, namely exciton generation, exciton diffusion, exciton dissociation, and charge collection were explained in detail. Conventional structures of OSCs, including the bilayer, BHJ and tandem cells, and the basic characterization methods of OSCs were described. This chapter provides the fundamental knowledge in OSCs to facilitate understanding of the work provided in the following chapter.

References

1. Akamatu H, Inokuchi H, Matsunaga Y (1954) Electrical conductivity of the perylene bromine complex. Nature 173(4395):168–169
2. Tang C (1987) Organic electroluminescent diodes. Appl Phys Lett 51(12):913

3. Bredas JL, Calbert JP, da Silva Filho DA, Cornil J (2002) Organic semiconductors: a theoretical characterization of the basic parameters governing charge transport. Proc Nat Acad Sci 99(9):5804–5809
4. Kymissis I (2009) The physics of organic semiconductors. In: Organic Field Effect Transistors. Integrated Circuits and Systems, Springer, US, pp 1-12
5. Hu D, Yu J, Padmanaban G, Ramakrishnan S, Barbara PF (2002) Spatial confinement of exciton transfer and the role of conformational order in organic nanoparticles. Nano Lett 2(10):1121–1124
6. Sundar VC, Zaumseil J, Podzorov V, Menard E, Willett RL, Someya T, Gershenson ME, Rogers JA (2004) Elastomeric transistor stamps: reversible probing of charge transport in organic crystals. Science 303(5664):1644–1646
7. Kietzke T (2007) Recent Advances in Organic Solar Cells. Advances in Opto Electronics 2007. doi: 10.1155/2007/40285
8. McCulloch I, Heeney M, Bailey C, Genevicius K, MacDonald I, Shkunov M, Sparrowe D, Tierney S, Wagner R, Zhang W, Chabinyc ML, Kline RJ, McGehee MD, Toney MF (2006) Liquid-crystalline semiconducting polymers with high charge-carrier mobility. Nat Mater 5(4):328–333
9. Anthopoulos TD (2006) High performance n-channel organic field-effect transistors and ring oscillators based on C60 fullerene films. Appl Phys Lett 89(21):213504
10. Gundlach DJ (2005) High mobility n-channel organic thin-film transistors and complementary inverters. J Appl Phys 98(6):064502
11. Koster LJ (2006) Ultimate efficiency of polymer/fullerene bulk heterojunction solar cells. Appl Phys Lett 88(9):093511
12. Gregg B (2003) Comparing organic to inorganic photovoltaic cells: theory, experiment, and simulation. J Appl Phys 93(6):3605
13. Mayer AC, Scully SR, Hardin BE, Rowell MW, McGehee MD (2007) Polymer-based solar cells. Mater Today 10:28–33
14. Brütting W (2006) Introduction to the physics of organic semiconductors. In: Physics of organic semiconductors. Wiley-VCH Verlag GmbH & Co. KGaA, Weinheim, pp 1–14
15. Coakley KM, McGehee MD (2004) Conjugated polymer photovoltaic cells. Chem Mater 16(23):4533–4542
16. Min C (2010) Enhancement of optical absorption in thin-film organic solar cells through the excitation of plasmonic modes in metallic gratings. Appl Phys Lett 96(13):133302
17. Lee JH, Kim DW, Jang H, Choi JK, Geng J, Jung JW, Yoon SC, Jung H-T (2009) Enhanced solar-cell efficiency in bulk-heterojunction polymer systems obtained by nanoimprinting with commercially available AAO membrane filters. Small 5(19):2139–2143
18. Andersson V (2008) Optical modeling of a folded organic solar cell. J Appl Phys 103(9):094520
19. Peumans P, Bulovic V, Forrest SR (2000) Efficient photon harvesting at high optical intensities in ultrathin organic double-heterostructure photovoltaic diodes. Appl Phys Lett 76(19):2650–2652
20. Jean-Michel N (2002) Organic photovoltaic materials and devices. CR Phys 3(4):523–542
21. Hoppe H, Sariciftci NS (2004) Organic solar cells: an overview. J Mater Res 19(07): 1924–1945
22. Tang C (1986) Two-layer organic photovoltaic cell. Appl Phys Lett 48(2):183
23. Brabec CJ, Zerza G, Cerullo G, De Silvestri S, Luzzati S, Hummelen JC, Sariciftci S (2001) Tracing photoinduced electron transfer process in conjugated polymer/fullerene bulk heterojunctions in real time. Chem Phys Lett 340(3–4):232–236
24. Günes S, Neugebauer H, Sariciftci NS (2007) Conjugated polymer-based organic solar cells. Chem Rev 107(4):1324–1338
25. Koster LJA, Smits ECP, Mihailetchi VD, Blom PWM (2005) Device model for the operation of polymer/fullerene bulk heterojunction solar cells. Phys Rev B 72(8):085205
26. Mihailetchi VD, Wildeman J, Blom PWM (2005) Space-charge limited photocurrent. Phys Rev Lett 94(12):126602

27. Koster LJ (2005) Origin of the light intensity dependence of the short-circuit current of polymer/fullerene solar cells. Appl Phys Lett 87(20):203502
28. Lenes M (2006) Thickness dependence of the efficiency of polymer: fullerene bulk heterojunction solar cells. Appl Phys Lett 88(24):243502
29. Shrotriya V (2006) Effect of self-organization in polymer/fullerene bulk heterojunctions on solar cell performance. Appl Phys Lett 89(6):063505
30. Brabec CJ, Cravino A, Meissner D, Sariciftci NS, Fromherz T, Rispens MT, Sanchez L, Hummelen JC (2001) Origin of the open circuit voltage of plastic solar cells. Adv Funct Mater 11(5):374–380
31. Parker I (1994) Carrier tunneling and device characteristics in polymer light-emitting diodes. J Appl Phys 75(3):1656
32. Scharber MC, Mühlbacher D, Koppe M, Denk P, Waldauf C, Heeger AJ, Brabec CJ (2006) Design rules for donors in bulk-heterojunction solar cells—towards 10% energy-conversion efficiency. Adv Mater 18(6):789–794
33. Mihailetchi V (2003) Cathode dependence of the open-circuit voltage of polymer: fullerene bulk heterojunction solar cells. J Appl Phys 94(10):6849
34. Brabec C (2002) Effect of LiF/metal electrodes on the performance of plastic solar cells. Appl Phys Lett 80(7):1288
35. Hayakawa A (2007) High performance polythiophene/fullerene bulk-heterojunction solar cell with a TiOx hole blocking layer. Appl Phys Lett 90(16):163517
36. Waldauf C (2006) Highly efficient inverted organic photovoltaics using solution based titanium oxide as electron selective contact. Appl Phys Lett 89(23):233517
37. Kuwabara T, Nakayama T, Uozumi K, Yamaguchi T, Takahashi K (2008) Highly durable inverted-type organic solar cell using amorphous titanium oxide as electron collection electrode inserted between ITO and organic layer. Sol Energy Mater Sol Cells 92(11):1476–1482
38. Keis K, Magnusson E, Lindström H, Lindquist S-E, Hagfeldt A (2002) A 5% efficient photoelectrochemical solar cell based on nanostructured ZnO electrodes. Sol Energy Mater Sol Cells 73(1):51–58
39. Kyaw AK (2008) An inverted organic solar cell employing a sol-gel derived ZnO electron selective layer and thermal evaporated MoO3 hole selective layer. Appl Phys Lett 93(22):221107
40. Schmidt H (2009) Efficient semitransparent inverted organic solar cells with indium tin oxide top electrode. Appl Phys Lett 94(24):243302
41. Han S, Shin WS, Seo M, Gupta D, Moon S-J, Yoo S (2009) Improving performance of organic solar cells using amorphous tungsten oxides as an interfacial buffer layer on transparent anodes. Org Electron 10(5):791–797
42. Jiang CY, Sun XW, Zhao DW, Kyaw AKK, Li YN (2010) Low work function metal modified ITO as cathode for inverted polymer solar cells. Sol Energy Mater Sol Cells 94(10):1618–1621
43. Tao C (2008) Performance improvement of inverted polymer solar cells with different top electrodes by introducing a MoO_3 buffer layer. Appl Phys Lett 93(19):193307
44. Xie F (2011) Improving the efficiency of polymer solar cells by incorporating gold nanoparticles into all polymer layers. Appl Phys Lett 99(15):153304
45. Peng B (2011) Performance improvement of polymer solar cells by using a solvent-treated poly(3,4-ethylenedioxythiophene):poly(styrenesulfonate) buffer layer. Appl Phys Lett 98(24):243308
46. Yu G, Gao J, Hummelen JC, Wudl F, Heeger AJ (1995) Polymer photovoltaic cells: enhanced efficiencies via a network of internal donor-acceptor heterojunctions. Science 270(5243):1789–1791
47. Chen L, Tang Y, Fan X, Zhang C, Chu Z, Wang D, Zou D (2009) Improvement of the efficiency of CuPc/C60-based photovoltaic cells using a multistepped structure. Org Electron 10(4):724–728
48. Park SH, Roy A, Beaupre S, Cho S, Coates N, Moon JS, Moses D, Leclerc M, Lee K, Heeger AJ (2009) Bulk heterojunction solar cells with internal quantum efficiency approaching 100%. Nat Photon 3(5):297–302

49. Savenije TJ, Kroeze JE, Yang X, Loos J (2005) The Effect of thermal treatment on the morphology and charge carrier dynamics in a polythiophene–fullerene bulk heterojunction. Adv Funct Mater 15(8):1260–1266
50. Li G, Yao Y, Yang H, Shrotriya V, Yang G, Yang Y (2007) Solvent annealing effect in polymer solar cells based on poly(3-hexylthiophene) and methanofullerenes. Adv Funct Mater 17(10):1636–1644
51. Chen H-Y, Hou J, Zhang S, Liang Y, Yang G, Yang Y, Yu L, Wu Y, Li G (2009) Polymer solar cells with enhanced open-circuit voltage and efficiency. Nat Photon 3(11):649–653
52. Schilinsky P (2002) Recombination and loss analysis in polythiophene based bulk heterojunction photodetectors. Appl Phys Lett 81(20):3885
53. Padinger F, Rittberger RS, Sariciftci NS (2003) Effects of postproduction treatment on plastic solar cells. Adv Funct Mater 13(1):85–88
54. Vanlaeke P, Swinnen A, Haeldermans I, Vanhoyland G, Aernouts T, Cheyns D, Deibel C, D'Haen J, Heremans P, Poortmans J, Manca JV (2006) P3HT/PCBM bulk heterojunction solar cells: relation between morphology and electro-optical characteristics. Sol Energy Mater Sol Cells 90(14):2150–2158
55. Kim Y, Cook S, Tuladhar SM, Choulis SA, Nelson J, Durrant JR, Bradley DDC, Giles M, McCulloch I, Ha C-S, Ree M (2006) A strong regioregularity effect in self-organizing conjugated polymer films and high-efficiency polythiophene: fullerene solar cells. Nat Mater 5(3):197–203
56. Hoppe H, Sariciftci NS (2006) Morphology of polymer/fullerene bulk heterojunction solar cells. J Mater Chem 16(1):45–61
57. Yao Y, Hou J, Xu Z, Li G, Yang Y (2008) Effects of solvent mixtures on the nanoscale phase separation in polymer solar cells. Adv Funct Mater 18(12):1783–1789
58. Li G, Shrotriya V, Huang J, Yao Y, Moriarty T, Emery K, Yang Y (2005) High-efficiency solution processable polymer photovoltaic cells by self-organization of polymer blends. Nat Mater 4(11):864–868
59. Dennler G (2006) Enhanced spectral coverage in tandem organic solar cells. Appl Phys Lett 89(7):073502
60. Janssen AG (2007) Highly efficient organic tandem solar cells using an improved connecting architecture. Appl Phys Lett 91(7):073519
61. Peumans P (2003) Small molecular weight organic thin-film photodetectors and solar cells. J Appl Phys 93(7):3693
62. Kim JY, Lee K, Coates NE, Moses D, Nguyen T-Q, Dante M, Heeger AJ (2007) Efficient tandem polymer solar cells fabricated by all-solution processing. Science 317(5835):222–225
63. Gilot J (2007) Double and triple junction polymer solar cells processed from solution. Appl Phys Lett 90(14):143512
64. Sista S, Hong Z, Park M-H, Xu Z, Yang Y (2010) High-efficiency polymer tandem solar cells with three-terminal structure. Adv Mater 22(8):E77–E80
65. Shrotriya V, Li G, Yao Y, Moriarty T, Emery K, Yang Y (2006) Accurate measurement and characterization of organic solar cells. Adv Funct Mater 16(15):2016–2023

Chapter 2
Active Layer Materials for Organic Solar Cells

Jianhui Hou and Xia Guo

Abstract Organic photovoltaic cell (OPV) has emerged as a new competitor to inorganic material-based solar cells, due to its potential application in large area, printable, and flexible solar panels. In particular, OPV cells with bulk heterojunction architecture (BHJ), in which the photoactive layer consists of a bicontinuous blend of an electron donor and an electron acceptor, has allowed power conversion efficiencies (PCEs) over 8 %. Electron donor and electron acceptor materials, with ideal properties are requisite for reaching high PCE. In this chapter, the relationship between molecular structure and photovoltaic property of active layer materials will be discussed, and also the rules of molecular design of organic photovoltaic materials will be presented. Furthermore, the latest progresses of electron donors and electron acceptors, especially for conjugated polymers and the fullerene derivatives, will be introduced.

2.1 Introduction

An Organic photovoltaic cell (OPV) cell is composed of a film of organic photovoltaic active layer, sandwiched between a transparent electrode and a metal electrode. As a successful branch of OPV, polymer solar cells (PSCs) have attracted much attention. Typically, the active layer PSC device is composed of a blend film of conjugated polymer (as electron donor) and a small molecular acceptor. The conjugated polymer donor and the fullerene derivative acceptor are

J. Hou (✉) · X. Guo
State Key Laboratory of Polymer Physics and Chemistry, Beijing National Laboratory for Molecular Sciences, Institute of Chemistry, Chinese Academy of Sciences, Beijing 100190, China
e-mail: hjhzlz@iccas.ac.cn

W. C. H. Choy (ed.), *Organic Solar Cells*, Green Energy and Technology,
DOI: 10.1007/978-1-4471-4823-4_2,

the key photovoltaic materials for high performance PSCs, and therefore, what are ideal properties and how to get photovoltaic materials with ideal properties are of great importance to photovoltaic materials design.

Bulk heterojunction (BHJ) structure is the most successful structure invented by Yu et al. [1], in which a blend of donor and acceptor with a bicontinual phase separation can be formed. When the sunlight getting through the transparent electrode is absorbed by the semiconducting donor and acceptor materials in the photoactive layer, excitons (bounded electron–hole pairs) are formed, and then the excitons diffuse to the interfaces of the donor/acceptor where the excitons dissociate into electrons on the LUMO level of the acceptor and holes on the HOMO level of the donor. The dissociated electrons and holes are driven by build-in electric field and then moved to negative and positive electrode, respectively, and then collected by the electrodes to realize the photon-to-electron conversion.

Figure 2.1 shows the electronic energy levels of the donor and acceptor in a P3HT/PCBM blend system. The absorption band of P3HT/PCBM covers the range from 380 to 670 nm, which means that the photons with energy between 2.0 and 3.3 eV can be absorbed by the active layer, and the excitons will be formed. In order to make better utilization of the sunlight, active layer materials with broad absorption band is required, and for this purpose, more and more low band gap (LBG) materials have been developed and great successes have been made in the past decade. Since, the LUMO and the HOMO of P3HT is higher than that of PCBM, the excitons will separate into positive and negative charges at the interface of the P3HT phase and PCBM phase. The negative charge will transport through the LUMO of PCBM and the positive charge will transport through the HOMO of P3HT, and then the charges can be collected by the electrodes. In order

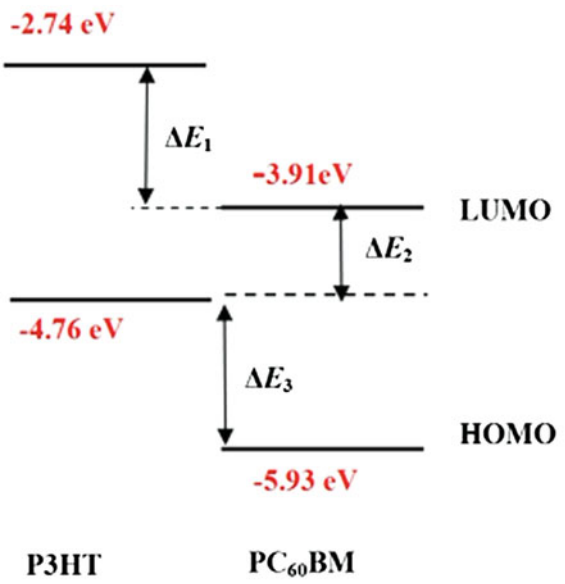

Fig. 2.1 Electronic energy level of P3HT and $PC_{60}BM$

to get efficient charge separation, HOMO and LUMO of the donor material should be 0.2–0.3 eV higher than that of the acceptor material, respectively. If the offset is too small, it would be hard to get efficient charge separation; if the offset is too big, much energy loss would be happened. As known, open-circuit voltage (V_{oc}) of BHJ OPV devices are directly proportional to the gap between HOMO of the donor and LUMO of the acceptor [2]. Although, the energy of the photon that can be utilized by the P3HT/PCBM system is higher than 2.0 eV, V_{oc} of P3HT/PCBM-based OPV device is typically around 0.6 eV, meaning that more than 70 % energy loss is taking place during the photoelectric conversion process. Therefore, to minimize the energy loss, HOMO and LUMO levels of the donors and the acceptors should be tuned carefully.

Furthermore, mobility of the donor and the acceptor materials is also an important issue for organic photovoltaic materials. In comparison with inorganic semiconductors, organic semiconducting materials exhibit much lower mobility, and therefore, how to improve hole or electron mobility of organic photovoltaic materials becomes one of the critical objectives of molecular design of materials. For an organic semiconducting material, both inter- and intra-molecular charge transfer properties are very important. The relationship between intra-molecular charge transfer property and molecular structure is still unclear. To enhance inter-molecular stacking properties has been proven to be an effective way, to improve inter-molecular charge transportation. For examples, the hole mobility of regio-regular P3HT is 2–3 orders higher than regioregular P3HT due to the stronger pi–pi stacking property of the former [3]; to reduce the steric hindrance caused by non-conjugated side chains is also an useful approach to improve the inter-chain pi–pi stacking property of organic semiconducting materials and hence higher mobility can be realized [4].

Besides absorption band, molecular energy levels (HOMO and LUMO), and mobility, there are still many other issues like solubility in different solvents and chemical stability, should be considered in molecular design of organic photovoltaic materials. Therefore, how to balance these properties is the key to get an organic photovoltaic material with ideal properties. Herein, several broadly used material systems will be introduced in this chapter to provide a general profile of molecular structure design of organic photovoltaic materials.

Poly(phenylene vinylene)s (PPV) and Polythiophenes (PTs) are two kinds of classic conjugated polymers which are broadly used in photovoltaic cells and light emitting diodes. MEH-PPV [5] and MDMO-PPV [6], as shown in Scheme 2.1 are two representatives of PPV-based materials. These two PPVs can be used as electron donor materials in solar cells, and they exhibited much similar photovoltaic properties. PCE of $\sim$2 % has been recorded by using MEH-PPV/PCBM-based solar cells. However, the absorption edges of MEH-PPV and MDMO-PPV are at about 550 nm, corresponding to a band gap of ca. 2.3 eV, and output current density of the solar cells based on them was limited due to the big mismatch between their absorption spectra and the solar irradiation spectrum. In comparison with MEH-PPV and MDMO-PPV, P3HT, one of the derivative of poly(3-alkyl-thiophene) exhibits lower band gap, broader absorption band and also better hole

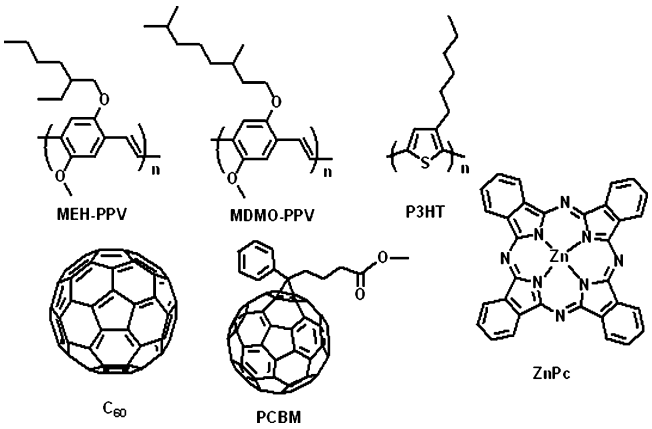

Scheme 2.1 Molecular structures of several representative organic photovoltaic materials

mobility, and therefore, this conjugated polymer exhibited much better photovoltaic properties. By using P3HT as donor material blending with PCBM as acceptor, over 4 % PCE has been well repeated by different research groups, and P3HT has attracted much attention in the OPV filed. Interestingly, photovoltaic properties of P3HT/PCBM system are very sensitive to the morphology of the blend, therefore, morphology study of this system has been well investigated. For example, by using annealing [7], post-annealing [8] or solvent annealing process [9], slow-growth process [10], additives [11], the morphology of the blend can be well controlled and thus photovoltaic performance of the P3HT/PCBM system can be improved. Small molecular organic semiconductors with appropriate properties can also be used as electron donor materials in OPV devices. ZnPc is one of the successful examples. Unlike conjugated polymers, ZnPc has poor solubility in commonly used solvents, thus thermal evaporation method under high vacuum is used to make ZnPc-based solar cells.

Fullerene and its derivatives are broadly used as electron acceptor materials in OPVs. The solubility of unsubstituted fullerene is quite poor, which limits its application in device fabrication process. Therefore, different substituents were introduced onto fullerene. In 1995, Hummelen and Wudl et al. reported a feasible approach to synthesize PCBM ([6,6]-phenyl-C61-butyric acid methyl ester), one of the most successful fullerene derivative, which exhibits excellent photovoltaic properties as electron acceptor material.

Although, $\sim$8 % PCEs have been achieved, efficiency of OPVs is still much lower than inorganic photovoltaic cells. New organic materials with ideal properties are still requisite. Therefore, in the following section, OPV materials will be sorted into different groups based on functions (donor and acceptor) and molecular structures to give a sketch of the relationship between molecular structures and photovoltaic properties.

2.1.1 Band Gap and Molecular Energy Level Control

Polymers, oligomers, and small molecular compounds with conjugated backbones can be used as electron donor material in OPV devices. Although, these three categories of compounds are different, as photovoltaic donor materials, the requirements for their properties are quite similar. Broad absorption bands and appropriate molecular energy levels are first required, and also the strategies used to modulate absorption bands, and molecular energy levels of polymers, oligomers, and small molecular compounds are similar. In this section, conjugated polymers will be used as examples. Band gap (Eg) of conjugated polymer based on the absorption edge obtained at long wavelength direction (Eg = 1240/λedge) is used as a ruler to evaluate the absorption band of conjugated polymers. In order to utilize more sunlight, absorption edge of conjugated polymer should be extended to near-infrared region. Therefore, to find efficient way to lower band gap of conjugated polymer is crucial to molecular design. As known, the band gap and the molecular energy levels (HOMO and LUMO) of a conjugated polymer is closely related to the molecular weight, molecular configuration and conformation, intermolecular interaction, effective conjugating length, and so on, and most of LBG polymers were designed based on these parameters.

Two strategies are well used in molecular design of LBG polymer. To make a conjugated structure with enhanced quinoid structure is an effective way to get LBG material. When a quinoid structure is formed, the conjugation of the backbone will be enhanced and the pi-electrons will be more delocalized, and hence the polymer's band gap will be lowered greatly. For example, molecular structure of 2,1,3-benzothiadiazole (BT) is similar as that of thieno[3,4-b]pyrazine (TPZ) (see Scheme 2.2), but these two components exhibited much different influence on band gaps of conjugated polymers. When TPZ is copolymerized with a conjugated building block, band gap of the resulting polymer is much lower than that of BT-based polymer. For instance, the onset of the absorption spectrum of the alternating copolymer of benzo[1,2-b:4,5-b′]dithiophene (BDT) and BT (PBDTBT in Scheme 2.2) was at $\sim$700 nm, corresponding to a Eg of 1.7 eV; however, the onset of the absorption spectrum of PBDTTPZ was at $\sim$1000 nm, corresponding to a Eg of 1.2 eV. As shown in Scheme 2.2, BT and TPZ are formed by a five-member ring fused with a six-member ring. For PBDTBT, the polymerization was taken place on 4 and 7 positions on the five-member ring of the BT unit; and for PBDTTPZ, the polymerization was taken place on 5 and 7 positions on the six-member ring of the TPZ unit. The quinoid structure of the polymer PBDTTPZ can be stabilized by the six-member ring of the TPZ units, and thus to form a more stable aromatic electron structure for the six-member ring, whereas the electron structure of the five-member ring of BT has no change in its aromatic and quinoid structures. Based on this scheme, it can be seen that the six-member ring of TPZ will stabilize the quinoid structure of the conjugated backbone of the polymer better than the five-member ring of BT, and thus a more stable quinoid structure will be formed in polymer PBDTPTZ than in PBDTBT. Since, the quinoid form

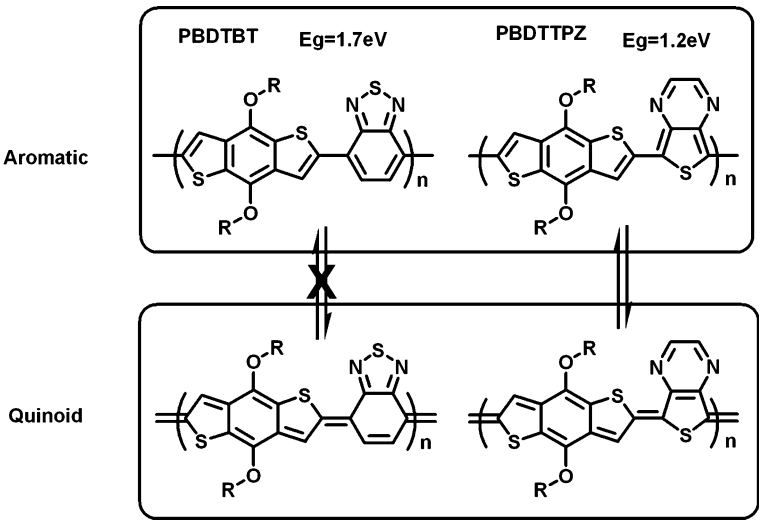

Scheme 2.2 Aromatic and quinoid forms of two conjugated polymers, PBDTBT and PBDTTPZ

has a smaller band gap than the aromatic form [12], the band gap of PBDTTPZ is lower than that of PBDTBT. Besides of TPZ unit, several other conjugated components and their derivatives with strong quinoid characteristics, as shown in Scheme 2.3, can also be used in LBG polymers.

To build a conjugated structure with alternative electron donor and electron acceptor units (D/A structure) is another effective approach to get LBG polymer. Many LBG polymers for solar cells were successfully designed based on this method, but it is still hard to get an exact theoretical calculation for the band gap of a newly designed conjugated structure. As known, the enhanced intra-molecular charge transfer is helpful to get a broadened valance and conducting bands, and hence lower band gap of a conjugated polymer with D/A structure can be reduced by increasing electron donating effect of the electron donor units or by increasing electron withdrawing effect of the electron acceptor units; the band gap of conjugated polymer with D/A structure is also tunable by changing the ratio of the donor and acceptor moieties in the polymer backbone.

2.1.2 Molecular Energy Level

As discussed above, performance of an OPV device is closely related to molecular energy levels of its active layer materials. Therefore, how to modulate HOMO and

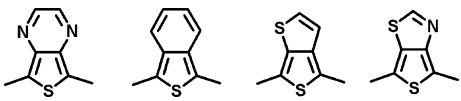

Scheme 2.3 Several aromatic building blocks that can form stable quinoid structures

LUMO levels of active layer materials are very important issue for molecular design. For organic semiconductors, HOMO and LUMO can be tuned by modifying their backbones or side groups. Poly(*p*-phenylene) (PPP) and its derivatives, like polyfluorene (PF), are not electron-rich materials, and hence HOMO levels of this kind of polymers are quite low (typically below −5.3 eV); polymers or oligomers built by electron-rich conjugated components, like thiophene or pyrrole, exhibit much strong electron donating property and hence high HOMO levels. Side groups (substituents on the backbones) have great influence on molecular energy levels of organic semiconductors. The comparison of molecular energy levels of PBDTTT-E, PBDTTT-C, PBDTTT-CF, and PBDTTT-S provides a good example for the effect of side groups. As shown in Scheme 2.4, these four polymers have identical conjugated backbones and different side groups. The basic properties of these four polymers are shown in Table 2.1. From PBDTTT-E to PBDTTT-S, the electron withdrawing effect of side groups were increased stepwise (electron withdrawing effect: ester < carbonyl < carbonyl + F < sulfonyl), and therefore, the HOMO and LUMO levels were gradually lowered.

2.1.3 Mobility Improvement

To improve mobility of an organic semiconductor is a more complicated task, than to modulate its band gap and molecular energy level. In order to get good mobility, several issues should be considered during molecular structure design. Inorganic semiconductors have well-defined crystalline structure and the charges (hole or electron) can be transported easily through the conduction band; for organic semiconductor, the charges are localized due to their low dielectric constants. Therefore, organic semiconductors have much lower mobilities than inorganic semiconductors. Since, the molecules of an organic semiconductor are stacked together by weak forces, like van der Waals force, and the charges are transported through a hopping mode, compact stacking is necessary to facilitate the intermolecular charge transport. For example, regioregular poly(3-alkylthiophene) shows much better hole mobility than its regioregular analog [3].

Band gap, molecular energy level, mobility, solubility, and the other issues of conjugated polymers and small molecular materials are quite susceptible to their

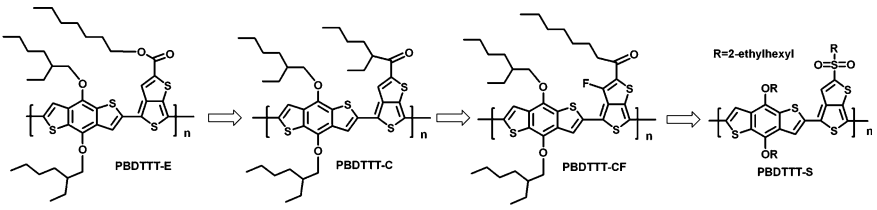

Scheme 2.4 Molecular structures of four PBDTTTs

Table 2.1 Properties and devices characteristics for the BDT-based low band gap polymers

Polymer	Eg(opt) (eV)	HOMO/LUMO (eV/eV)	J_{sc} (mA/cm^2)	V_{oc} (V)	FF	PCE (%)	Refs
PBDTTT-E	1.77	−5.01/− 3.24	13.2	0.62	0.630	5.15	[13]
PBDTTT-C	1.67	−5.12/− 3.35	14.7	0.70	0.641	6.58	[14]
PBDTTT-CF	1.77	−5.22/− 3.45	15.2	0.76	0.669	7.73	[15]
PBDTTT-S	1.63	−5.12/− 3.49	14.1	0.76	0.580	6.22	[16]

molecular structures. Since, it is hard to get a clear and exhaustive conclusion to guide molecular design of photovoltaic materials with conjugated structures, to have a comprehensive understanding of the properties of more organic photovoltaic materials would be the best way to understand the mechanisms of molecular design.

2.2 Active Layer Materials

2.2.1 Electron Donors

Numerous donor materials, including polymers and small molecular compounds, have been developed in the past decades. It is hard to categorize these materials. In this section, polythiophenes were used as an example for polymer materials with homoconjugated backbones; polymers with 2,1,3-benzothiadiazole, pyrrolo[3,4-c]-pyrrole-1,4-dione, and benzo[1,2-b;4,5-b′]dithiophene were used as three examples for molecular structure design of conjugated materials with D/A structures.

2.2.1.1 Polythiophene and Its Derivatives

Poly(3-alkylthiophene)s (P3AT) have been used as active material for optoelectronic devices, especially for photovoltaic cells. As mentioned above, P3HT is the best one in P3ATs as photovoltaic material. Typically, P3ATs can be synthesized easily through different methods. The repeating units of P3ATs were asymmetric, so three relative orientations are available when two thiophene rings are coupled between the 2- and 5-positions (Usually, the 2-position is called as head, and the 5-position is called as tail). So, the first of these is head-to-tail (HT) coupling, the second is head-to-head (HH) coupling, and the third is tail-to-tail (TT) coupling. As shown in Scheme 2.5, this leads to a mixture of four chemically distinct triad regioisomers when 3-substituted (or asymmetric) thiophene monomers are employed [17]. The HT–HT structure of polythiophenes are denoted as regioregular, the other three structures are denoted as regioregular or regiorandom, and

Scheme 2.5 Several polythiophene derivatives

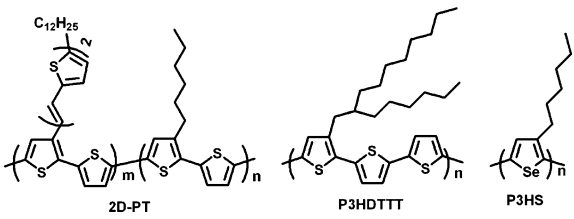

the HT–HT isomer proportion in polymers is named as regioregularity. Regioregular poly(3-substituted thiophene) can easily access a low energy planar conformation, leading to highly conjugated polymers. An increase of the torsion angles between thiophene rings leads to greater band gaps, with consequent destruction of high conductivity and other desirable properties, hence the regioregularity is an important factor in characterization of poly(3-substituted thiophene), and P3HT with high regioregularity (>98 %) is first required for high photovoltaic performance. Currently, the influence of regioregularity on photovoltaic properties of the other polymer systems has not been well studied, but this parameter would be one of the keys to do further improvement of molecular structures.

Although, P3HT exhibited promising photovoltaic properties, the absorption band (from 500 to 650 nm) of this polymer is still not broad enough to get good harvest of the sunlight. Two-dimensional conjugated polythiophenes (2D-PTs) provided a feasible way to broaden absorption band. A representative structure of 2D-PT, absorption band of 2D-PT is formed by two parts [18]. One part located at short wavelength direction is from the conjugated side chain; and another located at long wavelength direction is from the conjugated main chain. By adjusting the conjugated length of the side chain, the absorption peak position at short wavelength direction can be tuned, and by adjusting the *m*:*n* value, a broad and strong absorption band can be obtained. 2D-PTs also exhibited better hole mobilities than P3ATs, and 2 and 3 orders improvement of hole mobilities have been observed in some kinds of 2D-PTs [19].

To replace the alkyl side groups of P3ATs by alkoxy groups is an effective way to reduce the band gap of polythiophenes. Band gaps of poly(3-alkyloxythiophene)s (P3AOTs in Scheme 2.4) are ~1.55 eV, which is much lower than that of P3ATs. Although, P3AOTs have much better absorption band compared to that of P3ATs, P3AOTs are not suitable as electron donors due to their high-lying HOMO levels. Since, the alkoxy has much stronger electron donating effect than alkyl, HOMO levels of P3AOTs were ca. 0.4 eV higher than those of P3ATs. Since, the electron donating effect of side groups of polythiophenes is one of the keys to tune their HOMO levels and alkyls can be seen as weak electron donating groups, to use less alkyl substituents should be helpful to get deep HOMO level. P3HDTTT (see Scheme 2.5) was designed based on this strategy. It can be seen that for P3HT, each thiophene unit has one alkyl; for P3HDTTT, three thiophene units possess one alkyl. As a result, P3HDTTT exhibits deeper HOMO level than that of

P3HT, and thus, a V_{oc} of 0.84 V has been achieved from P3HDTTT/PCBM-based device, which is 0.24 V higher than that of P3HT/PCBM-based device [20].

Another strategy to lower the band gap of rr-P3HT was the synthesis of regioregular poly(3-hexylselenophene) (rr-P3HS). Ballantyne et al. successfully completed the synthesis of this polymer and applied it in OPVs [21]. The optical band gap (i.e., 1.60 eV) of the resulting polymer was much lower than that of the P3HT. The cells were fabricated by following similar conditions as used in P3HT-based devices, and a PCE of 2.7 % was achieved.

2.2.1.2 Polymers with 2,1,3-Benzothiadiazole

2,1,3-Benzothiadiazole (BT) has been widely used as electron deficient building block in conjugated polymers with D/A structure. This category of polymer donors has been extensively studied and showed outstanding photovoltaic performances (the performances of the copolymers are summarized in Table 2.2). As known, thiophene is a typical electron-rich unit with weak aromatic property and hence thiophene derivatives are broadly used as electron donating building blocks in conjugated polymers. Several copolymers, based on derivatives of dithiophene and BT are shown in Scheme 2.6. It can be seen that the dithiophene derivatives shown in Scheme 2.6 possess well planar structures, which were confined by the bridge atoms, like N, C, or Si, or by a planar conjugated unit.

PCPDTBT is the first low band gap polymer which was successfully synthesized and used in PSCs [22, 25]. PCPDTBT has strong and broad absorption band extending to near-infrared region, corresponding to a band gap of 1.50 eV, and this polymer also exhibited a good hole mobility, 1×10^{-3} cm^2/V s by field effect transistor (FET) [23]. Initially, the PCE of PCPDTBT/PCBM system was $\sim$3.2 % [22]. Then, the morphology of the blend was optimized by using diiodooctane (DIO) or 1,8-dithiol-octane (ODT) as additive during the spin-coating process, and hence the PCE was improved to >5 % [26]. Since, the solubility of PCBM in DIO

Table 2.2 Properties and devices characteristics for polymers of Schemes 2.6 and 2.7

Polymer	Eg(opt) (eV)	HOMO/LUMO (eV/eV)	J_{sc} (mA/cm^2)	V_{oc} (V)	FF	PCE (%)	Refs
PCPDTBT	1.40	−5.30/− 3.57	16.2	0.62	0.55	5.5	[26]
PSBTBT	1.37	N.A.	17.3	0.57	0.61	5.9	[24]
PDTPBT	1.43	−4.81/− 3.08	11.9	0.54	0.44	2.8	[30]
PFDTBT	N.A.	N.A.	7.70	1.00	0.54	4.2	[31]
PFSiDTBT	1.86	−5.70/− 3.81	9.40	0.90	0.51	5.4	[32]
PCDTBT	1.88	−5.50/− 3.60	10.6	0.88	0.66	6.1	[33]
PDTPDTBT	1.46	−5.00/− 3.43	9.47	0.52	0.44	2.2	[34]
PCPDTDTBT	1.55	N.A.	8.75	0.60	0.4	2.1	[35]
PBDTDTBT	1.75	−5.31/− 3.44	10.7	0.92	0.57	5.66	[36]
PSiDTBT	1.53	−4.99/− 3.17	10.67	0.62	0.52	3.4	[37]

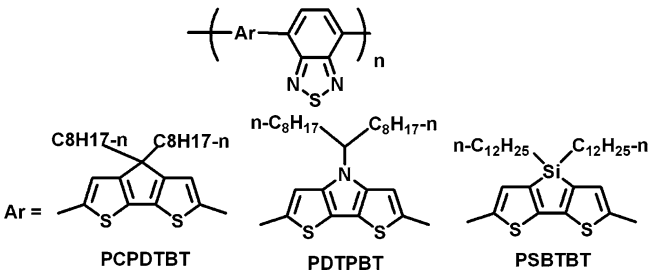

Scheme 2.6 Several representatives of BT-based polymers with D/A structure

is better than that of the polymer, and DIO has much lower vapor pressure than the commonly used solvents during device fabrication process, like *o*-dichlorobenzene (DCB) and chlorobenzene (CB), during the spin-coating process, the polymer can be crystallized or separated from the blended solution while avoiding excessive crystallization of PCBM [27]. This method has been proved to be an effective way to improve photovoltaic properties in many other polymer/PCBM systems, and a lot of good results were developed by using DIO as additive. The success of this method indicates that the morphology control of polymer/PCBM blend is of great importance to OPVs.

A silo-contained polymer, PSBTBT, with similar molecular structure as PCPDTBT was synthesized and also exhibited excellent photovoltaic properties [28]. In PSBTBT, an Si atom was introduced to the bridge point (3, 3′ positions) on the bithiophene unit. Band gap and HOMO level of PSBTBT are 1.55 eV and −5.1 eV [29]. As mentioned above, in PCPDTBT/PCBM blend photovoltaic system, in order to optimize the morphology and hence to get higher performance, additives were necessary during the spin-coating process. For PSBTBT/PCBM blend, thermal annealing less than 140 °C for 15 min was enough to get optimized morphology of the blend. Without annealing, the PCE of PSBTBT/PCBM-based devices were ∼3.5 %; after annealing, the PCE increased to 5.6 %. However, for PCPDTBT/PCBM system, annealing had no help. The interesting phenomenon was ascribed to the difference between atom diameter values of carbon and silicon. As known, the diameter of silicon atom is 50 % bigger than that of carbon, so the bulky alkyl side chains of PCPDTBT is closer to the conjugated backbone than that of PSBTBT. The conjugated backbone of PSBTBT would stack tighter than that of PCPDTBT. Therefore, the former exhibits better hole transport property than the latter [24].

The silicon atom of PSBTBT can also be replaced by a nitrogen atom, and the polymer PDTPBT was obtained [30]. PDTPBT exhibited much lower band gap (1.4 eV) and higher HOMO level (−4.6 eV) than those of PCPDTBT and PSBTBT due to the strong electron donating effect of the amino group. Since, the HOMO level of PDTPBT was higher than the other two analogs, PDTPBT/PCBM-based solar cell exhibited a V_{oc} of ∼0.4 V, which limited its photovoltaic performance tremendously. The polymer PBDTBT exhibited a broader band gap

(1.7 eV) and deeper HOMO level (−5.3 eV) compared to PDTPBT. Although, band gap and HOMO level of PBDTBT are suitable for solar cell and V_{oc} over 0.8 V has been recorded, the photovoltaic performance of PBDTBT/PCBM blend system has not been well optimized, and PCE of this polymer was still below 2 %.

In order to develop more efficient photovoltaic materials, thiophene units were introduced to the 4- and 7-positions of BT, and an important derivative named as DTBT was designed and synthesized. DTBT-based conjugated polymers have been well investigated as photovoltaic materials, and seven representatives are shown in Scheme 2.7. The basic information of these polymers is listed in Table 2.2. It can be seen that the band gaps and as well the HOMO and LUMO levels of polymers were influenced by the electron donating properties of the building blocks. For example, in those seven building blocks, DTP is more electron-rich than the others, and hence the polymer PDTPDTBT exhibited much lower band gap and higher HOMO level than the rest [38]; fluorene unit is the weakest electron donating effect compared to the other building blocks, and therefore, its HOMO level reached −5.5 eV, the lowest one in these DTBT-based polymers [39]. All of these DTBT polymers exhibited very potential photovoltaic properties, and 5–7 % of PCEs have been achieved based on them and some interesting phenomena have been reveals. For instance, V_{oc} values of PFDTBT [39], PCDTBT [40, 41], and PFSiDTBT [42, 43]—based devices were 1, 0.9 and 0.88 V, respectively, which are among the highest values in OPV cells.

2.2.1.3 Pyrrolo[3,4-c]pyrrole-1,4-dione (DPP) Derivatives

DPP and its derivatives, usually have strong absorption bands in the visible range. Thiophene-based DPP derivatives have well-confined conjugated structures, and exhibit good charge-carrier mobilities for both holes and electrons. One of the first

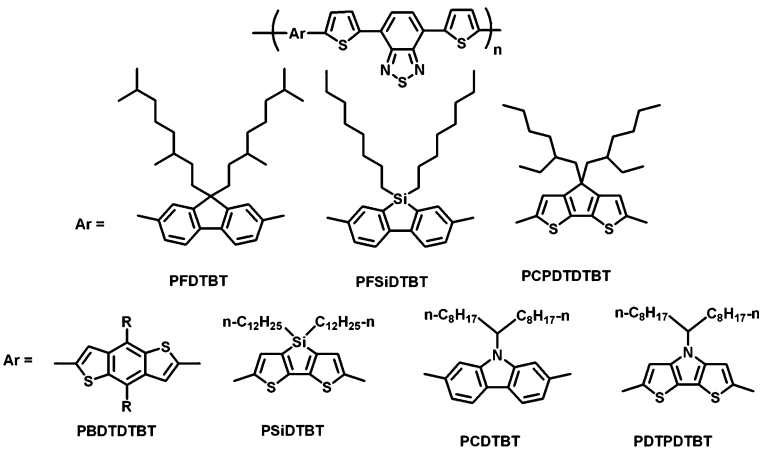

Scheme 2.7 Several representatives of DTBT-based polymers with D/A structure

organic electronic applications for DPP-based polymers was in ambipolar organic FETs. A DPP-based polymer having a mobility of 0.1 $cm^2\ V^{-1}\ s^{-1}$ for both holes and electrons were reported by Winnewisser et al. [44]. On the other hand, the DPP core can be synthesized easily with good yield (see Scheme 2.8). Therefore, DPP-based polymers and small molecular materials attracted much attention and more and more DPP-based photovoltaic materials have been developed in the recent years.

A large number of low band gap polymers have been synthesized since 2008, with the DPP unit and some of them are shown in Scheme 2.8 and their basic properties are listed in Table 2.3. The homopolymer (PDPP) was synthesized through Yamamoto coupling polymerization [45]. The band gap of this polymer is very low (1.24 eV). Moreover, the polymer is stable under ambient condition due to its low-lying HOMO level. However, the PCE of PDPP/PCBM-based solar cell was only 0.3 %. One of the main reasons given by the authors is the energy difference between the LUMO of the donor and the LUMO of the acceptor, which is only 0.18 eV [46, 47]. To extend the conjugation of the backbone, a third thiophene was added as shown in PTDPP. The polymerization was performed via a Suzuki cross-coupling polymerization, using 2,5-thiophenebis(boronic ester) as monomer [48]. The band gap of PTDPP was ~1.30 eV, and a PCE of 4.7 % was recorded (Scheme 2.9).

DPP was also copolymerized with the other commonly used conjugated components. It is worthy to mention that in comparison with DTBT-based polymers, DPP-based polymers possess much lower band gaps. For example, band gap of PFDPP and PCZDPP are 1.77 and 1.57 eV [45, 49], respectively, which are lower than their DTBT-based counterparts (PFDTBT and PCDTBT). Not only DPP-

Scheme 2.8 Synthesis of the DPP core

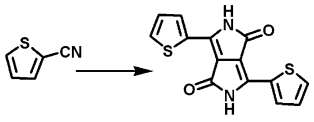

Table 2.3 Polymer properties and device characteristics for the DPP-based polymers

Polymer	Eg(opt) (eV)	HOMO/LUMO (eV/eV)	J_{sc} (mA/cm^2)	V_{oc} (V)	FF	PCE (%)	Refs
PTDPP	1.30	−5.17/− 3.16	11.8	0.65	0.60	4.7	[48]
PFDPP	1.77	−5.43/− 3.67	2.41	0.91	0.41	0.9	[45]
PCPDTDPP	1.39	−5.25/− 3.74	5.73	0.61	0.49	1.7	[45]
PPDTDPP	1.40	−5.10/− 3.40	11.3	0.61	0.58	4.0	[50]
PPPDPP	1.53	−5.35/− 3.53	10.8	0.80	0.65	5.5	[51]
PDPP	1.24	−5.29/− 3.99	0.76	0.64	0.58	0.3	[45]
PCZDPP	1.57	−5.44/− 3.92	8.6	0.80	0.47	3.2	[49]
PFGeDPP	1.63	−5.38/− 3.70	4.10	0.76	0.62	1.5	[52]
PTPDDPP	1.13	−4.90/− 3.63	14.9	0.38	0.48	2.7	[53]
PBDTDPP	1.43	−5.15/− 3.69	6.72	0.74	0.56	2.8	[54]

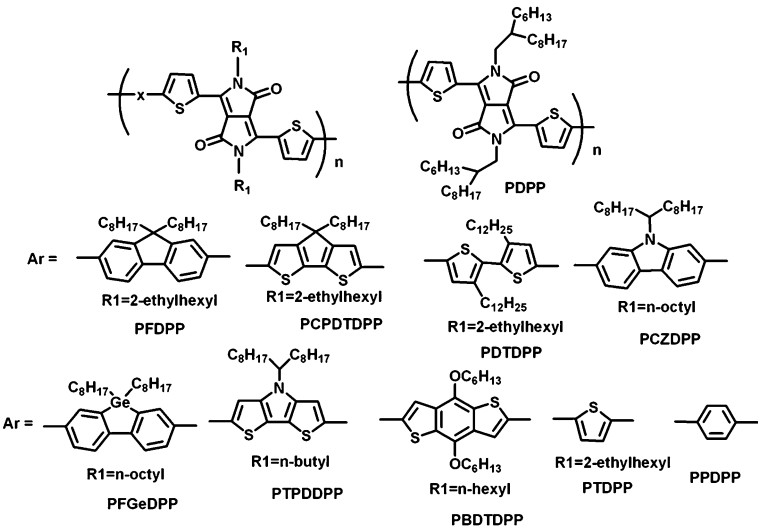

Scheme 2.9 Molecular structures of DPP-based polymers

based polymers, but also DPP-based small molecular compounds exhibited very potential photovoltaic properties. For instance, several solution-processable DPP-based small molecules (1.5−1.8 eV) with PCEs better than 4 % have been reported.

2.2.1.4 Benzo[1,2-b;4,5-b′]dithiophene-Based Polymers

As reported, three kinds of functional groups, including alkoxy, alkyl, and alkylthiophene, were used as side groups on the 4- and 8-positions of the BDT unit to make solution-processable polymers. The alkoxy-substituted BDT can be synthesized easily through a one-pot two-step reaction [55]. Typically, the yield of the alkoxy substituted BDT was between 70 and 90 %. The alkyl-substituted BDT compounds can be synthesized by the three-step reaction as reported [56]. The alkylthiophene-substituted BDT compounds were synthesized by the similar reaction for alkynyl-substituted BDTs, but 2-lithium-5-alkyl-thiophene was used instead of alkynyl lithium [57]. BDT has a symmetric and planar conjugated structure, and hence tight and regular stacking can be expected for the BDT-based conjugated polymers. Therefore, BDT-based polymers were first used in organic field effect transistors (OFETs). In 2007, a BDT-thiophene-based polymer was reported and exhibited a hole mobility of 0.25 $cm^2\ V^{-1}\ s^{-1}$, which was one of the highest values for polymer-based OFET [58] (Scheme 2.10).

Band gap and molecular energy level of BDT-based polymers can be readily tuned in a wide range by copolymerizing with conjugated building blocks with different electron withdrawing effect. Hou et al., first designed and synthesized

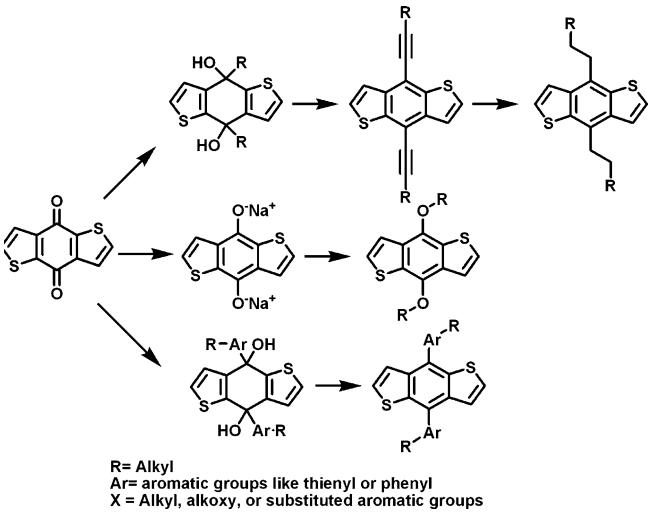

Scheme 2.10 Synthesis of three kinds of substituted BDTs

eight BDT-based polymers, as shown in Scheme 2.11, to investigate the correlation among conjugated backbones, band gaps, and molecular energy levels [59]. Furthermore, the correlation between HOMO levels of those polymers and the V_{oc} values of the devices based on them were also studied in this work. It can be seen that V_{oc} of the devices was directly proportional to the offset between HOMO level of the electron donor material and LUMO level of PCBM. Although, the polymer PBDTTPZ exhibited strong and broad absorption band, but V_{oc} of the PBDTTPZ/PCBM-based device was only 0.2 V due to the high-lying HOMO level of the polymer, meaning that the balance between band gap and HOMO level would be of great importance to the molecular structure design Fig. 2.2.

In the mean time, more and more BDT-based polymers were designed, synthesized, and applied in PSCs. The BDT derivatives were copolymerized with many kinds of building blocks, like derivatives of thiophene, BT and the likes,

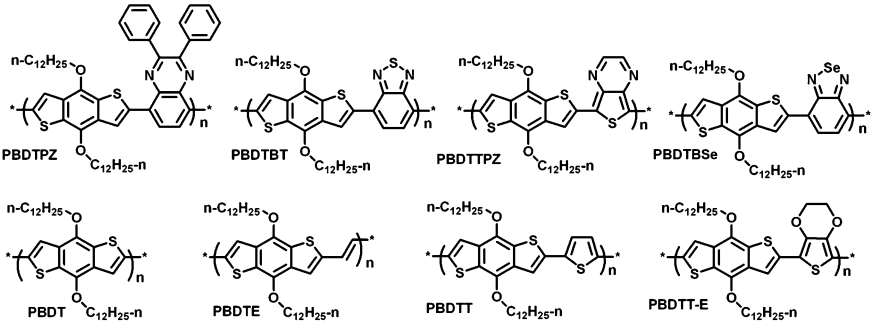

Scheme 2.11 Eight BDT-based polymers with identical BDT moieties

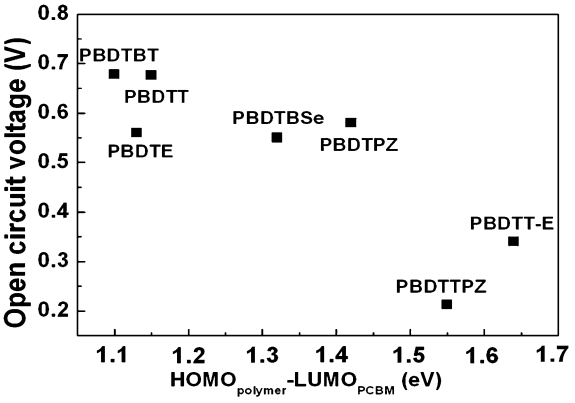

Fig. 2.2 Open-circuit voltage distribution of the devices based on BDT polymers; average values are shown as *squares*

imides and diimide-containing conjugated components. These polymers made great success in PSCs. Molecular structures of several highly efficient BDT-based photovoltaic materials (PCE = ~7 %) were shown in Scheme 2.12, and their basic properties were listed in Table 2.4.

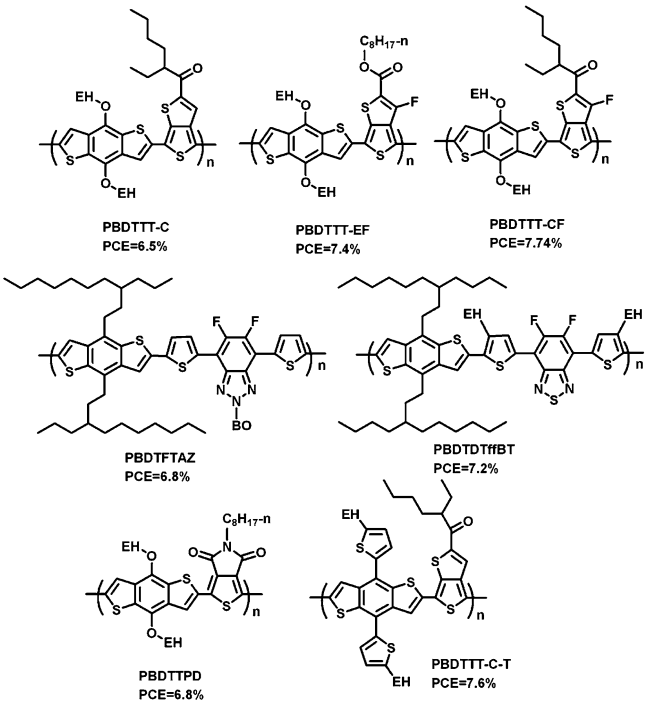

Scheme 2.12 Molecular structures of BDT-based polymers with PCE ~7 %

Table 2.4 Properties and devices characteristics for the BDT-based low band gap polymers

Polymer	Eg(opt) (eV)	HOMO/LUMO (eV/eV)	J_{sc} (mA/cm^2)	V_{oc} (V)	FF	PCE (%)	Refs
PBDT	2.13	−5.16/− 2.67	N.A.	N.A.	N.A.	N.A.	[59]
PBDTE	2.03	−5.07/− 2.86	1.16	0.56	0.38	0.25	[59]
PBDTT	2.06	−5.05/− 2.69	3.78	0.75	0.56	1.60	[59]
PBDTT-E	1.97	−4.56/− 2.66	2.46	0.37	0.40	0.36	[59]
PBDTPZ	1.63	−4.78/− 3.28	1.54	0.60	0.26	0.23	[59]
PBDTBT	1.70	−5.10/–3.19	2.97	0.68	0.44	0.90	[59]
PBDTTPZ	1.05	−4.65/− 3.46	1.41	0.22	0.35	0.11	[59]
PBDTBSe	1.52	−4.88/− 3.33	1.05	0.55	0.32	0.18	[59]
PBDTTT-C	1.61	−5.12/− 3.35	14.7	0.70	0.64	6.58	[14]
PBDTTT-CF	1.60	−5.22/− 3.45	15.2	0.76	0.67	7.73	[15]
PBDTTT-EF	1.63	−5.12/− 3.13	14.5	0.74	0.69	7.4	[60]
PBDTTTPD	1.73	−5.40/N.A.	11.5	0.85	0.70	6.8	[61]
PBDTFTAZ	2.0	−5.36/− 3.05	11.8	0.79	0.73	6.81	[62]
PBDTDTffBT	1.70	−5.54/− 3.33	12.91	0.91	0.61	7.2	[63]
PBDTTT-C-T	1.58	−5.11/− 3.25	17.48	0.74	0.59	7.59	[57]

2.2.2 Electron Acceptors

Organic materials with appropriate properties, including conjugated polymers and small molecular compounds, can be used as electron donor materials in OPV. Many organic compounds exhibited potential properties as electron acceptor material, but only a very few electron acceptor materials can be used in highly efficient OPV devices. Fullerene and its derivatives are the most successful electron acceptor materials.

2.2.2.1 PCBM and the Likes

Fullerene C60 has well-symmetric structure and exhibits good electron mobility, and as known, one molecule of C60 can receive four electrons. Therefore, C60 and its derivatives can be used as electron acceptor materials. In 1992, Sariciftci et al. first used C60 as electron acceptor and discovered the photoinduced ultrafast electron transfer between electron donor and acceptor [64]. Although, C60 can be dissolved in CB and DCB, it exhibits very limited solubility in most of the commonly used organic solvents. In order to improve its solubility and also to avoid severe phase separation of D/A blend, [6,6]-phenyl-C61-butyric acid methyl ester ($PC_{60}BM$) was applied in OPVs. In the past decade, $PC_{60}BM$ and its corresponding C70 derivative ($PC_{70}BM$) has been dominantly used as acceptors in OPVs. In comparison with $PC_{60}BM$, $PC_{70}BM$ possesses stronger absorption in visible range, and hence it attracted much interest recently. However, C70 is much expensive than that of C60 due to its tedious purification process, which limits its application. The molecular structures and the synthetic route of $PC_{60}BM$, $PC_{70}BM$

are shown in Scheme 2.13. $PC_{60}BM$ was crystalline dark-brown powder, and possesses good solubility in common organic solvents such as chloroform, toluene, and *o*-dichlorobenzene [65].

Absorption spectra of PC60BM and PC70BM are shown in Fig. 2.3. It can be seen that both the two materials show strong absorption at ultraviolet region, from 200 to 400 nm, but PC70BM shows stronger absorption in visible region compared to PC60BM. Since, OPV devices using PC70BM as acceptor will harvest more sunlight, many OPVs using PC70BM as acceptor show bigger J_{sc} and hence better PCEs than that of PC60BM-based devices.

The electrochemical properties and energy level of the fullerene derivatives is very important for PSCs. The open-circuit voltage (V_{oc}) of PSCs is determined by the difference between the LUMO energy level of the fullerene acceptors and the HOMO energy level of the polymer donors [66, 67]. Therefore, the LUMO energy level of the fullerene derivatives is a key parameter for the application of an acceptor to match with a polymer donor. LUMO level of electron donors or acceptors can be measured by cyclic voltammogram (CV) method. LUMO level of unsubstituted C60 and PCBM were ~ -4.2 and -4.0 eV, respectively [68, 69]. Based on the difference of the LUMO levels of those two compounds, it is easy to conclude that LUMO level of C60 can be elevated by adding the substituent. As discussed in the above section, higher LUMO level of electron acceptor materials would be helpful to get higher V_{oc}, and for the purpose to get higher LUMO level, the bisadducts and multiadducts of fullerene were used in OPVs. For example, the LUMO level of bis-PCBM was 0.1–0.15 eV higher than that of PCBM, and when bis-PCBM was used as electron acceptor in P3HT-based OPV device, a V_{oc} of 0.72 V was recorded, which was 0.12 V higher than the PCBM/P3HT-based devices [70]. Furthermore, multiadducts can also be used in OPVs, and higher V_{oc} of the device can be realized. However, since the substituent of PCBM is inert for electron transport and the symmetric property of fullerene can be weakened, electron transport properties of the bis- or multiadducts were not as good as that of PCBM. Therefore, PC60BM and PC70BM are still among the best electron acceptors in OPVs. The photovoltaic properties of the fullerene derivatives were studied by fabricating the PSCs based on P3HT as donor and the fullerene derivatives as acceptor, and the results are listed in Table 2.5 [70–72] Scheme 2.14.

Scheme 2.13 Molecular structures of $PC_{60}BM$ and $PC_{70}BM$

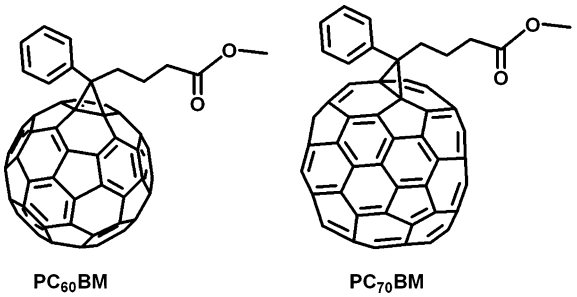

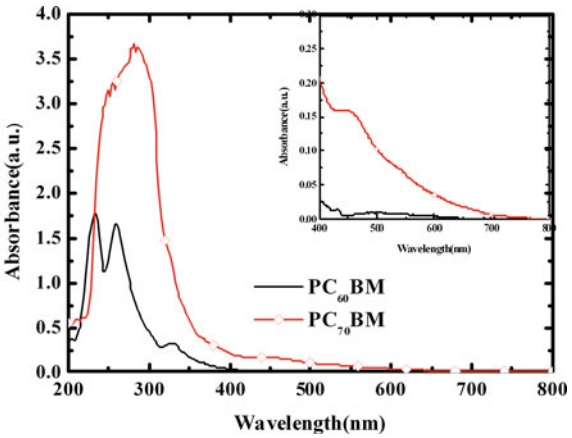

Fig. 2.3 Absorption spectra of $PC_{60}BM$ and $PC_{70}BM$

Table 2.5 Photovoltaic performance of the fullerene multiadduct acceptors

Donor/acceptor (weight ratio)	J_{sc} (mA/cm^2)	V_{oc} (V)	FF	PCE (%)	Refs
P3HT/$PC_{60}BM$(1:0.8)	10.9	0.62	0.62	4.18	[72]
P3HT/bis$ThC_{60}BM$(1:1.2)	5.91	0.72	0.41	1.73	[72]
P3HT/tri$ThC_{60}BM$(1:1.4)	1.88	0.64	0.28	0.34	[72]
P3HT/bis$PC_{60}BM$(1:1.2)	9.14	0.724	0.68	4.5	[71]
P3HT/$PC_{60}BM$(1:1)	8.94	0.61	0.60	2.4	[70]
P3HT/bis$PC_{60}BM$(1:1.2)	7.30	0.73	0.63	2.4	[70]
P3HT/bis$PC_{70}BM$(1:1.2)	7.03	0.75	0.62	2.3	[70]
P3HT/bis$ThC_{60}BM$(1:1.2)	7.31	0.72	0.66	2.5	[70]

2.2.2.2 Indene-C_{60} Bisadduct and Indene-C_{70} Bisadduct (ICBA)

Indene-fullerene adducts were used as electron acceptor materials in OPVs [73–75]. This kind of compounds can be synthesized easily by a one-pot reaction. The solution of indene and fullerene (C60 or C70) in DCB was heated to reflux for several hours, and a mixture of unreacted fullerene, indene-fullerene monoadduct (ICMA), indene-fullerene bisadduct (ICBA), and indene-fullerene multiadduct can be obtained, which can be separated readily through column chromatography. LUMO levels of ICMA and ICBA are −3.86 and −3.74 eV respectively [73]; both are higher than that of PCBM, and thus ICMA/P3HT- and ICBA/P3HT-based devices showed higher V_{oc} than that of P3HT/PCBM-based devices. ICMA has poor solubility in CB or DCB, which limits the photovoltaic performance of the devices; ICBA can be easily dissolved into CB or DCB, and its LUMO level was higher than ICMA and PCBM.

ICBA was successfully used in P3HT-based solar cells. Typically, V_{oc} of P3HT/PCBM system is ∼0.6 V; in P3HT/ICBA system, V_{oc} of 0.84 V can be obtained without sacrificing the other parameters, including FF and J_{sc}. The great increase on V_{oc} should be benefited from the high-lying LUMO of ICBA. The

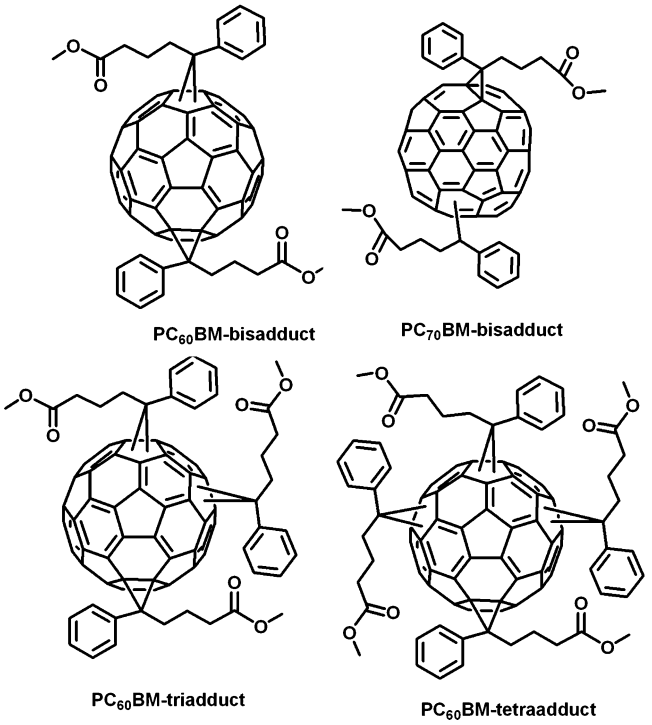

Scheme 2.14 Molecular structures of fullerene multiadduct derivatives

PCE values of the PSCs based on P3HT/IC60BA and P3HT/IC70BA reached 5.44 and 5.64 %, respectively [73, 75], which is more than 40 % increased in comparison with that of the PSCs based on P3HT/PC60BM. After further device optimization, the PSCs based on P3HT/IC60BA displayed a V_{oc} of 0.84 V, a J_{sc} of 10.61 mA cm^{-2}, a FF of 72.7 %, and a PCE of 6.48 % [74]. The photovoltaic properties of the fullerene derivatives were studied by fabricating the PSCs based on P3HT as donor and the fullerene derivatives as acceptor, and the results are listed in Table 2.6 [73–75] Scheme 2.15.

2.2.2.3 Other Fullerenes

In addition to the above-mentioned fullerene derivative acceptors, there are some other fullerene derivatives for application as acceptors in PSCs reported in literature. Such as PC84BM [76] and endohedral fullerenes [77] and so on.

Table 2.6 Photovoltaic performance of the fullerene multiadduct acceptors

Donor/acceptor (weight ratio)	I_{sc} (mA/cm^2)	V_{oc} (V)	FF	PCE (%)	Refs
P3HT/$PC_{60}BM$(1:1)	10.8	0.58	0.62	3.88	[73]
P3HT/$IC_{60}MA$(1:1)	9.66	0.63	0.64	3.89	[73]
P3HT/$IC_{60}BA$(1:1)	9.67	0.84	0.67	5.44	[73]
P3HT/$IC_{60}BA$(1:1)	10.61	0.84	0.73	6.48	[74]
P3HT/$IC_{70}BA$(1:1)	9.73	0.84	0.69	5.64	[75]

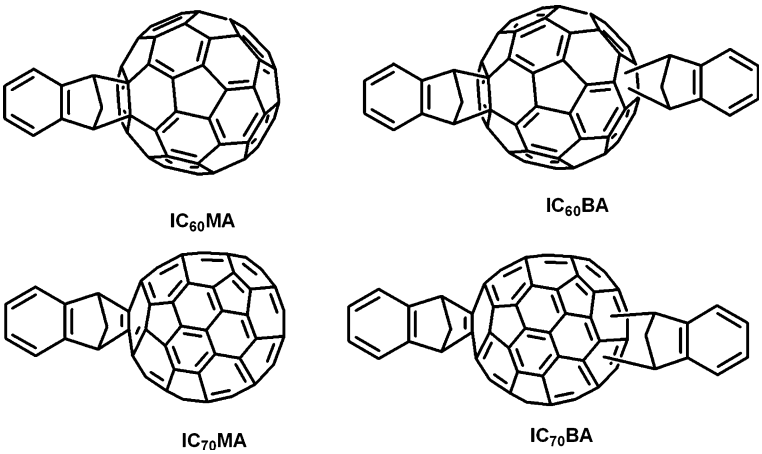

Scheme 2.15 Molecular structures of indene-fullerene adducts

2.3 Conclusion

In the past two decades, a number of organic photovoltaic materials have been designed, synthesized, and applied in OPVs. Although, PCE of OPV cells has been reached over 8 %, the development of active layer materials is still the key to boost the efficiency. In order to get better photovoltaic properties, many properties, like band gap, molecular energy level, mobility, solubility, etc., should be considered, and how to balance these parameters is the most important part to molecular design.

References

1. Yu G, Gao J, Hummelen JC, Wudl F, Heeger AJ (1995) Polymer photovoltaic cells: enhanced efficiencies via a network of internal donor-acceptor heterojunctions. Science 270:1789–1791. doi:10.1126/science.270.5243.1789
2. Scharber MC, Muhlbacher D, Koppe M, Denk P, Waldauf C, Heeger AJ, Brabec CJ (2006) Design rules for donors in bulk-heterojunction solar cells—towards 10% energy-conversion efficiency. Adv Mater 18:789–794. doi:10.1002/adma.200501717

3. Osaka I, Mccullough RD (2008) Advances in molecular design and synthesis of regioregular polythiophenes. Acc Chem Res 41:1202–1214. doi:10.1021/ar800130s
4. Chen MH, Hou JH, Hong Z, Yang G, Sista S, Chen LM, Yang Y (2009) Efficient polymer solar cells with thin active layers based on alternating polyfluorene copolymer/fullerene bulk heterojunctions. Adv Mater 21:4238–4242. doi:10.1002/adma.200900510
5. Shrotriya V, Wu EHE, Li G, Yao Y, Yang Y (2006) Efficient light harvesting in multiple-device stacked structure for polymer solar cells. Appl Phys Lett 88:064104. doi:10.1063/1.2172741
6. Shaheen SE, Brabec CJ, Sariciftci NS, Padinger F, Fromherz T, Hunnelen JC (2001) 2.5% Efficient organic plastic solar cells. Appl Phys Lett 78:841–843. doi:10.1063/1.1345834
7. Ma WL, Yang CY, Gong X, Lee KH, Heeger A (2005) Thermally stable, efficient polymer solar cells with nanoscale control of the interpenetrating network morphology. Adv Funct Mater 15:1617–1622. doi:10.1002/adfm.200500211
8. Moulé AJ, Meerholz K (2008) Controlling morphology in polymer–fullerene mixtures. Adv Mater 20:240–245. doi:10.1002/adma.200701519
9. Li G, Shrotriva V, Huang JS, Yao Y, Moriarty T, Emery K, Yang Y (2005) High-efficiency solution processable polymer photovoltaic cells by self-organization of polymer blends. Nat Mater 4:864–868. doi:10.1038/nmat1500
10. Zhao Y, Xie ZY, Qu Y, Geng YH, Wang L (2007) Organic light emitting device having multiple separate emissive layers. Appl Phys Lett 90: 043504-1–3. doi:10.1063/1.2434173
11. Peet J, Kim JY, Coates NE, Ma WL, Heeger AJ, Moses D, Bazan GC (2007) Efficiency enhancement in low-bandgap polymer solar cells by processing with alkane dithiols. Nat Mater 6:497–500. doi:10.1038/nmat1928
12. Bredas JL (1985) Relationship between band gap and bond length alternation in organic conjugated polymers. J Chem Phys 82:3808–3811. doi:10.1063/1.448868
13. Liang YY, Feng DQ, Wu Y, Tsai ST, Li G, Ray C, Yu LP (2009) Highly efficient solar cell polymers developed via fine-tuning of structural and electronic properties. J Am Chem Soc 131:7792–7799. doi:10.1021/ja901545q
14. Hou JH, Chen HY, Zhang SQ, Chen RI, Yang Y, Wu Y, Li G (2009) Synthesis of a Low Band Gap Polymer and Its Application in Highly Efficient Polymer Solar Cells. J Am Chem Soc 131:5586–15587. doi:10.1021/ja9064975
15. Chen HY, Hou JH, Zhang SQ, Liang YY, Yang GW, Yang Y, Yu LP, Wu Y, Li G (2009) Polymer solar cells with enhanced open-circuit voltage and efficiency. Nat Photon 3:649–653. doi:10.1038/nphoton.2009.192
16. Huang Y, Huo LJ, Zhang SQ, Guo X, Han C, Li YF, Hou JH (2011) Sulfonyl: a new application of electron-withdrawing substituent in highly efficient photovoltaic polymer. Chem Commun 47:8904–8906. doi:10.1039/C1CC12575C
17. Sato M, Morii H (1991) Polym Commun 32:42–44
18. Hou JH, Tan ZA, Yan Y, He YJ, Yang CH, Li YF (2006) Synthesis and photovoltaic properties of two-dimensional conjugated polythiophenes with bi(thienylenevinylene) side chains. J Am Chem Soc 128:4911–4916. doi:10.1021/ja060141m
19. Zhou EJ, Tan Z, Yang Y, Huo LJ, Zou YP, Yang CH, Li YF (2007) Synthesis, hole mobility, and photovoltaic properties of cross-linked polythiophenes with vinylene-terthiophene-vinylene as conjugated bridge. Macromolecules 40:1831–1837. doi:10.1021/ma062633p
20. Hou JH, Chen TL, Zhang SQ, Huo LJ, Sista S, Yang Y (2009) An easy and effective method to modulate molecular energy level of poly(3-alkylthiophene) for high voc polymer solar cells. Macromolecules 42:9217–9219. doi:10.1021/ma902197a
21. Ballantyne AM, Chen L, Nelson J, Bradley DDC, Astuti Y, Maurano A, Shuttle CG, Durrant JR, Heeney M, Duffy W, McCulloch I (2007) Studies of highly regioregular poly(3-hexylselenophene) for photovoltaic applications. Adv Mater 19:4544–4547. doi:10.1002/adma.200701265
22. Muhlbacher D, Scharber M, Morana M, Zhu Z, Waller D, Gaudiana R, Brabec C (2006) High photovoltaic performance of a low-bandgap polymer. Adv Mater 18:2884–2889. doi:10.1002/adma.200600160

23. Tsao HN, Cho D, Andreasen JW, Rouhanipour A, Breiby DW, Pisula W, Mullen K (2009) The influence of morphology on high-performance polymer field-effect transistors. Adv Mater 21:209–212. doi:10.1002/adma.200802032
24. Coffin RC, Peet J, Rogers J, Bazan GC (2009) Streamlined microwave-assisted preparation of narrow-bandgap conjugated polymers for high-performance bulk heterojunction solar cells. Nat Chem 1:657–661. doi:10.1038/NCHEM.403
25. Zhu ZG, Waller D, Gaudiana R, Morana M, Mühlbacher D, Scharber M, Brabec C (2007) Panchromatic conjugated polymers containing alternating donor/acceptor units for photovoltaic applications. Macromolecules 40:1981–1986. doi:10.1021/ma062376o
26. Peet J, Kim JY, Coates NE, Ma WL, Moses D, Heeger AJ, Bazan GC (2007) Efficiency enhancement in low-bandgap polymer solar cells by processing with alkane dithiols. Nat Mater 6:497–500. doi:10.1038/nmat1928
27. Su MS, Kuo CY, Yuan MC, Jeng US, Su CJ, Wei KH (2011) Improving device efficiency of polymer/fullerene bulk heterojunction solar cells through enhanced crystallinity and reduced grain boundaries induced by solvent additives. Adv Mater 23:3315–3319. doi:10.1002/adma.201101274
28. Hou J, Chen HY, Zhang S, Li G, Yang Y (2008) Synthesis, characterization, and photovoltaic properties of a low band gap polymer based on silole-containing polythiophenes and 2,1,3-benzothiadiazole. J Am Chem Soc 130:16144–16145. doi:10.1021/ja806687u
29. Chen HY, Hou J, Hayden AE, Yang H, Houk KN, Yang Y (2010) Silicon atom substitution enhances interchain packing in a thiophene-based polymer system. Adv Mater 22:371–375. doi:10.1002/adma.200902469
30. Yue W, Zhao Y, Shao S, Tian H, Xie Z, Geng Y, Wang F (2009) Novel NIR-absorbing conjugated polymers for efficient polymer solar cells: effect of alkyl chain length on device performance. J Mater Chem 19:2199–2206. doi:10.1039/b818885h
31. Chen MH, Hou J, Hong Z, Yang G, Sista S, Chen LM, Yang Y (2009) Efficient polymer solar cells with thin active layers based on alternating polyfluorene copolymer/fullerene bulk heterojunctions. Adv Mater 21:4238–4242. doi:10.1002/adma.200900510
32. Wang E, Wang L, Lan L, Luo C, Zhuang W, Peng J, Cao Y (2008) High-performance polymer heterojunction solar cells of a polysilafluorene derivative. Appl Phys Lett 92: 033307-1–3. doi:10.1063/1.2836266
33. Blouin N, Michaud A, Gendron D, Wakim, Blair E, Neagu-Plesu R, Belletete M, Durocher G, Tao Y, Leclerc M (2008) Toward a rational design of poly(2,7-carbazole) derivatives for solar cells. J Am Chem Soc 130:732–733. doi:10.1021/ja0771989
34. Zhou EJ, Nakamura M, Nishizawa T, Zhang Y, Wei QS, Tajima K, Yang CH, Hashimoto K (2008) Synthesis and photovoltaic properties of a novel low band gap polymer based on n-substituted dithieno[3,2-b:2′,3′-d]pyrrole. Macromolecules 41:8302–8305. doi:10.1021/ma802052w
35. Moulé J, Tsami A, Bünnagel TW, Forster M, Kronenberg NM, Scharber M, Koppe M, Morana M, Brabec CJ, Meerholz K, Scherf U (2008) Two novel cyclopentadithiophene-based alternating copolymers as potential donor components for high-efficiency bulk-heterojunction-type solar cells. Chem Mater 20:4045–4050. doi:10.1021/cm8006638
36. Huo LJ, Hou JH, Zhang SQ, Chen HY, Yang YA (2010) Polybenzo[1,2-b:4,5-b′]dithiophene derivative with deep homo level and its application in high-performance polymer solar cells. Angew Chem Int Ed 49:1500–1503. doi:10.1002/anie.200906934
37. Huo LJ, Guo X, Li YF, Hou JH (2011) Synthesis of a polythieno[3,4-b]thiophene derivative with a low-lying HOMO level and its application in polymer solar cells. Chem Commun 47:8850–8852. doi:10.1039/c1cc12643a
38. Liu J, Zhang R, Sauve G, Kowalewski T, McCullough RD (2008) Highly disordered polymer field effect transistors: n-alkyl dithieno[3,2-b:2',3'-d]pyrrole-based copolymers with surprisingly high charge carrier mobilities. J Am Chem Soc 130:13167–13176. doi:10.1021/ja803077v

39. Slooff LH, Veenstra SC, Kroon JM, Moet DJD, Sweelssen J, Koetse MM (2007) Determining the internal quantum efficiency of highly efficient polymer solar cells through optical modeling. Appl Phys Lett 90: 143506-1–3. doi:10.1063/1.2718488
40. Blouin N, Michaud A, Leclerc M (2007) A low-bandgap poly(2,7-carbazole) derivative for use in high-performance solar cells. Adv Mater 19:2295–2300. doi:10.1002/adma.200602496
41. Blouin N, Michaud A, Gendron D, Wakim S, Blair E, Neagu-Plesu R, Belletete M, Durocher G, Tao Y, Leclerc M (2008) Toward a rational design of poly(2,7-carbazole) derivatives for solar cells. J Am Chem Soc 130:732–742. doi:10.1021/ja0771989
42. Boudreault PLT, Michaud A, Leclerc MA (2007) New poly(2,7-dibenzosilole) derivative in polymer solar cells. Macromol Rapid Commun 28:2176–2179. doi:10.1002/marc.200700470
43. Wang E, Wang L, Lan L, Luo C, Zhuang W, Peng J, Cao Y (2008) High-performance polymer heterojunction solar cells of a polysilafluorene derivative. Appl Phys Lett 92:033307-1–3. doi:10.1063/1.2836266
44. Burgi L, Turbiez M, Pfeiffer R, Bienewald F, Kirner HJ, Winnewisser C (2008) High-mobility ambipolar near-infrared light-emitting polymer field-effect transistors. Adv Mater 20:2217–2224. doi:10.1002/adma.200702775
45. Zoombelt AP, Mathijssen SGJ, Turbiez MGR, Wienk MM, Janssen RAJ (2010) Small band gap polymers based on diketopyrrolopyrrole. J Mater Chem 20:2240–2246. doi:10.1039/b919066j
46. Zoombelt AP, Fonrodona M, Wienk MM, Sieval AB, Hummelen JC, Janssen RA (2009) Photovoltaic performance of an ultrasmall band gap polymer. J Org Lett 11:903–906. doi:10.1021/ol802839z
47. Zoombelt AP, Fonrodona M, Turbiez MGR, Wienk MM, Janssen RAJ (2009) Synthesis and photovoltaic performance of a series of small band gap polymers. J Mater Chem 19:5336–5342. doi:10.1039/b821979f
48. Bijleveld JC, Zoombelt AP, Mathijssen SGJ, Wienk MM, Turbiez M, de Leeuw DM, Janssen RAJ (2009) Poly(diketopyrrolopyrrole-terthiophene) for ambipolar logic and photovoltaics. J Am Chem Soc 131:16616–16617. doi:10.1021/ja907506r
49. Zou YP, Gendron D, Aich RB, Najari A, Tao Y, Leclerc M (2009) High-mobility low-bandgap poly(2,7-carbazole) derivative for photovoltaic. applications. Macromolecules 42:2891–2894. doi:10.1021/ma900119x
50. Wienk MM, Turbiez M, Gilot J, Janssen RA (2008) Narrow-bandgap diketo-pyrrolo-pyrrole polymer solar cells: the effect of processing on the performance. J Adv Mater 20:2556–2560. doi:10.1002/adma.200800456
51. Bijleveld JC, Gevaerts VS, Di Nuzzo D, Turbiez M, Mathijssen SGJ, de Leeuw DM, Wienk MM, Janssen RAJ (2010) Efficient solar cells based on an easily accessible diketopyrrolopyrrole polymer. Adv Mater 22:E242–E246. doi:10.1002/adma.201001449
52. Allard N, Aich RB, Gendron D, Boudreault PLT, Tessier C Alem S, Tse SC, Tao Y, Leclerc M (2010) Germafluorenes: new heterocycles for plastic electronics. Macromolecules 43:2328–2333. doi:10.1021/ma9025866
53. Zhou E, Wei Q, Yamakawa S, Zhang Y, Tajima K, Yang C, Hashimoto K (2010) Diketopyrrolopyrrole-based semiconducting polymer for photovoltaic device with photocurrent response wavelengths up to 1.1 μm. Macromolecules 43:821–826. doi:10.1021/ma902398q
54. Kanimozhi C, Balraju P, Sharma GD, Patil S (2010) Synthesis of diketopyrrolopyrrole containing copolymers: a study of their optical and photovoltaic properties. J Phys Chem B 114:3095–3103. doi:10.1021/jp909183x
55. Hou J, Park MH, Zhang S, Yao Y, Chen LM, Li JH, Yang Y (2008) Bandgap and molecular energy level control of conjugated polymer photovoltaic materials based on benzo[1,2-b:4,5-b′]dithiophene. Macromolecules 41:6012–6018. doi:10.1021/ma800820r
56. Pan H, Li Y, Wu Y, Liu P, Ong BS, Zhu S, Xu G (2006) Synthesis and thin-film transistor performance of poly(4,8-didodecylbenzo[1,2-b:4,5-b′]dithiophene. Chem Mater 18:3237–3241. doi:10.1021/cm0602592

57. Huo LJ, Zhang SQ, Guo X, Xu F, Li YF, Hou JH (2011) Replacing alkoxy groups with alkylthienyl groups: a feasible approach to improve the properties of photovoltaic polymers. Angew Chem Int Ed 50:9697–9702. doi:10.1002/anie.201103313
58. Pan H, Li Y, Wu Y, Liu P, Ong BS, Zhu S, Xu G (2007) Low-temperature, solution-processed, high-mobility polymer semiconductors for thin-film transistors. J Am Chem Soc 129:4112–4113. doi:10.1021/ja067879o
59. Hou JH, Park MH, Zhang SQ, Yao Y, Chen LM, Li JH, Yang Y (2008) Bandgap and molecular energy level control of conjugated polymer photovoltaic materials based on benzo[1,2-b:4,5-b′]dithiophene. Macromolecules 41:6012–6018. doi:10.1021/ma800820r
60. Liang YY, Yu LP (2010) A new class of semiconducting polymers for bulk heterojunction solar cells with exceptionally high performance. Acc Chem Res 43:1227–1236. doi:10.1021/ar1000296
61. Piliego C, Holcombe TW, Douglas JD (2010) Synthetic Control of Structural Order in N-Alkylthieno[3,4-c]pyrrole-4,6-dione-Based Polymers for Efficient Solar Cells. J Am Chem Soc 132:7595–7597. doi:10.1021/ja103275u
62. Price SC, Stuart AC, Yang LQ (2011) Fluorine substituted conjugated polymer of medium band gap yields 7% efficiency in polymer—fullerene solar cells. J Am Chem Soc 133:4625–4631. doi:10.1021/ja1112595
63. Zhou HX, Yang LQ, Stuart AC (2011) Development of fluorinated benzothiadiazole as a structural unit for a polymer solar cell of 7% efficiency. Angew Chem Int Ed 50:2995–2998. doi:10.1002/anie.201005451
64. Sariciftci NS, Smilowitz L, Heeger AJ, Wudl F (1992) Photoinduced electron transfer from a conducting polymer to buckminsterfullerene. Science 258:1474–1476. doi:10.1126/science.258.5087.1474
65. Hummelen JC, Knight BW, Lepeq F, Wudl F (1995) Preparation and characterization of fulleroid and methanofullerene derivatives. J Org Chem 60:532–538. doi:10.1021/jo00108a012
66. Brabec CJ, Sariciftci NS, Hummelen JC (2001) Plastic solar cells. origin of the open circuit voltage of plastic solar cells. Adv Funct Mater 11:15–26. doi:1616-301X/01/0510-0379
67. Scharber MC, Wuhlbacher D, Koppe M (2006) Design rules for donors in bulk-heterojunction solar cells—towards 10% energy-conversion efficiency. Adv Mater 18:789–794. doi:10.1002/adma.200501717
68. Sariciftci NS, Braun D, Zhang C, Srdanov VI, Heeger AJ, Stucky G, Wudl F (1993) Semiconducting polymerbuckminsterfullerene heterojunctions: diodes, photodiodes, and photovoltaic cells. Appl Phys Lett 62:585–587. doi:10.1063/1.108863
69. He YJ, Li YF (2011) Fullerene derivative acceptors for high performance polymer solar cells. Phys Chem Chem Phys 13:1970–1983. doi:10.1021/ja103275u
70. Lenes M, Shelton SW, Sieval AB, Kronholm DF, Hummelen JC, Blom PWM (2009) Electron trapping in higher adduct fullerene-based solar cells. Adv Funct Mater 19:3002–3007. doi:10.1002/adfm.200900459
71. Lenes M, Wetzelaer G, Kooist FB, Veenstra SJJC, Blom PWM (2008) Fullerene bisadducts for enhanced open-circuit voltages and efficiencies in polymer solar cells. Adv Mater 20:2116–2119. doi:10.1002/adma.200702438
72. Choi JH, Son KI, Kim T, Kim K, Ohkubo K, Fukuzumi S (2010) Thienyl-substituted methanofullerene derivatives for organic photovoltaic cells. J Mater Chem 20:475–482. doi:10.1039/B916597E
73. He YJ, Chen HY, Hou JH, Li YF (2010) Indene—C60 bisadduct: a new acceptor for high-performance polymer solar cells. J Am Chem Soc 132:1377–1382. doi:10.1021/ja908602j
74. Zhao GJ, He YJ, Li YF (2010) 6.5% efficiency of polymer solar cells based on poly(3-hexylthiophene) and indene-C60 bisadduct by device optimization. Adv Mater 22:4355–4358. doi:10.1002/adma.201001339
75. He YJ, Zhao GJ, Peng B, Li YF (2010) High-yield synthesis and electrochemical and photovoltaic properties of indene-c70 bisadduct. Adv Funct Mater 20:3383–3389. doi:10.1002/adfm.201001122

76. Kooistra FB, Mihailetchi VD, Popescu LM, Kronholm D, Blom PWM, Hummelen JC (2006) New C84 derivative and its application in a bulk heterojunction. Solar Cell Chem Mater 18:3068–3073. doi:10.1021/cm052783z
77. Stevenson S, Rice G, Glass T, Harich K, Cromer F, Jordan MR, Craft J, Hadju E, Bible R, Olmstead MM, Maitra K, Fisher AJ, Balch A, Dorn HC (1999) Small-bandgap endohedral metallofullerenes in high yield and purity. Nature 401:55–57. doi:10.1038/43415

Chapter 3
Interface Engineering for High Performance Bulk-Heterojunction Polymeric Solar Cells

Chunhui Duan, Chengmei Zhong, Fei Huang and Yong Cao

Abstract The nature of electrical contact between the bulk-heterojunction (BHJ) layer and the electrodes is critical to the overall performance and stability of polymer solar cells (PSCs). In recent years, considerable efforts have been devoted to the interface engineering of BHJ–PSCs. In this chapter, we reviewed the development of interface modification materials and their applications in BHJ–PSCs. The discussions were divided into several sections according to the device configuration of BHJ–PSCs, i.e., conventional device, inverted device, and tandem device. For single junction devices (including conventional and inverted devices), we highlighted the interface modification materials which were applied at both electron-collecting and hole-collecting electrodes, including inorganic materials (such as metals, salts, semiconducting oxides, etc.), self-assembled monolayers (SAMs) or SAMs-modified functional layers, and organic/polymeric materials. For tandem devices, the discussions were focused on the functional materials utilized as intermediate connectors. As discussed in this chapter, the development of interface modification materials has resulted in great progress in BHJ–PSCs, which can potentially pave the way for the commercialization of BHJ–PSCs.

3.1 Introduction

Bulk-heterojunction (BHJ) polymer solar cell (PSC) is one of the most promising photovoltaic techniques to directly convert the terrestrial solar radiation into electricity because of their compatibility with low-cost, large-scale fabrication by

C. Duan · C. Zhong · F. Huang (✉) · Y. Cao
State Key Laboratory of Luminescent Materials and Devices, Institute of Polymer Optoelectronic Materials and Devices, South China University of Technology, Guangzhou 510640, P. R. China
e-mail: msfhuang@scut.edu.cn

W. C. H. Choy (ed.), *Organic Solar Cells*, Green Energy and Technology,
DOI: 10.1007/978-1-4471-4823-4_3,

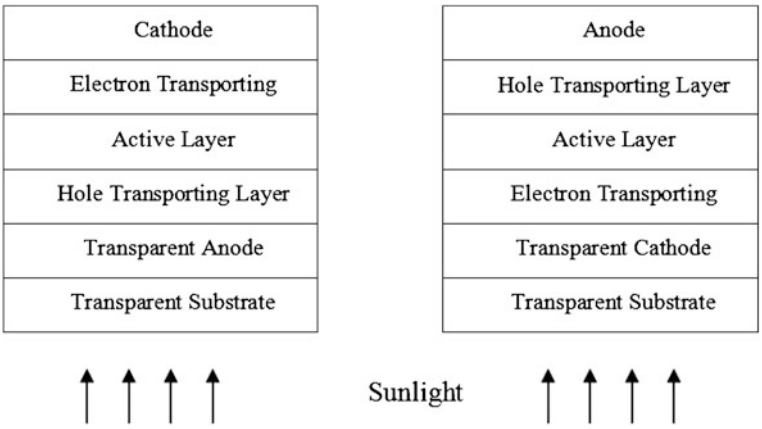

Fig. 3.1 Comparison of conventional device structure (*left*) and inverted device structure (*right*) for BHJ–PSCs

solution processing [1–3]. In the last two decades, great progress in the field of BHJ–PSCs has been achieved with the power conversion efficiency (PCE) increasing from around 1 % to more than 9 % [4]. Such great advancement was driven by the efforts in various aspects including the development of new low-band-gap conjugated polymers and new fullerene-based acceptor materials [5–7], the usage of new device processing methods [8–10], the invention of new device structures [11, 12], the application of innovative interface modification materials [13–15], and so forth. The simplest structure of BHJ–PSC is the so-called sandwich device structure, where the blend of conjugated polymer donor and fullerene derivative acceptor was sandwiched between a transparent metal oxide, such as indium tin oxide (ITO), and a metal electrode [16]. For conventional devices, ITO and low work-function metal are used as anode and cathode, respectively. While in an inverted device, the modified ITO and high work-function metal are cathode and anode, respectively. The configurations of conventional and inverted device for BHJ–PSCs are demonstrated in Fig. 3.1. It is well-known that the nature of electrical contact between the organic active layer and the electrodes is critical to the overall device performance, for both the conventional and inverted devices [13–15]. The ideal Ohmic contact in the organic blend layer/electrode interface with an energy barrier height as low as possible is thus desired for efficient charge carrier extraction and transport, and thereby reduce the recombination loss caused by the accumulation of charge in the interface. Indeed, a barrier height of several tens of mV may lead to severe charge accumulation. Therefore, the modification of organic active layer/electrode interface is critical to achieve high efficiency and long-term stability for BHJ–PSCs. As a result, in recent years, a lot of efforts from research groups all around the world are devoted to the development of new interfacial materials with different functions and their applications. The aim is to achieve high PCE and long-term stability for BHJ–PSC devices [13–15].

In principle, ideal interfacial materials should first function as charge extraction or transporting layer to minimize the barrier height in organic active layer/electrode interfaces, which will help to form Ohmic contact in interface to reduce recombination loss and consequently obtain enhanced short circuit current density (J_{sc}). Additionally, this layer should also function as exciton blocking layer to selectively transport only one type of carrier and block the other, i.e., an electron extraction/transporting layer with hole blocking property, and a hole extraction/transporting layer with electron-blocking ability. Moreover, the interfacial layer usually functions as buffer layer to prevent the chemical reaction between organic active layer and metal electrode, and the diffusion of metal ions into organic layer. Furthermore, it was found that some interfacial materials can also function as optical spacers to modulate the incident light distribution in BHJ–PSCs, so that the maximum incident light intensity located around the center of the active layer to ensure as much as incident light harvested by the device and consequently to obtain maximum J_{sc} [13, 15].

In this chapter, we will review interfacial materials applied at the interfaces between organic active layer and electrodes, including both anode and cathode, and their influence on the photovoltaic performance of BHJ–PSC devices. The design of interfacial materials and their applications will be divided into several sections by the device structure, including conventional device, inverted device, and tandem device. For single junction devices (including conventional and inverted devices), the interfacial materials applied at both cathode and anode will be separately reviewed in the categories of inorganic materials (including metals, salts, semiconducting oxides, etc.), self-assembled monolayers (SAMs) or SAMs modified functional layers, as well as organic/polymeric materials. For tandem devices, we will focus on the functional materials used as intermediate connectors.

3.2 Interface Engineering for Conventional Solar Cell Devices

3.2.1 Cathode Interlayer

For a conventional BHJ–PSC, the efficient electron extraction at cathode is of critical importance for the high J_{sc} and the overall photovoltaic performance. Aluminum (Al) is a most widely used electrode materials for BHJ–PSCs because of its abundance and proper work function of 4.3 eV, which is very close to the lowest unoccupied molecular orbital (LUMO) energy levels of acceptor materials such as (6,6)-phenyl-C_{61}-butylric acid methyl ester ($PC_{61}BM$) and (6,6)-phenyl-C_{71}-butylric acid methyl ester ($PC_{71}BM$) (see Scheme 3.1). However, the organic optoelectronic devices with Al cathode usually suffer from poor stability, because the reactive hot Al atoms generated at the thermal evaporation process can diffuse into the organic layer and result in chemical reaction at the metal/organic interface [17, 18]. Moreover, it was reasoned that Al–C bond formation at the Al/organic

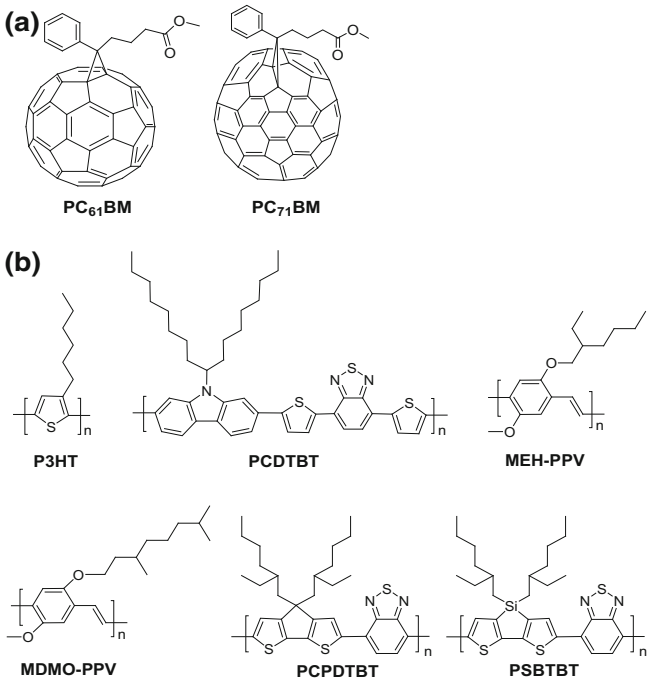

Scheme 3.1 Chemical structures of the most widely used (**a**) acceptors ($PC_{61}BM$ and $PC_{71}BM$) and (**b**) donors (P3HT, PCDTBT, MEH-PPV, MDMO-PPV, PCPDTBT, and PSBTBT)

interface can inevitably break the π-conjugated system of organic layer, and thereby lead to poor stability of Al cathode [19, 20]. Hence, various interfacial materials were inserted into the organic active layer/Al junction to improve the interface contact properties and thereby photovoltaic performance of BHJ–PSCs. The summary of performance of conventional PSCs using different cathode interlayer designs are listed in Table 3.1 and the chemical structures of organic materials used as cathode interlayer in conventional PSCs are shown in Scheme 3.2.

3.2.1.1 Metal and Inorganic Compounds as Cathode Interlayer

Low work-function metals, such as calcium (Ca) or barium (Ba), which were two widely used interfacial materials for polymeric light-emitting diodes (PLEDs) [21, 22], were also usually inserted into the interface between Al and organic active layer to further improve the device performance via the formation of ideal Ohmic contact at interface. The BHJ–PSCs with a thin layer of Ca or Ba between Al and organic active layer usually exhibited superior device performance, especially open circuit voltage (V_{oc}) with respect to PSCs with bare Al as cathode.

Table 3.1 Summary of device characteristics of representative conventional PSCs employing different cathode interlayers

Cathode	Anode	Active layer	PCE	J_{sc} (mA cm^{-2})	V_{oc} (V)	FF	Ref
Ca/Al	ITO/PEDOT:PSS	P3HT:$PC_{61}BM$	4.37	10.60	0.61	0.67	[9]
LiF/Al	ITO/PEDOT:PSS	MDMO-PPV:$PC_{61}BM$	2.50	5.25	0.82	0.61	[23]
Cs_2CO_3/Al	ITO/PEDOT:PSS	P3HT:$PC_{61}BM$	3.10	9.50	0.56	0.60	[30]
TiO_x/Al	ITO/PEDOT:PSS	P3HT:$PC_{61}BM$	5.00	11.10	0.61	0.66	[36]
TiO_x/Al	ITO/PEDOT:PSS	PCDTBT:$PC_{71}BM$	6.10	10.60	0.88	0.66	[37]
ZnO/SAM/Al	ITO/PEDOT:PSS	P3HT:$PC_{61}BM$	4.21	11.61	0.65	0.55	[40]
PEO/Al	ITO/PEDOT:PSS	APFO-5:$PC_{61}BM$	1.84	4.00	0.90	0.51	[45]
PFNBr-DBT15/Al	ITO/PEDOT:PSS	PFO-DBT35:$PC_{61}BM$	1.9	3.9	0.95	0.39	[48]
WPF-6-oxy-F/Ag	ITO/PEDOT:PSS	P3HT:$PC_{61}BM$	3.69	9.86	0.64	0.58	[52]
PFN/Al	ITO/PEDOT:PSS	PECz-DTQx:$PC_{71}BM$	6.07	11.4	0.81	0.66	[54]
PF-*b*-P3TMAHT/Al	ITO/PEDOT:PSS	PCDTBT:$PC_{71}BM$	6.2	10.6	0.89	0.67	[56]
$SnCl_2Pc$/LiF/Al	ITO/PEDOT:PSS	MEH-PPV:$PC_{61}BM$	2.49	6.77	0.82	0.45	[57]
F-PCBM/Al	ITO/PEDOT:PSS	P3HT:$PC_{61}BM$	3.79	9.51	0.57	0.70	[58]
PDMS-*b*-PMMA/Al	ITO/PEDOT:PSS	P3HT:$PC_{61}BM$	3.86	9.61	0.60	0.67	[59]
P(VDF-TrFE)	ITO/PEDOT:PSS	P3HT:$PC_{71}BM$	4.5	12.8	0.589	0.60	[61]

However, both Ca and Ba are active metals, and thus are sensitive to the moisture in the ambient atmosphere. Although the stability of the solar cell devices could be improved in some degree by depositing a thick layer of Al or Ag onto Ca or Ba to

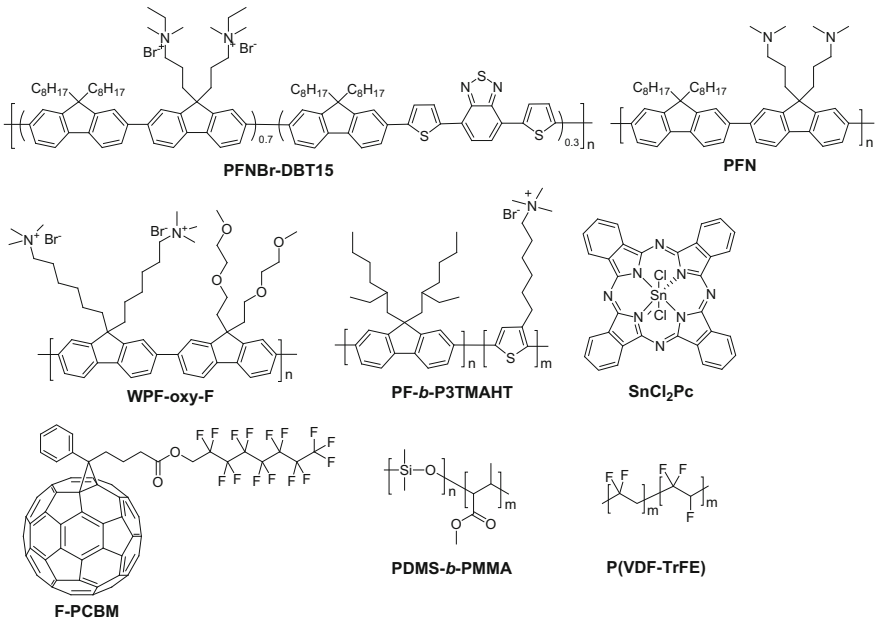

Scheme 3.2 Chemical structures of organic materials for cathode interlayer

form bilayer cathodes, such as Ca/Al and Ba/Al, the development of new interfacial materials to use as cathode interlayer is still required.

Inorganic fluorides, such as lithium fluoride (LiF), are promising electron extraction materials for BHJ–PSCs. A bilayer electrode of LiF/Al is usually chosen to replace a pristine Al cathode, because a thin layer of LiF can guarantee a good Ohmic contact between the metal and the organic active layer [23]. The formation of a favorable dipole moment or a LiF buffer layer at the organic active layer/LiF/Al interface is usually considered to be the reason why LiF could improve the performance of BHJ–PSCs. It was considered that a monolayer covered LiF can be decomposed upon Al deposition and resulting in Li-doping of the organic layer to deliver a low work-function contact; while a thick LiF usually generates a dipole layer to lower the work function of electrode [24–26].

Caesium carbonate (Cs_2CO_3) is another efficient electron extraction material used to fabricate bilayer cathode for BHJ–PSCs [27, 28]. Interestingly, the Cs_2CO_3 layer can be deposited by either thermal evaporation or solution spin coating. The implementation of Cs_2CO_3 is beneficial for reducing the electron extraction barrier and series resistance (R_s). Compared to bare Al device, the device with inserted Cs_2CO_3 exhibited enhanced V_{oc} and fill factor (FF) [29, 30]. However, whether the actual product of thermally evaporated Cs_2CO_3 is Cs_2O or Cs_2CO_3 is still uncertain[27, 31–33]. Anyway, it is widely accepted that the formation of Al–O–Cs complex yields the low work-function contact and thus facilitates the electron extraction [27].

n-Type semiconducting metal oxides such as titanium suboxide (TiO_x), which is a well-known photocatalyst and is widely used in dye-sensitized solar cells [34, 35], had attracted considerable attention recently due to its solution processability from sol to gel process [36], nontoxicity, and transparency. TiO_x possesses a conduction band edge and valence band edge of −4.4 and −8.1 eV, respectively, which would endow TiO_x good electron extraction ability from active layer and outstanding hole-blocking ability [36]. Hence, TiO_x is an ideal cathode modification material for BHJ–PSCs application [36]. The TiO_x layer can also resist the permeation of oxygen and moisture into the organic active layer, because the formation of robust titanium oxide film via annealing the titanium oxide film deposited by sol–gel process at 150 °C. Moreover, the TiO_x layer can also function as an optical spacer via spatially redistributing the incident light intensity to further improve the light harvesting property of BHJ–PSCs [36]. Recently, Park et al. reported a promising PCE of 6.1 % for BHJ–PSCs with poly[*N*-9′-heptadecanyl-2,7-carbazole-*alt*-5,5-(4′,7′-di-2-thienyl-2′,1′,3′-benzothiadiazole)] (PCDTBT, see Scheme 3.1):$PC_{71}BM$ blend as active layer by inserting TiO_x as an electron extraction layer and optical spacer. Notably, the device exhibited internal quantum efficiency (IQE) closing to 100 % around 450 nm, which indicates the high efficient conversion of incident photon into charge carrier [37]. However, the intrinsic electrical properties of the TiO_x film are dominated by the processing conditions. Additionally, the electron mobility of TiO_x is 1.7×10^{-4} cm^2 V^{-1} s^{-1}, which is almost two orders of magnitude lower than that of $PC_{61}BM$, and this may

potentially limit the device performance. To further improve the property of a TiO_x interlayer, Park et al. fabricated Cs-doped film TiO_2 by mixing Cs_2CO_3 solution with a nanocrystalline TiO_2 solution prepared from a sol to gel process. The work function of TiO_2 was successfully downshifted by Cs doping to yield a better Ohmic contact between organic active layer and metal electrode. The improved electron extraction combining the preserved hole-blocking ability of the TiO_x interlayer afforded a much better photovoltaic performance for the poly(3-hexylthiophene) (P3HT, see Scheme 3.1)/$PC_{61}BM$ solar cell than that of cell using sole TiO_x interlayer [38].

ZnO is another *n*-type metal oxide, which possesses a high electron mobility of 0.066 $cm^2\ V^{-1}\ s^{-1}$ [39] and a Fermi level of 4.4 eV [40]. The high electron mobility, ideal Fermi level, and solution processability of ZnO nanoparticles (NPs) indicate that ZnO would be a good interfacial material to facilitate not only the efficient charge transfer from $PC_{61}BM$ (or $PC_{71}BM$) to ZnO, but also the effective electron collection at cathode. In addition, the wide band gap of ZnO (3.2 eV) would endow it good hole blocking ability and good transparency. Moreover, Gilot et al. had proved that ZnO can also serve as an effective optical spacer for thin (<60 nm) active layers [41]. These advantages of ZnO render its widely application in inverted BHJ–PSCs. However, the direct use of ZnO as cathode buffer layer for conventional PSCs is scarce.

3.2.1.2 Self-Assembled Monolayer on Metal Oxide Surface

The contact property of ZnO/metal bilayer cathode and resulted device performance could be further improved by spin coating the functional SAM on the ZnO surface [42, 43]. Modifying the ZnO NPs surface with a benzoic acid group constituted with electron donating end groups (such as $–OCH_3$, $–CH_3$, –H), which form a negative dipole (toward metal and away from ZnO), the band offset between the conduction band of ZnO and the work function of metal can be decreased, and thereby the Ohmic contact was formed. Compared to the unmodified devices, the devices with SAMs-modified ZnO NPs interlayers showed significant improvement in all the *J*–*V* characteristics including J_{sc}, V_{oc}, FF, and PCE. On the other hand, opposite effect was observed when the ZnO NPs layer was modified with electron-withdrawing end groups substituted SAM molecules [40]. PCE of 4.2 % was achieved for device with SAM modification with respect to 3.2 % for the control device with unmodified cathode [40]. A further enhanced PCE of 4.6 % was obtained when the ZnO NPs layer was modified with captoundecanoic acid [44]. More importantly, the stable high work-function metals such as Ag and Au can also be used as cathodes, and the PCE of 3.65 % and 3.22 % were achieved for P3HT:$PC_{61}BM$ devices with ZnO/SAM/Ag and ZnO/SAM/Au cathodes, respectively [40].

3.2.1.3 Water/Alcohol Soluble Polymers as Cathode Interlayer

Although the above-mentioned inorganic materials exhibited outstanding cathode modification functions, the thermal evaporation of most of them requires high vacuum, which leads to increases in fabrication costs and thereby limits their applications. Organic interfacial materials were thus widely developed to improve the interface property of metal electrode, because of their solution processability, facile modification of chemical structures, and in turn electrical and electronic properties. The commonly used organic interfacial materials for cathode modification are summarized in Scheme 3.2. Zhang et al. had reported the use of environment friendly aqueous solution processable poly(ethylene oxide) (PEO) as interlayer to modify the cathode in BHJ–PSCs, which showed similar function as LiF. The PSCs with PEO modified cathode showed not only enhanced V_{oc}, but also J_{sc} and FF [45].

Water/alcohol soluble conjugated polyelectrolytes (CPEs) and related neutral polymers, which bear pendant hydrophilic polar groups, were widely used as promising interfacial materials in organic optoelectronic devices such as polymer light-emitting diodes, field effect transistors (FETs), and solar cells. Their special solubility in environment friendly solvents such as alcohol and water provide the convenience of fabricating multilayer organic devices by avoiding the problem of corrupting the low-lying neutral organic semiconducting layers which are usually dissolved in nonpolar solvents. It was generally considered that the interfacial dipoles were formed by inserting a CPE layer, and thereby the reduction of electron extraction barrier to electron collection and transporting at cathode. In addition, UV photoelectron spectroscopy has shown that this kind of polymers can effectively influence the work function of adjacent electrodes. Moreover, a large amount of water/alcohol soluble fluorene-based CPEs and related neutral polymers were successfully used as electron injection/transporting materials in PLEDs [46, 47]. Luo et al. reported the use of a thin layer of alcohol-soluble fluorene-based CPE PFNBr-DBT15 between the active layer and metal electrode, and the V_{oc} of the resulted PSCs can be enhanced by 0.3 V [48]. Based on Luo's work, He et al. has insightfully investigated five different alcohol-soluble fluorene-based conjugated polymers or CPEs as cathode interlayers for PSCs based different donor materials system. He's results revealed that the V_{oc} enhancement is only observed in devices that contain a polyfluorene copolymer as the donor material, while no significant enhancement in V_{oc} was found for P3HT and poly(2-methoxyl-5-((2′-ethylhexyl)oxyl)-1,4-phenylenevinylene) (MEH-PPV, see Scheme 3.1) devices [49]. Similar works of using other fluorene-based alcohol polymers as interfacial materials for cathode modifications were also demonstrated by Na et al. and Zhao et al. almost at the same time [50, 51]. Notably, BHJ–PSCs with high work-function metals such as Ag, Au, and Cu also showed encouraging device performances with PCE above 3 % with the implementation of fluorene-based CPE WPF-6-oxy-F [52]. After that, the use of alcohol-soluble conjugated polymer as cathode interlayer gradually become a commonly applied approach to further improve the performance of PSCs [53, 54], and the encouraging PCE of 6.07 %

was achieved by inserting a thin layer of PFN (see Scheme 3.2) for the BHJ–PSC based on a newly developed low-band-gap donor material [54]. Recently, new water-/alcohol-soluble conjugated polymers and ionic conjugated di-block copolymer based on carbazole or thiophene were also developed to use as cathode interfacial materials [55, 56]. Compared to the device with sole Al as cathode, the PCE of PSCs can be enhanced from 5 to 6.5 % by inserting an ultra-thin, ionic conjugated, di-block copolymer poly[9,9-bis(2-ethylhexyl)-fluorene]-*b*-poly[3-(6-trimethylammoniumhexyl)thiophene] (PF2/6-b-P3TMAHT) [56]. These encouraging results indicate that water-/alcohol-soluble conjugated polymers would be good candidates of cathode interfacial materials for the future development of printable large-scale solar cells.

3.2.1.4 *n*-Type Organic Semiconductors as Cathode Interlayer

n-Type organic semiconductors having low-lying LUMO levels, which are close to the LUMO of $PC_{61}BM$ and the work function of Al cathode, are potentially electron extraction and transporting materials for BHJ–PSCs. Recently, Zuo et al. had reported the use of *n*-type phthalocyanine tin (IV) dichloride ($SnCl_2Pc$) as cathode interlayer to form $SnCl_2Pc$/LiF/Al trilayer cathode for PSCs. The integration of $SnCl_2Pc$ into the solar cell not only enhances the electron transporting and collection efficiencies due to the step-like electron injection barrier to cathode after the implementation of $SnCl_2Pc$ interlayer, but also improves the exciton dissociation efficiency because of the formation of additional MEH-PPV/$SnCl_2Pc$ exciton dissociation junction. Consequently, the 15.2 % enhancement of PCE up to 2.49 % was achieved for PSCs with the thermally evaporated $SnCl_2Pc$ as cathode interlayer [57].

3.2.1.5 Organic Cathode Interlayer Formed by Surface Self-Segregation

Compared to the thermal evaporation, the formation of a interfacial layer of *n*-type organic semiconductor by controlling the surface segregation of the materials during spin coating may be a much milder approach for the low-lying organic active layer. Wei et al. had reported that when a small amount of a fullerene derivative with a fluorinated alkyl chain (F-PCBM) is mixed with the blend of P3HT and $PC_{61}BM$, the F-PCBM spontaneously migrates to the surface of the organic layer during spin coating due to the low surface energy of the fluorinated alkyl chain. The interfacial dipole moment toward the Al cathode caused by the perfluoroalkyl chains is favorable for the reduction of the work function of Al for better alignment with $PC_{61}BM$ energy levels. The energy barrier for electron collection and the R_s of the modified device were hence reduced, and consequently the enhanced PCE of the device was achieved [58]. The surface self-segregation approach was also applied to incorporate a thin layer of poly(dimethylsiloxane)-*b*-poly(methylmethacrylate) (PDMS-*b*-PMMA) di-block copolymer at the interface between organic active layer

and Al electrode to function as a buffer layer for improving the performance of PSC. An enhancement of the PCE of the PSCs from 3.05 % to 3.56 % on average, and the highest PCE of 3.86 % were achieved by inserting a PDMS-*b*-PMMA into the P3HT:$PC_{61}BM$ solar cells due to the reduction of charge carrier recombination at the organic/metal interface [59].

3.2.1.6 Ferroelectric Polymer as Cathode Interlayer

It is well-known that a sufficient intrinsic internal electric field is required to efficiently dissociate the charge transfer excitons generated in active layer [60]. However, most widely used electrode materials deliver a work function offset of <2 eV, affording a much smaller internal electric field for efficient charge transfer excitons dissociation in BHJ–PSCs [36]. Therefore, an external bias voltage is generally needed to efficiently dissociate the electrons and holes. Most recently, Yuan et al. demonstrated another innovative method to provide sufficient intrinsic internal electric field in BHJ–PSCs by inserting a ultra-thin ferroelectric polymer layer of vinylidene fluoride-trifluoroethylene copolymer (P(VDF-TrFE)) between organic active layer and Al electrode [61]. After poling, an induced net polarization electric field is generated, which is ten times-higher than that achieved by the use of electrodes with different work functions. As a consequence, an enhanced PCE from 1–2 % without the ferroelectric film to 4–5 % was demonstrated for BHJ–PSCs based on several different active layers. Also note that these improved PCEs are higher than those achieved by other methods, including active layer morphology and electrode work-function optimization [61].

3.2.2 Anode Interlayer

3.2.2.1 PEDOT: PSS as Anode Interlayer

Interface engineering at the hole-collecting electrode is also of paramount importance for the improvement of the performance of BHJ–PSCs. The summary of performance of conventional PSCs using different anode interlayer designs is listed in Table 3.2 and the chemical structures of organic materials used as anode interlayer in conventional PSCs are shown in Scheme 3.3. In conventional device configuration using ITO as the anode, the polymer complex of poly(3,4-ethylenedioxythiophene):poly(styrene sulfonate) (PEDOT:PSS) has been commonly used as the anode interlayer to improve the contact property between ITO and organic active layer, and to increase the work function of ITO for effective hole collection and transporting [62, 63]. However, it was revealed by Rutherford backscattering (RBS) studies and XPS that the acidic nature of PEDOT:PSS etches the ITO and results in the poor chemical stability at the ITO/PEDOT:PSS interface [64–66]. Moreover, the electrical inhomogeneities of PEDOT:PSS limit its

Table 3.2 Summary of device characteristics of representative conventional PSCs employing different anode interlayers

Anode	Cathode	Active layer	PCE	J_{sc} (mA cm^{-2})	V_{oc} (V)	FF	Ref
ITO/PEDOT:PSS	Al	MEH-PPV:$PC_{61}BM$	0.46	2.1	0.75	0.23	[62]
ITO/PEDOT:PSS/EG	Ca/Al	P3HT:$PC_{61}BM$	4.70	11.5	0.57	0.71	[68]
ITO/MoO_3	Ca/Al	P3HT:$PC_{61}BM$	3.33	8.94	0.60	0.62	[70]
ITO/MoO_3	TiO_x/Al	PCDTBT:$PC_{71}BM$	6.50	10.88	0.89	0.67	[72]
ITO/NiO	LiF/Al	P3HT:$PC_{61}BM$	5.2	11.3	0.64	0.69	[73]
ITO/V_2O_5	Ca/Al	P3HT:$PC_{61}BM$	3.10	8.83	0.59	0.59	[70]
ITO/WO_3	Ca/Al	P3HT:$PC_{61}BM$	3.10	–	–	0.69	[76]
ITO/AgO_x	Ca/Al	P3HT:$PC_{61}BM$	4.80	12.70	0.60	0.51	[77]
ITO/TFB:$TPDSi_2$	Al	MDMO-PPV:$PC_{61}BM$	2.23	4.62	0.89	0.54	[78]
ITO/MoO_3/TFB	Al	MDMO-PPV:$PC_{61}BM$	2.01	4.28	0.85	0.55	[80]
ITO/SPDPA	Ca/Al	P3HT:$PC_{61}BM$	4.20	10.33	0.60	0.68	[81]
ITO/PTFE	Al	P3HT:$PC_{61}BM$	2.27	7.4	0.52	0.49	[82]
ITO/PEDOT:PSS/P3HT	Ca/Al	P3HT:$PC_{61}BM$	5.05	12.00	0.60	0.69	[85]
FTO/PEDOT:PSS/HAT4	Al	P3HT:$PC_{61}BM$	3.0	9.2	0.57	0.57	[86]
ITO/TPA-PFCB/PEDOT:PSS	Ca/Al	P3HT:$PC_{61}BM$	3.90	9.43	0.61	0.67	[87]
ITO/SWNT/PEDOT:PSS [a]	Al	P3HT:$PC_{61}BM$	4.9	21.0	0.59	0.51	[89]
ITO/PEDOT:PSS/SWNT [a]	Al	P3HT:$PC_{61}BM$	4.9	24.1	0.59	0.44	[89]
ITO/CF_3-SAM	LiF/Al	P3HT:$PC_{61}BM$	3.15	13.87	0.60	0.38	[91]

[a] Measured under light intensity of 130 mW cm^{-2}

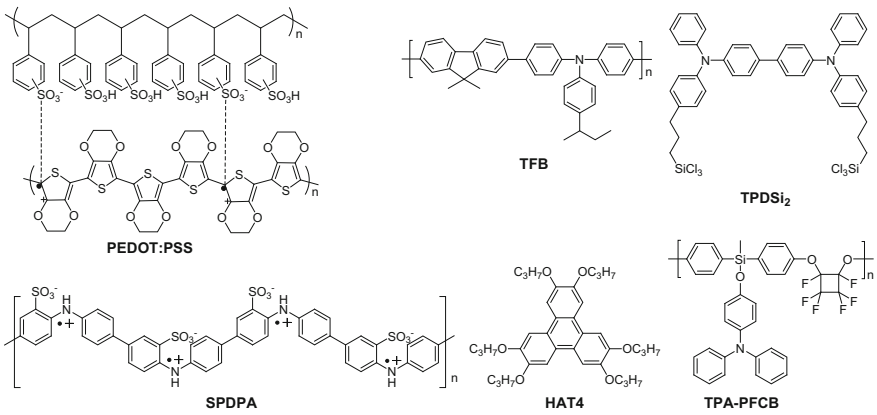

Scheme 3.3 Chemical structures of organic materials for anode interlayer

electron-blocking ability and thus usually lead to electron leakage at the anode [65, 67]. Therefore, many efforts were devoted to modify PEDOT:PSS in order to achieve the improvement of PSCs performance. Recently, Xiao et al. reported the

enhanced PCE of 4.7 % of P3HT:$PC_{61}BM$ solar cell when a layer of ethylene glycol was spin coated over PEDOT:PSS. The enhancement was achieved by the increase of PEDOT:PSS conductivity that improves charge extraction, and enhanced PEDOT:PSS transparency that contributes to enhanced P3HT:$PC_{61}BM$ absorption [68]. Soon after, similar work was also reported by Peng et al., who treated PEDOT:PSS layer by ethanol and 2-propanol. Similar enhancement of PCE was also observed when using this treated PEDOT:PSS as anode buffer layer, and this enhancement was attributed to higher conductivity and optimized surface morphology of the PEDOT:PSS [69].

3.2.2.2 Semiconducting Oxides as Anode Interlayer

Aside from the modification of PEDOT:PSS, the development of new materials for hole-collecting/transporting is also vigorously conducted. In principle, an efficient anodic interlayer to substitute PEDOT:PSS should first possess the capability to withstand the organic solvent erosion. Second, a good transparency is desired for the anodic interlayer to guarantee the efficient incident light absorption in organic active layer. Moreover, it should be taken into account as well that the surface properties of the anodic interlayer can significantly influence the phase separation process and morphology of the BHJ active layer.

p-Type semiconducting transition metal oxides such as molybdenum oxide (MoO_3), vanadium oxide (V_2O_5), nickel oxide (NiO), and tungsten oxide (WO_3) were hence widely employed as anodic buffer layers to modify the interface between ITO and organic active layer in the conventional BHJ–PSCs. These oxides have relatively large band gap, which guarantee the good optical transparency in visible and near infrared light region of the anode, and consequently allow incident solar photons to reach the organic active layer. More importantly, the Fermi level of these oxides usually positions in the range between 5.0 and 5.4 eV, which align well with the HOMO energy level of most donor conjugated polymers to form ideal Ohmic contact for efficient hole extraction and transporting. Furthermore, the lowest energy level of the conduction band of these *p*-type oxides usually located above 2.5 eV, which is much higher than the LUMO energy level of most organic photovoltaic (OPV) materials (including both acceptors and donors), indicating the good electron-blocking ability of these oxides.

Shrotriya et al. first reported the use of thermally-evaporated MoO_3 as the anodic interlayer for BHJ–PSCs to replace PEDOT:PSS [70]. The BHJ–PSCs with 5 nm of MoO_3 as anodic interlayer exhibited slightly better performance (3.36 % PCE) than that of PEDOT:PSS device (3.10 % PCE). They revealed as well that an optimized thickness is critical to obtain ideal device performance: a thinner layer of MoO_3 results in a smaller V_{oc} and leakage current because of the incomplete coverage, whereas a thicker layer of MoO_3 increases the R_s and in turn leads to a smaller J_{sc} and FF [70]. Similar solar cell performance enhancement was also observed by Kim et al. when MoO_3 was inserted as anodic buffer layer between ITO and organic active layer [71]. Most recently, Sun et al. reported encouraging

results about the use of thermally-evaporated MoO_3 as the anodic buffer layer of BHJ–PSCs with the configuration of ITO/MoO_3/PCDTBT:$PC_{71}BM$/TiO_x/Al. The implementation of MoO_3 improved the light absorption with the organic active layer, and thereby resulted in a PCE over 6 % at BHJ layer thickness up to 200 nm. A further enhancement in PCE up to 7.2 % was achieved by using an antireflection coating. In addition, BHJ–PSC with MoO_3 as anodic buffer layer demonstrated much better long-term air stability than that of solar cell fabricated with PEDOT:PSS. The PCE remains at approximately 50 % of the original value after the storage in air for 720 h, while the PCE of control PEDOT:PSS device fell to <10 % of the original value after storage in air for 480 h [72].

Deposition of a thin layer of *p*-type NiO by pulsed laser onto ITO to replace PEDOT:PSS as anodic interlayer led to significant performance enhancement of BHJ–PSC based on P3HT:PCBM blend. A 5–10 nm NiO layer gives rise to the PCE as high as 5.2%, while the PCE of control PEDOT:PSS device is only 2.4 %. The enhancement was initially attributed to the ideal work function of NiO (5.0–5.4 eV) to match well with the HOMO level of P3HT (5.0), and large band gap (ca. 3.6 eV) of NiO to deliver high transparency and sufficient barrier for electron blocking [73]. After that, Irwin et al. via a multifaceted analysis further revealed that NiO grows as smooth, crystalline, and oriented thin films on ITO substrates to form an optically transparent, electrically uniform, and passivated semiconducting anode coating, which prevents anode electron injection and facilitates anode hole injection [74]. However, the pulsed laser deposition of NiO layer is neither scalable nor a cost effective method. Steirer et al. deposited a thin layer of NiO onto ITO by spin coating a diluted nickel metal organic ink followed by thermal annealing at 250 °C. The BHJ–PSCs from this solution-processed NiO exhibited comparable performances with that of PSCs from pulsed laser deposited NiO and PEDOT:PSS [75].

Thermally evaporated thin layers of V_2O_5 and WO_3 were employed as effective buffer layers on ITO to improve the performance of BHJ–PSCs based on P3HT:$PC_{61}BM$ blend. The devices based on both oxides exhibited comparable performances with those of PEDOT:PSS control device. It was suggested that the ideal work function (4.7 eV) and the relatively high-positioning of the lowest energy level of the conduction band (2.4 eV) of V_2O_5 are beneficial for forming efficient hole-collection injection contact with the organic active layer and to provide sufficient barrier for electron leakage at anode [70]. Han et al. revealed that the uniform amorphous film of WO_3 can effectively planarize an originally rough ITO. P3HT films, grown on WO_3 film, have a higher degree of ordering and larger hole mobility than those grown on PEDOT:PSS [76]. An ultra-thin layer of AgO_x generated through plasma oxidized Ag (1 nm) deposited on ITO was found to be able to improve the contact property of ITO/PEDOT:PSS interface. The enhancement of device performance is suggested to the formation of an interface energy step between ITO and PEDOT:PSS that could improve the charge collection efficiency and the overall efficiency of solar cell devices [77].

3.2.2.3 Organic/Polymer Materials as Anode Interlayer

Despite that *p*-type transition metal oxides exhibited outstanding anode interface modification functions, the fabrication of thin films based on these oxides usually involves high-cost thermal evaporation, which limits their application in large-area devices. Organic hole-collecting/transporting materials were thus greatly desired due to their solution processabilities and their facile tunable properties. A cross-linkable blend of poly[9,9-dioctylfluorene-*co*-*N*-[4-(3-methylpropyl)]-diphenylamine] (TFB) and 4,4′-bis[(p-trichlorosiylpropylphenyl)phenylamino]biphenyl ($TPDSi_2$) was spin coated onto a ITO substrate to form a robust, optical transparent, homogeneous film after thermal annealing, which can be used as an effective PEDOT:PSS alternative. TFB:$TPDSi_2$ possesses HOMO and LUMO energy levels of −5.3 and −2.3 eV, respectively, which endow the buffer layer good hole-collecting and electron-blocking ability. As a result, BHJ–PSCs of poly(2-methoxyl-5-((3′,7′-dimethyloctyl)oxyl)-1,4-phenylenevinylene) (MDMO-PPV):PCBM with TFB:$TPDSi_2$ anodic buffer layer delivered much better photovoltaic performance and thermal stability than those of PEDOT:PSS control devices [78]. Interestingly, the use of a double interfacial layer of PEDOT:PSS + TFB:$TPDSi_2$ could decrease the FF of the solar cells, but increase electron blocking to suppress charge leakage and thereby enhance V_{oc} more than using either PEDOT:PPS or TFB:$TPDSi_2$ independently [79]. After that, Subbiah et al. demonstrated that a double interlayer of MoO_3/TFB could also improve the photovoltaic performance of the BHJ–PSC with respect to solar cells with a sole PEDOT:PSS or MoO_3 anodic buffer layer, due to the enhanced electron blocking and hole collecting from organic active layer to the anode [80].

Li et al. demonstrated the use of a novel self-doped polymer of sulfonated poly(diphenylamine) (SPDPA) as the anodic buffer layer to replace PEDOT:PSS in P3HT:$PC_{61}BM$ solar cell. The polar surface of SPDPA film induces the oriented arrangement of P3HT in the active layer during the spin-coating and film-growing processes, which is beneficial for enhancing the hole mobility, producing a better Ohmic contact at the anode junction and thereby gives rise to an enhanced PCE [81]. The implementation of a thin layer of polytetrafluoroethylene (PTFE) between ITO and P3HT:$PC_{61}BM$ was found to form an dipole layer at the anode junction, and thereby facilitate the hole extraction. Compared to the PEDOT:PSS control device, solar cells based on PTFE showed obviously enhanced photovoltaic performance. Note that such an insulated PTFE thin layer was deposited by thermally evaporation, and it thereby can be prepared at low substrate temperatures, which is compatible to the flexible polymer substrates for BHJ–PSCs applications [82].

In addition to the modification of PEDOT:PSS or development of PEDOT:PSS alternatives, the implementation of hole selective transporting materials below or above PEDOT:PSS layers is another effective approach to facilitate hole-collecting and electron-blocking at anode junction, and thereby to improve the performance of BHJ–PSCs. It is well-known that there is a vertical composition gradient in organic blend layer with a profile of $PC_{61}BM$- or $PC_{71}BM$-rich blend adjacent to

PEDOT:PSS and conjugated polymer-rich blend near the cathode side, which is possibly detrimental to charge extraction efficiency [83, 84]. Liang et al. hence simply inserted a thin layer of high molecular weight P3HT between PEDOT:PSS and P3HT:$PC_{61}BM$ blend layer to increase the electron-blocking ability of PEDOT:PSS. The extra donor/acceptor interfaces adjacent to the bottom of the composite were created as well, leading to an enhanced photoinduced electron transfer efficiency and photocurrent density. Relative to the 3.98 % PCE of the reference device, the extra P3HT inserted PSC delivered PCE of 5.05 % [85]. The insertion of a discotic liquid crystal of hexabutoxytriphenylene (HAT4) at the interface between anodic buffer layers (PEDOT:PSS, MoO_3 or NiO) and organic active layer was also found to be an effective method to improve the photovoltaic performance of P3HT:$PC_{61}BM$ solar cell. Atomic force microscopy (AFM) measurement indicate that the ordered hexagonal columnar phase formed in HAT4 layer provides a more efficient pass way for hole transporting, and thereby leads to an enhanced J_{sc} and FF [86].

The insertion of an in situ polymerized triphenylamine-containing polyperfluorocyclobutane (TPA-PFCB) thin layer between ITO and PEDOT:PSS was revealed to be an effective approach to block the electron leakage at anode. After the coverage of TPA-PFCB, the surface roughness of ITO was substantially reduced. Compared to the control PEDOT:PSS solar cell, the implementation of the TPA-PFCB layer increases both V_{oc} and J_{sc}, and thereby gives rise to enhanced PCE. The HOMO and LUMO of TPA-PFCB was measured to be −5.2 and −1.7 eV, respectively, which verified its good charge selective hole-transporting and electron-blocking properties. In addition, FET measurement confirmed that electron transporting is completely blocked by implementation of TPA-PFCB between the organic active layer and the Al source and drain electrodes [87].

3.2.2.4 Carbon Nanotubes as Anode Interlayer

Carbon nanotubes (CNTs) possess high electrical conductivity, approximate work function of ∼5.0 eV which match well the work function of ITO and HOMO of most donor polymers, and outstanding optical transparency in a broad spectral range from UV to deep infrared region, making CNTs potential hole-collecting materials for BHJ–PSCs [88]. Chaudhary et al. had inserted CNTs at different interfaces (ITO/PEDOT:PSS, PEDOT:PSS/P3HT:$PC_{61}BM$, and P3HT:$PC_{61}BM$/Al) of P3HT:$PC_{61}BM$ solar cell, and had found that only CNTs were incorporated into the interfaces of ITO/PEDOT:PSS or PEDOT:PSS/P3HT:$PC_{61}BM$ and the solar cells exhibited obvious enhancement in PCE [89]. Most recently, Hatton et al. had demonstrated that the use of partially oxidized CNTs as anodic buffer layer to replace PEDOT:PSS can effectively facilitate the hole extraction. P3HT:$PC_{61}BM$ solar cells with this neutral aqueous processed CNTs anodic buffer layer exhibited comparable photovoltaic performance with that of PEDOT:PSS control device [90].

3.2.2.5 Self-Assembled Monolayers as Anode Interlayer

SAMs with different end groups (–CH_3, –NH_2, –CF_3) were also employed to modify the work function of ITO, and thereby to improve the performance of P3HT:PC_{61}BM solar cell. The work function of ITO increased initially from 4.7 to 5.16 eV after the insertion of a –CF_3 substituted SAM molecules, affording a much better match with the HOMO of P3HT for efficient hole extraction at anode junction. Moreover, it was found that the surface properties of the inserted SAMs can greatly influence the morphology of the upper organic active layer. Active layer spin coated onto the hydrophobic surface of –CF_3 SAM exhibited little undesired phase separation, leading to a high PCE of 3.15 % for the corresponding solar cell [91].

3.3 Interface Engineering for Inverted Solar Cell Devices

The conventional device structure of BHJ–PSCs has some inherent device stability problems. The transparent conducting ITO used as the hole-collecting contact can be etched over time by the acidic PEDOT:PSS hole-transporting layer [64]. The thermo-deposition of low work-function cathode usually requires high vacuum, thus leading to increases in fabrication costs. Moreover, to avoid the exposure of low work-function cathode to air, encapsulation technologies have to be applied which further complicate the fabrication process. Therefore, device architectures that can remove the need of PEDOT:PSS (or at least separate it from ITO) and use nonvacuum-deposited air-stable high work-function metal electrodes at the top interface are desired. Based on these considerations, inverted solar cell device architecture was proposed. The device structure is shown in Fig. 3.1. This architecture has recently attracted considerable attention due to the device stability and processing advantages compared to the conventional architecture. In an inverted device, the polarity of charge collection is the opposite of the conventional architecture, allowing the use of higher work function and air-stable materials (Au, Ag, and Cu) as the top anode which is exposed to air. The use of higher work-function metals offer better ambient device stability and the possibility for using low-cost solution-processed techniques such as spray coating [92] or screen printing [93] to deposit the top anode. The focus of current research for the inverted device architectures is to understand how to improve the device efficiency and stability through the design and processing of the different interfacial layers in the device structure. In this section, we will review the recent progress of interface engineering for inverted solar cells in two aspects: the progress in anode interlayer design and the progress in cathode interlayer design.

3.3.1 Cathode Interlayer

In principle, ITO is capable of collecting either electrons or holes since its work function (4.5–4.7 eV) lies between the typical HOMOs and LUMOs of common OPV materials. Therefore, the polarity of ITO can be modified to efficiently collect either electrons or holes by coating functional interlayers of different work functions onto its surface [29]. For inverted solar cell application, electron transporting layers (ETL, or electron selective layer) with low work function are formed on top of ITO to modify the ITO interface for efficient electron extraction and collection from active layer. Such ETL materials typically include inorganic ones like Cs_2CO_3 [29, 33], Ca [94], Al_2O_3 [95], ZnO [96–98], and TiO_x [99, 100]. Since light needs to pass through the ETL to reach the active layer to generate photocurrent, the layers are typically very thin to maintain high optical transmittance. The electron mobility and work function of the ETL layer should also be optimized in order to realize efficient electron collection. The summary of performance of inverted PSCs using different ETL designs is listed in Table 3.3 and the chemical structures of organic materials used as ETL in inverted PSCs are shown in Scheme 3.4 (WPF-6-oxy-F is shown in Scheme 3.2).

3.3.1.1 Metal Oxide Thin Film as ETL

ZnO and TiO_x are the most commonly utilized ETL materials for inverted solar cells due to the high optical transparency in the visible and near infrared region, high carrier mobility, and its solution processibility. Many demonstrations of using these *n*-type metal oxide layers as the electron selective layer for inverted solar cells have been reported in literatures.

An efficient P3HT:PC_{61}BM BHJ inverted solar cell from a high-temperature processed sol–gel ZnO interlayer on ITO and an Ag electrode as the top hole-collecting contact was first demonstrated by White et al. [96]. The zinc acetate (ZnAc) sol–gel precursor was directly spin cast onto ITO and then thermally annealed at 300 °C for 5 min to hydrolyze and crystallize into amorphous ZnO thin film. Improved conductivity and mobility after annealing led to conversion efficiencies of 2.97 % of the inverted device. Interestingly, it was found that when these devices were exposed to air, the performance gradually improved. They attribute the improvement to the oxidation of Ag which formed Ohmic contact with P3HT. State-of-the-art inverted solar cell using ZnO as ETL and a low-band-gap donor material PCDTBT can yield PCE as high as 6.33 % [97]. To further improve the electronic properties of ZnO, Al doping was explored and inverted devices with Al-doped ZnO (AZO) as ETL were thus fabricated [101, 102]. Although the AZO device performance is not greatly improved compared to undoped ZnO devices, AZO layer can be made much thicker (>100 nm) than ZnO layer without hampering the solar cell performance; thus, it is more robust and easier to process.

Table 3.3 Summary of performances of inverted polymer solar cell devices using different ETL designs

ETL	Active Layer	Anode	PCE (%)	J_{sc} (mA cm^{-2})	V_{oc} (V)	FF (%)	Ref
Cs_2CO_3	P3HT:$PC_{61}BM$	V_2O_5/Al	2.25	8.4	0.56	62.1	[29]
Cs_2CO_3 [a]	P3HT:$PC_{61}BM$	V_2O_5/Al	2.10	8.8	0.55	56.3	[29]
Ca	P3HT:$PC_{61}BM$	MoO_3/Ag	3.55	8.3	0.65	65.9	[94]
Al_2O_3	P3HT:$PC_{61}BM$	PEDOT:PSS/Ag	2.82	7.7	0.57	64.0	[95]
ZnO	P3HT:$PC_{61}BM$	Ag	2.97	11.2	0.56	47.5	[96]
ZnO	PCDTBT:$PC_{71}BM$	MoO_3/Al	6.33	10.4	0.88	68.8	[97]
ZnO	PSiFDBT:$PC_{61}BM$	Au	3.80	5.03	0.90	60.0	[98]
TiO_x	P3HT;$PC_{61}BM$	PEDOT:PSS/Au	3.10	9.0	0.56	62.0	[99]
PTE/TiO_x	P3HT:$PC_{61}BM$	PEDOT:PSS/Ag	3.5	10.5	0.55	60.0	[100]
AZO [b]	P3HT:$PC_{61}BM$	PEDOT:PSS/Ag	2.59	9.6	0.57	47.7	[101]
ZnO NP [c]	P3HT:$PC_{61}BM$	PEDOT:PSS/Ag	3.61	10.7	0.62	54.2	[103]
ZnO NP/C_{60}SAM	P3HT:$PC_{61}BM$	PEDOT:PSS/Ag	4.54	12.0	0.63	60.6	[105]
TiO_x/C_{60}SAM	P3HT:$PC_{61}BM$	PEDOT:PSS/Ag	3.80	10.6	0.62	57.2	[110]
TiO_x/FPQ-Br	P3HT:$PC_{61}BM$	MoO_3/Au	3.55	8.9	0.58	70.0	[111]
ZnO/PCBSD	P3HT:$PC_{61}BM$	PEDOT:PSS/Ag	4.40	12.8	0.60	58.0	[112]
ZnO/PCBSD	P3HT:ICBA	PEDOT:PSS/Ag	6.22	12.4	0.84	60.0	[113]
PEO	APFO:$PC_{61}BM$	PEDOT-EL/PH500	0.70	2.3	0.67	45.0	[114]
WPF-6-oxy-F	P3HT:$PC_{61}BM$	PEDOT:PSS/Ag	3.38	8.8	0.66	59.0	[115]
WPF-6-oxy-F [d]	P3HT:$PC_{61}BM$	PEDOT:PSS/Ag	1.23	6.6	0.57	33.0	[116]
$P3PHT^+$/$(PEDOT:PSS)^-$	P3HT:$PC_{61}BM$	V_2O_5/Al	1.85	7.1	0.54	46.0	[117]
DCM doped PCBM-S	P3HT:$PC_{61}BM$	PEDOT: PSS/Ag	2.53	9.1	0.64	44.0	[118]
no ETL	P3HT:$PC_{61}BM$	PEDOT:PSS/Ag	4.10	11.7	0.62	57.0	[119]

[a] Solution processed
[b] Nanoparticles
[c] Aluminum doped ZnO
[d] On graphene substrate

TiO_x sol–gel layer ($\sim$10 nm) was also demonstrated as an effective ETL for inverted solar cells [99]. The devices with structure of ITO/TiO_x/P3HT:$PC_{61}BM$/PEDOT:PSS/Au showed a PCE of 3.1 %. O-xylene was used as solvent for

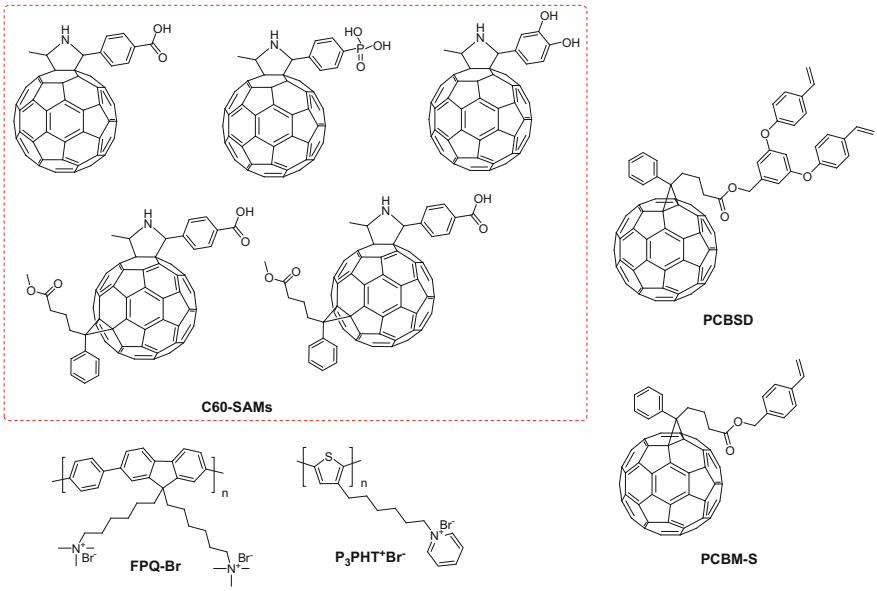

Scheme 3.4 Chemical structures of organic materials used in ETL for inverted polymer solar cells

P3HT:$PC_{61}BM$ instead of the commonly used chlorobenzene or dichlorobenzene to make the vertical phase segregation of donor and acceptor more favorable for inverted devices. Like in the case of conventional devices, controlling the bulk blend vertical phase segregation is also important in inverted devices; however, the optimal phase segregation is different from the case of conventional devices [84].

3.3.1.2 Metal Oxide Nanoparticle Layer

One of the problems of sol–gel process of ZnO and TiO_x is that they require high temperature annealing processing conditions in order to improve the crystallinity of the material to minimize resistive losses in the solar cell devices. These high temperature processing conditions can reach as high as 500 °C, which is not compatible with industry scale roll-to-roll process. To overcome this problem, ZnO NPs are introduced as ETL materials for inverted solar cells [41, 103]. The devices fabricated from the ZnO NPs on ITO-coated glass show an average PCE of ~3.6 %. This value is very similar to that obtained from the high temperature processed ZnO sol–gel devices on glass/ITO which show an average efficiency of ~3.5 %. This demonstrates that sol–gel ZnO and ZnO NPs thin film layers can both act as a good electron selective layer in the inverted device architecture.

3.3.1.3 Self-Assembled Monolayer on Metal Oxide Surface

Although reasonable efficiencies have been reached with *n*-type metal oxides as the electron selective layer in inverted solar, it still has great room for improvement, as the surface of metal oxides have hydroxyl groups that can cause charge trapping at the metal oxide/active layer interface [104]. These hydroxyl groups terminated surfaces lead to high-interface charge recombination due to poor charge transfer. One approach that can improve the electrical and morphological properties of metal oxide/active layer interface is to utilize a SAM between the inorganic and organic interface [40, 91, 105–109]. SAMs can be utilized to significantly modify the interfaces of oxide and metallic surfaces to improve adhesion, compatibility, charge-transfer properties, energy level alignment, and affect the upper layer growth of materials. It was demonstrated that modifying the metal oxide surfaces of TiO_2 and ZnO-based inverted solar cells with a fullerene-based SAM (C_{60}-SAM) can improve the device performance. The C_{60}-SAM affects the photo-induced charge transfer at the interface to reduce the recombination of charges, passivate inorganic surface trap states, improve the exciton dissociation efficiency at the polymer/metal oxide interface as well as act as a template to influence the overlayer BHJ distribution of phases and crystallinity leading to higher efficiency inverted solar cells [105, 110].

3.3.1.4 Polymer and Cross-Linked Interlayer on Metal Oxide Surface

The potential drawbacks for SAM formation on metal oxide surface are incomplete coverage at the molecular scale and probable desorption of this monolayer during wet processing, creating localized defects in this interlayer [109]. The other approach that can improve the metal oxide/active layer interface is to insert an organic ETL interlayer in between. In order to resist the solvent washing from the over-layer, this organic layer should have orthogonal solubility with active layer, or it should be cross-linkable. Choi et al. reported a remarkable improvement in inverted solar cell performance by employing a thin layer of CPE on top of TiO_x. The TiO_x/CPE composite ETL improves the electron injection and transport at the cathode and blocks the hole transport to the cathode, leading to a PCE improvement from 2.65 to 3.55 % [111]. The CPE material was alcohol soluble, and thus not affected by the solvent of the active layer. Hsieh et al. reported a $PC_{61}BM$-based *n*-type material [6,6]-phenyl-C_{61}-butyric styryl dendron ester (PCBSD) functionalized with a dendron containing two styryl groups as thermal cross-linkers [112]. By heating at 160 °C for 30 min a robust, adhesive, and solvent-resistant thin film can be generated on top of ZnO layer. An inverted solar cell device based on ITO/ZnO/cross-linked PCBSD/P3HT:$PC_{61}BM$/PEDOT:PSS/Ag configuration not only achieves enhanced device characteristics (PCE 4.4 %), but also exhibits an exceptional device lifetime without encapsulation; it greatly outperforms a reference device (PCE 3.5 %) based on an ITO/ZnO/P3HT:$PC_{61}BM$/PEDOT:PSS/Ag configuration without the interlayer. Changing the acceptor in the active layer from $PC_{61}BM$ to a novel fullerene derivative indene-C_{60} bis-adduct (ICBA) can further

improve the PCE of inverted solar cell device with PCBSD interlayer [113], yielding a record efficiency of 6.2 % for inverted organic solar cell devices at the time.

3.3.1.5 Polymer or Cross-linkable Organic Thin Film as Single ETL

Besides acting as an interlayer between metal oxide layer and active layer, polymer or cross-linkable organic thin films can also be implemented as independent ETL for inverted solar cells to completely replace the metal oxide layer. Zhou et al. reported the use of PEO thin film as single ETL on ITO for inverted solar cells. The insertion of PEO interlayer between ITO and APFO3:$PC_{61}BM$ active layer improved the PCE of the devices from 0.5 % to 0.7 % [114]. Na et al. later reported the use of a water-soluble polyfluorene CPE as a single ETL which can improve the PCE of P3HT:$PC_{61}BM$ inverted devices from 1.04 % without interlayer to 3.38 % [115]. The same group found out that the CPE material can also be an effective ETL for multilayered graphene (MLG) cathode [116]. An inverted solar cell device with configuration of MLG/CPE/P3HT:$PC_{61}BM$/PEDOT:PSS/Al has a PCE of 1.23 %, while the reference device without CPE interlayer has virtually no photovoltaic effect at all. In these studies, the increase in PCE is explained by the enhancement of built-in voltage due to work function lowering effect of the interlayer, and this is generally supported by work function measurement of ITO substrate with or without interlayer through ultraviolet photoelectron spectroscopy (UPS) or Kelvin probe.

Besides common solution process, polymer ETL can also be fabricated by layer-by-layer (LBL) method. Rider et al. reported an ETL generated by repeated LBL deposition of cationic water-soluble polythiophene poly[3-(6-pyridiniumylhexyl) thiophene bromide] ($P3PHT^+Br^-$) with anionic $(PEDOT:PSS)^-Na^+$ on ITO [117]. The inverted solar cell device of ITO/$(P3PHT^+/(PEDOT:PSS)^-)_5$/P3HT:$PC_{61}BM$/$V_2O_5$/Al has an efficiency of $\sim$2 % and operation lifetime >500 hours.

As the organic ETL materials generally suffer from their low electron conductivity compared to metal oxides, some researchers try to compensate this by doping the ETL layer. Cho et al. demonstrated that the n-doping of a cross-linkable $PC_{61}BM$ derivative PCBM-S using decamethylcobaltocene (DMC) can significantly increase the electron conductivity of the cross-linked ETL layer [118]. In the configuration of ITO/PCBM-S/P3HT:$PC_{61}BM$/PEDOT:PSS/Ag, device with PCBM-S layer of optimum DMC doping level yield a PCE of 2.53 %, compared to 1.24 % for devices with undoped PCBM-S interlayer.

Before the end of this section it should be noted that the electronic properties of the interface of ITO and metal oxide is complicated and our understanding is far from complete. For example, Wang et al. reported an interesting case that the PCE of the inverted solar cell device with the structure of ITO/P3HT:$PC_{61}BM$/PEDOT:PSS/Ag changes irreversibly from 1.46 to 4.1 % when the device is exposed to continuous illumination of simulated sunlight for 2 h [119]. Though the mechanisms behind the large enhancement in PCE is not thoroughly explained, the

fact that high PCE can be achieved in a device without ETL poses the question of how and to what extent an ETL can improve the electron-collecting ability of ITO in inverted devices.

3.3.2 Anode Interlayer

Direct contact of the top high work-function metal to the active layer can lead to degradation of the solar cell performance, therefore, a hole-transporting/electron-blocking layer (HTL/EBL) is generally deposited between these two layers to improve charge selectivity and collection of holes. The materials that have been utilized as HTL are various high work-function transition metal oxides such as MoO_3, or denoted as MoO_x because of oxygen vacancy formed during thermo-evaporation [97, 120, 121], WO_3 [122, 123] and V_2O_5 [29, 124], and solution-processed organic materials including PEDOT:PSS [99, 112, 113], SPDPA [125], dextran-doped poly(allylamine hydrochloride) (PAH-D) [126], and cross-linkable molecule N,N′-diphenyl-N,N′-bis-(3-methylphenyl)-(1,1′)-biphenyl -4,4′- diamine- bis (vinyl benzyl ether) (TPD-BVB) [127]. The chemical structures of the organic HTL materials are shown in Scheme 3.5 (PEDOT:PSS and SPDPA are shown in Scheme 3.3).

3.3.2.1 PEDOT:PSS as HTL or Anode

The literature on HTL design of inverted solar cells is relatively scarce compared to ETL. For solution-processed HTL PEDOT: PSS is often used. The challenge of using PEDOT:PSS as HTL in an inverted device is that PEDOT:PSS is an aqueous dispersion and it is difficult to coat it onto an organic active layer due to its hydrophobic property. Cosolvent [99] or surfactants [112] are added to improve interfacial compatibility of PEDOT: PSS and active layer. However, the conformation of PEDOT:PSS using these methods was different and consequently its work function and conductivity would be changed. Another way to uniformly

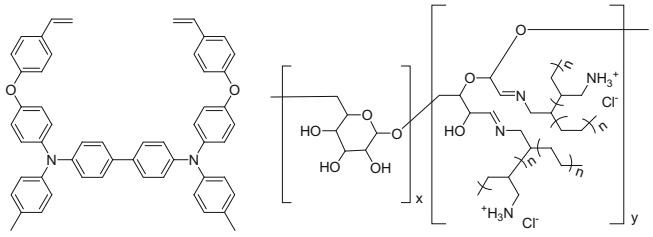

Scheme 3.5 Chemical structures of organic HTL materials for inverted polymer solar cells

deposit PEDOT:PSS onto an active layer is to use spray coating technique [128]. By incorporating D-sorbitol into PEDOT:PSS, a transparent "electric glue" can be formed, which is capable of laminating films together both mechanically and electrically [129]. Implementing the unique property of the "electric glue" into the inverted device, a semitransparent polymer solar cell based on the P3HT:$PC_{61}BM$ blend was fabricated by the lamination process with a 3 % PCE [130]. This method took advantage of the solution process, which also featured self-encapsulation and provided an alternative to the roll-to-roll production of inverted solar cells.

PEDOT:PSS in its high conductivity form can be directly used as anode for inverted solar cells. Lim et al. spray coated a layer of modified PH500 (300 S cm^{-1}) high conductivity PEDOT:PSS onto ITO/Cs_2CO_3/P3HT:$PC_{61}BM$ to form the anode, and the PCE of the device was 2 % [63]. Though the conductivity of PEDOT:PSS layer formed by spray coating was not optimized compared to spin-coating method, the advantage of spray deposition is that very thick films can be obtained, which makes up for the low conductivity. Zhou et al. went one step further to use PH1000 (900 S cm^{-1}) high conductivity PEDOT:PSS as both anode and cathode for semitransparent inverted solar cells [131]. The device structure was PH1000/ZnO/P3HT:$PC_{61}BM$/CPP-PEDOT (a low conductivity PEDOT:PSS)/PH1000, and the PCE was 1.8 %.

3.3.2.2 Solution Processable Metal Oxide HTL

Though the best inverted solar cells are fabricated with thermo-evaporated transitional metal oxide HTL such as MoO_3 or V_2O_5, solution processable HTL is preferred since vacuum evaporation could detract from the advantage of the ease of polymer solar cell fabrication. Therefore, some efforts are made to design solution-processing route for transitional metal oxide materials. Huang et al. dispersed V_2O_5 powder in isopropanol through ultrasonic agitation and spin cast the dispersion onto P3HT: $PC_{61}BM$ active layer to form HTL [124]. The device with configuration ITO/ZnO nanorod/P3HT:$PC_{61}BM$/V_2O_5/Ag has a PCE of 3.56 % under optimum V_2O_5 thickness, compared to 2.24 % for reference device without the V_2O_5 layer. Later, it was found that NiO NPs can also be dispersed in isopropanol and spin cast onto active layer to form HTL. Lim et al. reported solution-processed NiO as single HTL [132] and Lin et al. reported the solution process of NiO/plexcore HTL double layer HTL [133]. A sol–gel solution process of copper (I) oxide (Cu_2O) HTL similar to the sol–gel process of ZnO was recently reported [134]. Deionized water was added into the copper (II) acetate monohydrate precursor solution to trigger sol–gel reaction and the solution is then spin cast onto active layer to form Cu_2O layer in situ. PCE of the devices with the Cu_2O HTL are improved from 3.34 to 4.02 %.

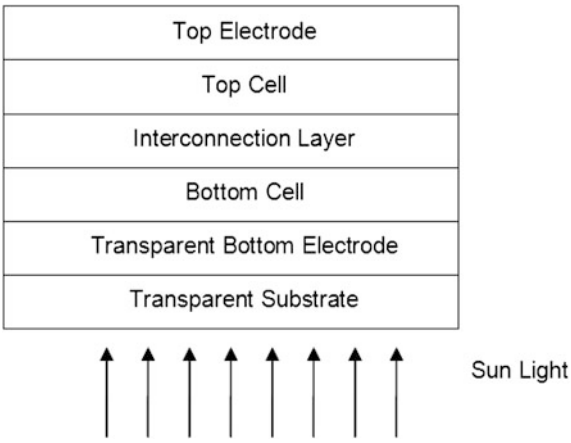

Fig. 3.2 Schematics of common double junction tandem solar cell device structure

3.4 Interface Engineering for Organic Tandem Solar Cell Devices

To improve the absorption of the sunlight photons by organic solar cells, active materials with a broader absorption spectrum have to be designed. This is generally achieved by reducing the band gap of the material which could lead to lower V_{OC} in the devices. Another strategy is to apply tandem device structure in which multiple absorbers with different band gaps are to be stacked or mixed in multiple junctions. When two or more donor materials with nonoverlapping absorption spectra are used in a tandem solar cell, broader range of the solar spectrum can be covered without sacrificing V_{OC} of the device, as the thermalization of hot carriers can be minimized [135]. The most commonly employed tandem cell structure is a two terminal monolithic device in which two subcells are connected in series through an interconnecting layer (ICL), as shown in Fig. 3.2. Several approaches for organic tandem cells have been reported in recent years, depending on the materials used for the active layer and the respective interconnection layers. In general, the organic tandem solar cells can be divided into three classes [136]: (1) Tandem organic solar cells in which low-molecular-weight molecules are used for both the bottom and the top cells; (2) Hybrid tandem organic solar cells in which the bottom cell is processed from polymers by solution-processing, while the top cell is made of vacuum-deposited low-molecular-weight molecules; (3) Fully solution-processed tandem organic solar cells in which both the bottom and the top cells are BHJ–PSCs. The third class of organic tandem solar cells began to receive enormous attentions since Kim et al. successfully fabricated an all solution-processed (except the cathode) tandem cell device with a record efficiency of 6.5 % in 2007 [12]. The interface problems in such tandem solar cell devices are much more complicated than single junction devices, as more layers are incorporated into a single device.

The ICL, both physically and electrically, connects the two subcells in an organic tandem solar cell device and it is critical in the fabrication of highly

Table 3.4 Summary of performances of organic tandem solar cell devices using different ICL designs

ICL	Bottom Cell	Top Cell	PCE (%)	J_{sc} (mA cm^{-2})	V_{oc} (V)	FF (%)	Ref
Au	H_2PC/Me-PTC	H_2PC/Me-PTC	~1	–	0.78	–	[137]
Ag	CuPc/PTCBI	CuPc/PTCBI	2.30	6.5	0.93	38.0	[138]
Au	P3HT/$PC_{61}BM$ [a]	ZnPc:C_{60}	2.30	4.8	1.02	45.0	[139]
n-doped C_{60}/Au/p-doped MeO-TPD	ZnPc:C_{60}	ZnPc:C_{60}	3.80	12.0 [b]	0.99	47.0	[140]
BPhen:Li/Au/ MTDATA:F4-TCNQ	P3HT:$PC_{61}BM$	CuPc/C_{60}	1.20	2.5	0.99	47.0	[141]
Al/WO_3	P3HT:$PC_{61}BM$	CuPc:C_{60}	4.60 [c]	–	–	–	[142]
LiF/Al/MoO_3	P3HT:$PC_{61}BM$	CuPc:C_{60}	2.82	6.1	1.01	46.2	[143]
ITO/PEDOT:PSS	MDMO-PPV:$PC_{61}BM$	MDMO-PPV:$PC_{61}BM$	3.10	4.1	1.34	56.4	[144]
LiF/Al/Au/PEDOT:PSS	PFDTBT/$PC_{61}BM$	PTBEHT/$PC_{61}BM$	1.40	0.9	55	57.0	[145]
ZnO/neutral PEDOT	MDMO-PPV:$PC_{61}BM$	P3HT:$PC_{61}BM$	1.90	3.0	1.53	42.0	[146]
TiO_2/Al/PEDOT:PSS	P3HT:$PC_{71}BM$	PSBDTBT:$PC_{71}BM$	5.84	7.4	1.25	63.2	[147]
TiO_x/PEDOT:PSS	PCPDTBT:$PC_{61}BM$	P3HT:$PC_{71}BM$	6.50	7.8	1.24	67.0	[12]
MoO_3/Al/ZnO(Inverted)	P3HT:$PC_{61}BM$	PSBDTBT:$PC_{71}BM$	5.10	7.8	1.20	54.1	[149]
MoO_3/Ag/Al/Ca (Inverted)	P3HT:$PC_{61}BM$	P3HT:$PC_{61}BM$	2.78	3.81	1.18	61.8	[150]

efficient tandem devices. Inappropriate design of the ICL could lead to electrical or optical losses which would in turn result in the loss of performance, and most notably the loss of V_{OC}. The role of the ICL in tandem devices is threefold: (1) it should efficiently collect electrons from one subcell and holes from another subcell; (2) it should act as an efficient recombination zone so that charge accumulation in this layer is minimized; (3) for all solution-processed tandem devices, it should also act as effective separation layer to protect the bottom cell from dissolving during processing of the top cell.

In this section, we focus on the design and fabrication of ICLs in organic tandem solar cells since the most important interfacial engineering problems are related to this layer. The summary of organic tandem solar cell performance using different ICL designs is listed in Table 3.4.

3.4.1 Thermally Evaporated ICL

In small molecule tandem cells, the acceptor layer of bottom cell and the donor layer of the top cell can be completely separated to prevent formation of an inverse p–n junction by the simple incorporation of an ultra-thin layer of Au [137] or Ag [138]. However, if a thin layer of metal is used as ICL in a tandem cell with at least one polymer BHJ as subcell, the interlayer contacts both the acceptor and donor domains of the BHJ, making the selective extraction of electrons or holes from the polymer BHJ impossible. To overcome this problem, diffused bilayer polymer

heterojunction can be used instead of a BHJ, so that only $PC_{61}BM$ contacts the metal layer [139]. Another approach is to have additional hole-blocking or electron-blocking layers in the ICL. Heavily doped p–n junction as ICL was proposed to ensure Ohmic contact between the subcells [140, 141]. This approach allowed the addition of the V_{OC} of individual subcells in tandem architectures with minimal loss due to absorption or reflection in the interlayer. More importantly, the good electrical contact of the ICL does not depend on the choice of photoactive materials.

More commonly used ICL design for tandem cells is the bilayer composite consisting of a low work-function (*n*-type) layer and a high work-function (*p*-type) layer [142]. Typical materials used for *p*-type layer are high work-function metal oxides such as MoO_3 or WO_3. These metal oxides can easily form Ohmic contact with organic active layers and they are also highly transparent. Zhao et al. used MoO_3 as high work-function contact for the top cell and a bilayer of LiF and Al forming a low work-function contact with the bottom cell [143]. Negligible optical loss in the ICL was observed because of almost 100 % transmittance of the interlayer and no potential losses were observed either.

A major challenge in fabricating polymer tandem cells is the processing of the top cell without damaging the underlying layers. Thus, the criterion for choosing the materials for ICL, besides Ohmic contact forming ability, is the robustness of the thin film so that it can withstand any solution process and protect the bottom cell layers. Kawano et al. demonstrated a polymer tandem cell using ITO/PEDOT:PSS as ICL [144]. The ITO layer in the ICL was sputtered onto bottom cell active layer in 1 Pa of argon gas so that the damage in active layer can be prevented during sputtering. It was found that 20 nm of ITO was sufficient to protect the underlying active layer from solution process of the top cell. Hadipour et al. used an efficient multilayer ICL consisting of *n*-type and *p*-type layers [145]. The *n*-type layers were LiF/Al and the *p*-type layers were Au/PEDOT:PSS. Au layer was deposited to protect the bottom LiF/Al contact from the solution process of the top cell. V_{OC} of the tandem cell was equal to the sum of V_{OC} of the component cells which shows the effectiveness of the ICL. However, the disadvantage of using metal layers is the loss of incident photons for the top cell.

3.4.2 Solution-Processed ICL

The real advantage of polymer solar cells is the ease of fabrication using solution process, thus the development of solution-processed ICL for tandem cells is necessary in order not to compromise this advantage. There were many reports on solution-processed electron transport layers such as ZnO and TiO_2 (or TiO_x), that can be used as *n*-type layers in the ICL. These electron transport layers are wide-band-gap semiconductors and are highly transparent to sunlight. PEDOT:PSS, being a high work-function conducting polymer, is predominantly used to form Ohmic contact for holes with the polymer BHJ and is an alternative to thermally

evaporated high work-function metal oxides. The first demonstration of all solution-processed polymer tandem cells was using ZnO NPs dissolved in acetone to deposit the *n*-type layer, and aqueous-based neutral pH PEDOT:PSS as the *p*-type layer [146]. ZnO has been shown to form an efficient contact for electron extraction from polymer BHJ because of its matching energy level with $PC_{61}BM$. The alcohol dispersed ZnO NPs does not damage the bottom polymer layer and aqueous-based neutral PEDOT:PSS layer does not affect the ZnO layer. Such an ICL is robust enough to protect the bottom polymer cell from any subsequent solution process. It was thus guaranteed that during the entire fabrication process, none of the solution process steps damaged the previously formed layers. Using these solution-processed ICLs, double and triple junction tandem cells were shown with only minor losses in V_{OC}.

Sol–gel derived TiO_2 is another potential candidate as an *n*-type contact. Kim et al. and Sista et al. used sol–gel based TiO_2 layer for efficient electron extraction from the bottom cell and PEDOT:PSS as a *p*-type layer [12, 147]. Though the synthesis approaches of TiO_2 employed by the two groups are totally different, highly efficient tandem cells were both demonstrated without V_{OC} losses. Kim et al. used a TiO_x precursor solution to coat 20–30 nm thick dense films on polymer layer that was followed by baking in air for hydrolysis of precursor into solid state TiO_x. The purpose of the TiO_x layer was threefold: being an electron transport layer, a hole-blocking layer, and an optical spacer. On the other hand, Sista et al. used crystalline NPs of TiO_2 dispersed in alcohol solvent to form an electron transport layer [148]. Several other reports on solution-processed tandem cells have used ZnO or TiO_2 via various processes as *n*-type contact and PEDOT:PSS for *p*-type contact, yielding efficient tandem cells.

3.4.3 Efficient Recombination Inside ICL

The charge recombination rate inside the ICL should match the charge extraction rate from the two sub cells, otherwise it will lead to accumulation of charges in the ICL, increasing the R_s and even induces significant loss in the photocurrent near V_{OC}, resulting in low efficiency devices with S-shaped *J*–*V* curves.

Gilot et al. observed such S-shaped *J*–*V* curves in their tandem solar cell devices and they attributed the problem to the non-Ohmic contact between ZnO and PEDOT:PSS in the ICL, which would form a counterdiode, and thus hinders charge recombination [146]. To restore efficient charge recombination in the ICL, a thin Ag layer was inserted between ZnO and PEDOT layer, and the S-shaped curve disappeared. Alternatively, an Ohmic contact between *n*-type and *p*-type layers inside ICL can be formed by heavily doping the two layers. In the case of PEDOT:PSS/ZnO ICL, further doping of PEDOT:PSS is not necessary, and the doping level of ZnO was increased by UV irradiation. Gilot et al. observed that the S-shaped curve disappears soon after UV irradiation and the V_{OC} of the tandem cell increases. Similar cases were reported by Sista et al. in tandem solar cell

devices using PEDOT:PSS/TiO_2 ICL [147]. They observed S-shaped curves in such tandem devices, and when the devices were irradiated with UV light of wavelength below 400 nm, the *J–V* characteristics returned to normal and the PCE was thus greatly improved.

The UV activation phenomenon described above is useful to study the interface interaction between transitional metal oxides and heavily-doped conjugated polymers. A similar behavior was observed for single junction devices with TiO_2/PEDOT:PSS/Al as the composite cathode, confirming the theory that this transition from a high resistance state to a low resistance state is the result of Schottky-to-Ohmic transition of PEDOT:PSS/TiO_2 contact [147]. The *p*-type PEDOT:PSS and *n*-type TiO_2 form a metal–semiconductor contact with a triangular barrier at the TiO_2/PEDOT:PSS interface. At a low doping level of TiO_2, the triangular barrier width is large and blocks electrons in TiO_2 to recombine with holes from PEDOT:PSS. After irradiating with UV light, the free carrier concentration in TiO_2 increases significantly and the barrier width decreases to an extent that electrons can tunnel through the barrier. However, this transition to Ohmic contact is not permanent, as the device reverts back to the high resistance state after prolonged storage in the dark. Thus, methods that can realize stable doping of metal oxides are desired. One approach is the chemical doping using electron-donating species. Park et al. reported the doping of TiO_2 NPs by Cs_2CO_3 [148], causing a significant energy level shift of TiO_2. It was observed that Ti ions were partially reduced by Cs ion through charge transfer, thus increasing the *n*-type doping.

3.4.4 ICL for Inverted Tandem Solar Cells

As reported by Chou et al., the advantages of the tandem and inverted structure can be combined by employing a metal oxide-only interlayer (MoO_3/Al/ZnO) to connect two inverted BHJs devices [149]. An inverted tandem solar cell with P3HT:$PC_{61}BM$ and poly[(4,4′-bis(2-ethylhexyl)dithieno[3,2-b:2′,3′-d] silole)-2,6-diyl-alt-(2,1,3-benzothiadiazole)-4,7-diyl] (PSBTBT, see Scheme 3.1):$PC_{71}BM$ as bottom cell and top cell respectively can reach a PCE of 5.1 %. A low temperature hydrolysis process was developed to form a dense and smooth amorphous ZnO layer with excellent diode properties, while the crystalline ZnO appears rougher and more porous. In addition, the MoO_3 provides a much robust resilience against the sol–gel process compared to V_2O_5 or Al. As a result, the materials and configurations of the interlayer for the tandem architecture were no longer limited by the acidic PEDOT:PSS. Compared to PEDOT:PSS, the absorption of the metal oxide-based interlayer is also smaller, resulting in higher photocurrent for both single and tandem cells. Sun et al. also reported a multilayered ICL in inverted tandem cells [150]. MoO_3/Ag/Al/Ca interlayer was vacuum deposited, and followed by deposition of the rear cell via spin-coating process. Such an interlayer structure features high transparency and low R_s, as well as effective charge

recombination, rendering an exact summation of V_{oc} (1.18 V) of the two subcells and a high FF (61.8 %). Maximum PCE of 2.78 % is mainly due to the fact of using identical subcells.

3.5 Summary and Outlook

The overall performance of BHJ–PSCs (for either conventional device, inverted device, or tandem device) is determined by a series of sequential optoelectronic processes including charge separation, transporting, and extraction, which can be controlled by the manipulation of intrinsic properties of the photoactive materials, the morphology of active layer and the electrical contact of interfaces between different layers, etc. The interface problems between different thin film layers inside a polymer solar cell device is neglected for a long time by researchers as most of their efforts were devoted to the development of new active materials, the optimization of active layer morphology. Thus only until recently did the mainstream researchers realize the importance of interface engineering on the photovoltaic performance of devices. Great improvements in performance were thus achieved for BHJ–PSCs field via the understanding of interface function and the development of highly efficient interface modification materials. As discussed in this chapter, the interlayers function in many aspects, such as improving interfacial electrical contact, passivating charge trapping states, altering electrode work function, controlling energy alignment, enhancing charge collection, inducing active layer phase separation, redistributing the incident light field, and even improving the yield and quality of device fabrication process. However, most of the reported interfacial materials function only the above-mentioned aspects partially and may result in some side effects. Moreover, some interfacial materials are sensitive to the active layer, i.e., functional for some certain photovoltaic materials but not for others. Therefore, the integration of all kinds of different functions into one material is still challenging and in the near future, the development of more efficient interfacial materials is still required. Nevertheless, the great progress in the field of BHJ–PSCs gives the researchers opportunity and confidence to develop more powerful interfacial materials and roll-to-roll compatible fabrication methods, and thereby pave the way for commercialization of polymer solar cells.

References

1. Günes S, Neugebauer H, Sariciftci NS (2007) Conjugated polymer-based organic solar cells. Chem Rev 107:1324–1338
2. Thompson BC, Fréchet JMJ (2008) Polymer–fullerene composite solar cells. Angew Chem Int Ed 47:58–77
3. Helgesen M, Sondergaard R, Krebs FC (2010) Advanced materials and processes for polymer solar cell devices. J Mater Chem 20:36–60

4. Service RF (2011) Outlook brightens for plastic solar cells. Science 332:293
5. Cheng Y-J, Yang S-H, Hsu C-S (2009) Synthesis of conjugated polymers for organic solar cell applications. Chem Rev 109:5868–5923
6. He Y, Li Y (2011) Fullerene derivative acceptors for high performance polymer solar cells. Phys Chem Chem Phys 13:1970–1983
7. Chen J, Cao Y (2009) Development of novel conjugated donor polymers for high-efficiency bulk-heterojunction photovoltaic devices. Acc Chem Res 42:1709–1718
8. Ma W, Yang C, Gong X, Lee K, Heeger AJ (2005) Thermally stable, efficient polymer solar cells with nanoscale control of the interpenetrating network morphology. Adv Funct Mater 15:1617–1622
9. Li G, Shrotriya V, Huang J, Yao Y, Moriarty T, Emery K, Yang Y (2005) High-efficiency solution processable polymer photovoltaic cells by self-organization of polymer blends. Nat Mater 4:864–868
10. Peet J, Kim JY, Coates NE, Ma WL, Moses D, Heeger AJ, Bazan GC (2007) Efficiency enhancement in low-bandgap polymer solar cells by processing with alkane dithiols. Nat Mater 6:497–500
11. Hau SK, Yip HL, Jen AKY (2010) A review on the development of the inverted polymer solar cell architecture. Polym Rev 50:474–510
12. Kim JY, Lee K, Coates NE, Moses D, Nguyen T-Q, Dante M, Heeger AJ (2007) Efficient tandem polymer solar cells fabricated by all-solution processing. Science 317:222–225
13. Chen L-M, Xu Z, Hong Z, Yang Y (2010) Interface investigation and engineering—achieving high performance polymer photovoltaic devices. J Mater Chem 20:2575–2598
14. Ma H, Yip H-L, Huang F, Jen AKY (2010) Interface engineering for organic electronics. Adv Funct Mater 20:1371–1388
15. Po R, Carbonera C, Bernardi A, Camaioni N (2011) The role of buffer layers in polymer solar cells. Energy Environ Sci 4:285–310
16. Yu G, Gao J, Hummelen JC, Wudl F, Heeger AJ (1995) Polymer photovoltaic cells: enhanced efficiencies via a network of internal donor-acceptor heterojunctions. Science 270:1789–1791
17. Hirose Y, Kahn A, Aristove VPS (1996) Chemistry, diffusion, and electronic properties of a metal/organic semiconductor contact: In/perylenetetracarboxylic dianhydride. Appl Phys Lett 68:217–219
18. Oji H, Ito E, Furuta M, Kajikawa K, Ishii H, Ouchi Y, Seki K (1999) P-sexiphenyl/metal interfaces studied by photoemission and metastable atom electron spectroscopy. J Electron Spectrosc Relat Phenom 103:517–521
19. Lögdlund M, Brédas JL (1994) Theoretical studies of the interaction between aluminum and poly(p-phenylenevinylene) and derivatives. J Chem Phys 101:4357–4364
20. Antoniadis H, Hsieh BR, Abkowitz MA, Jenekhe SA, Stolka M (1994) Photovoltaic and photoconductive properties of aluminum/poly(p-phenylene vinylene) interfaces. Synth Met 62:265–271
21. Yu G, Zhang C, Heeger AJ (1994) Dual—function semiconducting polymer devices: Light—emitting and photodetecting diodes. Appl Phys Lett 64:1540–1542
22. Yu G, Pakbaz K, Heeger AJ (1994) Semiconducting polymer diodes: large size, low cost photodetectors with excellent visible—ultraviolet sensitivity. Appl Phys Lett 64:3422–3424
23. Shaheen SE, Brabec CJ, Sariciftci NS, Padinger F, Fromherz T, Hummelen JC (2001) 2.5% efficient organic plastic solar cells. Appl Phys Lett 78:841–843
24. Limketkai BN, Baldo MA (2005) Charge injection into cathode-doped amorphous organic semiconductors. Phys Rev B 71:085207
25. Gao D, Helander MG, Wang Z-B, Puzzo DP, Greiner MT, Lu Z-H (2010) C60:Lif blocking layer for environmentally stable bulk heterojunction solar cells. Adv Mater 22:5404–5408
26. Jönsson SKM, Carlegrim E, Zhang F, Salaneck WR, Fahlman M (2005) Photoelectron spectroscopy of the contact between the cathode and the active layers in plastic solar cells: the role of lif. Jpn J Appl Phys 44:3695–3701

27. Huang J, Xu Z, Yang Y (2007) Low-work-function surface formed by solution-processed and thermally deposited nanoscale layers of cesium carbonate. Adv Funct Mater 17:1966–1973
28. Huang JS, Hou W-J, Li J-H, Li G, Yang Y (2006) Improving the power efficiency of white light-emitting diode by doping electron transport material. Appl Phys Lett 89:133509
29. Li G, Chu CW, Shrotriya V, Huang J, Yang Y (2006) Efficient inverted polymer solar cells. Appl Phys Lett 88:253503
30. Chen FC, Wu JL, Yang SS, Hsieh KH, Chen WC (2008) Cesium carbonate as a functional interlayer for polymer photovoltaic devices. J Appl Phys 103:103721
31. Wu CI, Lin CT, Chen YH, Chen MH, Lu YJ, Wu CC (2006) Electronic structures and electron-injection mechanisms of cesium-carbonate-incorporated cathode structures for organic light-emitting devices. Appl Phys Lett 88:152104
32. Chen MH, Wu CI (2008) The roles of thermally evaporated cesium carbonate to enhance the electron injection in organic light emitting devices. J Appl Phys 104:113713
33. Liao HH, Chen LM, Xu Z, Li G, Yang Y (2008) Highly efficient inverted polymer solar cell by low temperature annealing of Cs2CO3 interlayer. Appl Phys Lett 92:3–173303
34. O'Regan B, Grätzel M (1991) A low-cost, high-efficiency solar cell based on dye-sensitized colloidal tio2 films. Nature 353:737–740
35. Fujishima A, Rao TN, Tryk DA (2000) Titanium dioxide photocatalysis. J Photochem Photobiol, C 1:1–21
36. Kim JY, Kim SH, Lee HH, Lee K, Ma W, Gong X, Heeger AJ (2006) New architecture for high-efficiency polymer photovoltaic cells using solution-based titanium oxide as an optical spacer. Adv Mater 18:572–576
37. Park SH, Roy A, Beaupre S, Cho S, Coates N, Moon JS, Moses D, Leclerc M, Lee K, Heeger AJ (2009) Bulk heterojunction solar cells with internal quantum efficiency approaching 100%. Nat Photonics 3:297–303
38. Park M-H, Li J-H, Kumar A, Li G, Yang Y (2009) Doping of the metal oxide nanostructure and its influence in organic electronics. Adv Funct Mater 19:1241–1246
39. Roest AL, Kelly JJ, Vanmaekelbergh D, Meulenkamp EA (2002) Staircase in the electron mobility of a ZnO quantum dot assembly due to shell filling. Phys Rev Lett 89:036801
40. Yip H-L, Hau SK, Baek NS, Ma H, Jen AKY (2008) Polymer solar cells that use self-assembled-monolayer- modified ZnO/metals as cathodes. Adv Mater 20:2376–2382
41. Gilot J, Barbu I, Wienk MM, Janssen RAJ (2007) The use of ZnO as optical spacer in polymer solar cells: Theoretical and experimental study. Appl Phys Lett 91:113520–113523
42. Monson TC, Lloyd MT, Olson DC, Lee Y-J, Hsu JWP (2008) Photocurrent enhancement in polythiophene- and alkanethiol-modified ZnO solar cells. Adv Mater 20:4755–4759
43. Salomon A, Berkovich D, Cahen D (2003) Molecular modification of an ionic semiconductor-metal interface: ZnO/molecule/Au diodes. Appl Phys Lett 82:1051–1053
44. Yip HL, Hau SK, Baek NS, Jen AKY (2008) Self-assembled monolayer modified ZnO/metal bilayer cathodes for polymer/fullerene bulk-heterojunction solar cells. Appl Phys Lett 92:3–193313
45. Zhang F, Ceder M, Inganäs O (2007) Enhancing the photovoltage of polymer solar cells by using a modified cathode. Adv Mater 19:1835–1838
46. Huang F, Wu H, Cao Y (2010) Water/alcohol soluble conjugated polymers as highly efficient electron transporting/injection layer in optoelectronic devices. Chem Soc Rev 39:2500–2521
47. Hoven CV, Garcia A, Bazan GC, Nguyen T-Q (2008) Recent applications of conjugated polyelectrolytes in optoelectronic devices. Adv Mater 20:3793–3810
48. Luo J, Wu HB, He C, Li AY, Yang W, Cao Y (2009) Enhanced open-circuit voltage in polymer solar cells. Appl Phys Lett 95:043301–043303
49. He C, Zhong CM, Wu HB, Yang RQ, Yang W, Huang F, Bazan GC, Cao Y (2010) Origin of the enhanced open-circuit voltage in polymer solar cells via interfacial modification using conjugated polyelectrolytes. J Mater Chem 20:2617–2622

50. Na S-I, Oh S-H, Kim S-S, Kim D-Y (2009) Efficient organic solar cells with polyfluorene derivatives as a cathode interfacial layer. Org Electron 10:496–500
51. Zhao Y, Xie Z, Qin C, Qu Y, Geng Y, Wang L (2009) Enhanced charge collection in polymer photovoltaic cells by using an ethanol-soluble conjugated polyfluorene as cathode buffer layer. Sol Energy Mater Sol Cells 93:604–608
52. Oh S-H, Na S-I, Jo J, Lim B, Vak D, Kim D-Y (2010) Water-soluble polyfluorenes as an interfacial layer leading to cathode-independent high performance of organic solar cells. Adv Funct Mater 20:1977–1983
53. Zhang LJ, He C, Chen JW, Yuan P, Huang LA, Zhang C, Cai WZ, Liu ZT, Cao Y (2010) Bulk-heterojunction solar cells with benzotriazole-based copolymers as electron donors: largely improved photovoltaic parameters by using PFN/A1 bilayer cathode. Macromolecules 43:9771–9778
54. He Z, Zhang C, Xu X, Zhang L, Huang L, Chen J, Wu H, Cao Y (2011) Largely enhanced efficiency with a PFN/A1 bilayer cathode in high efficiency bulk heterojunction photovoltaic cells with a low bandgap polycarbazole donor. Adv Mater 23:3086–3089
55. Xu X, Cai W, Chen J, Cao Y (2011) Conjugated polyelectrolytes and neutral polymers with poly(2,7-carbazole) backbone: Synthesis, characterization, and photovoltaic application. J Polym Sci Part A: Polym Chem 49:1263–1272
56. Seo JH, Gutacker A, Sun Y, Wu H, Huang F, Cao Y, Scherf U, Heeger AJ, Bazan GC (2011) Improved high-efficiency organic solar cells via incorporation of a conjugated polyelectrolyte interlayer. J Am Chem Soc 133:8416–8419
57. Zuo L, Jiang X, Xu M, Yang L, Nan Y, Yan Q, Chen H (2011) Enhancement of short current density in polymer solar cells with phthalocyanine tin (iv) dichloride as interfacial layer. Sol Energy Mater Sol Cells 95:2664–2669
58. Wei Q, Nishizawa T, Tajima K, Hashimoto K (2008) Self-organized buffer layers in organic solar cells. Adv Mater 20:2211–2216
59. Yamakawa S, Tajima K, Hashimoto K (2009) Buffer layer formation in organic photovoltaic cells by self-organization of poly(dimethylsiloxane)s. Org Electron 10:511–514
60. Mihailetchi VD, Koster LJA, Hummelen JC, Blom PWM (2004) Photocurrent generation in polymer-fullerene bulk heterojunctions. Phys Rev Lett 93:216601
61. Yuan Y, Reece TJ, Sharma P, Poddar S, Ducharme S, Gruverman A, Yang Y, Huang J (2011) Efficiency enhancement in organic solar cells with ferroelectric polymers. Nat Mater 10:296–302
62. Zhang F, Johansson M, Andersson MR, Hummelen JC, Inganäs O (2002) Polymer photovoltaic cells with conducting polymer anodes. Adv Mater 14:662–665
63. Lim YF, Lee S, Herman DJ, Lloyd MT, Anthony JE, Malliaras GG (2008) Spray-deposited poly(3,4-ethylenedioxythiophene):poly(styrenesulfonate) top electrode for organic solar cells. Appl Phys Lett 93:193301–193303
64. de Jong MP, van IJzendoorn LJ, de Voigt MJA (2000) Stability of the interface between indium-tin oxide and poly(3,4-ethylenedioxythiophene)/poly(styrenesulphonate) in polymer light-emitting diodes. Appl Phys Lett 77:2255–2257
65. Kim Y-H, Lee S-H, Noh J, Han S-H (2006) Performance and stability of electroluminescent device with self-assembled layers of poly(3,4-ethylenedioxythiophene)-poly(styrenesulfonate) and polyelectrolytes. Thin Sol Fi 510:305–310
66. Wong KW, Yip HL, Luo Y, Wong KY, Lau WM, Low KH, Chow HF, Gao ZQ, Yeung WL, Chang CC (2002) Blocking reactions between indium-tin oxide and poly (3,4-ethylene dioxythiophene): Poly(styrene sulphonate) with a self-assembly monolayer. Appl Phys Lett 80:2788–2790
67. Yan H, Lee P, Armstrong NR, Graham A, Evmenenko GA, Dutta P, Marks TJ (2005) High-performance hole-transport layers for polymer light-emitting diodes. Implementation of organosiloxane cross-linking chemistry in polymeric electroluminescent devices. J Am Chem Soc 127:3172–3183

68. Xiao T, Cui W, Anderegg J, Shinar J, Shinar R (2011) Simple routes for improving polythiophene: fullerene-based organic solar cells. Org Electron 12:257–262
69. Peng B, Guo X, Cui CH, Zou YP, Pan CY, Li YF (2011) Performance improvement of polymer solar cells by using a solvent-treated poly(3,4-ethylenedioxythiophene):poly(styrenesulfonate) buffer layer. Appl Phys Lett 98:3–243308
70. Shrotriya V, Li G, Yao Y, Chu CW, Yang Y (2006) Transition metal oxides as the buffer layer for polymer photovoltaic cells. Appl Phys Lett 88:3–073508
71. Kim DY, Subbiah J, Sarasqueta G, So F, Ding HJ, Irfan, Gao YL (2009) The effect of molybdenum oxide interlayer on organic photovoltaic cells. Appl Phys Lett 95:3–093304
72. Sun Y, Takacs CJ, Cowan SR, Seo JH, Gong X, Roy A, Heeger AJ (2011) Efficient, air-stable bulk heterojunction polymer solar cells using moO_x as the anode interfacial layer. Adv Mater 23:2226–2230
73. Irwin MD, Buchholz B, Hains AW, Chang RPH, Marks TJ (2008) P-type semiconducting nickel oxide as an efficiency-enhancing anode interfacial layer in polymer bulk-heterojunction solar cells. Proc Natl Acad Sci USA 105:2783–2787
74. Irwin MD, Servaites JD, Buchholz DB, Leever BJ, Liu J, Emery JD, Zhang M, Song J-H, Durstock MF, Freeman AJ, Bedzyk MJ, Hersam MC, Chang RPH, Ratner MA, Marks TJ (2011) Structural and electrical functionality of nio interfacial films in bulk heterojunction organic solar cells. Chem Mater 23:2218–2226
75. Steirer KX, Chesin JP, Widjonarko NE, Berry JJ, Miedaner A, Ginley DS, Olson DC (2010) Solution deposited nio thin-films as hole transport layers in organic photovoltaics. Org Electron 11:1414–1418
76. Han S, Shin WS, Seo M, Gupta D, Moon S-J, Yoo S (2009) Improving performance of organic solar cells using amorphous tungsten oxides as an interfacial buffer layer on transparent anodes. Org Electron 10:791–797
77. Yoon WJ, Berger PR (2008) 4.8% efficient poly(3-hexylthiophene)-fullerene derivative (1: 0.8) bulk heterojunction photovoltaic devices with plasma treated AgOx/indium tin oxide anode modification. Appl Phys Lett 92:3–013306
78. Hains AW, Marks TJ (2008) High-efficiency hole extraction/electron-blocking layer to replace poly(3,4-ethylenedioxythiophene): Poly(styrene sulfonate) in bulk-heterojunction polymer solar cells. Appl Phys Lett 92:3–023504
79. Hains AW, Liu J, Martinson ABF, Irwin MD, Marks TJ (2010) Anode interfacial tuning via electron-blocking/hole-transport layers and indium tin oxide surface treatment in bulk-heterojunction organic photovoltaic cells. Adv Funct Mater 20:595–606
80. Subbiah J, Kim DY, Hartel M, So F (2010) MoO3/poly(9,9-dioctylfluorene-co-N-[4-(3-methylpropyl)]-diphenylamine) double-interlayer effect on polymer solar cells. Appl Phys Lett 96:3–063303
81. Li C-Y, Wen T-C, Guo T-F (2008) Sulfonated poly(diphenylamine) as a novel hole-collecting layer in polymer photovoltaic cells. J Mater Chem 18:4478–4482
82. Kang B, Tan LW, Silva SRP (2008) Fluoropolymer indium-tin-oxide buffer layers for improved power conversion in organic photovoltaics. Appl Phys Lett 93:133302–133303
83. Campoy-Quiles M, Ferenczi T, Agostinelli T, Etchegoin PG, Kim Y, Anthopoulos TD, Stavrinou PN, Bradley DDC, Nelson J (2008) Morphology evolution via self-organization and lateral, and vertical diffusion in polymer: fullerene solar cell blends. Nat Mater 7:158–164
84. Xu Z, Chen LM, Yang GW, Huang CH, Hou JH, Wu Y, Li G, Hsu CS, Yang Y (2009) Vertical phase separation in poly(3-hexylthiophene):fullerene derivative blends and its advantage for inverted structure solar cells. Adv Funct Mater 19:1227–1234
85. Liang CW, Su WF, Wang LY (2009) Enhancing the photocurrent in poly(3-hexylthiophene)/[6,6]-phenyl C-61 butyric acid methyl ester bulk heterojunction solar cells by using poly(3-hexylthiophene) as a buffer layer. Appl Phys Lett 95:3–133303
86. Zheng Q, Fang G, Bai W, Sun N, Qin P, Fan X, Cheng F, Yuan L, Zhao X (2011) Efficiency improvement in organic solar cells by inserting a discotic liquid crystal. Sol Energy Mater Sol Cells 95:2200–2205

87. Sun Y, Wang M, Gong X, Seo JH, Hsu BBY, Wudl F, Heeger AJ (2011) Polymer bulk heterojunction solar cells: function and utility of inserting a hole transport and electron blocking layer into the device structure. J Mater Chem 21:1365–1367
88. Sgobba V, Guldi DM (2008) Carbon nanotubes as integrative materials for organic photovoltaic devices. J Mater Chem 18:153–157
89. Chaudhary S, Lu H, Müller AM, Bardeen CJ, Ozkan M (2007) Hierarchical placement and associated optoelectronic impact of carbon nanotubes in polymer-fullerene solar cells. Nano Lett 7:1973–1979
90. Hatton RA, Blanchard NP, Tan LW, Latini G, Cacialli F, Silva SRP (2009) Oxidised carbon nanotubes as solution processable, high work function hole-extraction layers for organic solar cells. Org Electron 10:388–395
91. Kim JS, Park JH, Lee JH, Jo J, Kim D-Y, Cho K (2007) Control of the electrode work function and active layer morphology via surface modification of indium tin oxide for high efficiency organic photovoltaics. Appl Phys Lett 91:112111–112113
92. Hau SK, Yip H-L, Leong K, Jen AK-Y (2009) Spraycoating of silver nanoparticle electrodes for inverted polymer solar cells. Org Electron 10:719–723
93. Zeng W, Wu H, Zhang C, Huang F, Peng J, Yang W, Cao Y (2007) Polymer light-emitting diodes with cathodes printed from conducting ag paste. Adv Mater 19:810–814
94. Zhao DW, Liu P, Sun XW, Tan ST, Ke L, Kyaw AKK (2009) An inverted organic solar cell with an ultrathin ca electron-transporting layer and MoO3 hole-transporting layer. Appl Phys Lett 95:3–153304
95. Zhou Y, Cheun H, Postcavage WJ Jr, Fuentes-Hernandez C, Kim S-J, Kippelen B (2010) Inverted organic solar cells with ITO electrodes modified with an ultrathin Al2O3 buffer layer deposited by atomic layer deposition. J Mater Chem 20:6189–6194
96. White MS, Olson DC, Shaheen SE, Kopidakis N, Ginley DS (2006) Inverted bulk-heterojunction organic photovoltaic device using a solution-derived ZnO underlayer. Appl Phys Lett 89:3–143517
97. Sun YM, Seo JH, Takacs CJ, Seifter J, Heeger AJ (2011) Inverted polymer solar cells integrated with a low temperature-annealed sol-gel-derived ZnO film as an electron transport layer. Adv Mater 23:1679–1683
98. Yang TB, Cai WZ, Qin DH, Wang EG, Lan LF, Gong X, Peng JB, Cao Y (2009) Solution-processed zinc oxide thin film as a buffer layer for polymer solar cells with an inverted device structure. J Phys Chem C 114:6849–6853
99. Waldauf C, Morana M, Denk P, Schilinsky P, Coakley K, Choulis SA, Brabec CJ (2006) Highly efficient inverted organic photovoltaics using solution based titanium oxide as electron selective contact. Appl Phys Lett 89:3–233517
100. Steim R, Choulis SA, Schilinsky P, Brabec CJ (2008) Interface modification for highly efficient organic photovoltaics. Appl Phys Lett 92:3–093303
101. Oh H, Krantz J, Litzov I, Stubhan T, Pinna L, Brabec CJ (2011) Comparison of various sol-gel derived metal oxide layers for inverted organic solar cells. Sol Energy Mater Sol Cells 95:2194–2199
102. Stubhan T, Oh H, Pinna L, Krantz J, Litzov I, Brabec CJ (2011) Inverted organic solar cells using a solution processed aluminum-doped zinc oxide buffer layer. Org Electron 12:1539–1543
103. Hau SK, Yip H-L, Baek NS, Zou J, O'Malley K, Jen AKY (2008) Air-stable inverted flexible polymer solar cells using zinc oxide nanoparticles as an electron selective layer. Appl Phys Lett 92:253301–253303
104. Chua L-L, Zaumseil J, Chang J-F, Ou ECW, Ho PKH, Sirringhaus H, Friend RH (2005) General observation of n-type field-effect behaviour in organic semiconductors. Nature 434:194–199
105. Hau SK, Yip HL, Ma H, Jen AKY (2008) High performance ambient processed inverted polymer solar cells through interfacial modification with a fullerene self-assembled monolayer. Appl Phys Lett 93:3–233304

106. Hau SK, Cheng Y-J, Yip H-L, Zhang Y, Ma H, Jen AK-Y (2011) Effect of chemical modification of fullerene-based self-assembled monolayers on the performance of inverted polymer solar cells. ACS Appl Mater Interfaces 2:1892–1902
107. Khodabakhsh S, Sanderson BM, Nelson J, Jones TS (2006) Using self-assembling dipole molecules to improve charge collection in molecular solar cells. Adv Funct Mater 16:95–100
108. Armstrong NR, Carter C, Donley C, Simmonds A, Lee P, Brumbach M, Kippelen B, Domercq B, Yoo S (2003) Interface modification of ITO thin films: organic photovoltaic cells. Thin Sol Fi 445:342–352
109. Goh C, Scully SR, McGehee MD (2007) Effects of molecular interface modification in hybrid organic-inorganic photovoltaic cells. J Appl Phys 101:114503–114512
110. Hau SK, Yip HL, Acton O, Baek NS, Ma H, Jen AKY (2008) Interfacial modification to improve inverted polymer solar cells. J Mater Chem 18:5113–5119
111. Choi H, Park JS, Jeong E, Kim G-H, Lee BR, Kim SO, Song MH, Woo HY, Kim JY (2011) Combination of titanium oxide and a conjugated polyelectrolyte for high-performance inverted-type organic optoelectronic devices. Adv Mater 23:2759–2763
112. Hsieh C-H, Cheng Y-J, Li P-J, Chen C-H, Dubosc M, Liang R-M, Hsu C-S (2010) Highly efficient and stable inverted polymer solar cells integrated with a cross-linked fullerene material as an interlayer. J Am Chem Soc 132:4887–4893
113. Cheng Y-J, Hsieh C-H, He Y, Hsu C-S, Li Y (2010) Combination of indene-c60 bis-adduct and cross-linked fullerene interlayer leading to highly efficient inverted polymer solar cells. J Am Chem Soc 132:17381–17383
114. Zhou Y, Li F, Barrau S, Tian W, Inganäs O, Zhang FL (2009) Inverted and transparent polymer solar cells prepared with vacuum-free processing. Sol Energy Mater Sol Cells 93:497–500
115. Na S-I, Kim T-S, Oh S-H, Kim J, Kim S-S, Kim D-Y (2010) Enhanced performance of inverted polymer solar cells with cathode interfacial tuning via water-soluble polyfluorenes. Appl Phys Lett 97:3–223305
116. Jo G, Na S-I, Oh S-H, Lee S, Kim T-S, Wang G, Choe M, Park W, Yoon J, Kim D-Y, Kahng YH, Lee T (2010) Tuning of a graphene-electrode work function to enhance the efficiency of organic bulk heterojunction photovoltaic cells with an inverted structure. Appl Phys Lett 97:213301–213303
117. Rider DA, Worfolk BJ, Harris KD, Lalany A, Shahbazi K, Fleischauer MD, Brett MJ, Buriak JM (2010) Stable inverted polymer/fullerene solar cells using a cationic polythiophene modified PEDOT:PSS cathodic interface. Adv Funct Mater 20:2404–2415
118. Cho N, Yip H-L, Hau SK, Chen K-S, Kim T-W, Davies JA, Zeigler DF, Jen AKY (2011) N-doping of thermally polymerizable fullerenes as an electron transporting layer for inverted polymer solar cells. J Mater Chem 21:6956–6961
119. Wang J-C, Lu C-Y, Hsu J-L, Lee M-K, Hong Y-R, Perng T-P, Horng S-F, Meng H-F (2011) Efficient inverted organic solar cells without an electron selective layer. J Mater Chem 21:5723–5728
120. Kyaw AKK, Sun XW, Jiang CY, Lo GQ, Zhao DW, Kwong DL (2008) An inverted organic solar cell employing a sol–gel derived ZnO electron selective layer and thermal evaporated MoO3 hole selective layer. Appl Phys Lett 93:3–221107
121. Tao C, Ruan SP, Zhang XD, Xie GH, Shen L, Kong XZ, Dong W, Liu CX, Chen WY (2008) Performance improvement of inverted polymer solar cells with different top electrodes by introducing a MoO3 buffer layer. Appl Phys Lett 93:193307–1993307
122. Tao C, Ruan SP, Xie GH, Kong XZ, Shen L, Meng FX, Liu CX, Zhang XD, Dong W, Chen WY (2009) Role of tungsten oxide in inverted polymer solar cells. Appl Phys Lett 94:043311–043313
123. Chan MY, Lee CS, Lai SL, Fund MK, Wong FL, Sun HY, Lau KM, Lee ST (2006) Efficient organic photovoltaic devices using a combination of exciton blocking layer and anodic buffer layer. J Appl Phys 100:094506–094504

124. Huang JS, Chou CY, Liu MY, Tsai KH, Lin WH, Lin CF (2009) Solution-processed vanadium oxide as an anode interlayer for inverted polymer solar cells hybridized with ZnO nanorods. Org Electron 10:1060–1065
125. Li CY, Wen TC, Lee TH, Guo TF, Huang JCA, Lin YC, HY J (2009) An inverted polymer photovoltaic cell with increased air stability obtained by employing novel hole/electron collecting layers. J Mater Chem 19:1643–1647
126. Dong Q, Zhou Y, Pei J, Liu Z, Li Y, Yao S, Zhang J, Tian W (2010) All-spin-coating vacuum-free processed semi-transparent inverted polymer solar cells with PEDOT: PSS anode and PAH-D interfacial layer. Org Electron 11:1327–1331
127. Sun YM, Gong X, Hsu BBY, Yip HL, Jen AKY, Heeger AJ (2010) Solution-processed cross-linkable hole selective layer for polymer solar cells in the inverted structure. Appl Phys Lett 97:193310–193313
128. Weickert J, Sun H, Palumbiny C, Hesse HC, Schmidt-Mende L (2010) Spray-deposited PEDOT: PSS for inverted organic solar cells. Sol Energy Mater Sol Cells 94:2371–2374
129. Ouyang JY, Yang Y (2006) Conducting polymer as transparent electric glue. Adv Mater 18:2141–2144
130. Huang JS, Li G, Yang Y (2008) A semi-transparent plastic solar cell fabricated by a lamination process. Adv Mater 20:415–419
131. Zhou Y, Cheun H, Choi S, Potscavage JWJ, Fuentes-Hernandez C, Kippelen B (2010) Indium tin oxide-free and metal-free semitransparent organic solar cells. Appl Phys Lett 97:3–153304
132. Lim DC, Kim YT, Shim WH, Jang A-Y, Lim J-H, Kim YD, Jeong Y, Kim YD, Lee KH (2011) Wet-chemically prepared nio layers as hole transport layer in the inverted organic solar cell. Bull Korean Chem Soc 32:1067–1070
133. Lin Y-H, Yang P-C, Huang J-S, Huang G-D, Wang I-J, Wu W-H, Lin M-Y, Su W-F, Lin C-F (2011) High-efficiency inverted polymer solar cells with solution-processed metal oxides. Sol Energy Mater Sol Cells 95:2511–2515
134. Lin MY, Sun JY, Shia CH, Chen CS, Huang YA, Yang PC, Shen YM, Lin CF (2010) The inverted polymer solar cells using cuprous oxide as a hole transportation layer, pp 1171–1174
135. Ameri T, Dennler G, Lungenschmied C, Brabec CJ (2009) Organic tandem solar cells: a review. Energy Environ Sci 2:347–363
136. Hadipour A, Boer Bd, Blom PWM (2008) Organic tandem and multi-junction solar cells. Adv Funct Mater 18:169–181
137. Hiramoto M, Suezaki M, Yokoyama M (1990) Effect of thin gold interstitial-layer on the photovoltaic properties of tandem organic solar cell. Chem Lett 19:327–330
138. Yakimov A, Forrest SR (2002) High photovoltage multiple-heterojunction organic solar cells incorporating interfacial metallic nanoclusters. Appl Phys Lett 80:1667–1669
139. Dennler G, Prall HJ, Koeppe R, Egginger M, Autengruber R, Sariciftci NS (2006) Enhanced spectral coverage in tandem organic solar cells. Appl Phys Lett 89:073502–073503
140. Drechsel J, Mannig B, Kozlowski F, Pfeiffer M, Leo K, Hoppe H (2005) Efficient organic solar cells based on a double p-i-n architecture using doped wide-gap transport layers. Appl Phys Lett 86:244102–244103
141. Colsmann A, Junge J, Kayser C, Lemmer U (2006) Organic tandem solar cells comprising polymer and small-molecule subcells. Appl Phys Lett 89:3–203506
142. Janssen AGF, Riedl T, Hamwi S, Johannes HH, Kowalsky W (2007) Highly efficient organic tandem solar cells using an improved connecting architecture. Appl Phys Lett 91:3–073509
143. Zhao DW, Sun XW, Jiang CY, Kyaw AKK, Lo GQ, Kwong DL (2008) Efficient tandem organic solar cells with an Al/MoO_3 intermediate layer. Appl Phys Lett 93:3–083305
144. Kawano K, Ito N, Nishimori T, Sakai J (2006) Open circuit voltage of stacked bulk heterojunction organic solar cells. Appl Phys Lett 88:3–073514

145. Hadipour A, Bd Boer, Wildeman J, Kooistra FB, Hummelen JC, Turbiez MGR, Wienk MM, Janssen RAJ, Blom PWM (2006) Solution-processed organic tandem solar cells. Adv Funct Mater 16:1897
146. Gilot J, Wienk MM, Janssen RAJ (2007) Double and triple junction polymer solar cells processed from solution. Appl Phys Lett 90:143512–143513
147. Sista S, Park M-H, Hong Z, Wu Y, Hou J, Kwan WL, Li G, Yang Y (2010) Highly efficient tandem polymer photovoltaic cells. Adv Mater 22:380–383
148. Park MH, Li JH, Kumar A, Li G, Yang Y (2009) Doping of the metal oxide nanostructure and its influence in organic electronics. Adv Funct Mater 19:1241–1246
149. Chou C-H, Kwan WL, Hong Z, Chen L-M, Yang Y (2011) A metal-oxide interconnection layer for polymer tandem solar cells with an inverted architecture. Adv Mater 23:1282–1286
150. Sun XW, Zhao DW, Ke L, Kyau AKK, Lo GQ, Kwang DL (2010) Inverted tandem organic solar cells with a MoO_3/Ag/Al/Ca intermediate layer. Appl Phys Lett 97:3–053303

Chapter 4
Graphene for Transparent Electrodes and Organic Electronic Devices

Xiangjian Wan, Guankui Long and Yongsheng Chen

Abstract Graphene has been regarded as a promising material in organic electronics owing to its outstanding electronic, optical, thermal, and mechanical properties. In this chapter, first, we summarize and discuss the application of graphene as transparent electrode in organic photovoltaic (OPV) cells and organic light emitting diodes (OLED). Improving the conductivity of graphene without compromising the transparency and tuning its work function to match the interface and/or active materials are proposed to focus on the future study for graphene-based transparent electrode. Then, the application of graphene as acceptor material in OPV has been addressed. The factors of size, energy level, and functionalization of graphene should be considered first. Last, graphene-based all-carbon electronics have been introduced, which indicates that graphene exhibits great potential for fabricating the highly demanded all-carbon, flexible devices and electronics.

4.1 Introduction

Graphene, a single sheet composed of sp^2-hybridized carbon, is regarded as the basic building block of all dimensional graphitic materials; it can be stacked to form 3D graphite, rolled to form 1D nanotubes, and wrapped to form 0D fullerenes. In recent years, graphene has been of great interests owing to its outstanding electronic, optical, thermal, and mechanical properties [1, 2]. Due to its unique and superior optical and electronic properties such as good transparency, high

X. Wan · G. Long · Y. Chen (✉)
Key Laboratory of Functional Polymer Materials and the Centre of Nanoscale Science and Technology, Institute of Polymer Chemistry, College of Chemistry, Nankai University, Tianjin 300071, China
e-mail: yschen99@nankai.edu.cn

W. C. H. Choy (ed.), *Organic Solar Cells*, Green Energy and Technology,
DOI: 10.1007/978-1-4471-4823-4_4,

mobility, high electrical conductivities, and low contact resistance with organic materials, graphene has been extensively studied in the field of organic electronic devices [2], such as organic photovoltaics (OPVs) [3–5], organic light-emitting diodes (OLEDs) [6, 7], field effect transistors (FETs) [8, 9], and etc. There are quite some broad reviews about graphene in many aspects [10–15], Herein, we will restrict ourselves to summarize and discuss transparent electrodes based on graphene and application of graphene in the electronic devices, especially our works for OPVs.

4.2 Graphene for Transparent Electrode

As the essential part of optoelectronic devices, the ideal transparent electrodes should have high transparency, low sheet resistance, proper work function, and low preparation cost. Currently, indium tin oxide (ITO) plays a dominant role and is the market standard for most of transparent electrode applications. However, the use of ITO as transparent electrode may be limited for its intrinsic drawbacks such as the costly preparative methods (sputtering, evaporation, pulsed laser deposition, and electroplating), limited source of indium on the Earth, toxic property of indium for environment and humans, its intrinsic brittleness property, etc. Thus, developing new transparent conducting materials has become necessary. Graphene-based transparent electrodes have drawn great attentions owing to its excellent properties such as high mobility, high transparency, etc. Several excellent reviews have discussed the updated progress and comprehensive applications of the transparent electrodes based on graphene [16, 17]. Herein, we will give a brief summarization of the graphene-based transparent electrode for organic electronic devices, especially for OPVs.

4.2.1 Transparent Electrode Based on rGO

In contrast with graphene based on other preparation methods such as micromechanical exfoliation [18], epitaxial growth [19], and chemical vapor deposition (CVD) [20], reduced graphene oxide (rGO) [21–23] has been studied primarily owing to the advantages of high throughput preparation, low cost, and the simplicity of the fabrication technique.

In our initial work, we have studied spin-coated GO thin films by different reduction treatments with hydrazine reduction and/or high-temperature annealing, producing films with sheet resistances as low as 10^2–10^3 Ω/sq with 80 % transmittance for 550 nm light (Fig. 4.1a) [24]. Using the neat rGO film as the transparent anode, we have demonstrated solution-processed polymer OPVs with poly-(3-hexylthiophene) (P3HT) as the electron donor and phenyl-C_{61}-butyric acid methyl ester (PCBM) as the acceptor (Fig. 4.1b) [25]. After spin-coating

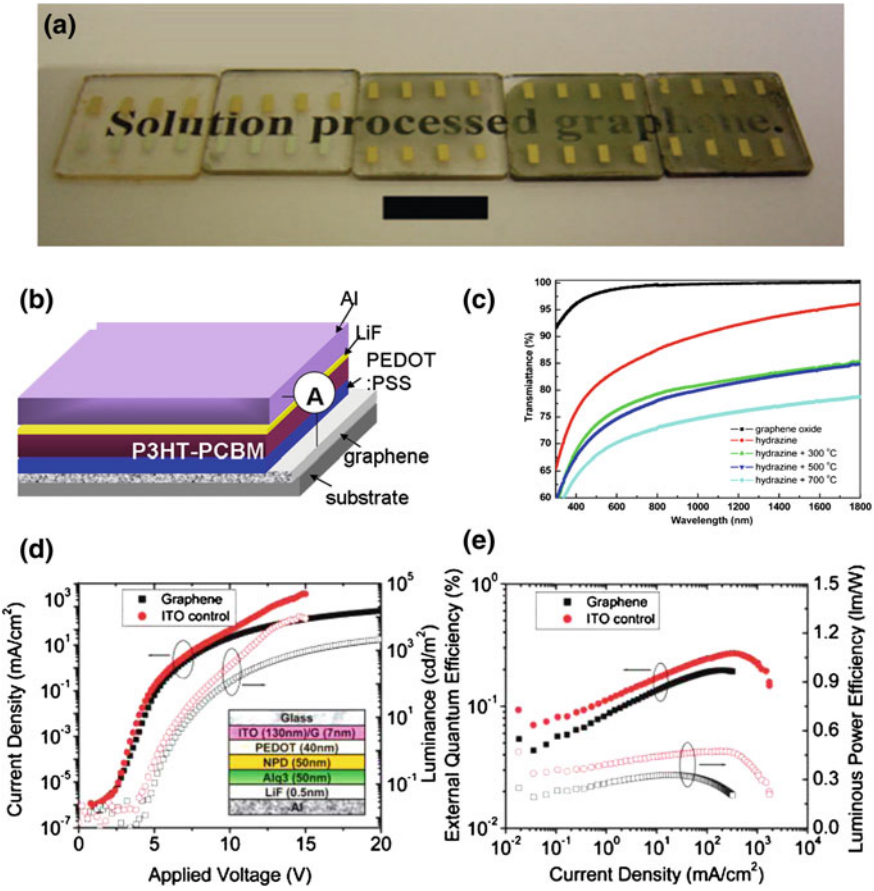

Fig. 4.1 (**a**) Photograph of an unreduced (*left most*) and a series of high-temperature reduced GO films of increasing thickness. Black scale bar is 1 cm. (**b**) Device structure and energy diagram of the fabricated device with structure quartz/graphene/PEDOT:PSS/P3HT:PCBM/LiF/Al. (**c**) Optical transmittance spectra of graphene oxide film (~40 nm) and graphene films (~25 nm) with different reduced methods. (**d**) Current density (*filled symbols*) and luminance (*open symbols*) versus applied forward bias for an OLED on graphene (*squares*) and ITO (*circles*), with OLED device structure anode/PEDOT:PSS/NPD(50 nm)/Alq_3(50 nm)/LiF/Al as shown in the inset. (**e**) External quantum efficiency (EQE) (*filled symbols*) and luminous power efficiency (LPE) (*open symbols*) for an OLED on graphene film (*squares*) and ITO glass (*circles*). (**a**) Reproduced with permission [24]. Copyright 2008, ACS. (**b**–**c**) Reproduced with permission [25]. Copyright 2010, Elsevier. (**d**–**e**) Reproduced with permission [6]. Copyright 2010, ACS

deposition, the insulating graphene oxide films were reduced through exposure to hydrazine vapor and then annealed under inert conditions to render the material electrically conductive. The electrical conductivity of the as-prepared graphene film is closely related to the annealing temperature. At a given film thickness of ~25 nm, graphene film conductivity increased with the increase of the annealing

temperatures (Fig. 4.1c). The reduced graphene films could have a sheet resistance of 17.9 KΩ/sq (transmittances of 69 % at 550 nm) and a conductivity of 22.3 S/cm. The OPV device under illumination of simulated solar light (AM 1.5G) shows a short-circuit photocurrent density (J_{sc}) of 1.18 mA/cm^2 with an open-circuit voltage (V_{oc}) of 0.46 V, a filling factor (FF) of 0.25, and PCE of 0.13 %. The low PCE is due to the high sheet resistance of graphene films and the hydrophobic graphene film surface, which makes it rather hard to get a uniform PEDOT:PSS layer.

Wu et al. used rGO as transparent conductive anodes for an organic bilayer small molecule OPV cells [26]. The transparent electrodes based on graphene were obtained by vacuum annealing of graphene oxide or by a combination of a hydrazine treatment and argon annealing at 400 °C. The thickness of graphene films used to fabricate OPV cells is between 4 and 7 nm, and the corresponding values of the transmittance and sheet resistance are 95–85 %, and 100–500 kΩ/sq, respectively. Devices with structure of anode/CuPc/C_{60}/BCP/Ag were fabricated. The J_{sc}, V_{oc}, FF, and PCE are 2.1 mA/cm^2, 0.48 V, 0.34, and 0.4 %, respectively, for the cell on graphene, and 2.8 mA/cm^2, 0.47 V, 0.54, and 0.84 %, respectively, for the cell on ITO for comparison. The poor solar cells performance is mainly caused by the high sheet resistance of the graphene thin films, which need to be reduced without compromising transmittance.

Wu et al. also demonstrate OLEDs with solution-processed graphene film as transparent conductive anodes (Fig. 4.1d, e) [6]. The graphene electrodes were deposited on quartz substrates by spin coating of an aqueous dispersion of functionalized graphene, followed by a vacuum anneal step to afford the graphene films with resistance and transmittance of 800 Ω/sq and 82 % (550 nm). OLED device with structure of anode/PEDOT:PSS/N,N′-di-1-naphthyl-N,N′-diphenyl-1,1′-biphenyl-4,4′-diamine(NPD)/tris(8-hydroxyquinoline)aluminum(Alq_3)/LiF/Al was fabricated. The OLEDs on graphene exhibited a current drive and light emission intensity comparable to those of ITO-based devices when the current density was <10 mA/cm^2. Meanwhile, the external quantum efficiency (EQE) and the luminous power efficiency (LPE) of graphene-based OLEDs nearly matched that of the ITO-based device. The turn-on voltage of the OLED with graphene-based transparent electrode was 4.5 V, slightly higher than the 3.8 V of the ITO-based device.

Similar, works have been reported and comparable PCE results were achieved using rGO as transparent electrode in OPVs. For example, Eda et al. reported the preparation of transparent and conductive graphene film by vacuum filtration of graphene oxide to form a film, followed by a combination of hydrazine vapor and low-temperature annealing (200 °C) in nitrogen or vacuum [27]. Using above rGO film as the transparent electrode, OPV device with P3HT and PCBM as active layer gave the PCE of approximately 0.1 %, which is limited by the large resistance with the order of 10^5 Ω/sq for the rGO electrodes. Yin et al. fabricated flexible OPV devices by using a transferred rGO film as the transparent electrode. The highest PCE obtained is 0.78 %, employing the flexible rGO/polyethylene terephthalate (PET)-based transparent electrodes with a transparency of 55 % and resistance of 1.6 kΩ/sq [28]. Geng et al. reported the preparation of transparent

conductive graphene films by a two-step reduction method that consisted of the controlled chemical reduction of GO in an aqueous suspension and the thermal annealing of the resultant films [29]. OPV devices with P3HT and PCBM as active layer showed PCE of 1.01 %.

4.2.2 Transparent Electrode Based on CVD graphene

CVD is an important and successful method to obtain high-quality graphene films [30–32]. Recently, films with sheet resistance of 280 Ω/sq (80 % transparency) and 770 Ω/sq (90 % transparency) have been reported for CVD graphene synthesized on Ni films [20].

Wang et al. synthesized a large-area graphene film on Ni-coated SiO_2/Si wafer using a CVD process [33]. For 6–30 nm thick graphene films, the average sheet resistance varies from 1350 to 210 Ω/sq with an optical transparency from 91 to 72 % in the visible light wavelength range. As shown in Fig. 4.2, a BHJ structure solar cell using the graphene anode was fabricated. The J_{sc}, V_{oc}, FF, and PCE are 2.39 mA/cm^2, 0.32 V, 0.27, and 0.21 %, respectively. The poor performance was caused by the hydrophobic property of graphene, which could not form the uniform coating of PEDOT:PSS. After the UV treatment of graphene film for 10 min to improve the surface wettability, the device PCE was increased to 0.74 %. In order to avoid the disruption of the aromatic structures caused by covalent bonding with oxygen groups after the UV treatment, the graphene anode was modified by self-assembled pyrene buanoic acid succidymidyl ester (PBASE). A well-improved performance (V_{oc} = 0.55 V, J_{sc} = 6.05 mA/cm^2, FF = 0.51, and PCE = 1.71 %) was obtained. In contrast, the device made with ITO anode showed V_{oc}, J_{sc}, FF, and PCE of 0.56 V, 9.03 mA/cm^2, 0.61, and 3.10 %, respectively.

Similar works employing CVD graphene as transparent electrode for OPV application have been reported recently. For example, Arco et al. reported a transparent graphene film by CVD with sheet resistance 230 Ω/sq and 72 % transparency at the wavelength of 550 nm [34]. OPV devices using CVD graphene and ITO electrodes were fabricated side-by-side on flexible PET substrates and were confirmed to offer comparable performance, with PCE 1.18 and 1.27 %, respectively. Loh et al. reported a layer-by-layer (LBL) transfer method of CVD graphene sheets. The LBL, acid-doped, four layer graphene film exhibited a sheet resistance of 80 Ω/sq and a transmittance of 90 % at 550 nm, which is comparable to the ITO [35]. OPVs with the structure of graphene/PEDOT:PSS/P3HT:PCBM/LiF/Al exhibited the best performance with a PCE of 2.5 %, which is comparable with the PCE of 3 % for ITO-based devices. Lee and his coworkers reported the preparation of multilayer graphene (MLG) film grown by CVD [36]. OPV devices using graphene with sheet resistances of 606 Ω/sq and transmittances of 87 % as electrodes showed the best performance with PCE up to 2.58 ± 0.45 %.

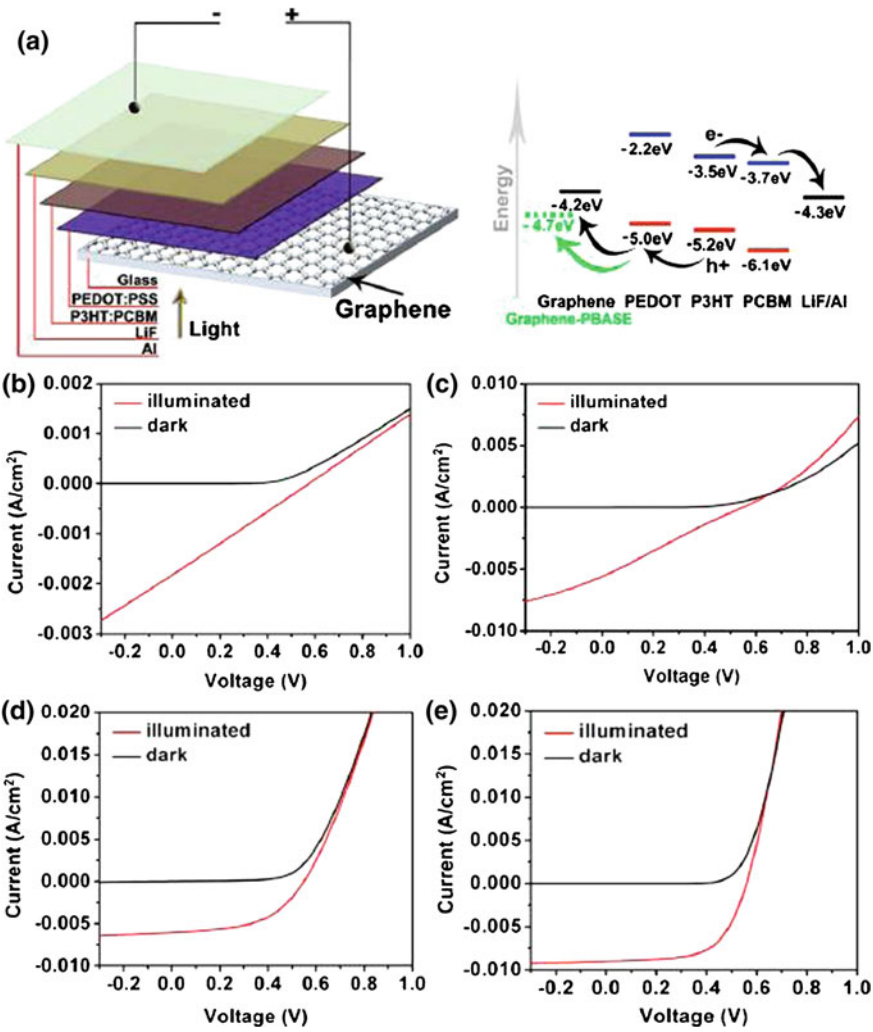

Fig. 4.2 (**a**) Energy diagram of the fabricated device with structure graphene/PEDOT:PSS/P3HT:PCBM/LiF/Al. (**b**–**e**) Current voltage characteristics of the photovoltaic devices based on graphene films in *dark* and under illumination, where (**b**) is from pristine graphene film, (**c**) graphene film treated by UV light, (**d**) graphene film modified by PBASE, (**e**) ITO anode for comparison. Reproduced with permission [33]. Copyright 2009, AIP

4.2.3 Improving the Conductivity of Graphene-Based Transparent Electrode

The high sheet resistance is one of the most important factors for the poor performance of organic electronic devices employing transparent electrodes based on graphene. A strategy to improve the conductivity of the graphene films is to

incorporate a conductive material into them. Chen et al. have reported a hybrid material prepared from graphene and poly(3,4-ethyldioxythiophene) (PEDOT) [37], which showed good transparency and electrical conductivity flexibility together with high thermal stability and was easily processed in both water and organic solvents (Fig. 4.3a, b). Conductivities of 0.2 S/cm and light transmittance of greater than 80 % in the 400–1800 nm wavelength range were observed for films with thickness of tens of nm. In the view of the vacancies and topological defects on the rGO sheet owing to the release of oxygen-containing functional groups, another strategy to improve the conductivity is to repair the defects. Liu et al. reported a method for real-time repair of the newborn vacancies by introducing carbon radicals in the thermal annealing process via a rapid-heating process (Fig. 4.3c–f) [38]. The sheet conductivity of thus-obtained single-layer graphene was raised more than sixfold to 350–410 S/cm (while retaining >96 % transparency). This method provides a simple and efficient process for obtaining highly conductive transparent graphene films. Considering the high conductivity of carbon nanotubes, Tung et al. reported a hybrid nanocomposite comprised rGO and carbon nanotubes (G-CNT) (Fig. 4.3g) [39]. By introducing CNTs, the conductivity of the hybrid material was enhanced, while sacrificing little in transparency. G-CNT film by spin coating with sheet resistance of 240 Ω/sq and 86 % transmittance was obtained. In addition, G-CNT hybrid film exhibited better mechanical stabilities than ITO. In a comparison experiment, after bending to 60° more than 10 times, the resistance of the brittle ITO film increased by three orders of magnitude, while the G-CNT electrode remained nearly unchanged. P3HT:PCBM BHJ device using G-CNT hybrid material as the transparent electrode exhibited a PCE of 0.85 %. The J_{sc}, V_{oc}, and FF were 3.47 mA/cm^2, 0.583 V, and 0.42, respectively. The low J_{sc} and FF are likely due to poor contact at the interface between the G-CNT and the polymer blend.

4.2.4 *Tuning the Work Function of Graphene-Based Transparent Electrode*

In organic electronic devices, work functions of electrodes play an important role and have to be tuned to minimize the energy barriers for charge injection/extraction and improve the device performance. For example, in the common OPV device, the work function of ITO anode should be improved to match with the HOMO of the donor. UV–ozone treatment can improved the work function of ITO, however, a PEDOT:PSS layer with high work function (5.2 eV) are still need to facilitate the hole transfer as well as improve the surface quality. For graphene, its work function is presumed to be 4.5 eV [40]. However, the work function of graphene is variable according to the different sizes, layer structures, functionalizations, doping, and surface modification. Recently, Hang et al. reported to use alkali carbonates to dope the rGO-SWCNT composites and modify their work functions [41]. The doping and work functions were characterized by XPS (Fig. 4.4a). A clear trend

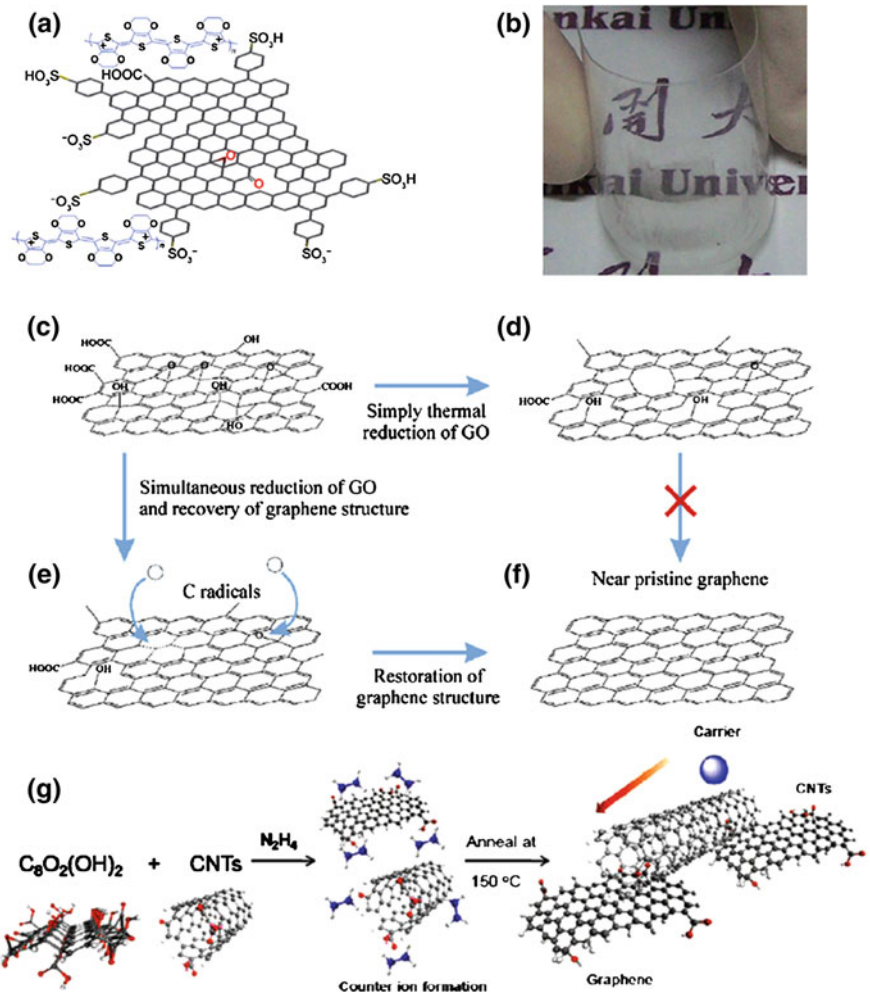

Fig. 4.3 (**a**) Schematic representation of part of the structure of graphene-PEDOT. (**b**) A picture of a graphene-PEDOT film with a thickness of ~32 nm on a transparent PMMA substrate. (**c**–**f**). Structure of GO (**c**) and thermally reduced GO (**d**); Simultaneous reduction of GO and recovery of graphene structure (**e**), to obtain near pristine graphene (**f**). (**g**) Scheme of the composite of CNT and GO. (**a**–**b**) Reproduced with permission [37]. Copyright 2009, Springer (**c**–**f**) Reproduced with permission [38]. Copyright 2011,(**g**) Reproduced with permission [39]. Copyright 2009,ACS

was observed: the values of Φ_w of the rGO-SWCNT electrodes decreased from 4.6 eV when doped with Li_2CO_3 to 3.4 eV when doped with Cs_2CO_3 (Fig. 4.4b). The formation of interfacial dipoles was presumed to be the reason for decreasing the work function of the rGO-SWCNT composites. Inverted P3HT/PCBM solar cells employing Cs_2CO_3 doped rGO-SWCNTs as transparent electrode (transparency 65.8 % at 550 nm and sheet resistance 331 Ω/sq) was fabricated and gave

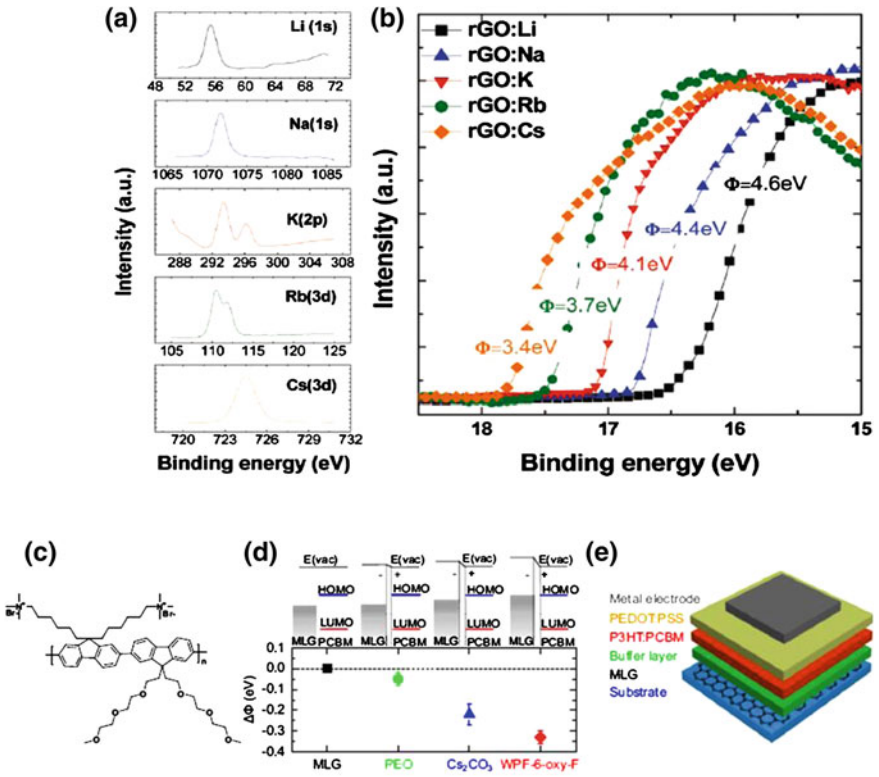

Fig. 4.4 Measurements of the values of Φ_w of the rGO-SWCNT films after doping with various alkali carbonates. (**a**) XPS and (**b**) UPS spectra of the rGO doped with various alkali carbonates. The pronounced peaks for the alkali metals indicate the successful doping of the alkali carbonates. The work functions of the rGO-SWCNT films after doping with Li_2CO_3 and Cs_2CO_3 were 4.6 and 3.4 eV, respectively. The values of Φ_w of the rGO-SWCNT films were determined from the UPS secondary electron cutoff. (**c**) Molecular structure of WPF-6-oxy-F. (**d**) Changes to the effective work functions of MLG films with interfacial dipole layers. (**e**) Schematics of an inverted-structure OPV with the work-function-engineered MLG electrode. (**a**–**b**) Reproduced with permission [41]. Copyright 2011,ACS (**c**–**e**) Reproduced with permission [42]. Copyright 2010, AIP

PCE of 1.27 %, which is comparable with that of the normal structure device. Lee and his coworkers reported that the work function of MLG film grown by CVD could be tuned by using thin interfacial dipole layers [42]. First, the MLG film was transferred to the glass substrate, and one of the following three types of interfacial dipole layers was spin coated onto it: 0.1 wt% solution of poly(ethylene oxide) (PEO) in methanol, 0.2 wt% solution of Cs_2CO_3 in 2-ethoxyethanol, or 0.2 wt% solution of poly[9,9-bis((6'-(N,N,N-trimethylammonium)hexyl)-2,7-fluorene)-alt-(9,9-bis(2-(2-(2-methoxyethoxy) ethoxy)ethyl)-9-fluorene)]dibromide (denoted as WPF-6-oxy-F, Fig. 4.4c) in methanol. The work function of the untreated MLG film was 4.58 ± 0.08 eV, it could be modified when different interfacial dipole

layers were used: 0.05 ± 0.03 eV with PEO, 0.22 ± 0.05 eV with Cs_2CO_3, and 0.33 ± 0.03 eV with WPF-6-oxy-F (Fig. 4.4d). As transparent cathode in inverted OPV device, WPF-6-oxy-F doping MLG film was found to be the best material because its work function had been reduced to be close to the LUMO of PCBM. It is to note that WPF-6-oxy-F had a negligible effect on the absorption properties of the MLG film in the visible wavelengths because the energy gap of WPF-6-oxy-F lies in the UV wavelength range. BHJ device with an inverted structure (Fig. 4.4e) MLG/WPF-6-oxy-F/P3HT:PCBM/PEDOT:PSS/Al gave PCE 1.23 %, which was almost half of the PCE 2.23 % of cells with WPF-6-oxy-F functionalized ITO electrodes.

Although the initial results demonstrate that graphene films prove to be effective and exhibit great potential as transparent electrodes, significant improvement is needed for organic electronic devices employing graphene as the transparent electrodes. In future studies, improvement of the conductivity without sacrifice of the transparency should be first considered. In general, defects in the graphene sheets for both from rGO and from CVD are the main factors for low conductivity. Thus, reducing defects in the preparation process as well as combining with post-treatment are necessary. On the other hand, for device fabrication, the hydrophility of graphene films has to be improved or modified to allow for spin coating with hole-transporting layers such as PEDOT:PSS. Finally, for commercialization consideration, low-cost and large-scale production is preferred for the graphene-based transparent electrodes. In addition, roll-to-roll process is preferable for low-cost and large-scale production for OPVs. How to fulfill the requirement of roll-to-roll process is also a challenge for graphene-based transparent electrodes.

4.3 Graphene for Acceptor Material in OPVs

Currently, the most successful organic solar devices are fabricated in BHJ structure, with low band-gap polymers as the donor and fullerene derivatives such as PCBM as the acceptor. In contrast to the widely focused attentions on the design and synthesis of low band-gap donor materials [43, 44], unfortunately, few acceptor materials other than the fullerene derivatives have been developed. As the most widely used acceptor, C_{60} based acceptors have some limits [45–47], e.g., very weak absorption in the visible range, low LUMO energy level which is hard to tune for high V_{oc} in BHJ devices. Although much efforts have been made on modifying fullerene and its derivatives, only limited improvement has been achieved. This has prompted studies for new acceptor materials with energy levels different from those of C_{60} derivatives, and wide versatility in terms of derivatization and functionalization [48, 49]. In view of its excellent electronic properties such as high mobility, tunable energy level, well dispersion ability in organic solution, etc., it is expected that graphene and its derivatives should be a good alternative acceptor material in OPVs.

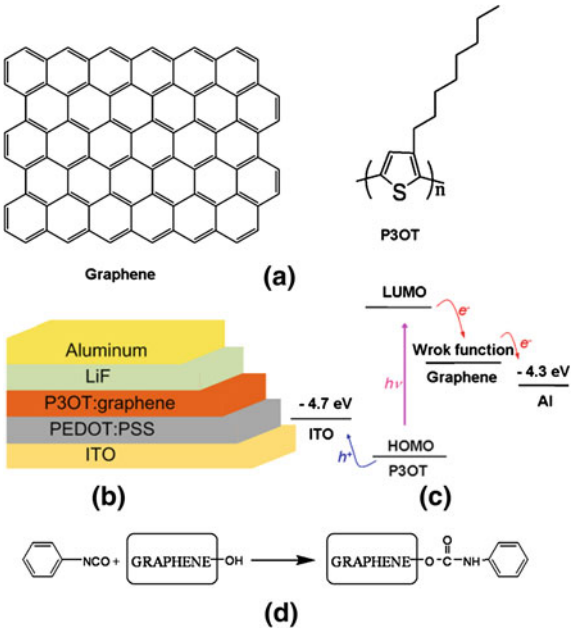

Fig. 4.5 (**a**) The idealized chemical structures of graphene and P3OT. (**b**) Schematic of the device with P3OT/graphene thin film as the active layer and the structure ITO/PEDOT:PSS (40 nm)/P3OT:graphene (100 nm)/LiF (1 nm)/Al (70 nm). (**c**) Energy level diagram of P3OT and SPFGraphene. (**d**) Schematic representation of the reaction of phenyl isocyanate with graphene oxide to form SPF Graphene. (**a**–**d**) Reproduced with permission [4]. Copyright 2008, Wiley-VCH

Chen et al. have reported the fabrication and comprehensive studies of the BHJ structure solar cells employing solution processable functionalized graphene (SPF Graphene) as the acceptor and P3OT as the donor (Fig. 4.5) [4]. As shown in Fig. 4.6, the strong photoluminescence (PL) of P3OT is remarkably reduced after the introduction of SPF Graphene, showing that efficient energy transfer occurs along the P3OT–SPF Graphene interface. The PL quenching behavior has been in detail studied by Hill et al. through electrochemical studies of GO sheets and P3HT utilizing a surfactant-assisted method [50]. The efficient quenching of PL emission with GO indicates that graphene is a promising electron-accepting material for OPV applications. SPF Graphene-based solar cells by spin coating a dichlorobenzene solution with different ratios of SPF Graphene and P3OT have been studied in details. As shown in Table 4.1, the performance of the P3OT/SPFG-based photovoltaic device was much higher than that of the device based on pristine P3OT, indicating that there was an obvious charge transfer from P3HT donor to SPFGraphene acceptor. Under simulated 100 mW AM 1.5G illumination, a PCE of 0.32 % for the P3OT/SPF Graphene-based devices with 5 % SPFGraphene in the active layer was obtained. After annealing treatment, the performance of the devices is greatly improved. The device without annealing treatment had a PCE of only 0.32 %, V_{oc} of 0.56 V, J_{sc} of 2.5 mA/cm^2, and FF of 0.23. After annealing at 160 °C for 20 min, the PCE increased to 1.4 %, with V_{oc}, J_{sc}, and FF increasing to 0.92 V, 4.2 mA/cm^2, and 0.37, respectively. Two factors should contribute to the improvement of the device performance. During the annealing process, graphene sheet should be recovered at least partially again with

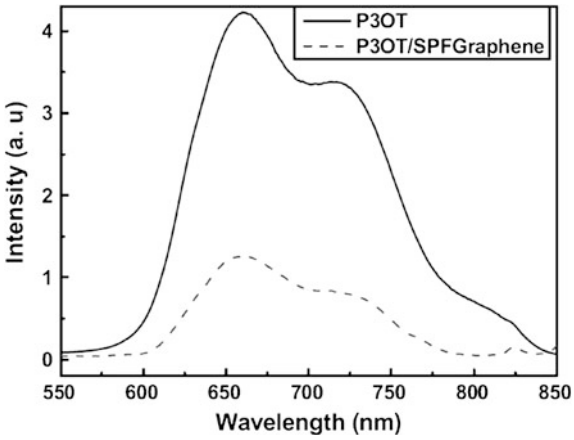

Fig. 4.6 PL spectra of P3OT and P3OT/SPF Graphene composite films at an excitation wavelength of 433 nm. The films were made by spin coating from solutions of P3OT (15 mg mL^{-1}) and P3OT/SPF Graphene (P3OT: 15 mg mL^{-1}, SPF Graphene content 5 %) at 2,000 rpm for 9 s. The films are ca. 100 nm thick. Reproduced with permission [4]. Copyright 2008, Wiley-VCH

Table 4.1 PV characteristics (V_{oc}, J_{sc}, FF, and PCE) of the devices with the structure ITO/PEDOT:PSS (40 nm)/P3OT:SPFGraphene 100 nm)/LiF (1 nm)/Al (70 nm) under simulated 100 mW AM 1.5G illumination, having different graphene content with different annealing treatment. Reproduced with permission [4]. Copyright 2008, Wiley-VCH

SPFGraphene content [%]	Annealing		V_{oc} (V)	J_{sc} (mA/cm^2)	FF	PCE %
	Temperature(°C)	Time(min)				
0	No		0.38	0.014	0.18	0.0095
1	No		0.38	0.54	0.26	0.052
1	160	10	0.94	0.37	0.24	0.083
5	No		0.56	2.5	0.23	0.32
5	160	10	0.98	3.2	0.32	0.98
5	160	20	0.92	4.2	0.37	1.4
5	210	10	1.0	3.2	0.31	0.98
15	No		0.38	0.35	0.24	0.034
15	160	10	0.92	0.35	0.25	0.080

the removal of the functional groups, resulting in improved charge transport mobility of these graphene sheets. In addition, the morphology of the P3OT matrix can be improved, during the annealing process, with an increase in degree of crystallinity and then an enhancement of the charge transport mobility. We also fabricated similar OPV devices using P3HT/SPF Graphene as the active layer [5]. The detailed results were summarized in Table 4.2. The P3HT/SPF Graphene-based OPV devices also showed good OPV performance and similar graphene loading and annealing treatment dependence as for the P3OT/SPF Graphene-based

Table 4.2 Performance details (V_{oc}, J_{sc}, FF, and h) of the P3HT/graphene-based photovoltaic devices without annealing and after annealing at 160 and 210 °C for 10 and 20 min under a simulated AM 1.5G 100 mW illumination. Reproduced with permission [5]. Copyright 2009, Wiley-VCH

SPFGraphene content (%)	Annealing		V_{oc} (V)	J_{sc} (mA/cm^2)	FF	PCE %
	Temperature(°C)	Time(min)				
0	–	–	0.42	0.04	0.27	0.005
2.5	–	–	0.84	0.48	0.23	0.09
5	–	–	0.88	0.364	0.28	0.10
10	–	–	1.10	0.46	0.30	0.15
15	–	–	0.72	0.75	0.25	0.13
2.5	160	10	0.78	2.9	0.24	0.54
5	160	10	0.86	2.7	0.30	0.69
10	160	10	0.72	4.0	0.38	1.10
15	160	10	0.78	2.1	0.21	0.35
2.5	160	20	0.66	4.1	0.25	0.68
5	160	20	0.78	2.6	0.31	0.63
10	160	20	0.88	3.3	0.39	1.10
15	160	20	0.72	1.8	0.27	0.35
2.5	210	10	0.56	2.4	0.25	0.33
5	210	10	0.58	2.7	0.26	0.40
10	210	10	0.40	5.6	0.25	0.57
15	210	10	0.36	3.5	0.35	0.23
2.5	210	20	0.42	2.8	0.23	0.27
5	210	20	0.34	4.7	0.24	0.39
10	210	20	0.48	3.8	0.26	0.47
15	210	20	0.44	1.6	0.26	0.18

ones were observed. The highest PCE 1.10 % was obtained, which was slightly lower than that for the P3OT-based devices.

In addition, with a high specific surface area for a large interface, high mobility and tunable band gap, graphene quantum dots (GQDs) exhibit great potential as an electron acceptor in photovoltaic devices. Li et al. report an electrochemical approach for the direct preparation of functional GQDs with a uniform size of 3–5 nm, exhibiting a green luminescence and good stability [51]. Using these GODs as the acceptor, devices with the structure of ITO/PEDOT:PSS/P3HT:GQDs/Al were fabricated. The best performance with a PCE of 1.28 %, J_{sc} of 6.33 mA/cm^2, V_{oc} of 0.67 V and FF 0.3 was achieved, which is comparable with most organic photovoltaic cells with electron acceptors other than fullerenes. Most recently, Gupta et al. employed aniline functionalized GQDs prepared from GSs by a hydrothermal approach as the acceptor to fabricate organic solar cells (Fig. 4.7) [52]. P3HT/ANI-GQD-based hybrid solar cells were fabricated with the device structure ITO/PEDOT:PSS/P3HT:ANI-GQDs/LiF/Al. Best performance with a PCE of 1.14 %, V_{oc} of 0.61 V, J_{sc} of 3.51 mA/cm^2, and FF of 0.53 were obtained for 1 wt% ANI-GQD in P3HT.

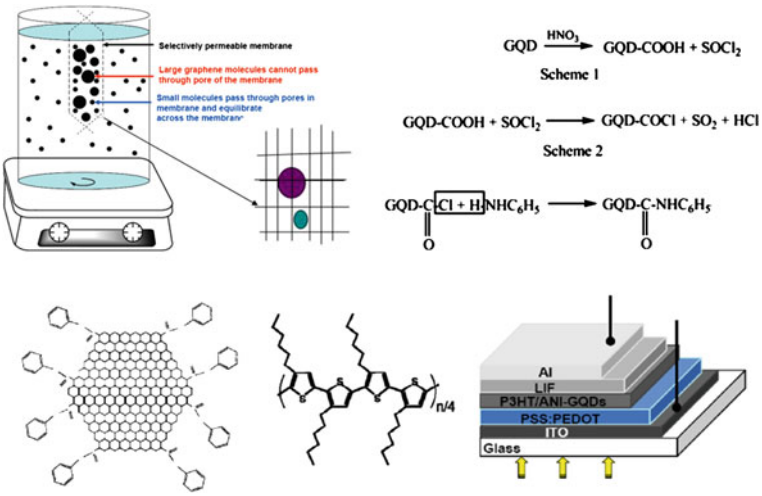

Fig. 4.7 **a** Schematic diagram of the graphene dialysis process. **b** Scheme of functionalization of graphene quantum dot (GQD) with aniline (ANI). **c**, **d** The idealized chemical structure of ANI-GQD and P3HT. **e** Schematic of the device with P3HT/ANI-GQD thin film as the active layer and the structure ITO/PEDOT:PSS (100 nm)/P3HT:ANI-GQD (100 nm)/LiF (1 nm)/Al (70 nm). Reproduced with permission [52]. Copyright 2011, ACS

The study using graphene as acceptor materials has just begun and the performance of OPVs employing graphene as the acceptor is still lower than that of fullerene derivatives. But, considering the intrinsic and superior properties of graphene, it is believed extremely important to advance the studies in this direction. In this regard, several factors are worth being considered: (1) the size of graphene. For the BHJ structure devices, the donor–acceptor (D–A) interface should be maximized for efficient exciton dissociation, and a nanoscale interpenetrating network should be formed for efficient charge transport to the electrodes. Thus, a proper size of graphene relative to the donor molecular size is important to form a well D–A interface and nanoscale interpenetrating network. (2) The functionalization of graphene and its batch-to-batch reproducibility. It is necessary to functionalize graphene in order to fabricate the device by solution process. In general, the performance of organic solar cell is very sensitive to even extremely little change of each materials and fabrication steps, especially for the active layer. Thus, the batch-to-batch reproducibility of both graphene and the functionalized graphene is important. (3) The HOMO/LUMO matching between graphene acceptor and the donors. The energy level of graphene and functionalized graphene are more-or-less different owing to their different sizes, layer structures, and reduction degrees. In addition, design and synthesis of new donor polymers matching graphene-based acceptor's energy level are necessary because most of the donors nowadays are designed based on the acceptor of fullerene derivatives.

4.4 Graphene for All-Carbon Electronics

With its remarkable electronic and mechanical properties, graphene exhibits great potential in the preparation of all-carbon electronics. For the research of low-cost and flexible all-carbon devices or integrated circuits (ICs) based on graphene, one key is to develop an easy method to fabricate the device with simple process such as spin coating, inkjet printing, etc. Graphene films prepared by reduction of graphene oxide demonstrate some great advantages, especially when they are used as electrode materials with transparency requirement. In this section, we will give a brief introduction of graphene-based all-carbon electronics mainly based on our recent works.

4.4.1 All-Carbon Flexible FET

OFETs are the essential building blocks for state-of-the-art and next-generation electronics, which exhibit the advantages of low cost, large-area flexibility, etc. To fully exploit these advantages in practical applications, solution fabrication processes are strongly desired. Currently, metals like gold (Au) are widely used for the source/drain (S/D) electrodes in the fabrication of OFETs on SiO_2/Si substrates with doping Si as the gate (G) electrode, which make it difficult to achieve fully flexible, solution-processed, and low-cost devices. Thus, electrode materials with high carrier injection efficiency, excellent interface compatibility with organic semiconductors, and, especially, easy solution processability and suitability for use in flexible electronics are in high demand. As an alternative electrode material, graphene has demonstrated great potential to fulfill above requirements. Bao et al. have reported that OFET devices fabricated with rGO as bottom-contact electrodes have been demonstrated with lower contact resistances compared with those fabricated with gold contacts and desirable morphological features [53]. Recently, our group has fabricated OFETs using rGO for all the electrodes (source, drain, and gate) for the first time [54]. Patterned graphene electrodes and OFETs were fabricated as outlined in Fig. 4.8, Graphene was used for all S/D/G electrodes, and polyimide (PI) was used as the dielectric layer. In the device fabrication, the G electrode (graphene), dielectric layer PI, and S/D electrodes (graphene) were all fabricated by solution processes on a flexible PI substrate. These OFETs show performance comparable to corresponding devices using Au electrodes as the S/D electrodes on SiO_2/Si substrates with n-doped Si as the gate electrode. Also, these devices demonstrate excellent flexibility without performance degradation over severe bending cycles.

4.4.2 All-Carbon Flexible OPV

For all-carbon flexible OPV, metal electrodes should not be incorporated in the device. As discussed above, graphene acts as window electrode, the back electrode

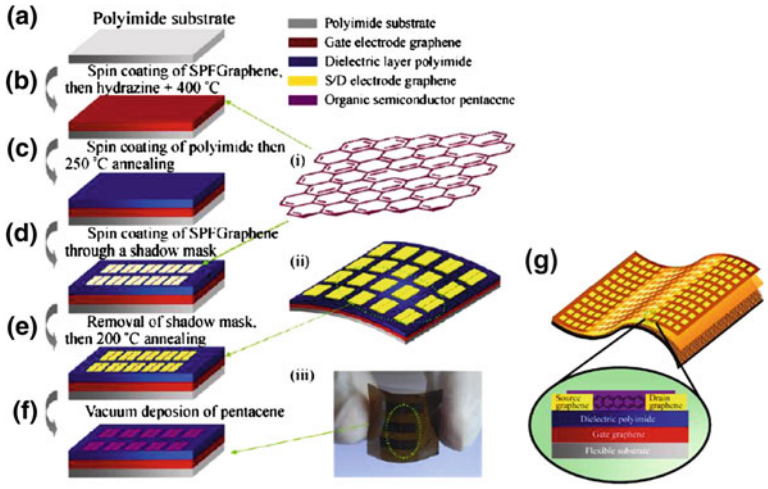

Fig. 4.8 (**a**–**f**) Schematic illustration of the fabrication of pentacene OFET devices. (**i**) Structure of graphene; (**ii**) a schematic representation of the unfinished OFET before adding the pentacene layer, showing its good flexibility; (**iii**) the finished pentacene OFET on a flexible PI substrate when bent under force. (**g**) A schematic illustration of the structure of flexible bottom-contact OFETs based on a pentacene film. Reproduced with permission [54]. Copyright 2011, Springer

is generally Al. Recently, Lee et al. reported a semitransparent inverted-type polymer solar cell using a top laminated graphene electrode [55]. The device was fabricated with a standard inverted structure using ZnO as electron transport layer, replacing the PEDOT:PSS hole-transporting layer by GO and the top metal electrode by the laminated CVD graphene film (Fig. 4.9a). The detailed fabrication process was presented in Fig. 4.9b. The resulting device structure was ITO/ZnO/P3HT:PCBM/GO/graphene. As illuminated from the ITO side, the semitransparent device achieves a best PCE of 2.50 % when the top electrode with 10 layers of graphene was employed, corresponding to 76 % of that of the standard opaque cell. The detailed performances were summarized in Table 4.3. Similar work has also been reported by Cox et al. using CVD graphene as back electrode for small molecule OPV device [56]. These results indicate that besides employed as window electrode in OPV, it can be used as back electrode. So, flexible, all-carbon solar cells can be constructed using graphene as both anode and cathode.

4.4.3 All-Carbon Conductive Circuit

From solution-processing graphene films, we fabricated various graphene-based microcosmic patterns and structures by computer controlled laser cutting (Fig. 4.10a–d, steps i–v) [57]. Furthermore, a complete working prototype of a flexible WORM memory card coupled with a real data retrieving system

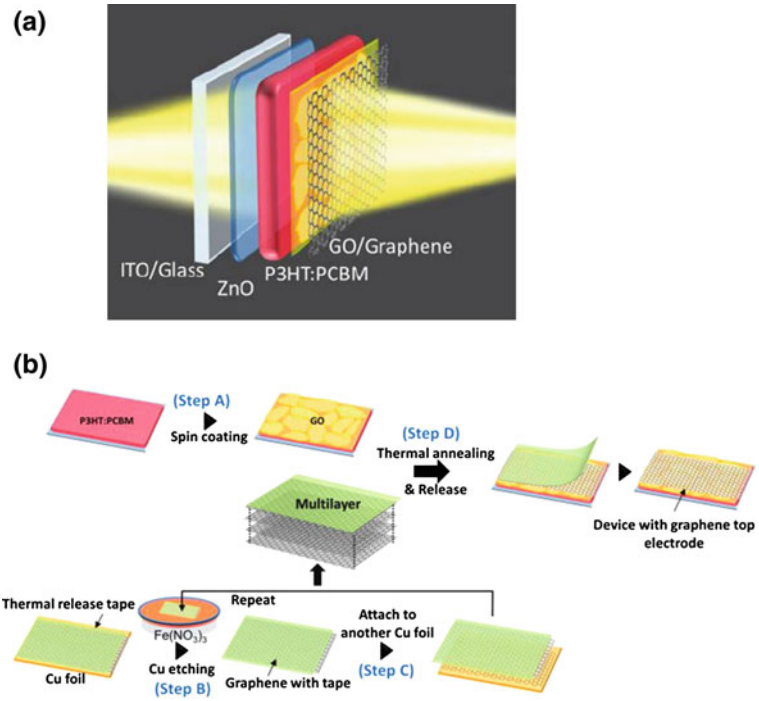

Fig. 4.9 **a** Semitransparent inverted polymer solar cell with a structure of ITO/ZnO/P3HT:PCBM/graphene oxide (GO)/graphene top electrode. **b** Fabrication of the ITO/ZnO/P3HT:PCBM/GO device before depositing the top electrode (step A). Top lamination processes of graphene electrodes by the graphene film transferring (steps B, C) and thermal annealing/releasing processes (step D). **a** Reproduced with permission [55]. Copyright 2011, ACS **b** Reproduced with permission [56]. Copyright 2011 AIP

Table 4.3 Summary of the device performances of the semitransparent polymer solar cells under illumination (AM1.5G, 100 mW/cm^2) from the ITO side and the graphene side (parentheses) and the device performance of the reference standard opaque device

ITO (grapheme)	V_{oc} (V)	J_{sc} (mA/cm^2)	FF	PCE %
10 layers	0.54 (0.54)	10.50 (7.53)	0.44 (0.47)	2.50 (1.88)
8 layers	0.54 (0.54)	10.10 (7.70)	0.44 (0.49)	2.40 (2.04)
6 layers	0.54 (0.54)	8.62 (5.71)	0.39 (0.44)	1.82 (1.36)
3 layers	0.54 (0.54)	4.05 (3.19)	0.32 (0.33)	0.69(0.57)
Standard cell (Ag electrode)	0.52	11.5	0.55	3.30

constructed by maskless laser writing to store data directly has been demonstrated. The data density reaches 500,000 bits/cm^2 using our current very limited processing ability. The data storage has a high ON/OFF ratio and almost infinite lifetime.

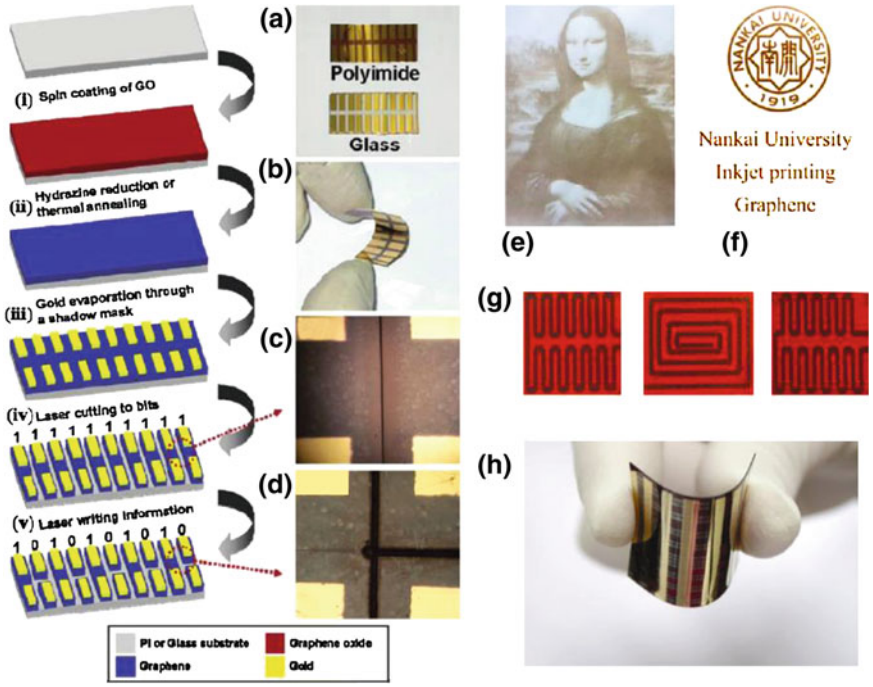

Fig. 4.10 Steps **i**–**v**: Schematic illustrations and photographs of the fabrication of a prototypical graphene-based WORM memory card with 10 bits. **a** Optical image for graphene films on flexible PI and glass substrates patterned with 10 pairs of gold electrodes. **b** Device on the PI substrate that exhibits well flexibility. **c** and **d** Optical microscope images of the laser-cutting channels for the prototypical graphene-based WORM memory card on a flexible PI substrate. The light part is the gold electrode, and the black lines are the cut channels. **e**–**g** Different patterns printed on various substrates by using GO or FGO inks with high resolution: patterns printed **e** on normal office printing paper using FGO ink with a concentration of 5 mg/mL. **f** on PET using GO ink with a concentration of 9 mg/mL. **g** on PI using FGO ink with a concentration of 5 mg/mL. **h** Photograph of a printed pattern on a PI substrate bent outwards by nearly 75°. The FGO ink printed pattern was reduced by thermal annealing. (**i**–**v** and **a**–**d**) Reproduced with permission [57]. Copyright 2011, ACS. **e**–**h** Reproduced with permission [58]. Copyright 2011, Springer

Printing techniques, such as inkjet printing, are competitive alternatives to conventional photolithography for the production of electronic devices with advantages including low cost, ease of mass production, and flexibility. In contrast with conventional ink materials, such as metals like Au and Ag, CNTs and conducting materials, graphene-based inks demonstrate great advantages such as low cost, water solution process and high dispersity, etc. We reported a series of inkjet printing processes using graphene-based inks [58]. Under optimized conditions, using water-soluble single-layered GO and few-layered GO, various high image quality patterns could be printed on diverse flexible substrates, including paper, PET and PI, with the simple inkjet printing technique (Fig. 4.10e–h).

The graphene-based patterns printed on plastic substrates demonstrated a high electrical conductivity after thermal reduction, and more importantly, they retained the same conductivity over severe bending cycles (Fig. 4.10h). Accordingly, flexible electric circuits and a hydrogen peroxide chemical sensor were fabricated and showed excellent performances, demonstrating the applications of this simple and practical inkjet printing technique using graphene inks.

These results indicate that graphene could be an ideal material for fabricating the highly demanded all-carbon, flexible devices and electronics using the simple and efficient printing and spin-coating process and that the long-sought dream for all-carbon and flexible electronics is now much closer to reality.

4.5 Conclusion

In this chapter, transparent electrodes based on graphene and application of graphene in the electronic devices, especially OPVs, have been discussed. For transparent electrode, graphene has exhibited great potentials and achieved promising initial results. Improving the conductivity without sacrifice of the transparency is the first consideration for the further study. For OPVs using graphene as the transparent electrode or acceptor materials, the performance is still lower than that using the conventional materials. However, the performance such as PCE is more a device parameter than an intrinsic material parameter. Keep in mind that all the studies have been in the very initial stage for only 2–3 years. Therefore, there is great room for the improvement of the devices performance including that of all-carbon electronic devices. We fully expect that graphene is a great promising material in organic electronic devices and more and more exciting research results would be achieved in this direction.

Acknowledgments The authors gratefully acknowledge financial support from the NSFC (Grants 50933003, 50902073 and 50903044), MOST (Grants 2009AA032304, 2011CB932602 and 2011DFB50300) and NSF of Tianjin City (Grant 10ZCGHHZ00600)

References

1. Geim AK, Novoselov KS (2007) The rise of graphene. Nat Mater 6:183–191
2. Bonaccorso F, Sun Z, Hasan T, Ferrari AC (2010) Graphene photonics and optoelectronics. Nat Photonics 4:611–622
3. Liu Q, Liu ZF, Zhang XY, Zhang N, Yang LY, Yin SG, Chen Y (2008) Organic photovoltaic cells based on an acceptor of soluble graphene. Appl Phys Lett 92:223303
4. Liu ZF, Liu Q, Huang Y, Ma YF, Yin SG, Zhang XY, Sun W, Chen YS (2008) Organic photovoltaic devices based on a novel acceptor material: graphene. Adv Mater 20:3924–3930
5. Liu Q, Liu ZF, Zhong XY, Yang LY, Zhang N, Pan GL, Yin SG, Chen Y, Wei J (2009) Polymer photovoltaic cells based on solution-processable graphene and P3HT. Adv Funct Mater 19:894–904

6. Wu JB, Agrawal M, Becerril HA, Bao Z, Liu ZF, Chen Y, Peumans P (2010) Organic light-emitting diodes on solution-processed graphene transparent electrodes. ACS Nano 4:43–48
7. Matyba P, Yamaguchi H, Eda G, Chhowalla M, Edman L, Robinson ND (2010) Graphene and mobile ions: the key to all-plastic, solution-processed light-emitting devices. ACS Nano 4:637–642
8. Di CA, Wei DC, Yu G, Liu YQ, Guo YL, Zhu DB (2008) Patterned graphene as source/drain electrodes for bottom-contact organic field-effect transistors. Adv Mater 20:3289–3293
9. Pang SP, Tsao HN, Feng XL, Müllen K (2009) Patterned graphene electrodes from solution-processed graphite oxide films for organic field-effect transistors. Adv Mater 21:3488–3491
10. Rao CNR, Sood AK, Subrahmanyam KS, Govindaraj A (2009) Graphene: the new two-dimensional nanomaterial. Angew Chem Int Ed 48:7752–7777
11. Allen MJ, Tung VC, Kaner RB (2010) Honeycomb carbon: a review of graphene. Chem Rev 110:132–145
12. Huang X, Yin ZY, Wu SX, Qi XY, He QY, Zhang QC, Yan QY, Boey F, Zhang H (2011) Graphene-based materials: synthesis, characterization, properties and applications. Small 7:1876–1902
13. Hu YH, Wang H, Hu B (2010) Thinnest two-dimensional nanomaterial-graphene for solar energy. ChemSusChem 3:782–796
14. Liang MH, Luo B, Zhi LJ (2009) Application of graphene and graphene-based materials in clean energy-related devices. Int J Energy Res 33:1161–1170
15. Sun YQ, Wu QO, Shi GQ (2011) Graphene based new energy materials. Energy Environ Sci 4:1113–1132
16. Wassei JK, Kaner RB (2010) Graphene, a promising transparent conductor. Mater Today 13:52–59
17. Pang S, Hernandez Y, Feng X, Müllen K (2011) Graphene as transparent electrode material for organic electronics. Adv Mater 23:2779–2795
18. Novoselov KS, Geim AK, Morozov SV, Jiang D, Zhang Y, Dubonos SV, Grigorieva IV, Firsov AA (2004) Electric field effect in atomically thin carbon films. Science 306:666–669
19. Forbeaux I, Themlin JM, Debever JM (1998) Heteroepitaxial graphite on 6H-SiC(0001): interface formation through conduction-band electronic structure. Phys Rev B 58:16396–16406
20. Kim KS, Zhao Y, Jang H, Lee SY, Kim JM, Kim KS, Ahn JH, Kim P, Choi JY, Hong BH (2009) Large-scale pattern growth of graphene films for stretchable transparent electrodes. Nature 457:706–710
21. Dikin DA, Stankovich S, Zimney EJ, Piner RD, Dommett GH, Evmenenko G, Nguyen ST, Ruoff RS (2007) Preparation and characterization of graphene oxide paper. Nature 448:457–460
22. Eda G, Chhowalla M (2010) Chemically derived graphene oxide: towards large-area thin-film electronics and optoelectronics. Adv Mater 2:2392–2415
23. Park S, Ruoff RS (2009) Chemical methods for the production of graphenes. Nat Nanotech 4:217–224
24. Becerril HA, Mao J, Liu Z, Stoltenberg RM, Bao Z, Chen Y (2008) Evaluation of solution-processed reduced graphene oxide films as transparent conductors. ACS Nano 2:463–470
25. Xu Y, Long G, Huang L, Huang Y, Wan X, Ma Y, Chen Y (2010) Polymer photovoltaic devices with transparent graphene electrodes produced by spin-casting. Carbon 48:3308–3311
26. Wu J, Becerril HA, Bao Z, Liu Z, Chen Y, Peumans P (2008) Organic solar cells with solution-processed graphene transparent electrodes. Appl Phys Lett 92:263302
27. Eda G, Lin YY, Miller S, Chen CW, Su WF, Chhowalla M (2008) Transparent and conducting electrodes for organic electronics from reduced graphene oxide. Appl Phys Lett 92:23305
28. Yin ZY, Sun SY, Salim T, Wu SX, Huang XA, He QY, Lam YM, Zhang H (2010) Organic photovoltaic devices using highly flexible reduced graphene oxide films as transparent electrodes. ACS Nano 4:5263–5268
29. Geng JX, Liu LJ, Yang SB, Youn SC, Kim DW, Lee JS, Choi JK, Jung HT (2010) A simple approach for preparing transparent conductive graphene films using the controlled chemical

reduction of exfoliated graphene oxide in an aqueous suspension. J Phys Chem C 114:14433–14440
30. De Arco LG, Zhang Y, Kumar A, Zhou CW (2009) Synthesis, transfer, and devices of single- and few-layer graphene by chemical vapor deposition. IEEE T Nanotechnol 8:135–138
31. Yu QK, Lian J, Siriponglert S, Li H, Chen YP, Pei SS (2008) Graphene segregated on Ni surfaces and transferred to insulators. Appl Phys Lett 93:113103
32. Reina A, Jia XT, Ho J, Nezich D, Son HB, Bulovic V, Dresselhaus MS, Kong J (2009) Large area, few-layer graphene films on arbitrary substrates by chemical vapor deposition. Nano Lett 9:30–35
33. Wang Y, Chen XH, Zhong YL, Zhu FR, Loh KP (2009) Large area, continuous, few-layered graphene as anodes in organic photovoltaic devices. Appl Phys Lett 95:063302
34. De Arco LG, Zhang Y, Schlenker CW, Ryu K, Thompson ME, Zhou CW (2010) Continuous, highly flexible, and transparent graphene films by chemical vapor deposition for organic photovoltaics. ACS Nano 4:2865–2873
35. Wang Y, Tong SW, Xu XF, Özyilmaz B, Loh KP (2011) Interface engineering of layer-by-layer stacked graphene anodes for high-performance organic solar cells. Adv Mater 23:1514–1518
36. Choe M, Lee BH, Jo G, Park J, Park W, Lee S, Hong WK, Seong MJ, Kahng YH, Lee K, Lee T (2010) Efficient bulk-heterojunction photovoltaic cells with transparent multi-layer graphene electrodes. Org Electron 11:1864–1869
37. Xu Y, Wang Y, Liang J, Huang Y, Ma Y, Wan X, Chen Y (2009) Hybrid material of graphene and poly (3,4-ethyldioxythiophene) with high conductivity, flexibility, and transparency. Nano Res 2:343–348
38. Dai B, Fu L, Liao L, Liu N, Yan K, Chen Y, Liu Z (2011) High-quality single-layer graphene via reparative reduction of graphene oxide. Nano Res 4:434–439
39. Tung VC, Chen LM, Allen MJ, Wassei JK, Nelson K, Kaner RB, Yang Y (2009) Low-temperature solution processing of graphene-carbon nanotube hybrid materials for high-performance transparent conductors. Nano Lett 9:1949–1955
40. Wildoeer JWG, Venema LC, Rinzler AG, Smalley RE, Dekker C (1998) Electronic structure of atomically resolved carbon nanotubes. Nature 391:59–62
41. Huang JH, Fang JH, Liu CC, Chu CW (2011) Effective work function modulation of graphene/carbon nanotube composite films as transparent cathodes for organic optoelectronics. ACS Nano 5:6262–6271
42. Jo G, Na SI, Oh SH, Lee S, Kim TS, Wang G, Choe M, Park W, Yoon J, Kim DY, Kahng YH, Lee T (2010) Tuning of a graphene-electrode work function to enhance the efficiency of organic bulk heterojunction photovoltaic cells with an inverted structure. Appl Phys Lett 97:213301
43. Cheng YJ, Yang SH, Hsu CS (2009) Synthesis of conjugated polymers for organic solar cell applications. Chem Rev 109:5868–5923
44. Chen JW, Cao Y (2009) Development of novel conjugated donor polymers for high-efficiency bulk-heterojunction photovoltaic devices. Acc Chem Res 42:1709–1718
45. Anthony JE (2011) Small-molecule, nonfullerene acceptors for polymer bulk heterojunction organic photovoltaics. Chem Mater 23:583–590
46. Liu YX, Summers MA, Scully SR, McGehee MD (2006) Resonance energy transfer from organic chromophores to fullerene molecules. J Appl Phys 99:093521
47. He YJ, Li YF (2011) Fullerene derivative acceptors for high performance polymer solar cells. Phys Chem Chem Phys 13:1970–1983
48. Brunetti FG, Gong X, Tong M, Heeger AJ, Wudl F (2010) Strain and huckel aromaticity: driving forces for a promising new generation of electron acceptors in organic electronics. Angew Chem Int Ed 49:532–536
49. Brunetti FG, Kumar R, Wudl F (2010) Organic electronics from perylene to organic photovoltaics: painting a brief history with a broad brush. J Mater Chem 20:2934–2948
50. Hill CM, Zhu Y, Pan S (2011) Fluorescence and electroluminescence quenching evidence of interfacial charge transfer in poly(3-hexylthiophene): graphene oxide bulk heterojunction photovoltaic devices. ACS Nano 5:942–951

51. Li Y, Hu Y, Zhao Y, Shi GQ, Deng LE, Hou YB, Qu LT (2011) An electrochemical avenue to green-luminescent graphene quantum dots as potential electron-acceptors for photovoltaics. Adv Mater 23:776–780
52. Gupta V, Chaudhary N, Srivastava R, Sharma GD, Bhardwaj R, Chand S (2011) Luminscent graphene quantum dots for organic photovoltaic devices. J Am Chem Soc 133:9960–9963
53. Becerril HA, Stoltenberg RM, Tang ML, Roberts ME, Liu ZF, Chen Y, Kim DH, Li BL, Lee SY, Bao Z (2010) Fabrication and evaluation of solution-processed reduced graphene oxide electrodes for p- and n-channel bottom-contact organic thin-film transistors. ACS Nano 4:6343–6352
54. Chen Y, Xu Y, Zhao K, Wan X, Deng J, Yan W (2010) Towards flexible all-carbon electronics: flexible organic field-effect transistors and inverter circuits using solution-processed all-graphene source/drain/gate electrodes. Nano Res 3:675–684
55. Lee YY, Tu KH, Yu CC, Li SS, Hwang JY, Lin CC, Chen KH, Chen LC, Chen CW (2011) Top laminated graphene electrode in a semitransparent polymer solar cell by simultaneous thermal annealing/releasing method. ACS Nano 5:6564–6570
56. Cox M, Gorodetsky A, Kim B, Kim KS, Jia Z, Kim P, Nuckolls C, Kymissis I (2011) Single-layer graphene cathodes for organic photovoltaics. Appl Phys Lett 98:123303
57. Liang J, Chen Y, Xu Y, Liu Z, Zhang L, Zhao X, Zhang X, Tian J, Huang Y, Ma Y, Li F (2011) Toward all-carbon electronics: fabrication of graphene-based flexible electronic circuits and memory cards using maskless laser direct writing. Acs Appl Mater Interfaces 2:3310–3317
58. Huang L, Huang Y, Liang J, Wan X, Chen Y (2011) Graphene-based conducting inks for direct inkjet printing of flexible conductive patterns and their applications in electric circuits and chemical sensors. Nano Res 4:675–684

Chapter 5
Exciton and Charge Dynamics in Polymer Solar Cells Studied by Transient Absorption Spectroscopy

Hideo Ohkita and Shinzaburo Ito

Abstract Transient absorption spectroscopy is a powerful tool for studying the photovoltaic conversion events in polymer solar cells, which occur on a wide temporal scale from $\sim 10^{-15}$ s for exciton generation by photon absorption to $\sim 10^{-5}$ s for charge collection to the electrode. This chapter describes first how to assign transient species such as singlet and triplet excitons, polarons, and other charge carriers by transient absorption spectroscopy. On the basis of the assignments, the exciton and charge dynamics are analyzed to discuss photophysical fundamental events related to the photovoltaic conversion such as exciton delocalization, energy transfer, triplet formation, and charge generation and recombination. Finally, the relevance to the device performance is summarized.

5.1 Introduction

In recent years, polymer solar cells are attracting increasing interest because of their potential advantages: lightweight, flexibility, and high throughput and large-area production based on the printing and coating techniques [1–3]. Although the power conversion efficiency (PCE) of polymer solar cells was less than 1 % in the 1990s, it has steadily increased every year in the past decade owing to extensive research. In particular, regioregular poly(3-hexylthiophene) (RR-P3HT) has been

H. Ohkita (✉) · S. Ito
Department of Polymer Chemistry, Graduate School of Engineering, Kyoto University, Katsura, Nishikyo, Kyoto 615-8510, Japan
e-mail: ohkita@photo.polym.kyoto-u.ac.jp

H. Ohkita
Japan Science and Technology Agency (JST), PRESTO, 4-1-8, Honcho Kawaguchi, Saitama 332-0012, Japan

W. C. H. Choy (ed.), *Organic Solar Cells*, Green Energy and Technology,
DOI: 10.1007/978-1-4471-4823-4_5,

studied thoroughly as a donor material in polymer/fullerene solar cells [4–9]. It is noteworthy that this polymer has a good balance between solubility and optoelectronic properties [10–13], while most conjugated polymers generally have faced a trade-off between them. Regioregular P3HT is likely to be crystalline in solid films even with high solubility in various organic solvents, because each monomer unit attached with a hexyl group is regularly bound in a head-to-tail linkage. Consequently, RR-P3HT:PCBM solar cells have been reported to be strongly dependent on the fabrication conditions, particularly annealing treatments. After thermal or solvent annealing, RR-P3HT:PCBM solar cells exhibit a reproducible PCE approaching 5 % and excellent external quantum efficiency (EQE) up to >80 % [5–9]. Therefore, this polymer solar cell is still being intensively studied as a benchmark. Thereafter, owing to syntheses of various new materials, optimization of blend morphology, and development of new device structures, a certified PCE in excess of 8 % has been listed in the solar cell efficiency table (version 37) [14]. In 2012, a certified PCE of 10.0 % has been listed in the solar cell efficiency table (version 39) [15].

For the improvement of the device efficiency, new materials and device structures are developed mainly on the basis of macroscopic properties of *J*–*V* characteristics. However, the *J*–*V* characteristics just provide us the final result of a series of fundamental photovoltaic conversion events including photon absorption, exciton generation, exciton migration, charge separation, charge recombination, charge dissociation, charge transport, and charge collection. In other words, the essential problem causing a poor device performance cannot be specified only from the *J*–*V* characteristics. Thus, it is of particular importance to elucidate each fundamental event to design new materials and develop new device structures rationally. Photovoltaic conversion events occur in a range of over nine orders of magnitude on a temporal scale from $\sim 10^{-14}$ s for ultrafast charge separation to $\sim 10^{-5}$ s for charge collection to the electrode. Transient absorption spectroscopy is therefore a powerful tool for studying such conversion events in photovoltaic devices directly. By analyzing the transient spectra in detail, we can assign all the transient species such as exciton, polaron pair, free polaron, and trapped polaron separately and discuss their dynamics quantitatively [16–21]. This chapter describes the assignment of excitons and charge species and the photophysics of photovoltaic conversion events in polymer solar cells studied by transient absorption spectroscopy.

5.2 Temporal Scale of Photovoltaic Conversion

Here, we describe the temporal scale of photovoltaic conversion events in polymer solar cells. Figure 5.1 shows a schematic illustration of the most simple polymer solar cells with a bilayered structure of the hole-transporting (donor) and electron-transporting (acceptor) materials, which is similar to silicon-based solar cells consisting of *p*-type and *n*-type semiconductors. In polymer solar cells, as shown in

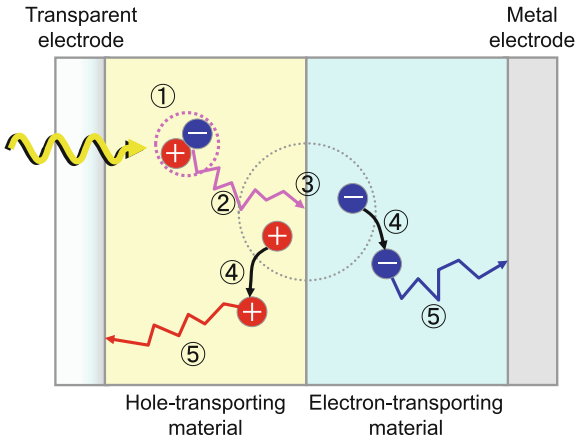

Fig. 5.1 Photovoltaic conversion events in polymer solar cells with a bilayered structure of hole-transporting and electron-transporting materials: (*1*) exciton generation by photon absorption, (*2*) exciton diffusion into a donor–acceptor interface, (*3*) charge transfer at the interface, (*4*) charge dissociation into free carriers, and (*5*) charge transport to each electrode

the figure, the photon absorption first produces singlet excitons that are electron–hole pairs tightly bound by the Coulomb attraction. This exciton generation results from an electronic transition from the ground state to an excited state due to the photon absorption, which typically occurs on a time scale of femtosecond ($\sim 10^{-15}$ s). In contrast, the photon absorption in silicon-based solar cells produces not excitons but freely mobile charge carriers directly at room temperature. This is the most critical difference between them, which results from the lower dielectric constant and larger effective mass (lower charge carrier mobility) in organic semiconductors than in inorganic semiconductors [22]. A critical distance r_C at which the thermal energy of a charge carrier is equal to the Coulomb attractive potential energy [23] would be as long as 14–19 nm in organic materials at room temperature because dielectric constant is small ($\varepsilon = 3 - 4$), while it would be only 5 nm in crystalline silicon with a high dielectric constant ($\varepsilon = 11.9$). Furthermore, excitons are typically localized in organic materials as Frenkel excitons or charge transfer (CT) excitons, while they are delocalized in crystalline silicon as Wannier excitons with a radius much larger than the lattice spacing [23]. Consequently, excitons generated in organic materials cannot be dissociated into free carriers at room temperature. Instead, they can migrate randomly in films before deactivating to the ground state (exciton diffusion). As a result, some excitons can reach a donor–acceptor interface where they can be dissociated into free carriers. The diffusion time is limited by the lifetime of excitons (typically <1 ns) and is dependent on the phase-separated structures in donor–acceptor blend films. In a finely mixed donor–acceptor blend, no exciton diffusion is required to generate free carriers. In a large phase-separated blend such as RR-P3HT:PCBM annealed films, the exciton diffusion is observed on a time scale of tens picoseconds ($\sim 10^{-11}$ s) as described in Sect. 5.6.1. At the donor–acceptor interface, excitons can be separated into the electron on the acceptor material (radical anion) and the hole on the donor material (radical cation or polaron) if the energy gap at the interface is enough to break the Coulomb attraction. The charge separation is promptly completed in the order of $\sim 10^{-14}$ s [19, 24]. The electron and hole pair generated at the interface is

often called bound radical pairs to be distinguished from tightly bound electron–hole pairs of excitons in the bulk. Some bound radical pairs can be dissociated into free carriers (charge dissociation) in competition with the geminate recombination to the ground state or triplet state (charge recombination) on a time scale of 10^{-12} to 10^{-9} s [19]. The dissociated free carriers are transported to each electrode through repetitive charge hoppings in an energetically disordered matrix (charge transport). Some of them escaping from the bimolecular recombination are collected to the electrode (charge collection). The charge collection time is dependent on the charge mobility, the thickness of the active layer, and the electric field applied to the layer. Recent studies have shown that it takes 10^{-6} to 10^{-5} s for charge carriers to be collected to the electrode [25]. Finally, the photocurrent is generated as a result of the series of photovoltaic conversion events. In other words, the device performance of *J*–*V* characteristics is just the final result of the series of photovoltaic conversion events ranging from 10^{-14} to 10^{-5} s (nine orders of magnitude on a temporal scale). In this chapter, we focus on such rapid photovoltaic conversion events studied by transient absorption spectroscopy and discuss the findings obtained from the kinetics analysis.

5.3 Transient Absorption Spectroscopy

Transient absorption spectroscopy is the most useful method for directly observing photovoltaic conversion events ranging from 10^{-14} to 10^{-5} s. However, it is difficult to measure the absorption of thin films such as polymer solar cells where the active layer is typically as thin as 100 nm (=10^{-5} cm). For example, the absorbance would be as small as 10^{-5} in the case of a molar absorption coefficient of 10^4 M^{-1} cm^{-1}, which is a typical value for organic dye molecules, a molar concentration of 0.1 mM, and an optical path length of 10^{-5} cm. To detect an absorbance change of 10^{-5}, it is necessary to measure only 1/50000 of the change in the optical probe signal separately from various noises.

Figure 5.2 shows a block diagram of the highly sensitive microsecond transient absorption spectroscopy system [17]. In this system, a probe light is provided from a tungsten lamp with a power source stabilized to reduce fluctuation of the probe intensity. To reduce unnecessary scattering light, stray light, and emission from the sample, two monochromators and appropriate optical cut-off filters are placed before and after the sample. An excitation light is supplied from a dye laser pumped by a nitrogen laser, which can excite the absorption peak of thin-film samples to give a high yield of photoexcitations. The probe light passing through the sample is detected with a PIN photodiode such as Si or InGaAs depending on the measuring wavelength. The signal from the photodiode is pre-amplified and sent to the main amplification system with electronic band-pass filters to improve the signal to noise ratio. The amplified signal is collected with a digital oscilloscope, which is synchronized with a trigger signal of the laser pulse from a photodiode. In our system, the detectable absorbance change is as small as 10^{-5} to

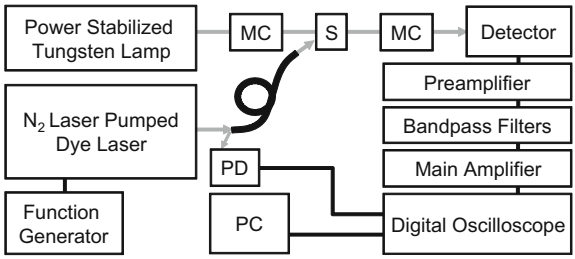

Fig. 5.2 Block diagram of highly sensitive microsecond transient absorption measurement system: *MC* monochromator, *S* sample, *PC* computer, and *PD* PIN photodiode to detect a part of a pump laser pulse as a trigger signal, which is sent to the digital oscilloscope. The detector is replaceable: Si PIN photodiode for the visible wavelength range and InGaAs PIN photodiode for the near-IR wavelength range. The *black* and *gray* lines represent electric signals and optical probe and pump light, respectively

10^{-6} depending on the measuring time domain after appropriate accumulation owing to the amplification and noise reduction system.

For ultrafast phenomena on a time scale of <1 ns, the pump and probe method is widely employed. In this method, ultrashort laser pulses serve as the pump light for the sample excitation and the probe light for the transmittance measurement. Transient absorption can be measured at various delay times by controlling the arrival time of each laser pulse at the sample. The arrival time of each laser pulse can be tuned with an optical delay line: the probe light is delayed relative to the pump light because of the additional path length in the optical delay line. For example, when the total optical delay length is set at 3 cm the probe light is delayed by 100 ps relative to the pump light, and therefore, the transmittance at 100 ps after the laser excitation can be measured. Figure 5.3 shows a block diagram of a typical pump and probe spectroscopy system we employ [17–21]. This system consists of a transient absorption spectrometer and a regenerative amplified

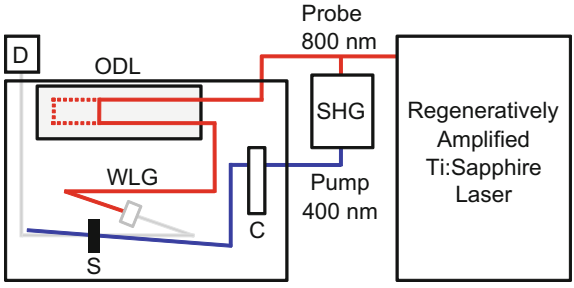

Fig. 5.3 Block diagram of pump and probe femtosecond transient absorption measurement system: *SHG* second harmonic generator, *ODL* optical delay line, *C* chopper, *WLG* white light generator, *S* sample, *D* detector. The detector is replaceable: a linear CCD array for the visible wavelength range and a digital line scan InGaAs camera for near-IR wavelength range

Ti:sapphire laser. The amplified Ti:sapphire laser provides 800-nm fundamental pulses at a repetition rate of 1 kHz with an energy of 0.8 mJ and a pulse width of 100 fs (FWHM), which are split into two optical beams with a beam splitter to generate pump and probe pulses. One fundamental beam is converted into pump pulses at 400 nm with a second harmonic generator or pump pulses at other wavelengths with an ultrafast optical parametric amplifier. The other fundamental beam is converted into white light continuum pulses employed as probe pulses over the wide wavelength from 400 to 1700 nm. The pump pulses are modulated mechanically with a repetition rate of 100 Hz for visible and 500 Hz for near-IR measurements. The temporal evolution of the probe intensity is recorded with a Si CCD-array photodetector for the visible measurement and with an InGaAs digital line scan camera for the near-IR measurement. Transient absorption spectra and decays are collected over the time range from −5 ps to 3 ns. Typically, 200–1000 laser shots are averaged on each delay time to obtain a detectable absorbance change as small as 10^{-4}–10^{-3} depending on the monitor wavelength. The polarization direction of the linearly polarized probe pulse is set at a magic angle of 54.7° with respect to that of the pump pulse to cancel out orientation effects on the dynamics. In order to measure further the transient absorption in a longer time range, a longer optical delay line would be required. Alternately, additional laser is employed to provide delayed probe pulses with an electric delay generator synchronized with the pump laser pulse [26]. Note that it is necessary to correct signal jitters due to the electric circuit.

5.4 Assignment of Photoexcitations

Let us first describe how to assign transient species such as singlet and triplet excitons and polarons generated in polymer solar cells. Here, we explain the assignments on the basis of our recent studies [16–20].

5.4.1 Singlet and Triplet Excitons

Singlet and triplet excitons can be often observed for pristine films upon photoexcitation. In particular, singlet excitons can be easily observed as the initial product by photon excitation, because most conjugated polymers have $S_0 \rightarrow S_n$ spin-allowed absorption bands from the singlet ground state. In contrast, it is difficult to detect triplet excitons for highly emissive conjugated polymer films such as polyfluorene, because the intersystem crossing yield is low due to small spin–orbit coupling. On the other hand, triplet excitons can be observed for conjugated polymer films with high intersystem crossing yield such as regiorandom poly(3-hexylthiophene) (RRa-P3HT).

Figure 5.4a shows transient absorption spectra of RRa-P3HT pristine films. Immediately after the laser excitation, a large absorption band is observed at around 1000 nm. This band is ascribable to singlet exciton, because the decay constant is consistent with the lifetime of fluorescence measured by the time-correlated single photon counting (TC-SPC) method. Note that the averaged decay constant measured by transient absorption was typically shorter than the lifetime measured by the TC-SPC method because singlet–singlet exciton annihilation is involved in the transient absorption measurement with excitation intensity much higher than that in the TC-SPC measurement. Thus, a longer decay fraction independent of the excitation intensity should be extracted by changing the excitation intensity. If it is in agreement with the fluorescence lifetime, the initial product can be safely assigned to singlet exciton.

As shown in Fig. 5.4a, the singlet exciton band at around 1000 nm disappears at 100 ps after the laser excitation, and instead a small absorption band is observed at around 800 nm. This is indicative of the interconversion from singlet to triplet excitons. Figure 5.4b shows transient absorption spectra of RRa-P3HT pristine films on a time scale of microseconds, which is similar to the long-lived species observed on a time scale of nanoseconds mentioned above. As shown in the inset to the figure, the transient signal decays monoexponentially with a lifetime of 7 μs

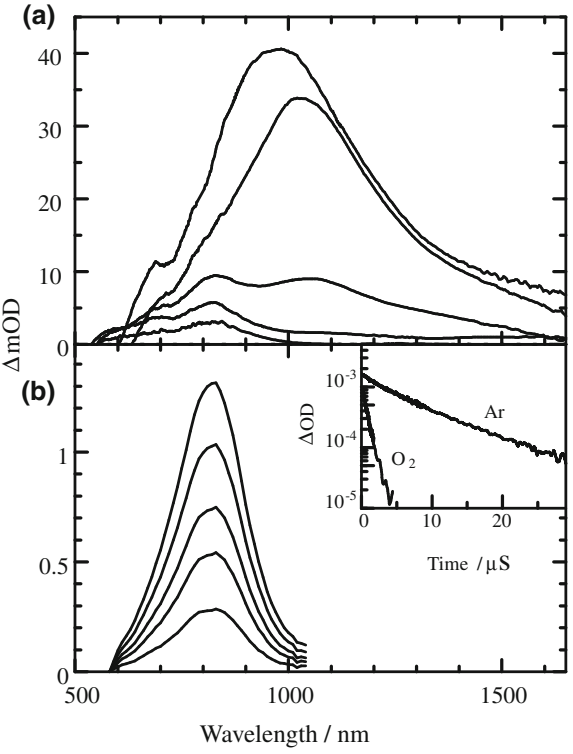

Fig. 5.4 **a** Transient absorption spectra of RRa-P3HT films excited at 400 nm measured at 0, 1, 10, 100, and 3000 ps from *top* to *bottom*. **b** Transient absorption spectra of RRa-P3HT films excited at 450 nm measured at 0.5, 2, 4, 6, and 10 μs from *top* to *bottom*. The inset shows the transient absorption decay at 850 nm under Ar and O_2 atmosphere. Adapted with permission from [18]. Copyright 2009 American Chemical Society

under a nitrogen atmosphere, while it decays more rapidly under an oxygen atmosphere. Molecular oxygen is a general and efficient quencher of singlet and triplet excitons in organic materials [27]. Thus, such a long lifetime is ascribable to triplet excitons, because it is too long to be assigned to singlet excitons. Although, electron spin resonance (ESR) is a useful method for distinguishing between singlet and triplet states as reported in the literatures [28–30], the oxygen quenching is most widely employed to assign triplet excitons. Note that not all triplet excitons are quenched by molecular oxygen because quenching is a diffusion-limited reaction. Roughly speaking, triplet excitons with a long lifetime (>μs) can be effectively quenched by molecular oxygen even in solid films depending on the oxygen permeability of the film.

In most cases, as described above, singlet excitons are observed as the initial product by photon absorption. However, this is not true for RR-P3HT pristine films excited by intense laser pulses. Figure 5.5 shows the transient absorption spectra of RR-P3HT pristine films under different excitation conditions. At an excitation intensity of 15 μJ cm^{-2}, a large absorption band is observed at around 1200 nm immediately after the laser excitation. As the excitation intensity is increased from 15 to 120 μJ cm^{-2}, this band disappears and instead a new absorption band is observed at around 1000 nm. From the intensity dependence of the initial transient signals, we ascribe the 1200-nm band to a singlet exciton and the 1000-nm band to polarons. At higher excitation intensities, polarons are generated even at 0 ps from hot exciton states formed by the singlet–singlet exciton annihilation. Note that no exciton diffusion is involved in the singlet–singlet exciton annihilation because the duration is too short. The energy of two photons at 400 nm corresponds to 6.2 eV, which is much larger than the ionization potential of RR-P3HT films. Thus, it would be more appropriate to assign the polaron formation to two-photon ionization. This finding suggests that the initial product by photon absorption is not always a singlet exciton particularly at a high excitation intensity. In conclusion, for the assignment of singlet excitons, it is essential to analyze not only the decay kinetics but also the intensity dependence of the spectrum and kinetics.

5.4.2 Polarons

As mentioned above, polarons are efficiently generated from excitons at a donor–acceptor interface. Thus, they can be more clearly observed in polymer–fullerene blend films rather than in pristine conjugated polymer films. Some polarons escaping from the geminate recombination at the interface can survive up to a time scale of microseconds or more. On such a longer time scale, therefore, polarons can often be observed separately from singlet and triplet excitons. Figure 5.6a shows the transient absorption spectra of RRa-P3HT:PCBM blend films from 0 to 3 ns after the laser excitation. In this time domain, the absorption spectrum varies with time, suggesting that the transient species changes with time. As will

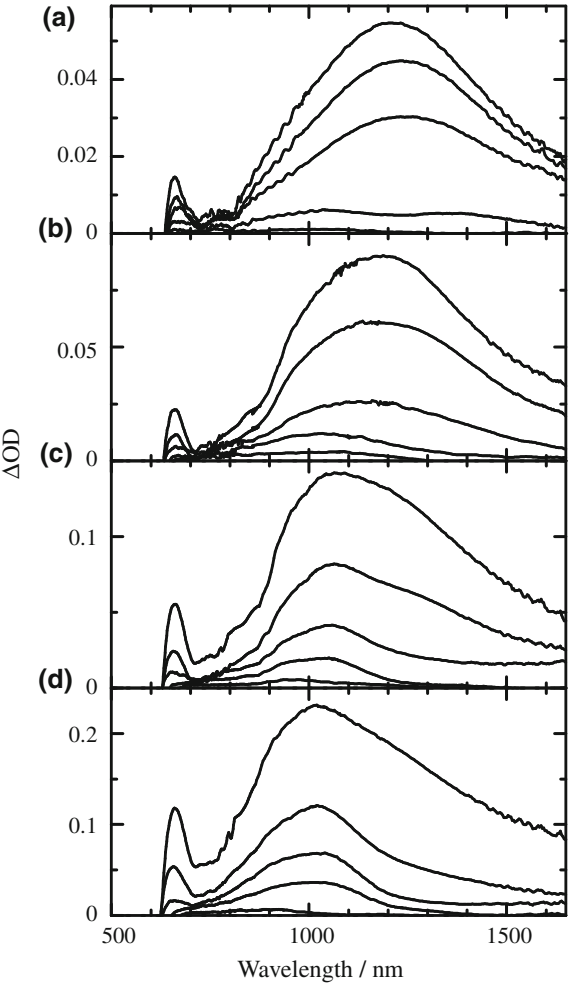

Fig. 5.5 Transient absorption spectra of RR-P3HT films measured at 0, 1, 10, 100, and 3000 ps from *top* to *bottom* in each panel. The excitation intensity is as follows: **a** 15, **b** 30, **c** 60, and **d** 120 μJ cm^{-2}. The excitation wavelength is 400 nm. Adapted with permission from [18]. Copyright 2009 American Chemical Society

be described in detail Sect. 5.6.1, there are spectral overlaps among P3HT singlet excitons, P3HT polarons, and PCBM radical anions at an early time stage. On the other hand, as shown in Fig. 5.6b, no change in transient absorption spectra is observed for RRa-P3HT:PCBM blend films on a time scale of microseconds, suggesting that transient species remains the same. The large absorption band at 900 nm and the small and sharp absorption band at 1030 nm are safely ascribed to P3HT hole polaron and to PCBM radical anion, respectively. Both bands exhibit power-law decay dynamics with an exponent of 0.35 over a long time range up to milliseconds. The power-law decay is characteristic of the bimolecular recombination of long lived, dissociated charge carriers. The subunit value for the exponent suggests trap-limited bimolecular recombination of polarons in an energetically disordered matrix while the exponent is unity for trap-free bimolecular recombination [31].

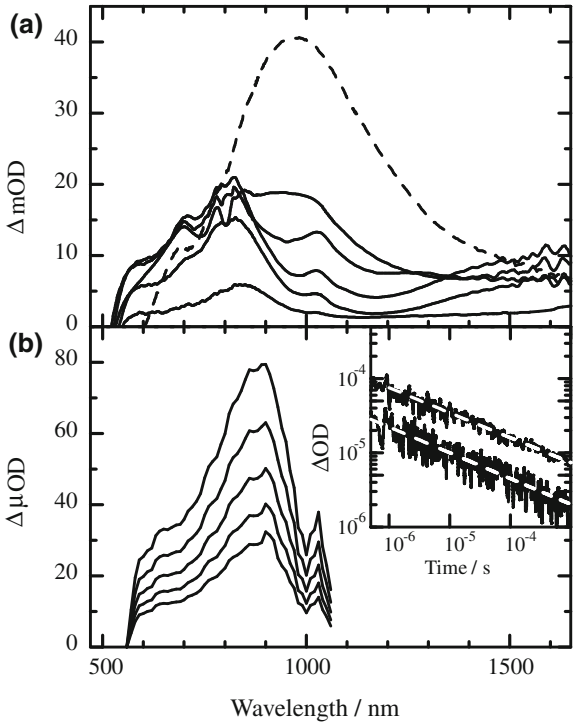

Fig. 5.6 **a** Transient absorption spectra of RRa-P3HT:PCBM (50:50 w/w) blend films (*solid lines*) measured at 0, 0.2, 1, 100, and 3000 ps (from *top* to *bottom*). The *broken line* represents transient absorption spectrum of an RRa-P3HT pristine film measured at 0 ps. The transient absorption is corrected for variation in the absorption at an excitation wavelength of 400 nm. **b** Transient absorption spectra of RRa-P3HT:PCBM (50:50 w/w) blend films excited at 450 nm measured at 0.5, 1, 2, 4, and 8 μs (from *top* to *bottom*). The inset shows transient absorption decays at 850 (*upper*) and 1030 nm (*lower*). The *white broken lines* represent fitting curves with a power-law equation: $\Delta OD(t) \propto t^{-\alpha}$. Adapted with permission from [19]. Copyright 2010 American Chemical Society

Figure 5.7a shows the transient absorption spectra of RR-P3HT:PCBM blend films from 0 to 3 ns after the laser excitation. In this time domain, as in the case with RRa-P3HT:PCBM blend films, the absorption spectrum varies with time. The large absorption band at around 1250 nm is in good agreement with that observed immediately after the laser excitation of RR-P3HT pristine films as described above, and therefore can be ascribed to P3HT singlet exciton. As shown in Fig. 5.7b, the broad absorption bands at 700 and 1000 nm are still observed on a time scale of microseconds. Interestingly, these two bands exhibit the power-law decay dynamics with different exponents, which remain the same under an oxygen atmosphere. Thus, they can be ascribed to P3HT polarons but must be different polarons as will be described in detail in Sect. 5.6.3. In other words, this spectral change shows the formation of P3HT polaron from P3HT singlet exciton.

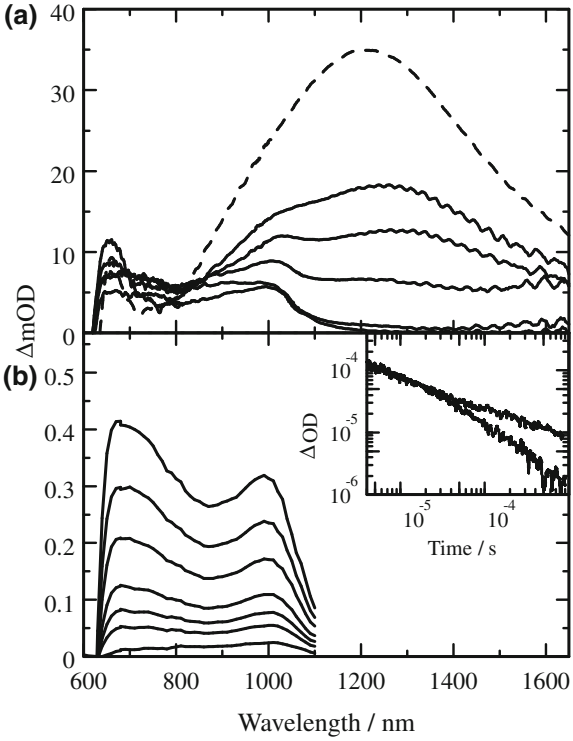

Fig. 5.7 **a** Transient absorption spectra of RR-P3HT:PCBM (50:50 w/w) blend films after thermal annealing (*solid lines*) measured at 0, 1, 10, 100, and 3000 ps (from *top* to *bottom*). The *broken line* represents transient absorption spectrum of an RR-P3HT pristine film (*broken line*) measured at 0 ps. The transient absorption is corrected for variation in the absorption at an excitation wavelength of 400 nm. **b** Transient absorption spectra of RR-P3HT:PCBM (50:50 w/w) blend films after thermal annealing excited at 400 nm measured at 0.5, 1, 2, 5, 10, 20 and 100 μs (from *top* to *bottom*). The inset shows transient absorption decays at 1000 (*upper*) and 700 nm (*lower*). Adapted with permission from [19, 20]. Copyright 2010 American Chemical Society

In the two cases described above, polarons are efficiently generated from singlet excitons and therefore can be separately observed on a time scale of microseconds. In some cases, however, a triplet exciton band overlaps with a polaron band. Here, we show an example of simultaneous observation of triplet excitons and polarons. Figure 5.8a shows transient absorption spectra of a blend film of poly[(4,4′-dide-cyl[2,2′-bithiophene]-5,5′-diyl)-1,4-phenylene] ($PT_{10}PhT_{10}$) and PCBM. A large absorption band is observed at 700 nm with a shoulder at around 850 nm at 10 μs after the laser excitation. The absorption spectrum varies with time, with the absorption peak shifting from 700 at 10 μs to ∼900 nm for time delays longer than 100 μs. This spectral change suggests that there are two different transient species in the blend film. Figure 5.8b shows transient absorption decays of $PT_{10}PhT_{10}$:PCBM blend films monitored at 700 nm. This decay dynamics can be fitted with the sum of a single exponential function and a power-law equation. As shown in the figure, the exponential decay component is quenched under oxygen atmosphere, and therefore ascribed to triplet exciton. On the other hand, the exponent of the power-law decay remains the same even under oxygen atmosphere, and therefore is ascribed to polymer polarons. In conclusion, for the assignment of polarons, it is essential to observe polarons separately from singlet and triplet excitons. Singlet excitons can be excluded by transient absorption measurements on a time scale of microseconds. In order to distinguish between triplet excitons and polarons, it is useful to analyze the

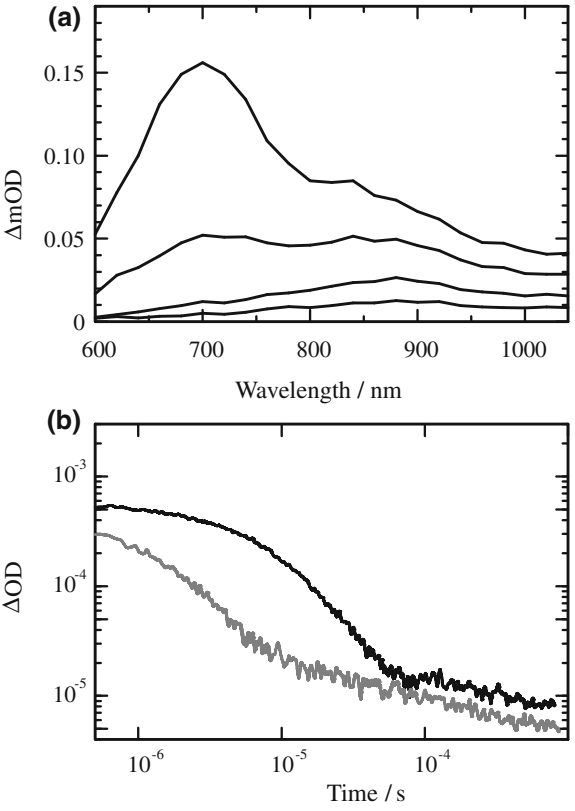

Fig. 5.8 **a** Transient absorption spectra of $PT_{10}PhT_{10}$:PCBM (95:5 w/w) blend films excited at 420 nm measured at 0, 1, 10, 100, and 3000 ps (from *top* to *bottom*). **b** Transient absorption decays of $PT_{10}PhT_{10}$:PCBM (95:5 w/w) blend films excited at 420 nm monitored at 700 nm under argon (*black line*) and oxygen (*gray line*) atmosphere. Reprinted with permission from [16]. Copyright 2008 American Chemical Society

decay kinetics and the oxygen quenching measurement. Triplet excitons generally decay monoexponentially while polarons typically exhibit the power-law decay dynamics on a time scale of microseconds. In the presence of molecular oxygen, the lifetime of triplet excitons is effectively shortened but the decay dynamics of polarons does not change.

5.4.3 Other Charge Carriers

In order to assign charge carriers of unknown or new materials, it is necessary to measure the absorption spectrum and to quantitatively evaluate the molar absorption coefficient of each carrier separately using a model system with known donor or acceptor materials. Here, we show an example of the assignment of PCBM anion by using tetramethyl-*p*-phenylenediamine (TMPD) as a known electron donor. Figure 5.9 shows transient absorption spectra of a polystyrene film doped with TMPD and PCBM. Two absorption bands are observed at 570 and 1020 nm after the laser excitation. The absorption band at 570 nm is in good agreement with that

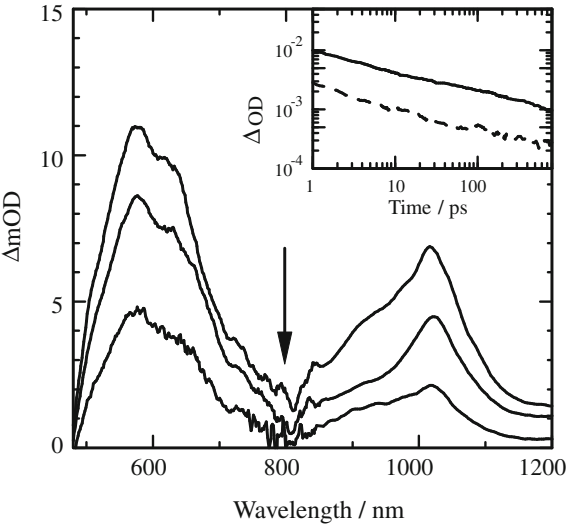

Fig. 5.9 Transient absorption spectra of a polystyrene film doped with TMPD(20 wt %) and PCBM(30 wt %) at 1, 2, and 10 ps after the laser excitation at 400 nm. The inset shows the transient decays at 600 nm (*solid line*) and 1050 nm (*broken line*). Reprinted with permission from [17]. Copyright 2008 Wiley–VCH Verlag GmbH & Co. KGaA

reported for the oxidation product of TMPD called Wurster's Blue [32], and is therefore safely assigned to the TMPD radical cation. As shown in the inset to the figure, both bands exhibit the power-law decay dynamics with the same exponent on a longer time scale (>10 ps), indicating the bimolecular recombination without other decay pathways. In other words, no other transient species such as singlet and triplet excitons contributes to the transient absorption spectra. Thus, the absorption band at 1020 nm is assigned to the PCBM radical anion, which is consistent with that of radical anions of other fullerene derivatives: a C_{60} radical anion (1,080 nm), a methanofullerene radical anion (1040 nm), and a fulleropyrrolidine radical anion (1010 nm) [33]. Furthermore, the molar absorption coefficient of the PCBM radical anion can be evaluated to be $\varepsilon = 6000\ \mathrm{M}^{-1}\ \mathrm{cm}^{-1}$ at 1020 nm on the basis of that of the TMPD radical cation ($\varepsilon = 12000\ \mathrm{M}^{-1}\ \mathrm{cm}^{-1}$) [32, 34]. In conclusion, it is useful to employ known donor or acceptor materials for the assignment of unknown charge carriers. Note that it is important to analyze the spectrum and the dynamics carefully to confirm that there is no contribution of other species.

5.5 Exciton Dynamics

Here, we focus on the dynamics of singlet and triplet excitons mainly in pristine polymer films [18] and also describe the energy transfer in a polymer/polymer blend [21].

5.5.1 Exciton Delocalization

As mentioned above, the absorption band of singlet excitons in P3HT films is red-shifted with time, suggesting delocalization of singlet excitons. Figure 5.10 summarizes the transient absorption spectra of RRa-P3HT and RR-P3HT pristine films. The singlet exciton band is red-shifted from 900 to 1060 nm for RRa-P3HT and from 1200 to 1250 nm for RR-P3HT from 0 to 100 ps after the excitation at 400 nm. Such a peak shift suggests that singlet excitons efficiently migrate on a time scale of picoseconds, resulting in the exciton delocalization into longer conjugated segments and the singlet–singlet exciton annihilation under an intense excitation. The stabilization energy corresponds to $\Delta E = 0.21$ eV for RRa-P3HT and $\Delta E = 0.04$ eV for RR-P3HT. The large ΔE for RRa-P3HT is probably because RRa-P3HT amorphous films have a relatively wide distribution of energetic disorders compared to RR-P3HT crystalline films. Interestingly, as shown in Fig. 5.10c, no peak shift is observed for RR-P3HT films excited at 620 nm that is

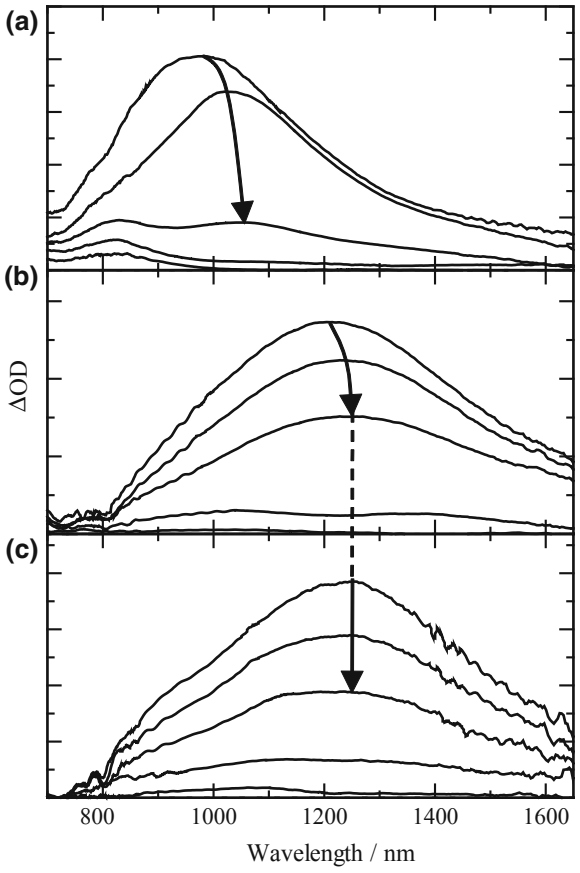

Fig. 5.10 Transient absorption spectra of P3HTpristine films measured at 0, 1, 10, 100, and 3000 ps from *top* to *bottom* in each panel: **a** RRa-P3HT excited at 400 nm, **b** RR-P3HT excited at 400 nm, and **c** RR-P3HT excited at 620 nm. Adapted with permission from [18]. Copyright 2009 American Chemical Society

the absorption edge of RR-P3HT. The absorption band is already observed at 1250 nm immediately after the laser excitation and still observed at 1250 nm at 100 ps. This finding shows that delocalized P3HT singlet excitons in crystalline domains can be selectively observed by selective excitation at 620 nm. As reported in the literatures [35–37], the exciton diffusion constant can be evaluated by analyzing the dynamics of singlet–singlet exciton annihilation under different excitation intensities.

As the excitation intensity increases further, the singlet–singlet exciton annihilation is observed even at 0 ps, because singlet excitons are likely to be generated in proximity to each other at high concentrations without diffusion. The threshold intensity is 7×10^{18} cm^{-3} for RRa-P3HT films excited at 400 nm, 3×10^{18} cm^{-3} for RR-P3HT films excited at 400 nm, and 8×10^{17} cm^{-3} for RR-P3HT films excited at 620 nm. Assuming a 3-dimensional sphere without taking their anisotropic distribution into consideration, an averaged interaction radius of two excitons at 0 ps can be estimated to be $\sim$3.2 nm for RRa-P3HT films excited at 400 nm, $\sim$4.3 nm for RR-P3HT films excited at 400 nm, and $\sim$6.7 nm for RR-P3HT films excited at 620 nm. The difference in the interaction radius is indicative of the difference in the exciton delocalization at 0 ps. In other words, singlet excitons are more delocalized in RR-P3HT crystalline films than in RRa-P3HT amorphous films and upon the excitation close to the band gap than upon the excitation above the band gap. These are consistent with the peak wavelengths of the singlet exciton band as discussed above.

5.5.2 *Energy Transfer*

In some donor–acceptor blends, the efficient energy transfer from photogenerated singlet excitons is observed before the charge generation at the interface. Here, we describe the energy transfer in polymer/polymer blends of RR-P3HT and poly(9,9-dioctylfluorene-*alt*-benzothiadiazole) (F8BT), which have a large spectral overlap between the fluorescence of F8BT and the absorption of RR-P3HT. Figure 5.11a shows the transient absorption spectra of RR-P3HT:F8BT blend films excited at 400 nm where 60 % of photons are absorbed by F8BT and the remaining 40 % are absorbed by RR-P3HT. The transient absorption spectra in a picosecond can be well reproduced by the sum of the S–S absorption spectrum observed for each pristine film of F8BT and RR-P3HT, suggesting that the major transient species are F8BT and RR-P3HT singlet excitons in the time domain of <1 ps. In other words, the broad absorption at around 1000 nm observed at 0 ps is ascribed to F8BT singlet excitons. The large absorption at around 1250 nm observed after 1 ps is ascribed to RR-P3HT singlet excitons. On the basis of the spectral simulation, the decay dynamics of each transient species can be obtained as shown in Fig. 5.11b. The F8BT singlet exciton decays monoexponentially with a lifetime of $\sim$0.3 ps. On the other hand, $\sim$40 % of RR-P3HT singlet excitons are promptly generated immediately after the laser excitation and the other $\sim$60 % of RR-P3HT

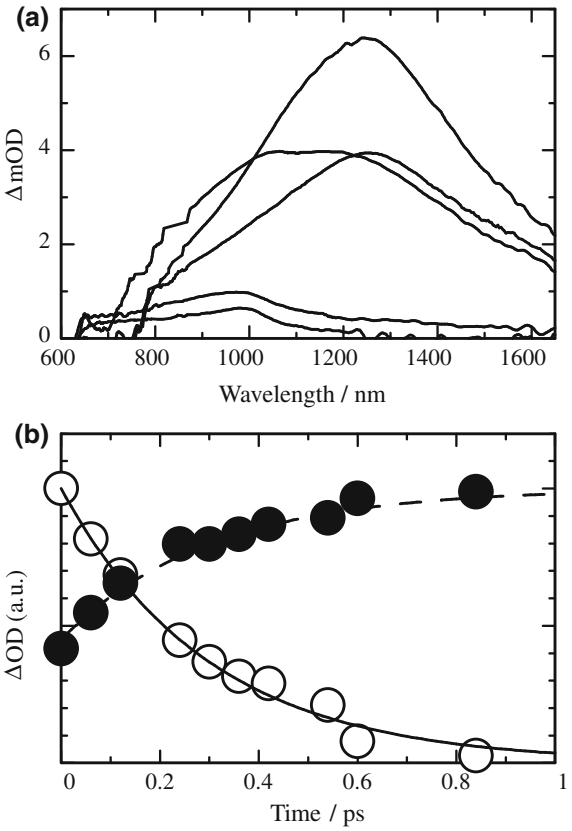

Fig. 5.11 **a** Transient absorption spectra of RR-P3HT:F8BT blend films excited at 400 nm measured at 0, 1, 10, 100, 1000 ps from *top* to *bottom*. **b** Time evolution of F8BT singlet excitons (*open circles*) and RR-P3HT singlet excitons (*closed circles*). The *rise* and *decay* curves are fitted with the following equation: $\Delta OD_R(t) = A[1 - \exp(-t/\tau_R)] + B$ and $\Delta OD_D(t) = A \exp(-t/\tau_D)$ ($\tau_R = \tau_D = 0.3$ ps). Adapted with permission from [21]. Copyright 2011 Society of Photo Optical Instrumentation Engineers

singlet excitons are generated with a rise constant of $\sim$0.3 ps. The prompt generation of RR-P3HT singlet excitons is ascribed to the direct excitation of RR-P3HT at 400 nm. The delayed generation of RR-P3HT singlet excitons is ascribed to the energy transfer from F8BT singlet excitons, because the rise time of RR-P3HT singlet excitons is in agreement with the decay constant of F8BT singlet excitons. Such rapid energy transfer within a picosecond suggests that all F8BT singlet excitons are efficiently transferred into RR-P3HT domains without exciton diffusion in the blend film. In other words, there are no large pure domains in the blend: F8BT is molecularly dispersed in RR-P3HT domains and/or RR-P3HT is dispersed in F8BT rich domains. This is probably because chloroform is so rapidly evaporated that largely phase-separated pure domains cannot be formed. On the basis of the Förster theory assuming point dipoles, such rapid energy transfer is possible at a separation distance of $\sim$0.9 nm between F8BT and RR-P3HT. Consequently, at least 60 % of RR-P3HT singlet excitons are located near the interface of RR-P3HT/F8BT because of the efficient energy transfer from F8BT singlet excitons. This would be beneficial for the subsequent charge separation but the charge generation efficiency is actually not as high as that in RR-P3HT:PCBM blends. This may be due to the difference in the interfacial structures [21].

5.5.3 Triplet Formation

Triplet excitons are generally converted through the intersystem crossing from the lowest singlet exciton. As mentioned in Sect. 5.4.1 (see Fig. 5.4), triplet excitons are generated from singlet excitons in RRa-P3HT films. Indeed, as shown in Fig. 5.12, the triplet rise ($\sim$4 ps) is in good agreement with the singlet decay ($\sim$4 ps), suggesting that triplet excitons are rapidly converted from singlet excitons. The rise and decay time is dependent on the excitation intensity, suggesting that the singlet exciton–exciton annihilation contributes to the rapid interconversion. Interestingly, the formation yield of triplet excitons is estimated to be as high as $\sim$25 % at 10 ps from the decay analysis [18, 38], even though singlet excitons are significantly quenched by the singlet exciton–exciton annihilation. If triplet excitons were formed via the intersystem crossing from relaxed singlet excitons, the triplet yield at 10 ps should be as small as $\sim$1 % because the intersystem crossing rate has been reported to be $\sim 1\ \mathrm{ns}^{-1}$ for poly(3-octylthiophene) in a xylene solution [38]. Therefore, such a short interconversion time of $\sim$4 ps cannot be simply explained in terms of the intersystem crossing from the lowest singlet exciton state to triplet exciton state. Rather, the rapid triplet formation results from a higher singlet exciton state generated by the singlet exciton–exciton annihilation in the picosecond time domain. The triplet formation from a higher exciton state should be completed before the relaxation to the lowest singlet exciton state, because the interconversion in the relaxed exciton states is limited by the slow intersystem crossing rate. We therefore conclude that the rapid triplet formation is in competition with the vibrational relaxation to the lowest exciton or polaron pair states within <100 fs. Such a rapid triplet formation is indicative of efficient spin-

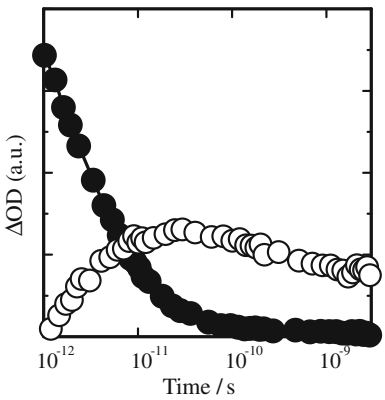

Fig. 5.12 Normalized transient absorption decays of RRa-P3HT pristine films excited at 400 nm ($\sim 30\ \mu\mathrm{J\ cm}^{-2}$). The *closed circles* represent time evolution of singlet excitons measured at 1000 nm. The *open circles* represent time evolution of triplet excitons, which is evaluated by subtracting the transient signals of singlet excitons at 1000 nm from that at 825 nm. Adapted with permission from [18]. Copyright 2009 American Chemical Society

mixing between singlet and triplet excitons. Higher exciton states in conjugated polymers are likely to be more mixed with CT states, resulting in a relatively longer electron–hole separation, and hence a smaller electron exchange integral $2J$. The small energy gap of $2J$ between the singlet and triplet states would promote the interconversion between them. For a very small exchange integral, hyperfine interaction (HFI) between the electron and nuclear spins generally plays an important role in the interconversion mechanism. In organic radicals, the HFI energy is typically in the order of $\sim$5 mT, which corresponds to an interconversion time of several nanoseconds [39, 40]. This is consistent with an interconversion time of $\sim$1 ns reported for poly(3-octylthiophene) in a xylene solution [38]. Thus, the ultrafast triplet formation on a short time scale of picoseconds suggests that the interconversion mechanism is different from the normal intersystem crossing from the lowest singlet exciton.

Fission of singlet excitons into two triplet exciton pairs is spin conserving and hence spin-allowed [23]. Singlet fission is primarily induced by spin dipole–dipole interaction while the normal intersystem crossing is induced by the spin–orbit coupling [41]. Triplet formation from singlet fission has been reported for molecular crystals [42–47], and also for conjugated polymer films [48–50]. The energy of the two triplet pair state ^{1}(TT) is approximated by twice the energy of isolated triplet excitons ($2E_{T1}$). This is in good approximation for molecular crystals with weak intermolecular interactions. Thus, $2E_{T1}$ is generally considered to be the threshold energy for singlet fission. Assuming that the energy difference between the lowest singlet and triplet states ΔE_{ST} is 0.7 eV for RRa-P3HT, which is a typical value for various amorphous conjugated polymers [51, 52], the energy level of the lowest triplet exciton state (E_{T1}) is roughly estimated to be 1.6 eV for RRa-P3HT amorphous films. Therefore, the threshold energy for singlet fission is estimated to be 3.2 eV for RRa-P3HT, which is slightly higher than the excitation energy (3.1 eV). In other words, the singlet fission by one photon excitation at 400 nm is thermodynamically unfavorable for RRa-P3HT. Indeed, no distinct triplet signal is observed for RRa-P3HT films immediately after the laser excitation under lower excitation intensities. On the other hand, singlet fission is thermodynamically possible from a higher singlet exciton state generated by the singlet exciton–exciton annihilation (singlet fusion). If triplet excitons are generated from singlet fission, the back recombination of the two triplet pair state ^{1}(TT) to the singlet exciton state is also spin-allowed, and therefore expected to be much faster than the normal spin-forbidden transition from isolated triplet excitons to the ground state. As shown in Fig. 5.12, the lifetime of triplet signals observed for RRa-P3HT is as short as 300 ps, which is much faster than that of "isolated" triplet excitons ($\sim$7 μs). This rapid decay is ascribed to the recombination of triplet exciton pairs to the singlet exciton state. We therefore conclude that triplet excitons observed for RRa-P3HT films are mainly generated through the singlet fission from a higher singlet exciton state produced by the singlet exciton–exciton annihilation (singlet fusion followed by singlet fission into triplet exciton pairs). Note that no triplet formation is observed for RR-P3HT crystalline films even though singlet fission is thermodynamically possible from a higher singlet exciton

state. This is probably because the formation of polarons or polaron pairs is more efficient than that of the singlet fission because of the larger interchain interaction in highly ordered crystalline RR-P3HT films.

Finally, we note the relevance of singlet fission to polymer solar cells. As mentioned above, singlet fission produces two triplet excitons from one singlet exciton. This is analogous to multiple exciton generation in semiconductor quantum dots [53, 54], which has attracted increasing interest because more than one excitons could be generated by one photon absorption. Recent studies have demonstrated that the singlet fission indeed contributes to the photocurrent in pentacene/C_{60} bilayered films [55, 56]. The singlet fission in RRa-P3HT films is not directly linked with the polaron formation. This is partly because the triplet exciton state is located lower in energy than the polaron state. Although further studies are needed for efficient singlet fission into triplet excitons followed by efficient charge generation, it is a challenging and attractive target to develop polymer solar cells based on singlet fission.

5.6 Charge Dynamics

Let us move on to the dynamics of charge species generated in polymer–fullerene blends. In particular, we focus on the charge dynamics in P3HT:PCBM blends and summarize the relevance to the device performance [19, 20].

5.6.1 Charge Generation

In RRa-P3HT:PCBM blend films, as shown in Fig. 5.6a, P3HT singlet exciton is already quenched to ~50 % even at 0 ps, and disappears rapidly in a picosecond, followed by P3HT polaron generation. Figure 5.13a shows the time evolution of P3HT singlet excitons and polarons in the RRa-P3HT:PCBM blend film. The P3HT singlet exciton decays monoexponentially with a time constant of 0.2 ps. On the other hand, more than half of the polarons are promptly generated even at 0 ps and the remaining polarons are also rapidly generated with the same rise constant of 0.2 ps. This agreement suggests that polarons are efficiently generated from P3HT singlet excitons in a picosecond. The rapid formation of polarons is ascribed to the prompt charge generation at the interface of RRa-P3HT/PCBM, because the exciton migration is negligible on such a short time scale (<0.2 ps). This is probably because PCBM molecules are more homogeneously dispersed in RRa-P3HT amorphous films than in RR-P3HT crystalline films. Assuming a homogeneous distribution of 50 wt % PCBM in RRa-P3HT films, the intermolecular distance of neighboring PCBM molecules would be less than 1 nm. As mentioned in Sect. 5.5.1, the delocalization radius of singlet excitons is estimated to be 3.2 nm in the RRa-P3HT film. This suggests that singlet excitons generated

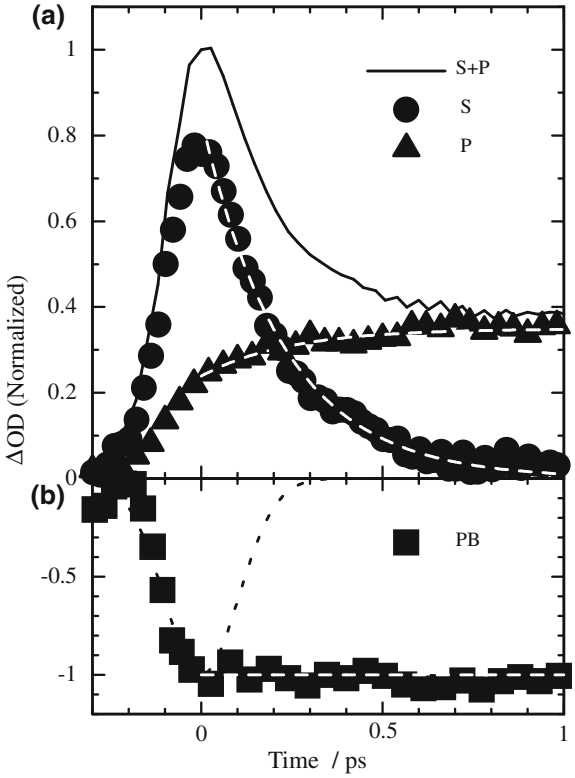

Fig. 5.13 **a** Normalized transient absorption signals of singlet exciton (*closed circles*) and polaron (*closed triangles*) generated in RRa-P3HT:PCBM (50:50 w/w) blend films excited at 400 nm. The *closed circles* are obtained by subtracting the transient signal of polaron at 1600 nm (*closed triangles*) from that at 1000 nm (*solid line*, singlet exciton and polaron). The subtracted signals (*closed circles*) are fitted with a monoexponential function: $\Delta OD(t) = A \exp(-t/\tau_D)$. The transient rise signals at 1600 nm are fitted with an exponential function and a constant: $\Delta OD(t) = A[1 - \exp(-t/\tau_R)] + B$ ($\tau_D = \tau_R = 0.2$ ps). **b** Normalized transient absorption signals of photobleaching at 470 nm (*closed squares*) for RRa-P3HT:PCBM (50:50 w/w) blend films excited at 400 nm. The photobleaching signals are fitted with a constant: $\Delta OD(t) =$ constant. The *white broken lines* represent the best-fitting curves. The *dotted line* indicates the instrument response function of the transient absorption spectroscope. Reprinted with permission from [19]. Copyright 2010 American Chemical Society

can promptly encounter a PCBM molecule without exciton migration. Furthermore, as shown in Fig. 5.13b, no decay is observed for the photobleaching at 470 nm, suggesting that all the singlet excitons are converted into polarons without deactivating to the ground state. We therefore conclude that both the exciton diffusion efficiency (η_{ED}) and the charge transfer efficiency (η_{CT}) are as high as 100 % in RRa-P3HT:PCBM blend films.

In RR-P3HT:PCBM blend films, as shown in Fig. 5.7a, P3HT singlet excitons are also already quenched to $\sim$50 % even at 0 ps, and decays on a time scale of

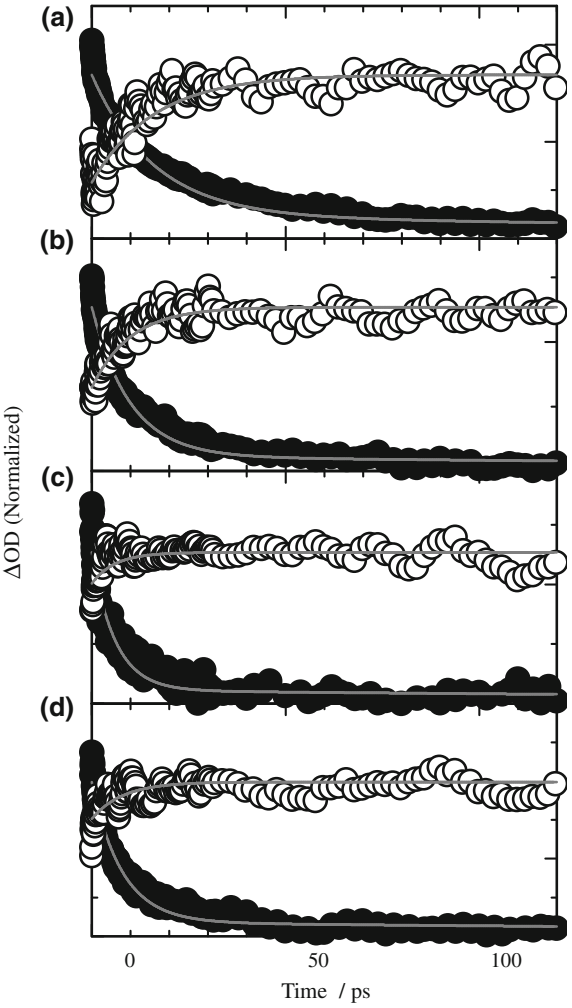

Fig. 5.14 Normalized transient absorption signals of RR-P3HT:PCBM blend films excited at 400 nm measured at 1200 nm (singlet excitons, *closed circles*) and 720 nm (polarons, *open circles*): **a** 5 wt % PCBM, **b** 20 wt % PCBM, **c** 50wt % PCBM before thermal annealing, and **d** 50 wt % PCBM after thermal annealing. The transient absorption decay at 1200 nm is fitted with a double exponential function: $\Delta OD(t) = A_{D1}\exp(-t/\tau_{D1}) + A_{D2}\exp(-t/\tau_{D2})$. The transient absorption decay at 720 nm is fitted with a double exponential function: $\Delta OD(t) = A_R[1 - \exp(-t/\tau_R)] + B$. The *gray lines* represent the best-fitting curves [19]

picoseconds, followed by efficient P3HT polaron generation. Figure 5.14 shows the time evolution of the singlet exciton band at 1200 nm and the polaron band at 720 nm. The decay of P3HT singlet excitons can be fitted by a double exponential function with a short lifetime of $\sim$10 ps and an intrinsic exciton lifetime of 330 ps. On the other hand, a part of P3HT polarons are promptly generated even at 0 ps and the others are gradually generated with the same time constant as the short lifetime of P3HT singlet excitons. The delayed polaron formation ($\sim$10 ps) is much slower than that observed for RRa-P3HT:PCBM blend films (<1 ps). Furthermore, the rise and decay constants depend on the P3HT domain size: both increase with increasing P3HT concentration and slightly increase after the thermal annealing. We therefore assign the delayed formation to the polaron generation via the exciton migration to the interface of RR-P3HT/PCBM. In other

words, the time constant of the delayed formation of polarons is limited by the exciton migration in relatively large crystalline domains of RR-P3HT. This is consistent with the recent transient studies [57, 58]. On the other hand, the prompt polaron formation ($>10^{13}$ s^{-1}) is ascribed to the charge generation at the interface of RR-P3HT/PCBM. The rate constant of the prompt polaron formation is 10^4 times faster than the deactivation rate constant (3.0×10^9 s^{-1}) of singlet excitons in RR-P3HT pristine films. Thus, the charge transfer efficiency (η_{CT}) is estimated to be $\sim$100 % at the interface of RR-P3HT/PCBM. Because $\eta_{CT} \approx 100$ %, the exciton diffusion efficiency is estimated to be $\eta_{ED} = \eta_q \eta_{CT} \approx \eta_q = k_q/(k_F + k_q) = 93$ % before the thermal annealing and 89 % after the thermal annealing in RR-P3HT:PCBM blend films. In other words, there is almost 10 % loss in η_{ED} in either case, although it is still high enough to collect singlet excitons into the interface of RR-P3HT/PCBM.

5.6.2 Monomolecular and Bimolecular Recombination

The charge recombination between electrons and holes can be typically classified into monomolecular (geminate) recombination and bimolecular recombination. It is important to distinguish between the two, because the photocurrent generation is critically dependent on whether the electron and hole are bound as a geminate pair at the interface or dissociated into free carriers. However, it is impossible to distinguish between geminate charge pairs and free carriers from transient absorption spectra alone, because the charge species are identical in either case. Monomolecular recombination is the first-order reaction, and hence the decay constant is, as shown in Fig. 5.15a, independent of the concentration of the transient species. On the other hand, bimolecular recombination is the second-order reaction, and hence the half-life is, as shown in Fig. 5.15b, dependent on the concentration of the transient species: it should be theoretically half at twice concentration. Therefore, we can distinguish whether electron and hole are bound as a geminate pair at the interface or dissociated into free carriers by analyzing the intensity dependence of the decay dynamics.

In RRa-P3HT:PCBM blend films, as described in Sect. 5.6.1, polarons are promptly generated in a picosecond with $\eta_{ED} = 100$ %. However, as shown in Fig. 5.16, the PCBM anion band at 1,030 nm decays monoexponentially to 30 % with a time constant of $\sim$0.8 ns. The photobleaching at 480 nm also recovers with the same constant of $\sim$0.8 ns. Furthermore, as shown in Fig. 5.17, all the decay dynamics of the P3HT polarons at 850 nm, the PCBM anions at 1030 nm, and the photobleaching at 480 nm are independent of the excitation intensity, and therefore can be ascribed to the monomolecular (geminate) recombination of P3HT polarons and PCBM anions. We therefore conclude that 70 % of P3HT polarons geminately recombine with PCBM anions to the ground state and the remaining 30 % of polarons can be dissociated into free carriers. The dissociated polarons survive until longer time domains, and hence can be observed on a time scale of

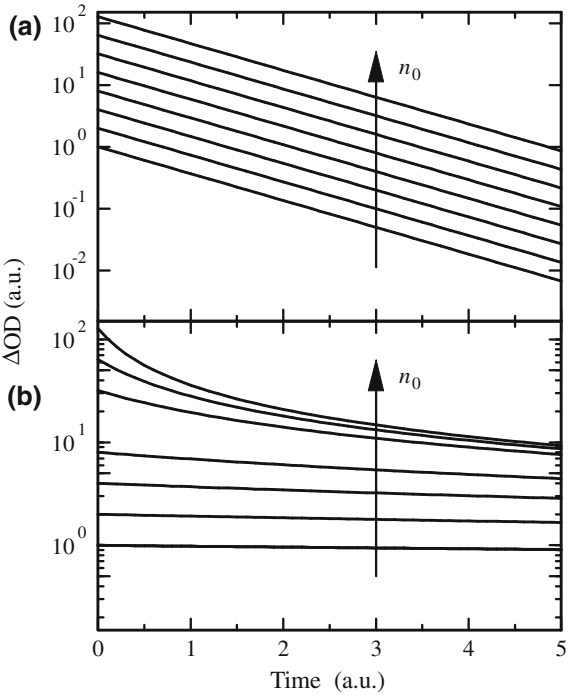

Fig. 5.15 Intensity dependence of the simulated transient absorption decays for **a** the monomolecular recombination (the first order reaction) and **b** the bimolecular recombination (the second order reaction). In the first-order reaction, the lifetime is independent of the initial concentration n_0. In the second-order reaction, the half-life is dependent on n_0: it is half at twice the initial concentration

microseconds as shown in Fig. 5.6b. In other words, the charge dissociation efficiency is as low as $\eta_{CD} = 30$ % in RRa-P3HT:PCBM blend films.

In RR-P3HT:PCBM blend films, there are two pathways for polaron generation: one is prompt generation (<100 fs) at the interface and the other is delayed generation ($\sim$10 ps) after the exciton migration to the interface. Here, we focus on the nanosecond dynamics of two polarons bands: the delocalized polarons at 700 nm and localized polarons at 1000 nm. This assignment is consistent with previous studies on P3HT pristine films where the 700 and 1000 nm bands are ascribed to interchain delocalized polarons and intrachain localized polarons, respectively [13, 29, 30]. As shown in Fig. 5.18, the decay dynamics of the two bands is dependent on the excitation intensity at higher excitation intensities, indicating the bimolecular recombination of free polarons. We therefore conclude that all of the polarons at 700 and 1000 nm are ascribed to dissociated free polarons on a time scale of nanoseconds. In contrast to RRa-P3HT:PCBM blends, no decay is observed for RR-P3HT:PCBM blends even at lower excitation intensities. In other words, the charge dissociation efficiency is estimated to be as high as $\sim$100 % for these two polarons. In addition, without going into detail, the other polaron in amorphous domains exhibits a charge dissociation efficiency of 38 % before the thermal annealing, which is similar to that observed for RRa-P3HT:PCBM blends, and 69 % after the thermal annealing. Consequently, the overall charge dissociation efficiency is as high as $\eta_{CD} = 80$ % before the

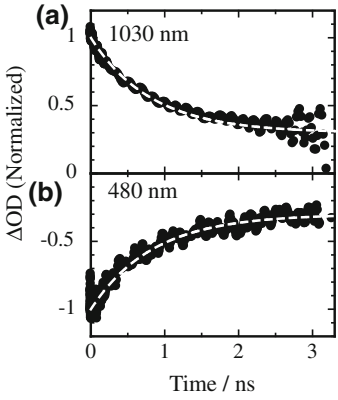

Fig. 5.16 Normalized transient absorption decays of RRa-P3HT:PCBM (50:50 w/w) blend films excited at 400 nm measured at **a** 1030 nm and **b** 480 nm. The transient decay is fitted with an exponential function and a constant: $\Delta OD(t) = A_D[1 - \exp(-t/\tau_D)] + B$. The *broken lines* represent the best-fitting curve. Adapted with permission from [19]. Copyright 2010 American Chemical Society

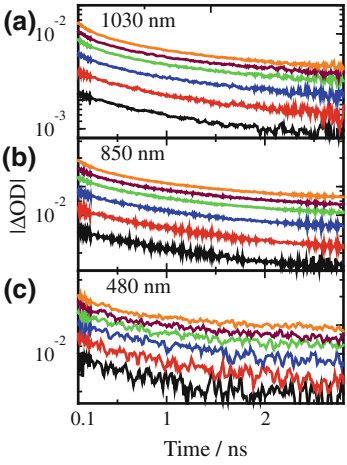

Fig. 5.17 Transient absorption decays of RRa-P3HT:PCBM (50:50 w/w) blend films excited at 400 nm measured at **a** 1030 nm, **b** 850 nm, and **c** 480 nm. The excitation intensity is varied over 6, 12, 24, 48, 72, 120 μJ cm^{-2} from *bottom* to *top* in each panel. The negative signals at 480 nm are converted to positive. Adapted with permission from [19]. Copyright 2010 American Chemical Society

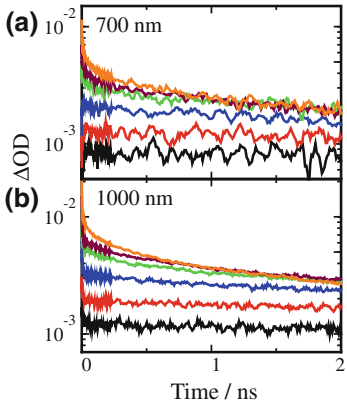

Fig. 5.18 Transient absorption decays of RR-P3HT:PCBM (50:50 w/w) blend films after thermal annealing excited at 400 nm measured at **a** 700 nm and **b** 1000 nm. The excitation intensity is 6, 12, 24, 48, 72, 120 μJ cm^{-2} from *bottom* to *top* in each panel. Adapted with permission from [19]. Copyright 2010 American Chemical Society

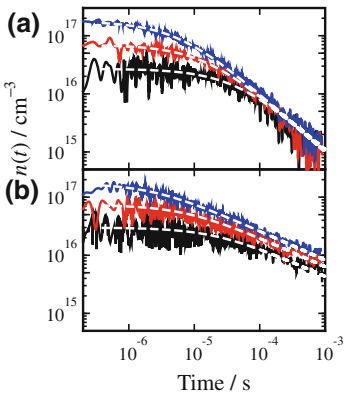

Fig. 5.19 Time evolution of the carrier density $n(t)$ in RR-P3HT:PCBM (50:50 w/w) blend films measured at **a** 700 nm and **b** 1000 nm. The excitation intensity at 400 nm is 0.8, 1.8, and 4.7 μJ cm^{-2} from *bottom* to *top* in each panel. The *broken lines* represent fitting curves with an empirical power equation: $n(t) = n_0/(1 + at)^{-\alpha}$. Reprinted with permission from [20]. Copyright 2010 American Chemical Society

thermal annealing, and increases to $\eta_{CD} = 93$ % after the thermal annealing, which is three times larger than that for RRa-P3HT:PCBM blend films.

Such a high dissociation efficiency is consistent with the efficient device performance of RR-P3HT:PCBM solar cells. However, it cannot be rationally explained by the classical models such as those of Onsager [59] and Braun [60]. Recent theoretical studies demonstrate that the presence of donor–acceptor phase-separated interface increases the charge dissociation probability in comparison with the homogeneous blend [61–63]. Recently, Durrant pointed out the importance of considering the change in entropy associated with changing from a single exciton to two separated charges, by which the effective Coulomb capture radius is estimated to be ~4 nm at a typical donor–acceptor heterojunction [64]. This is much shorter than the Onsager radius ($r_C = 14$–19 nm) in organic materials at room temperature as mentioned above. Interestingly, this effective Coulomb capture radius is comparable to our estimations of the delocalization radius of singlet excitons: singlet excitons with a radius of ~4.3–6.7 nm in RR-P3HT pristine films can be effectively dissociated into free polarons, while singlet excitons with a radius of ~3.2 nm in RRa-P3HT pristine films form bound radical pairs. This correlation suggests that the separation distance of two charges at the interface is closely related to the delocalization radius of singlet excitons. On the other hand, Deibel and his coworkers have demonstrated that the efficient charge dissociation can be explained by kinetic Monte Carlo simulations considering delocalization of charge carriers within conjugated segments in polymer chain [65]. This is also consistent with our findings of the different delocalization radius of singlet excitons, because delocalized singlet excitons would convert to delocalized polarons. We therefore conclude that the longer separation distance of bound radical pairs >4 nm can promote the dissociation of bound radical pairs and the formation of free polarons effectively, whereas the shorter separation distance of bound radical pairs <4 nm causes in a significant loss due to the geminate recombination of bound radical pairs at the interface. In addition, desirable phase-separated structures in RR-P3HT:PCBM blend films can also promote the dissociation of bound radical pairs effectively, whereas homogeneously mixed blend

structures in RRa-P3HT:PCBM blend films cause a significant loss due to the geminate recombination. Furthermore, the high charge mobility in RR-P3HT:PCBM blend films can also result in the efficient dissociation of bound radical pairs [60–66].

5.6.3 Trap-Free and Trap-Limited Recombination

As shown in Fig. 5.7b, two absorption bands are clearly observed at around 700 and 1000 nm and decay slowly on a microsecond time scale. These two bands can be ascribed to polarons: the 700 nm band to delocalized polarons and the 1000 nm band to localized polarons. Interestingly, the delocalized polaron band at 700 nm decays faster than the localized polaron band at 1000 nm. The delocalized polaron band almost disappears and instead the localized polaron band is dominant at 100 μs. This is indicative of the different recombination dynamics between delocalized polaron and localized polaron. Figure 5.19 shows the transient absorption decays at 700 and 1000 nm at different excitation intensities from 0.8 to 30 μJ cm^{-2}. Here, the charge carrier density is calculated on the basis of the molar absorption coefficient of each polaron. As shown in the figure, both decays can be well fitted with an empirical power-law equation.

$$n(t) = \frac{n_0}{(1+at)^{\alpha}} \tag{5.1}$$

The exponent α for the localized polaron band at 1000 nm is $\sim$0.5, which is consistent with previous reports [8, 16, 67, 68]. As mentioned above, this power-law decay with an exponent $\alpha < 1$ is the characteristic of bimolecular recombination of trapped carriers having an exponential tail of polaron trap states (trap-limited bimolecular recombination) [31, 69, 70]. On the other hand, the exponent α for the delocalized polaron band at 700 nm is as high as unity, suggesting trap-free bimolecular recombination.

The diffusion-limited bimolecular charge recombination dynamics is given by

$$\frac{dn(t)}{dt} = -\gamma(t)n^2(t) \tag{5.2}$$

where $n(t)$ is the carrier density and $\gamma(t)$ is the bimolecular recombination rate at a delay time t. Therefore, the bimolecular recombination rate can be expressed as a function of time by substituting Eq. (5.1) into Eq. (5.2)

$$\gamma(t) = -\frac{dn(t)}{dt}\frac{1}{n^2(t)} = \frac{a\alpha}{n_0}(1+at)^{\alpha-1} \tag{5.3}$$

Similarly, the bimolecular recombination rate can be also expressed as a function of the carrier density by substituting Eq. (5.1) into Eq. (5.3).

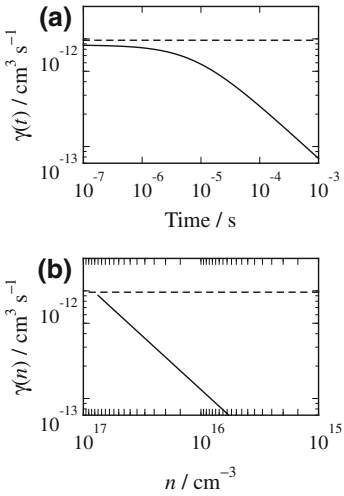

Fig. 5.20 Log–log plots of the bimolecular recombination rate γ at 1000 nm (*solid lines*) and 700 nm (*broken lines*) as a function of **a** time t and **b** the carrier density n. Adapted with permission from [20]. Copyright 2010 American Chemical Society

$$\gamma(n) = \frac{a\alpha}{n}\left(\frac{n}{n_0}\right)^{\frac{1}{\alpha}} \tag{5.4}$$

As mentioned above, α is equal to ~ 0.5 for the localized polaron band at 1000 nm and unity for the delocalized polaron band at 700 nm. Therefore, as shown in Fig. 5.20, the bimolecular recombination rate is time-dependent $\gamma(t)$ for the localized polaron band at 1000 nm, which decreases from 10^{-12} to 10^{-13} cm^3 s^{-1} over the time range from 10^{-6} to 10^{-3} s, while it is time-independent $\gamma = a\ n_0^{-1} \approx 10^{-12}$ cm^3 s^{-1} for the delocalized polaron band at 700 nm. Figure 5.21 shows the temperature dependence of the bimolecular recombination rate of (a) localized polarons at 1000 nm and (b) delocalized polarons observed at 700 nm over the carrier density range from 10^{16} to 10^{17} cm^{-3}. For the localized polarons, the activation energy estimated from the slope in the Arrhenius plots is as large as 0.097–0.178 eV, which depends on the carrier density. On the other hand, the activation energy for the delocalized polarons is as low as ~ 0.078 eV and independent of the carrier density. We therefore assign the localized polarons to trapped polarons and the delocalized polarons to trap-free polarons.

For localized polarons, the time-dependent trap-limited bimolecular recombination rate $\gamma(t)$ varies from 10^{-12} to 10^{-13} cm^3 s^{-1} depending on time or carrier density, as shown in Fig. 5.20, which is consistent with previous reports [67, 68, 71, 72]. The time-dependent bimolecular recombination rate is due to trap depths depending on the carrier density: the trap depth deepens with time because of lower carrier density, resulting in the slower bimolecular recombination rate on longer time scales [31, 68, 70]. As shown in Fig. 5.20b, the slope of log–log plots of $\gamma(n)$ against n is almost unity. In other words, $\gamma(n)$ can be expressed by $\gamma(n) \approx \gamma_0\, n$. Thus, Eq. (5.2) is rewritten as

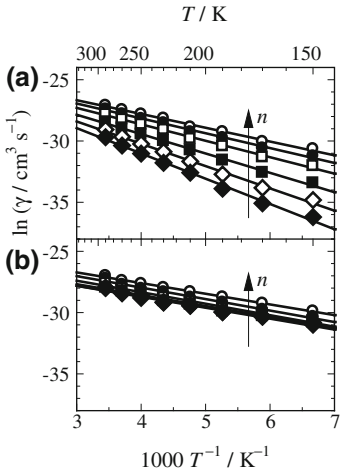

Fig. 5.21 Arrhenius plots of the bimolecular recombination rate γ at **a** 1000 nm and **b** 700 nm over the temperature range from 150 to 290 K. The carrier density n is 1.3×10^{16} (◆), 2.7×10^{16} (◇), 5.4×10^{16} (■), 1.1×10^{17} (□), 1.6×10^{17} (●), and 2.2×10^{17} cm^{-3} (○) at 700 nm and 1.3×10^{16} (◆), 2.5×10^{16} (◇), 5.0×10^{16} (■), 1.0×10^{17} (□), 1.5×10^{17} (●), and 2.0×10^{17} cm^{-3} (○) at 1000 nm from *bottom* to *top* in each panel. The *solid lines* represent fitting curves with the Arrhenius equation: $\ln \gamma = \ln A - E_A/(k_B T)$. Adapted with permission from [20]. Copyright 2010 American Chemical Society

$$\frac{dn(t)}{dt} \approx -\gamma_0 n^3(t) \tag{5.5}$$

This is consistent with the trimolecular recombination dynamics reported recently for RR-P3HT:PCBM blends [67, 68, 71–73]. More specifically, $\gamma(n)$ can be expressed by $\gamma(n) \propto n^{(1/\alpha)-1}$ where the exponent $(1/\alpha) - 1$ would vary from 4.3 to 2.4, because α varies from 0.3 to 0.7 depending on PCBM fractions or annealing conditions as reported previously [8, 16, 67, 68]. In other words, the time-dependent trap-limited bimolecular recombination rate is strongly dependent on the film morphology.

For delocalized polarons, on the other hand, the time-independent trap-free bimolecular recombination rate is $\gamma \approx 10^{-12}$ cm^3 s^{-1}, which is one order of magnitude higher than that estimated by photo-CELIV [74]. This is probably because the photo-CELIV measurement cannot distinguish these two polarons, and hence gives the averaged bimolecular recombination rate. Interestingly, the trap-free bimolecular recombination rate is several orders of magnitude lower than the Langevin recombination rate given by $\gamma_L = e(\mu_e + \mu_h)/\varepsilon\varepsilon_0$ where μ_e and μ_h are the electron and hole mobility, respectively, and ε and ε_0 are the relative permittivity of the film and the vacuum permittivity, respectively. Assuming $\mu_e \approx 10^{-2}$ cm^2 V^{-1} s^{-1} [75] and $\mu_h \approx 10^{-4}$ cm^2 V^{-1} s^{-1} [76], γ_L is estimated to be as high as $\sim 10^{-8}$ cm^3 s^{-1}. Considering the slowest mobility $\mu_h \approx 10^{-4}$ cm^2 V^{-1} s^{-1} [77], γ_L is estimated to be $\sim 10^{-10}$ cm^3 s^{-1}, which is

still two orders of magnitude higher than the time-independent trap-free bimolecular recombination rate $\gamma \approx 10^{-12}$ cm^3 s^{-1}. As reported previously, the reduced bimolecular recombination rate is partly ascribed to phase-separated bicontinuous networks of RR-P3HT and PCBM domains, which are beneficial for reducing bimolecular recombination loss [67, 74]. It is also possible that the recombination is not diffusion limited but depends on the electron transfer rate at the interface. More importantly, the lifetime of trap-free carriers is estimated to be $\tau = (\gamma\ n_0)^{-1} \approx 10$ μs under the 1 sun condition, which is longer than a charge collection time ($\sim$2 μs) to extract $\sim$50 % charges under the 1 sun open-circuit conditions [25]. This finding suggests that the majority of trap-free charge carriers could reach the electrode before the bimolecular recombination even under near open-circuit condition. Under the short-circuit condition, the recombination loss has been reported to be negligible, because the short-circuit current increases linearly with the illumination intensity. We therefore conclude that trap-free polarons play a major role in the charge transport, resulting in the recombination-lossless performance in RR-P3HT:PCBM solar cells under not only the short circuit but also near-open-circuit condition. This is consistent with the relatively high fill factors (0.6–0.7) and EQEs (>80 %) reported for this device in comparison with other combination devices [5–9].

5.6.4 Relevance to Device Performance

As summarized in Table 5.1, we can evaluate all the efficiency of photovoltaic events in polymer solar cells. As described above, we can evaluate the efficiency of η_{ED}, η_{CT}, and η_{CD} from the transient absorption study. The remaining charge collection efficiency η_{CC} can be estimated from the internal quantum efficiency (IQE) reported in previous studies [57, 78–80]. Note that the efficiency is not absolute one but should depend on the film morphology. Indeed, the difference in the IQE is due to the different film morphology depending on the preparation conditions. Nonetheless, the efficiency listed in the table demonstrates which loss process is dominant in the device performance qualitatively. For RR-P3HT:PCBM solar cells, all the efficiency is more than 90 % after the thermal annealing. For RRa-P3HT:PCBM solar cells, on the other hand, the low efficiency in η_{CD} and η_{CC} is a major cause of the poor device performance. More specifically, the exciton diffusion η_{ED} is $\sim$100 % for RRa-P3HT:PCBM blend films, 93 % for RR-P3HT:PCBM blend films before the thermal annealing, and 89 % after the thermal annealing. In terms of the exciton collection to the interface, therefore, homogeneously mixed blend structures of RRa-P3HT:PCBM films are more desirable than phase-separated blend structures of RR-P3HT:PCBM films. This is consistent with the PL quenching results, indicating that there is still room to further improve the exciton diffusion efficiency in RR-P3HT:PCBM [81]. Indeed, such unquenched P3HT excitons can be effectively collected to the interface through the long-range energy transfer by loading appropriate dye molecules into

Table 5.1 Efficiency of each photovoltaic conversion event in P3HT:PCBM solar cells[a]. Reprinted with permission from [19]. Copyright 2010 American Chemical Society

Blend films	η_{ED}	η_{CT}	η_{CD}	η_{CC}	IQE/ %
RRa-P3HT:PCBM	1	1	0.31	0.15	5[b]
RR-P3HT:PCBM before annealing	0.93	1	0.80	~0.6–0.7	42–55[c]
RR-P3HT:PCBM after annealing	0.89	1	0.93	>0.9	75–83[d]

[a] η_{ED}: Exciton diffusion efficiency to the interface of P3HT/PCBM, η_{CT}: Charge transfer efficiency at the P3HT/PCBM interface, η_{CD}: Overall charge dissociation efficiency, η_{CC}: Charge collection efficiency, IQE: internal quantum efficiency at 400 nm, which is calculated by IQE = EQE/η_A where EQE is the external quantum efficiency at 400 nm and η_A is estimated from twice the absorbance at 400 nm under the following assumptions: (a) 4 % incident light loss at the air/glass interface and (b) 100 % reflection of the Al electrode.
[b] Taken from Ref. 79.
[c] Taken from Refs. 57 and 78.
[d] Taken from Refs. 57, 78, and 80.

RR-P3HT:PCBM blends [78, 82]. For the charge transfer at the interface, η_{CT} is as high as ~100 % both for RRa-P3HT:PCBM and RR-P3HT:PCBM blend films, suggesting that it is dependent on the combination of donor and acceptor materials rather than blend structures. For the charge dissociation, η_{CD} is as low as ~30 % for RRa-P3HT:PCBM blend films, while it is as high as 80 % for RR-P3HT:PCBM blend films before the thermal annealing and is improved to 93 % after the thermal annealing. For the charge collection, η_{CC} is as low as 15 % for RRa-P3HT:PCBM blend films, while it is ~60–70 % for RR-P3HT:PCBM blend films before the thermal annealing and is improved up to >90 % after the thermal annealing. The large differences in η_{CD} and η_{CC} are mainly ascribed to the phase-separated networks and the crystallization of RR-P3HT, both of which result in improved carrier mobility and larger separation of bound radical pairs. The high charge collection efficiency is consistent with our conclusion in the previous section. In conclusion, there is not much difference in the charge generation yield between RRa-P3HT:PCBM and RR-P3HT:PCBM blend films. Rather, the charge dissociation and collection have a critical impact on the device performance of P3HT:PCBM solar cells. Further studies are required to address the origin of high efficiency in the charge dissociation and collection in polymer solar cells.

5.7 Concluding Remarks

Polymer solar cells have made rapid progress in the device performance during the last decade. In 2012, a PCE of 10 % has been listed in the solar cell efficiency tables. For such remarkable progress, development of various new materials has played a leading role. On the other hand, there still remain unsolved issues on the underlying mechanism of photovoltaic conversion in polymer solar cells. The

device performance based on *J–V* characteristics just gives us the final result of a series of fundamental photovoltaic conversion events such as photon absorption, exciton generation, exciton diffusion, charge separation, charge recombination, charge dissociation, charge transport, and charge collection. These range over nine orders of magnitude on temporal scale from 10^{-14} to 10^{-5} s. Here, we demonstrated how powerful and useful the transient absorption spectroscopy is for directly observing transient species such as excitons and polarons involved in photovoltaic conversion events. A transient absorption study will help us understand "what" is going on in the device and evaluate quantitatively "how" fast and efficient each event is. Consequently, we can discuss in detail "why" such device performance is obtained on the basis of not the final result but each fundamental photovoltaic conversion event. Such an in-depth understanding of the mechanism underlying polymer solar cells will lead to the development of new materials and progress in device engineering. In particular, the key to further improvements of polymer solar cells is to understand the origin of high charge dissociation and collection efficiency. The high dissociation efficiency cannot be explained rationally by the classical theory, and the reduced bimolecular recombination rate is inconsistent with the Langevin recombination. Further progress toward 15 % efficiency requires the synergy between developments of new materials and device structures and better understanding of the photovoltaic conversion mechanism.

Acknowledgments This work was partly supported by the Kansai Research Foundation for Technology Promotion, the JST PRESTO program (Photoenergy and Conversion Systems and Materials for the Next-Generation Solar Cells) and the Global COE program (International Center for Integrated Research and Advanced Education in Materials Science) from the Ministry of Education, Culture, Sports, Science, and Technology, Japan.

References

1. Shaheen SE, Ginley DS, Jabbour GE (2005) Organic-based photovoltaics: toward low-cost power generation. MRS Bull 30:10–19
2. Brabec CJ, Durrant JR (2008) Solution-processed organic solar cells. MRS Bull 33:670–675
3. Krebs FC (2009) Fabrication and processing of polymer solar cells: a review of printing and coating techniques. Sol Energy Mater Sol Cells 93:394–412
4. Padinger F, Rittberger RS, Sariciftci NS (2003) Effects of postproduction treatment on plastic solar cells. Adv Funct Mater 13:85–88
5. Li G, Shrotriya V, Huang J, Yao Y, Moriarty T, Emery K, Yang Y (2005) High-efficiency solution processable polymer photovoltaic cells by self-organization of polymer blends. Nat Mater 4:864–868
6. Ma W, Yang C, Gong X, Lee K, Heeger AJ (2005) Thermally stable, efficient polymer solar cells with nanoscale control of the interpenetrating network morphology. Adv Funct Mater 15:1617–1622
7. Kim JY, Kim SH, Lee HH, Lee K, Ma W, Gong X, Heeger AJ (2006) New architecture for high-efficiency polymer photovoltaic cells using solution-based titanium oxide as an optical spacer. Adv Mater 18:572–576

8. Kim Y, Cook S, Tuladhar SM, Choulis SA, Nelson J, Durrant JR, Bradley DDC, Giles M, McCulloch I, Ha CS, Ree M (2006) A strong regioregularity effect in self-organizing conjugated polymer films and high-efficiency polythiophene: fullerene solar cells. Nat Mater 5:197–203
9. Irwin MD, Buchholz DB, Hains AW, Chang RPH, Marks TJ (2008) p-type semiconducting nickel oxide as an efficiency-enhancing anode interfacial layer in polymer bulk-heterojunction solar cells. Proc Natl Acad Sci USA 105:2783–2787
10. McCullough RD, Lowe RD (1992) Enhanced electrical conductivity in regioselectively synthesized poly(3-alkylthiophenes). J Chem Soc, Chem Commun 70–72
11. Chen TA, Rieke RD (1992) The first regioregular head-to-tail poly(3-hexylthiophene-2,5-diyl) and a regiorandom isopolymer: Ni vs Pd catalysis of 2(5)-bromo-5(2)-(bromozincio)-3-hexylthiophene polymerization. J Am Chem Soc 114:10087–10088
12. Chen TA, Wu X, Rieke RD (1995) Reigocontrolled synthesis of poly(3-alkylthiophenes) mediated by Rieke zinc: their characterization and solid-state properties. J Am Chem Soc 117:233–244
13. Sirringhaus H, Brown PJ, Friend RH, Nielsen MM, Bechgaard K, Langeveld-Voss BMW, Spiering AJH, Janssen RAJ, Meijer EW, Herwig P, de Leeuw DM (1999) Two-dimensional charge transport in self-organized, high-mobility conjugated polymers. Nature 401:685–688
14. Green MA, Emery K, Hishikawa Y, Warta W (2011) Solar cell efficiency tables (version 37). Prog Photovolt Res Appl 19:84–92
15. Green MA, Emery K, Hishikawa Y, Warta W, Dunlop ED (2012) Solar cell efficiency tables (version 39). Prog Photovolt Res Appl 20:12–20
16. Ohkita H, Cook S, Astuti Y, Duffy W, Tierney S, Zhang W, Heeney M, McCulloch I, Nelson J, Bradley DDC, Durrant JR (2008) Charge carrier formation in polythiophene/fullerene blend films studied by transient absorption spectroscopy. J Am Chem Soc 130:3030–3042
17. Yamamoto S, Guo J, Ohkita H, Ito S (2008) Formation of methanofullerene cation in bulk heterojunction polymer solar cells studied by transient absorption spectroscopy. Adv Funct Mater 18:2555–2562
18. Guo J, Ohkita H, Benten H, Ito S (2009) Near-IR femtosecond transient absorption spectroscopy of ultrafast polaron and triplet exciton formation in polythiophene films with different regioregularities. J Am Chem Soc 131:16869–16880
19. Guo J, Ohkita H, Benten H, Ito S (2010) Charge generation and recombination dynamics in poly(3-hexylthiophene)/fullerene blend films with different regioregularities and morphologies. J Am Chem Soc 132:6154–6164
20. Guo J, Ohkita H, Benten H, Ito S (2010) Bimodal polarons and hole transport in poly(3-hexylthiophene) fullerene blend films. J Am Chem Soc 132:9631–9637
21. Ohkita H, Kosaka J, Guo J, Benten H, Ito S (2011) Charge generation dynamics in polymer/polymer solar cells studied by transient absorption spectroscopy. J Photon Energy 1:011118
22. Gregg BA (2004) Toward a unified treatment of electronic processes in organic semiconductors. J Phys Chem B 108:17285–17289
23. Pope M, Swenberg CE (1999) Electronic processes in organic crystals and polymers, 2nd edn. Oxford University Press, New York
24. Brabec CJ, Zerza G, Cerullo G, Silvestri SD, Luzzati S, Hummelen JC, Sariciftci S (2001) Tracing photoinduced electron transfer process in conjugated polymer/fullerene bulk heterojunctions in real time. Chem Phys Lett 340:232–236
25. Shuttle CG, Maurano A, Hamilton R, O'Regan B, de Mello JC, Durrant JR (2008) Charge extraction analysis of charge carrier densities in a polythiophene/fullerene solar cell: analysis of the origin of the device dark current. Appl Phys Lett 93:183501
26. Westenhoff S, Howard IA, Hodgkiss JM, Kirov KR, Bronstein HA, Williams CK, Greenham NC, Friend RH (2008) Charge recombination in organic photovoltaic devices with high open-circuit voltages. J Am Chem Soc 130:13653–13658
27. Turro NJ (1978) Modern molecular photochemistry. The Benjamin Cummings Publishing Company Inc., California

28. Schweiger A (2003) Pulsed electron spin resonance spectroscopy: basic principles, techniques, and examples of applications. Angew Chem Int Ed 30:265–292
29. Österbacka R, An CP, Jiang XM, Vardeny ZV (2000) Two-dimensional electronic excitations in self-assembled conjugated polymer nanocrystals. Science 287:839–842
30. Jiang XM, Österbacka R, Korovyanko O, An CP, Horovitz B, Janssen RAJ, Vardeny ZV (2002) Spectroscopic studies of photoexcitations in regioregular and regiorandom polythiophene films. Adv Funct Mater 12:587–597
31. Nelson J (2003) Diffusion-limited recombination in polymer–fullerene blends and its influence on photocurrent collection. Phys Rev B 67:155209
32. Steigman J, Cronkright W (1970) Formation of Wurster's Blue in benzene at 25°. J Am Chem Soc 92:6736–6743
33. Guldi DM, Prato M (2000) Excited-state properties of C60 fullerene derivatives. Acc Chem Res 33:695–703
34. Kawaguchi T, Seki S, Okamoto K, Saeki Y, Yoshida Y, Tagawa S (2003) Pulse radiolysis study of radical cations of polysilanes. Chem Phys Lett 374:353–357
35. Mikhnenko OV, Cordella F, Sieval AB, Hummelen JC, Blom PWM, Loi MA (2008) Temperature dependence of exciton diffusion in conjugated polymers. J Phys Chem B 112:11602–11604
36. Shaw PE, Ruseckas A, Samuel IDW (2008) Exciton diffusion measurements in poly(3-hexylthiophene). Adv Mater 20:3516–3520
37. Cook S, Liyuan H, Furube A, Katoh R (2010) Singlet annihilation in films of regioregular poly(3-hexylthiophene): estimates for singlet diffusion lengths and the correlation between singlet annihilation rates and spectral relaxation. J Phys Chem C 114:10962–10968
38. Kraabel B, Moses D, Heeger AJ (1995) Direct observation of the intersystem crossing in poly(3-octylthiophene). J Chem Phys 103:5102–5108
39. Sheng Y, Nguyen TD, Veeraraghavan G, Mermer Ö, Wohlgenannt M, Qiu S, Scherf U (2006) Hyperfine interaction and magnetoresistance in organic semiconductors. Phys Rev B 74:045213
40. Verhoeven JW (2006) On the role of spin correlation in the formation, decay, and detection of long-lived, intramolecular charge-transfer states. J Photochem Photobiol C Photochem Rev 7:40–60
41. Smith MB, Michl J (2010) Singlet fission. Chem Rev 110:6891–6936
42. Singh S, Jones WJ, Siebrand W, Stoicheff BP, Schneider WG (1965) Laser generation of excitons and fluorescence in anthracene crystals. J Chem Phys 42:330–342
43. Katoh R, Kotani M (1992) Fission of a higher excited state generated by singlet exciton fusion in an anthracene crystals. Chem Phys Lett 196:108–112
44. Merrifield RE, Avakian P, Groff RP (1969) Fission of singlet excitons into pairs of triplet excitons in tetracene crystals. Chem Phys Lett 3:386–388
45. Albrecht WG, Michel-Beyerle ME, Yakhot V (1978) Exciton fission in excimer forming crystal. Dynamics of an excimer build-up in α-perylene. Chem Phys 35:193–200
46. Zenz C, Cerullo G, Lanzani G, Graupner W, Meghdadi F, Leising G, Silvestri SD (1999) Ultrafast photogeneration mechanisms of triplet states in para-hexylphenyl. Phys Rev B 59:14336–14341
47. Katoh R, Kotani M, Hirata Y, Okada T (1997) Triplet exciton formation in a benzophenone single crystal studied by picosecond time-resolved absorption spectroscopy. Chem Phys Lett 264:631–635
48. Österbacka R, Wohlgenannt M, Shkunov M, Chinn D, Vardeny ZV (2003) Excitons, polarons, and laser action in poly(p-phenylene vinylene) films. J Chem Phys 118:8905–8916
49. Wohlgenannt M, Graupner W, Leising G, Vardeny ZV (1999) Photogeneration action spectroscopy of neutral and charged excitations in films of a ladder-type poly(para-phenylene). Phys Rev Lett 82:3344–3347
50. Kraabel B, Hulin D, Aslangul C, Lapersonne-Meyer C, Schott M (1998) Triplet exciton generation, transport and relaxation in isolated polydiacetylene chains: subpicosecond pump–probe experiments. Chem Phys 227:83–98

51. Köhler A, Wilson JS, Friend RH, Al-Suti MK, Khan MS, Gerhard A, Bässler H (2002) The singlet–triplet energy gap in organic and Pt-containing phenylene ethynylene polymers and monomers. J Chem Phys 116:9457–9463
52. Köhler A, Beljonne D (2004) The singlet–triplet exchange energy in conjugated polymers. Adv Funct Mater 14:11–18
53. Nozik AJ (2008) Multiple exciton generation in semiconductor quantum dots. Chem Phys Lett 457:3–11
54. Nozik AJ (2010) Nanoscience and nanostructures for photovoltaics and solar fuels. Nano Lett 10:2735–2741
55. Lee J, Jadhav P, Baldo MA (2009) High efficiency organic multilayer photodetectors based on singlet exciton fission. Appl Phys Lett 95:033301
56. Rao A, Wilson MWB, Hodgkiss JM, Albert-Seifried S, Bässler H, Friend RH (2010) Exciton fission and charge generation via triplet excitons in pentacene/C60 bilayers. J Am Chem Soc 132:12698–12703
57. Marsh RA, Hodgkiss JM, Albert-Seifreid S, Friend RH (2010) Effect of annealing on P3HT: PCBM charge transfer and nanoscale morphology probed by ultrafast spectroscopy. Nano Lett 10:923–930
58. Howard IA, Mauer R, Meister M, Laquai F (2010) Effect of morphology on ultrafast free carrier generation in polythiophene: fullerene organic solar cells. J Am Chem Soc 132:14866–14876
59. Onsager L (1938) Initial recombination of ions. Phys Rev 54:554–557
60. Braun CL (1984) Electric field assisted dissociation of charge transfer states as a mechanism of photocarrier production. J Chem Phys 80:4157–4161
61. Peumans P, Forrest SR (2004) Separation of geminate charge-pairs at donor–acceptor interfaces in disordered solids. Chem Phys Lett 398:27–31
62. Groves C, Marsh RA, Greenham NC (2008) Monte Carlo modeling of geminate recombination in polymer–polymer photovoltaic devices. J Chem Phys 129:114903
63. Wojcik M, Michalak P, Tachiya M (2010) Geminate electron–hole recombination in organic solids in the presence of a donor–acceptor heterojunction. Appl Phys Lett 96:162102
64. Clarke TM, Durrant JR (2011) Charge photogeneration in organic solar cells. Chem Rev 110:6736–6767
65. Deibel C, Strobel T (2009) Origin of the efficient polaron-pair dissociation in polymer–fullerene blends. Phys Rev Lett 103:036402
66. Hilczer M, Tachiya M (2010) Unified theory of geminate and bulk electron–hole recombination in organic solar cells. J Phys Chem 114:6808–6813
67. Shuttle CG, O'Regan B, Ballantyne AM, Nelson J, Bradley DDC, Durrant JR (2008) Bimolecular recombination losses in polythiophene: fullerene solar cells. Phys Rev B 78:113201
68. Clarke TM, Jamieson FC, Durrant JR (2009) Transient absorption studies of bimolecular recombination dynamics in polythiophene/fullerene blend films. J Phys Chem C 113:20934–20941
69. Montanari I, Nogueira AF, Nelson J, Durrant JR, Winder C, Loi MA, Sariciftci NS, Brabec CJ (2002) Transient optical studies of charge recombination dynamics in a polymer/fullerene composite at room temperature. Appl Phys Lett 81:3001–3003
70. Nogueira AF, Montanari I, Nelson J, Durrant JR, Winder C, Sariciftci NS, Brabec C (2003) Charge recombination in conjugated polymer/fullerene blended films studied by transient absorption spectroscopy. J Phys Chem B 107:1567–1573
71. Shuttle CG, O'Regan B, Ballantyne AM, Nelson J, Bradley DDC, de Mello J, Durrant JR (2008) Experimental determination of the rate law for charge carrier density in a polythiophene: fullerene solar cell. Appl Phys Lett 92:093311
72. Foertig A, Baumann A, Rauh D, Dyakonov V, Deibel C (2009) Charge carrier concentration and temperature dependent recombination in polymer–fullerene solar cells. Appl Phys Lett 95:052104

73. Juška G, Genevičius K, Nekrašas N, Sliaužys G, Dennler G (2008) Trimolecular recombination in polythiophene: fullerene bulk heterojunction solar cells. Appl Phys Lett 93:143303
74. Pivrikas A, Juška G, Mozer A, Scharber M, Arlauskas K, Sariciftci NS, Stubb H, Österbacka R (2005) Bimolecular recombination coefficient as a sensitive testing parameter for low-mobility solar-cell materials. Phys Rev Lett 94:176806
75. Tuladhar SM, Poplavskyy D, Choulis SA, Durrant JR, Bradley DDC, Nelson J (2005) Ambipolar charge transport in films of methanofullerene and poly(phenylenevinylene)/methanofullerene blends. Adv Funct Mater 15:1171–1182
76. Baumann A, Lorrmann J, Deibel C, Dyakonov V (2008) Bipolar charge transport in poly(3-hexyl thiophene)/methanofullerene blends: a ratio dependent study. Appl Phys Lett 93:252104
77. Koster LJA, Mihailetchi VD, Blom PWM (2006) Bimolecular recombination in polymer/fullerene bulk heterojunction solar cells. Appl Phys Lett 88:052104
78. Honda S, Nogami T, Ohkita H, Benten H, Ito S (2009) Improvement of the light-harvesting efficiency in polymer/fullerene bulk heterojunction solar cells by interfacial dye modification. ACS Appl Mater Interfaces 1:804–810
79. Campoy-Quiles M, Kanai Y, El-Basaty A, Sakai H, Murata H (2009) Ternary mixing: a simple method to tailor the morphology of organic solar cells. Org Electron 10:1120–1132
80. Takanezawa K, Tajima K, Hashimoto K Efficiency enhancement of polymer photovoltaic devices hybridized with ZnO nanorod arrays by the introduction of a vanadium oxide buffer. Appl Phys Lett 93:063308
81. Ayzner AL, Wanger DD, Tassone CJ, Tolbert SH, Schwartz BJ (2008) Room to improve conjugated polymer-based solar cells: understanding how thermal annealing affects the fullerene component of a bulk heterojunction photovoltaic devices. J Phys Chem C 112:18711–18716
82. Honda S, Yokoya S, Ohkita H, Benten H, Ito S (2011) Light-harvesting mechanism in polymer/fullerene/dye ternary blends studied by transient absorption spectroscopy. J Phys Chem C 115:11306–11317

Chapter 6
Interface Stability of Polymer and Small-Molecule Organic Photovoltaics

Degradation Mechanisms, Characterization Techniques, and Improvement Approaches

D. W. Zhao, L. Ke, W. Huang and X. W. Sun

Abstract In this chapter, the interface degradation mechanisms in organic photovoltaics (OPVs) will be discussed. The interface instability is mainly ascribed to the diffusion of oxygen and water into the electrode materials as well as the interface modification layer between electrode and organic layer. Furthermore, the commonly used characterization techniques are presented, which are quite helpful to understand the origin of the interface instability and their level of impact. In particular, these techniques reveal optical and electrical changes at the interface.

D. W. Zhao
School of Electrical and Electronic Engineering, Nanyang Technological University, Singapore 639798, Singapore
e-mail: dewei_zhao@hotmail.com

D. W. Zhao
Department of Electrical Engineering and Computer Science, The University of Michigan, Ann Arbor, Michigan 48109, USA

L. Ke
Institute of Materials Research and Engineering 3 Research Link, Singapore 117602, Singapore
e-mail: karen-kl@imre.a-star.edu.sg

W. Huang
Key Laboratory for Organic Electronics and Information Displays (KLOEID), Institute of Advanced Materials (IAM), Nanjing University of Posts and Telecommunications, 9 Wenyuan Road, Nanjing, Jiangsu 210046, China
e-mail: iamwhuang@njupt.edu.cn; wei-huang@njupt.edu.cn

X. W. Sun (✉)
Department of Electronic and Computer Engineering, South University of Science and Technology of China, Shenzhen, 518055 Guangdong, China
e-mail: xwsun@sustc.edu.cn

X. W. Sun
School of Electrical and Electronic Engineering, Nanyang Technological University, Singapore 639798, Singapore

W. C. H. Choy (ed.), *Organic Solar Cells*, Green Energy and Technology,
DOI: 10.1007/978-1-4471-4823-4_6,

Therefore, the analysis on the interface degradation and development of characterization techniques would contribute to the understanding of interface stability and further enhance the entire device lifetime.

6.1 Introduction

Polymer and small-molecule organic photovoltaics (OPVs) have been attracting great attention in the past few years due to their unique properties of low cost, easy process at low temperature, and flexibility. They are becoming one of the future photovoltaic (PV) technologies for the lowest cost clean energy production. The rapid increase of OPV efficiency from 1 % in 1999 to 8.33 % in 2010 has made the commercial products realistic [1–6].

The light harvesting of organic semiconductors can be tuned to match solar irradiative spectrum by chemical design and synthesis. The capability of being solution processed is the most potential for manufacture by printing or coating techniques, which significantly enhances possibility of realizing large-area and low-cost cells. To enter commercial PV market, OPVs have to satisfy a few basic and standard requirements in cost, efficiency, and lifetime. Actually, the low efficiency and short lifetime of OPVs are compensated by their low module cost, which provides a strong impetus to invest in OPV technology [7]. The low efficiency could be solved by organic semiconductor materials, transparent electrode, light management, device physics to drive the OPV technology toward much more developed.

One of the limitations to commercialization is the short lifetime or instability of OPVs. Typically, investigations on stability of OPVs have been focused on the effect of the water and oxygen on the degradation of photoactive layers and electrodes in encapsulated or unencapsulated devices under different environment conditions such as continuous illumination, oxygen, nitrogen, moisture, and vacuum [8], i.e., factors that affect stability are primarily oxygen, humidity, temperature, cycling of temperature, light, loading conditions, pre-treatment, packaging, electrodes, and so on. Figure 6.1 displays the effect of three main factors influencing device stability [9]. In general, most studies on degradation of OPVs are correlated with oxidative damage to the photoactive layer associated with illumination of the device in presence of molecular oxygen, and several light dependent degradation pathways have been identified [10–16]. It is well known that OPVs have to suffer a relatively high temperature during operation, which could also degrade organic photoactive materials and electrodes to a great degree. Since organic semiconductors are highly sensitive to photo-oxidation or photobleaching, encapsulation of OPVs is necessary, preventing the exposure of active materials and electrodes to oxygen and water. Additionally, polymerization-induced impurities have to be extracted as they are likely to form free radicals upon photolysis [8, 17].

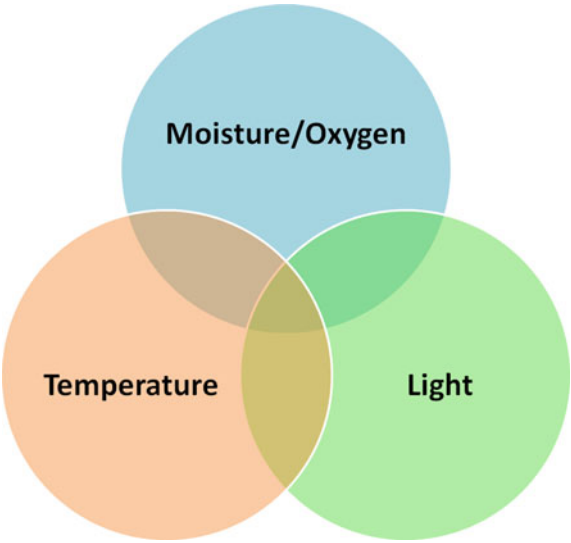

Fig. 6.1 The effect of three main factors that influence the device stability. The properties have been demonstrated separately, but usually they have a combined effect on the total device lifetime [9]

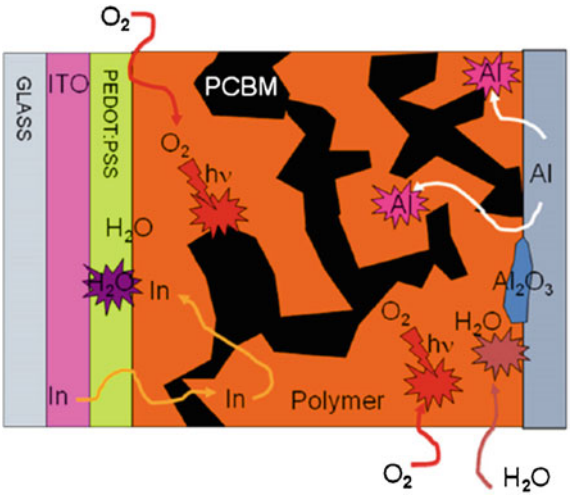

Fig. 6.2 A schematic illustration (cross-section view) of some degradation processes that take place in a typical bulk heterojunction (BHJ) OPV [8]. (Reprinted from [8], with permission from Elsevier) (http://www.sciencedirect.com/science/journal/09270248)

Figure 6.2 shows a cross-section view of the main processes that are considered to degrade OPVs. These processes represent extrinsic (diffusion of water and oxygen, mechanical stress, operation temperature under light illumination) and intrinsic mechanisms (photochemical degradation caused by singlet oxygen due to energy transfer from photoexcited polymer to adsorbed ground state oxygen molecules, movement of mobile species, such as indium and electrode materials like Al, interface degradation due to high energy excited stated chemistry at the interfaces and easy oxidization of metals, charge carrier density, and the morphology change of blend active layer) [8].

It is possible to classify the likelihoods of each mechanism as HIGH, MEDIUM, and LOW [9]. Diffusion of oxygen and water as well as electrodes (Indium Tin Oxide (ITO) and metals) possesses "HIGH" likelihood compared to other degradation mechanisms. It is obvious that the "HIGH" degradation has close relation with various interfaces. The "MEDIUM" likelihood of photo-oxidation of organic semiconductors and interfacial layer are followed. Furthermore, mechanical degradation has the relatively "LOW" likelihood. Therefore, the approaches to improve device stability can be conducted on the basis of likelihoods to overcome the degradation from the most significant level (HIGH) and to the least significant level (LOW).

Specifically, the efficient approaches to prevent the diffusion of oxygen and water are to develop mature device encapsulation to control the ability of O_2 oxygen transmission rate (OTR) and water water vapor transmission rate (WVTR) to cross an encapsulating membrane within a certain value, i.e., it is generally accepted that the lifetime of OPVs above 10, 100 h requires the upper limits of OTR of 10^{-3} $cm^3 \cdot m^{-2} \cdot day^{-1} \cdot atm^{-1}$ and WVTR of $10^{-6}g \cdot m^{-2} \cdot day^{-1}$, which are six to eight orders lower than the corresponding values of commercially available polymer films [18, 19]. The adhesives between layers should also be enhanced. Moreover, for electrode degradation, an alternative to ITO is remarkably required and interfacial engineering (hole-transporting layer (HTL)) is necessary correspondingly. On the other side, optimization of metal electrode such as electron-transporting layer (ETL) is of great importance to remain a good contact and insensitive to environment.

So far, there are many reports and reviews on study of device degradations [8, 20–23]. However, few reviews are concentrated on the effect of interface degradation on the device stability. In this chapter, we will mainly discuss the interface degradation mechanisms, followed by possible characterization techniques for detecting the change of interface structure. The understanding of interface degradation should serve as potential routes for improving interface stability and also entire device stability; therefore, highly promising improvement approaches of interface stability will be summarized. Finally, one of the challenging efforts on technology development is device encapsulation with low-cost and high-quality barrier. Thus, the encapsulation techniques will be introduced.

6.2 Mechanisms for Interface Degradation

For small-molecule organic light-emitting diodes (OLEDs), the luminescence degradation mechanisms have been systematically and comprehensively reviewed [20], which are mainly attributed to three individual and distinct modes as (i) dark-spot degradation, (ii) catastrophic failure, and (iii) intrinsic degradation. "Dark spots" refers to the formation of visible nonemissive defects or regions, leading to a decrease in device luminance due to the losses of emissive area. The underlying mechanisms might be electrochemical in nature or be thermally activated.

Catastrophic failure is primarily associated with defects existing in the organic active layers, resulting in a sudden decrease or total loss in luminescence as a result of large leakage currents due to electrical shorts. The underlying mechanisms are ascribed to morphological defects existing in organic layers or electrodes, or thermally induced during device operation with a temperature beyond glass transition temperature (T_g) of organic materials. The former two are considered to be correlated with surroundings. The intrinsic degradation, however, primarily material dependent, exhibit a progressive decrease in the brightness of the emissive area of a device with time during operation and no visible changes in device appearance. Aziz et al. attributed the intrinsic degradation to (1) the indium migration model, (2) the unstable cationic Alq_3 model, (3) the morphological instability model, (4) the immobile positive charge accumulation model, and (5) the mobile ionic impurities model.

For small molecules and polymer OPVs, they have similar device structures with OLEDs and also suffer similar issues associated with essential materials, electrodes, layer interface, and environmental conditions. In this section, we will focus on the discussion about the degradation mechanisms originating from interface instability at the adjacent layers such as anode and anode buffer layer, cathode and cathode buffer layer.

6.2.1 Anode and Anode Buffer Layer

ITO is the most commonly used anode for organic optoelectronic devices, which plays a significant role in injecting or extracting the holes from the active layer. Although ITO is relatively stable, it still suffers the degradation when exposed to special environments.

Carter et al. observed that the presence of ITO accelerates a long-term device failure in polymer OLEDs, induced by photo-oxidation of the light-emitting polymer via oxygen out of the ITO when polymer was fabricated directly onto ITO surface [24, 25]. The chemical reaction of the vinyl carbon with oxygen from the ITO anode induces the chain scission of active polymer [24]. Moreover, Stott et al. reported two major modes of degradations in ITO/MEH-PPV/Ca when they were operated in a dry inert atmosphere [24]: one originating from the oxidization of polymer MEH-PPV is likely caused by diffusion of the oxygen from ITO, resulting in luminescence quenching and increased impedance due to formation of aromatic aldehyde and chain scission, respectively; the other one is attributed to localized microscopic electrical shorts, however these shorts do not cause immediate failure of devices since self-induced fusing of the surrounding cathode metal isolates the shorts, which decreases the effective active area of each device. Only when the region of damaged cathode starts to coalesce does the ultimate failure happen.

Moreover, Krebs et al. found ITO etching indirectly due to the indium diffusion into the layers of device Al/C_{60}/P3CT/ITO [26]. The observation is the fact that

indium diffuses through all layers in the device and ends up on the outer surface of the counter electrode (Al).

It is clear that the interface between ITO and active layer is playing an important role in device performance and lifetime. Therefore, one effective solution is to incorporate poly(3,4-ethylenedioxythiophene):poly(styrenesulfonate) (PEDOT:PSS) as anode buffer layer between ITO and photoactive layer, which results in obvious improvement of lifetime and luminous efficiency [25]. Choice of polyaniline doped with conducting PSS could partially overcome the issue associated with the ITO/organic interface instability. Consequently, PEDOT:PSS has been widely used in organic electronic devices with the functions of (1) a barrier to prevent oxygen reaction, (2) a planarizing layer to inhibit electrical short points, (3) an interfacial layer to shift the work function of ITO, and (4) an adhesive layer to facilitate the adhesion between ITO and active layer [27]. The incorporation of PEDOT:PSS layer could also prevent the diffusion of indium containing etch products into organic active layer by trapping them.

However, the interface instability caused by PEDOT:PSS exists as well. de Jong et al. studied the interface stability between ITO and PEDOT:PSS by using Rutherford backscattering (RBS) [28]. It is found that the indium concentration in PEDOT:PSS increases from 0.02 to 0.2 at.% upon annealing in nitrogen at 100 °C for 2500 h. A more serious and faster degradation of ITO/PEDOT:PSS interface is observed when exposed to air, and the indium concentration reaches a saturated value of 1.2 at.% after a few days. Therefore, it is explained that the strong acidic nature of PEDOT:PSS makes the ITO etched. Furthermore, Girtan et al. compared two sets of devices with ITO/PEDOT:PSS or only PEDOT:PSS as transparent anode using MDMO-PPV:C_{60}BM or P3HT:PC_{60}BM blend system as the active layer [29]. It was found that V_{oc} of cells without ITO stays unchanged after aging (40 days in open atmosphere at room temperature) and this is not valid for cells with ITO. Meanwhile, for cells without ITO, the J_{sc} decreases by one or two orders of magnitude after aging, by contrast, for cells with ITO, the J_{sc} decreases by four to seven orders of magnitude. The results show that the work function of ITO changes with surface modification during aging. Kawano et al. studied the degradation of nonencapsulated OPVs (ITO/PEDOT:PSS/MDMO-PPV:PCBM/Al) under different ambient conditions such as white light irradiation, in dark, exposure to air, dry oxygen, and humid nitrogen atmospheres [30]. By comparing the devices with and without PEDOT:PSS, the main reason for degradation under air exposure is ascribed to water adsorption by the hygroscopic PEDOT:PSS layer, independent of light, therefore, the resistance at the PEDOT:PSS/blend layer interface is increased with degrading, proved by the change of charge mobility and hole injection after air exposure. Spatially inhomogeneous degraded PEDOT:PSS layer is correlated with insulating domains causing current loss.

Thus, it is summarized that the interface degradation caused by PEDOT:PSS should be as follows: (1) the ITO etching due to acidic nature of PEDOT:PSS; (2) the resistance increase due to the water adsorption by hygroscopic PEDOT:PSS; (3) the change of ITO work function due to aging.

6.2.2 Cathode and Cathode Buffer Layer

Low work function (LWF) metals, such as Ca, Mg, and Al, are used to inject or collect electrons as cathode. It is known that LWF metals are prone to be oxidized and to cause device degradation due to the diffusion of oxygen and water into itself or organic active layer. Moreover, at the organic/metal interface, instability might exist due to the intrinsic or extrinsic properties of metals. In order to achieve matched energy levels of organic layer and metal, a few interfacial layers can be incorporated in between organic active layer and metal to improve the charge injection or collection.

Aziz et al. studied the main mechanisms of degradation in OLEDs (ITO/PPV/Al), concluding that the electrochemical reaction between two electrodes is found to be a major cause, resulting in corrosion and microstructural changes in both electrode materials [20, 31, 32]. Therefore, the electrode materials can degrade significantly forming a complex with electrolyte-like polymer, leading to the increase of threshold voltage. At the same time, the additional conditions such as moisture or impurities in polymers will enhance the ionic conductivity of the active layer and accelerate the corrosion of the electrode at the affected locations. Subsequently, Aziz et al. further investigated the degradation mechanism in Alq_3 based OLEDs [32]. The results indicate that the short lifetime is mainly caused by the injection of holes into Alq_3, leading to a decrease in fluorescence quantum efficiency due to unstable cationic Alq_3 species as well as fluorescence quenching sites. Therefore, many stabilized OLEDs by doping the hole-transporting layer, or using a buffered hole-injection contact, or forming alternating hole and electron transporting based emitting layers, can be explained reasonably and correspondingly.

For OPVs, as investigated by Reese et al., the conclusion has been drawn that the organic/metal interface is a major source of device degradation for P3HT:PCBM OPVs [33, 34].

Krebs et al. systematically investigated the stability of MEH-PPV:PCBM-based devices in terms of atmosphere, handling, electrode treatment, mode of preparation, and barrier layers by the dependence of J_{sc} on time [15]. The authors separate various degradation processes responsible for the decay and carry on the study with the model of $I_{sc}(t)/I_{sc}(0) = Ae^{-bt} + Ce^{-dt} + \cdots$, where b and d are the time constants, A and C are the weighting of the individual exponential functions [15]. It is expected that individual responsibility for the device degradation could be linked to the experimental parameters by making changes correspondingly. These experimental parameters can be selected separately and in parallel. Then, the integrated charge could be achieved by $Q_{total} = A/b + C/d + \cdots$ when extrapolated to infinity [15]. Similarly, the degradation of P3HT:PCBM-based OPVs can be represented by an exponential term describing the fast initial decay and a second exponential term describing the long-term degradation, as $\eta = \eta_0[ae^{-\gamma t} + be^{-\delta t}]$, where η_0 is the initial efficiency and a, b, γ, δ are curve fitting parameters [35, 36]. The time constant γ indicates the fast decay process of degradation and γ is related to a slow decay. Schuller et al. developed various models for dynamic degradation, including

both a single exponential mode and a linear mode in which the latter one is preferred [37]. However, Krebs et al. found that such a linear model could represent degradation well only at the beginning of the device life [15], therefore it is suggested that a single exponential could be a good fitting in a few examples and several exponentials could fit better. It is found that the decay curves could be fitted with a two-term exponential function: an initial fast decay and a second slower decay. The fast decay is independent on atmospheric conditions such as device operation and various barrier layers at the active layer/Al interface. The slow decay depends on the atmosphere due to the reaction with oxygen [15].

Logdlund et al. demonstrated a theoretical investigation on the interaction of Al with PPV and its derivatives [38]. It is found that Al prefers the reaction with vinylene linkages in methoxy groups based PPV materials via forming covalent bonds, Al–C. This is actually useful for cathode in OPVs due to the LWF of Al. However, when methoxy groups are replaced with carbonyl groups, new reactive sites are induced, resulting in Al–O bonds and exhibiting comparable stability. Moreover, another explanation is proposed to be the existence of electron charge transfer from the Al atoms to the polymer chains. Karst et al. studied the small-molecule OPVs (ITO/PEDOT:PSS/CuPc/PTCDA(or DAAQ)/Al) with upper Al electrode exposed to air [39]. The results show that the device with no exposure to air yields a small V_{oc} (0.125 V), and meanwhile, the V_{oc} (0.5 V) increases largely when the device is exposed to air as a result of an oxide layer (probably Al_2O_3) present at the Al/organic interface. It is explained that the direct contact of organic acceptor with Al or Ag induces Fermi level pinning, resulting in small V_{oc}. Formation of such an oxide layer separates the organic and Al layers, leading to no more Fermi level pinning and high V_{oc}.

Jeranko et al. demonstrated decay processes by using two-dimensional mapping of PV response on the active area, concluding that a major degradation is attributed to the path along the edges of the active area and the variance in the photocurrent over the area of the device caused by the process of electrodes [12, 15].

A cathode buffer layer is essentially necessary for good charge extraction by cathode. Usually, it is thin enough to possibly prevent the opposite charge from being injected or collected due to the existence of energy barrier at the organic/metal interface.

Melzer et al. discussed the effect of inserting a C_{60} layer in between active layer and cathode by *I–V* characteristics and impedance spectroscopy, suggesting the presence of a strong dipole layer at the C_{60}/metal interface [40]. Krebs et al. also inserted a C_{60} layer at the MEH-PPV/Al interface [15], therefore, a significant improvement on device stability is observed on the first decay parameter due to the formation of an efficient barrier layer that conducts the electrons well and facilitates the exciton dissociation. Moreover, the authors claimed that high current density due to high illumination intensity could accelerate the degradation, indicating that the weight of the first exponential increases with the illumination intensity. This could be attributed to chemical reactions of photoinduced radical anions and radical cations at the Al interface. The concentration of charge carriers at the Al surface increases with the current density increasing, resulting in the

saturation of surface density and possible increase in chemical degradation. In addition, the effect of temperature on device degradation was studied by setting up a temperature-controlled platform via a fan for the measurement of the devices. It is confirmed that a higher temperature accelerates device degradation, which is correlated with glass transition temperature (T_g) of the polymer. It means if a fast degradation of devices at an operation temperature close to T_g could be observed, the motion of polymer chains is increased and the electrode diffuses.

BCP is also an effective electron-transporting material as an exciton-blocking layer and electron-transporting layer in organic optoelectronic devices. Vogel et al. [41] incorporated BCP buffer layer at the C_{60}/Al interface in small-molecule OPVs (ITO/PEDOT:PSS/Pc/C_{60}/BCP/Al) to reduce exciton quenching at the C_{60}/Al interface and to enhance electron transport from C_{60} to Al due to established Ohmic contact between C_{60} and Al, resulting in a significant improvement of efficiency. However, BCP does not have effect on blend geometry based OPVs (ITO/PEDOT:PSS/Pc:C_{60}/BCP/Al). Moreover, BCP prevents the diffusion of Al during deposition on top of C_{60} film, creating a highly structured interface. BCP also blocks the exciton recombination caused by chemical reactions which forms recombination centers at the interface.

An alternative to current organic electron-transporting materials is an insulator, such as Al_2O_3 or LiF, as cathode buffer layer. Zhang et al. found Al_2O_3 in a role of improving electron injection at the organic/cathode interface in Alq_3 based OLEDs [42]. The fact that holes are injected and accumulated at the organic/buffer interface could be beneficial to the enhancement of electron injection due to the tunneling barrier reduction by changing the Fermi level of the cathode and carrier transporting models. Hung et al. [43] demonstrated that an ultrathin LiF layer at the organic/Al interface enhances electron injection and electroluminescence efficiency in an OLED of ITO/CuPc/NPB/Alq_3/LiF/Al, which is primarily attributed to band bending of the organic active layer by more than 1 eV when Alq_3 contacts with the dielectric LiF, resulting in the reduction of electron injection barrier height at Alq_3/Al interfaces.

Brabec et al. summarized a few mechanisms of LiF used in organic electronic devices [44]: (1) lower the effective work function of Al; (2) dissociated LiF reacts with the organic layer via chemical doping; (3) form a dipole layer to make a vacuum level offset between organic layer and Al; (4) protect the Al atoms from diffusing to organic layer during thermal deposition. Subsequently, Brabec et al. [44] inserted an ultrathin LiF layer between BHJ active layer and metal cathode (Al and Au) to largely enhance the FF and to stabilize high V_{oc}. They proposed a combined mechanism of the formation of a dipole moment across the junction, due to either orientation of the LiF or chemical reactions leading to charge transfer across the interface. An alignment of LiF is ascribed to the fact that the Li^+ adheres preferably to the organic surface and the F^- points toward the Al surface. Furthermore, van Gennip et al. [45] studied and confirmed the mechanism of LiF at the interface of metal and active layer by using secondary ion mass spectrometry (SIMS) and X-ray photoelectron spectroscopy (XPS) measurements. SIMS spectra measured at the organic/LiF interface to determine the chemical state of LiF layer

on the surfaces of MDMO:PPV and PCBM substrates, showing that AlF_3 is absent at the Al/LiF/MDMO-PPV and Al/LiF/PCBM interfaces, proving that the occurrence of the reaction is missing, which is used to explain the improved electron injection and collection. Moreover, a reaction of Al with carboxylic oxygen of PCBM actually takes place, proved by XPS measurements; however, this reaction is inhibited by LiF layer at the PCBM/Al interface.

6.3 Characterization Techniques for Interface Degradation

Highly efficient characterization techniques for interface degradation are very significant in order to understand the variance of interfaces during the device operation and their correlation with device degradation [8].

In OLEDs, Aziz et al. [31] employed characterization techniques, such as impedance spectroscopy (IS), electrochemical measurement, and scanning electron microscopy (SEM) to provide a mechanistic picture for degradation process. Experimental observations are analyzed and correlated to reveal the presence of an electrochemical reaction which causes device failure.

Jorgensen et al. summarized the characterization techniques and classified them into two typical ones [8]: one is including the approaches which could offer morphological and chemical information from specific locations in the device; the other one is covering the approaches which provide information from nonspecific locations in the device, i.e., information from all layers or the whole averaged analysis over a large area. The characterization techniques from the specific locations are typically time-of-flight secondary ion mass spectrometry (TOF-SIMS), depth profiling, XPS, atomic force microscopy (AFM), SEM, interference microscopy, fluorescence microscopy, and RBS. Meanwhile, the characterization techniques from the nonspecific locations are usually IS, near-field scanning microscopy (NSOM), infrared spectroscopy (IRAS), X-ray reflectometry (XRR). In addition, various ambient conditions such as white light irradiation, in dark, exposures to air, dry oxygen, and humid nitrogen atmospheres, can be applied to support the characterization of device degradation [30].

In this section, we will emphasize the characterization techniques for interface degradation and their corresponding analysis divided into optical and electrical aspects.

6.3.1 Optical Techniques

It is easily understood that optical techniques are based on the optical characterization and measurement of degradation and provide information about the correlation between interface variance and device degradation.

NSOM is used to establish the relation between morphology of BHJ and photocurrent generation. It is a potential technique to characterize the solar cells at the nanoscale level although it does not conclude the influence of device morphology on the device degradation and only shows the possibility [8, 46].

X-ray reflectometry or X-ray reflectivity (XRR) technique is used to probe the interfacial properties of layered samples such as films on substrates, multiple layers, and superlattices, which is based on Snell rule [47]. In the energy dispersive (ED) mode, a polychromatic primary X-ray beam is used and the reflection patterns are collected at a fixed angle, by an ED solid-state detector [48, 49]. The in situ EDXRR could overcome the issues associated with probable intrinsic errors in removing and repositioning the samples and allow the high-accuracy recording of the film morphology with the time evolution [50]. It is said that the in situ EDXRR technique is a powerful nondestructive tool to study the aging effect at the interface of OPVs under working conditions.

Paci et al. studied the evolution of the morphology in OPVs of glass/ITO/MDMO-PPV:PCBM/Al during operation by using EDXRR, in which three steps are included [50]. The first step is a preliminary set of XRR measurements on three different samples ((1) Glass/ITO/MDMO-PPV:PCBM; (2) Glass/ITO; (3) Glass/ITO/MDMO-PPV:PCBM/Al), representing the successive stages of cell construction, which identifies the contributions from each layer to the overall cell reflection patterns and provides accurate data regarding the electronic densities of the different layers. The second step as shown in the inset of Fig. 6.3 is the verification of morphological stability of the device under ambient condition, representing repeatable measurements even after a few months. The third step shown in Fig. 6.3 is a collection of XRR results and patterns on an OPV, measured under controlled atmospheric conditions, i.e., both in the dark and during 15 h illumination, leading to systematically morphological variation at the electrode/organic layer interface. Therefore, it is concluded that the direct correlation between progressive thickening of this interface and the decrease in device performance, explained by a "real" effect—the formation of an Al oxide layer at the film surface and at the interface with organic active layer due to a photo-oxidation reaction, or a possible but indistinguishable change of the formation of a layer at the Al/organic interface due to indium diffusion from the ITO.

Paci et al. further confirmed the photoinduced oxidation of the metal electrode at the organic/metal interface by using EDXRR technique in cells without (Cell A) and with (Cell B) protection layer of LiF at the organic/metal interface [51]. It was suggested that the Al oxidation in Cell A is correlated with the first aging process exhibited by the exponential decay in Fig. 6.4. Meanwhile, Cell B does not show the same two-step process, exhibiting no loss of efficiency in the first 15 h due to the stable morphology at the LiF/Al interface and also the absence of oxidation process. Therefore, the insertion of LiF is beneficial to the protection of the fast photoinduced degradation in the first few hours. As highlighted by the authors, the conclusion that the formation of oxidization layer between organic layer and metal is prevented by inserting a LiF buffer layer has been drawn under the real-time in

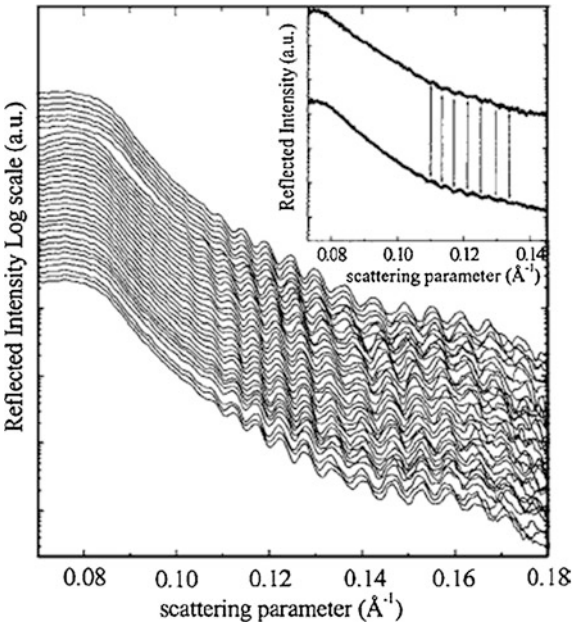

Fig. 6.3 In situ EDXRR measurements of the solar cells, collected under controlled atmosphere and upon illumination. The reflectivity profiles are shifted in height for clarity. Inset: the ex situ EDXRR measurements carried out at a distance of several months on the same cell [50]. (Reprinted with permission from Ref. [50]. Copyright [2005], American Institute of Physics)

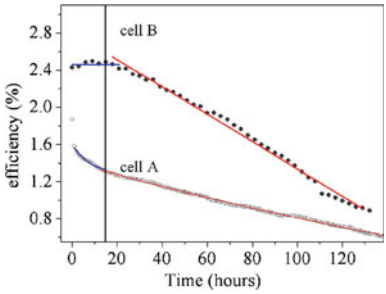

Fig. 6.4 Efficiency curves for cell A and cell B [51]. (Reprinted with permission from Ref. [51]. Copyright [2006], American Institute of Physics)

situ EDXRR measurements without any complementary technique for additional study on morphology and structure.

However, there is a contradictory discussion that Andreasen et al. [52] cannot correlate the fast degradation of OPVs to a substantial change of morphology, verified by XRR technique, instead the authors found that rough interfaces of stacking layers significantly inhibits the resolution of the XRR technique for in situ investigation on physical degradation mechanisms, implying that it is difficult to detect the changes at the interface of multiple layer-based OPVs (ITO/PEDOT:PSS/MEH-PPV:PCBM or P3HT:PCBM/Al) although different model fittings have been applied.

XPS is a quantitative spectroscopic technique measuring the elemental composition, empirical formula, chemical state, and electronic state of the elements in a material, which is performed under ultra-high vacuum. XPS is used to analyze

the surface chemistry with a probe depth of 1–10 nm away from the top. It is also used to analyze the elements giving information on the chemical state [8]. Gennip et al. [45] used XPS to detect and confirm the reaction of Al with the carboxylic group (O 1 s carboxylic oxygen peak) present in PCBM so that a LiF layer at the PCBM/Al interface blocks this reaction.

SIMS is the most sensitive surface analysis technique to analyze the composition of solid surfaces and thin films by sputtering surface of the specimen with a focused primary ion beam and collecting and analyzing ejected secondary ions. The measured secondary ions with a mass spectrometer are used to determine the elemental, isotopic, or molecular composition of the surface. TOF-SIMS is a method of mass spectrometry in which an ion's mass-to-charge ratio is determined via a time measurement. More importantly, TOF-SIMS technique is superior to XPS in view of the imaging capabilities and the sensitivity [8]. Gennip et al. [45] measured SIMS to show that LiF does not react with aluminum to form AlF_3, nor does it react in any other way to liberate Li, as mentioned in Sect. 2.2. Much more details on optical techniques for degradation characterization can be found in ref [8].

6.3.2 Electrical Techniques

Electrical techniques are based on the information provided by the characterization and measurements of electrical properties, which can be able to reveal the change of interface state and their influence on the interface stability.

Impedance spectroscopy (IS), also known as electrochemical impedance spectroscopy, measures the dielectric properties of a medium as a function of frequency. It is based on the interaction of an external field with the electric dipole moment of the sample. It is also widely applied in a broad field of inorganic, organic, and biological systems based devices.

In BHJ OPVs, IS is commonly used to study the electrical transport properties [8]. An equivalent circuit, as shown in Fig. 6.5, is modeled to translate the frequency response of the circuit to the correspondingly individual interfaces and consequent layers in the devices. In this case, the dielectric constants for various materials could be found via changing the film thickness and fitting the experimental data [53], such as the distributed resistors r_t (representing the electron transport), the distributed chemical capacitance $c_n = C_\mu$ and r_{rec} (representing the electron recombination resistance), a series resistance R_s (representing the contact and wire effects), a capacitor $C_g \approx \varepsilon\varepsilon_0 A/L$ (representing dielectric contribution of the diode), and two corresponding characteristic times: electron diffusion $\Gamma_g = r_t c_n$ (transit time) and effective lifetime $\Gamma_n = r_{\text{rec}} c_n$, respectively [53, 54]. In typical OPVs, due to special conditions during deposition of Al layer, the nature of the Al/polymer interface plays a key role in the electron and hole transfer. IS can also be used to monitor the effect of the annealing progress.

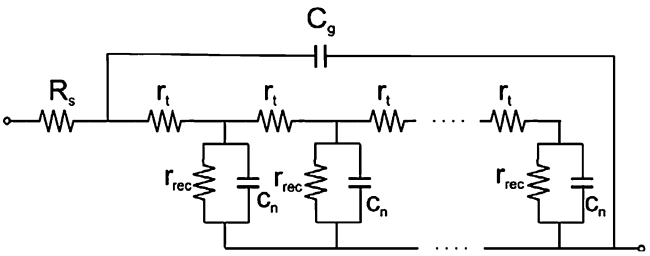

Fig. 6.5 An equivalent circuit accounting for the diffusion–recombination mechanism used for fitting. Modulation of stored excess minority carriers gives rise to distributed chemical capacitance c_n. Bimolecular recombination of conduction band electrons and valence band holes are modeled by resistive elements r_{rec}. Transport of electrons is represented by means of r_t. An additional series resistance is needed to model contact and wire effects, R_s. Finally, a capacitor $C_g \approx \varepsilon\varepsilon_0 A/L$ represents dielectric contribution of the diode [53]. (Reprinted from [53], with permission from Elsevier) (http://www.sciencedirect.com/science/journal/15661199)

There has been a very detailed review on application of IS technique in dye-sensitized solar cells (DSSCs), quantum dot based dye-sensitized solar cells (QD-DSSCs), and OPVs [55]. Fabregat-Santiago et al. speculated the understandings of measured capacitance as a function of voltage and IS spectra [55]. First, they summarized a characteristic measurement as shown in Fig. 6.6a and the subsequent four feature regions that can be distinguished as follows:

(I) at a large reverse bias ($V_{app} \ll V_{fb}$), the sample is considered as a dielectric capacitor with a constant capacitance, giving rise to a geometrical value C_g;
(II) at a moderate reverse and low forward bias ($V_{app} < V_{fb}$), the C–V characteristic is close to a Mott–Schottky model ($C_{sc} = A\varepsilon_r\varepsilon_0/W = A\varepsilon_r\varepsilon_0/W_0V_{sc}^{1/2}$), as shown in Fig. 6.6b, where C_{sc} is determined by the depletion layer modulation.
(III) at a proper forward voltage ($V_{app} \geq V_{fb}$), the capacitance (C_μ) is controlled by a chemical capacitance due to the excess carriers, which results in the collapsed depletion zone.
(IV) at a larger forward bias ($V_{app} \gg V_{fb}$), the capacitance goes saturated and finally decreases exhibiting negative limitation mechanisms.

Secondly, the authors present their interpretation on typical IS spectra, recorded under open-circuit conditions by varying the illumination level and characterized by a major RC arc plus additional minor features at high frequency [55, 56]. Generally, the information of charge transport, series resistance, and dielectric contributions might be reflected by the high-frequency arc of the spectra [53]; on the other hand, the recombination in the active layer will lead to the low-frequency arc of the spectra [57]. The values of the capacitance, resistance, and lifetime can be plotted as a function of V_{oc}.

Glatthaar et al. studied the effect of post-treatment on P3HT:PCBM BHJ OPVs by using IS [58]. The results indicate that a reduced doping level at the Al interface is observed as a depletion region evidenced by the bias dependence of IS (Fig. 6.7), leading to an improved rectification behavior at the organic/metal

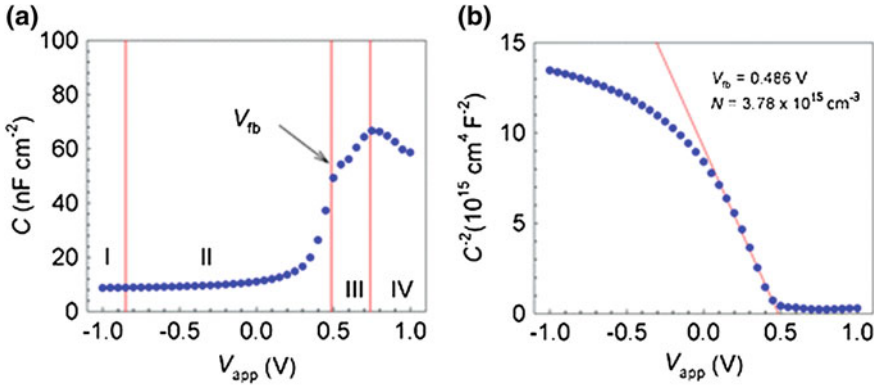

Fig. 6.6 **a** Characteristic capacitance response (100 Hz) of a device (ITO/PEDOT:PSS/P3HT:PCBM/Al), as a function of bias voltage. Vertical lines separate voltage regions for different capacitances. **b** Mott–Schottky curve (100 Hz) which exhibits a straight line from which the values $V_{fb} = 0.49$ V and $N_A = 3.8 \times 10^{15}$ cm^{-3} are determined, assuming $\varepsilon = 3$ for P3HT:PCBM [55]. (Reproduced by permission of the PCCP Owner Societies)

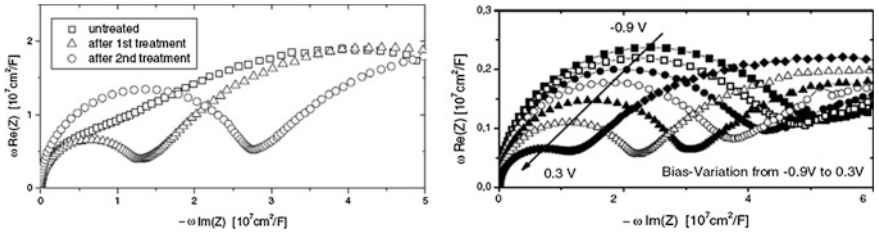

Fig. 6.7 (*left*) IS in the dark of the nontreated device, after the first post-treatment (30 s at 110 °C and 1 V forward bias) and after the second post-treatment (450 s at 110 °C and 2 V forward bias); (*right*) IS after the two consecutive post-treatment steps at different bias voltages [58]. (Copyright John Wiley and Sons. Reproduced with permission)

contacts. The device performance is also likely enhanced by the large space charge region and a positive doping gradient toward the hole contact due to the post-treatment, where charge separation is improved and electron recombination is reduced at the hole contact side due to possible electron transport in PEDOT:PSS layer.

Furthermore, Glatthaar et al. demonstrated that electrical IS can be a useful tool to identify two limiting factors in OPV efficiency by providing information about the conductivity of different regions within the device [59]. One is that the existence of *p*-type impurity doping in organic semiconductor results in a Schottky type contact at the Al interface, decreasing the charge collection efficiency and photocurrent, as there is no electrical field in the bulk region, which facilitates the charge separation. The other one is that a poor interface is permeating charge carriers due to the Al corrosion, leading to low FF. The authors explained that

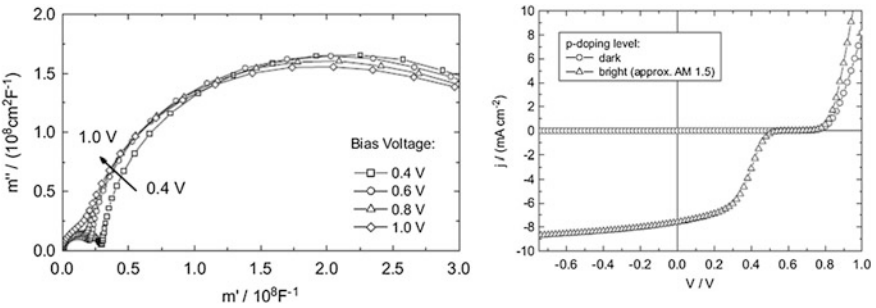

Fig. 6.8 (*left*) Electrical impedance of an inverted layer sequence device, where a TiO_2 layer was added between the electron contact of Ti and the absorber. In the modulus-plot, a semicircle can be observed at high bias, where built-in potential should be compensated and thus, the depletion region being vanished; (*right*) Modeled I–V curve of a device with a low extraction/injection rate for both charge carrier types at the electron contact [59]. (Reprinted from [59], with permission from Elsevier) (http://www.sciencedirect.com/science/journal/09270248)

the kink of *I–V* curve under illumination is caused by a slow charge transfer at the Al/organic interface, evidenced by the large capacitance for low frequencies as shown in Fig. 6.8 (left) due to the accumulated charges injected from the good contact at the blocking contact. Additionally, a one-dimensional model for such *I–V* curves, as shown in Fig. 6.8 (right) was developed by selecting small extraction velocities for the charge transfer at one interface (10^{-4} cm/s instead of 1000 cm/s). Both experiments and simulations are in good agreement.

6.4 Improvement Approaches to Interface Stability

6.4.1 Interface Engineering

In order to improve the interface stability, one effective way is to introduce a stable interfacial layer in between electrodes and organic photoactive layer. On the one hand, an air-stable *n*-type metal oxide can be inserted between active layer and Al cathode to replace the commonly used Ca or other LWF metals. On the other hand, at the anode side, an alternative to current PEDOT:PSS is *p*-type-like or transition metal oxides as the interfacial layer.

6.4.1.1 Cathode Buffer Layer

Wang et al. presented an extended lifetime of P3HT:PCBM-based BHJ OPVs by inserting a thin layer of CuO_x in between active layer and Al cathode, which was fabricated by thermal evaporation [60]. Figure 6.9 shows the comparison of various parameters as a function of storage time for the OPVs with the interfacial

layer of LiF, CuO_x, CuO_x/LiF, LiF/CuO_x. The device degradation is strongly dependent on the decrease of the photocurrent during the storage time. The results indicate that the CuO_x functions not only as a charge transport layer but also as a protection layer, preventing the formation of thick organic/Al interdiffusion area. Thus, an air-stable cathode/organic interface is achieved. Wang et al. also found chromium oxide (CrO_x) as Al cathode interfacial layer to improve the efficiency and stability in air since the device stability of OPVs depends on the cathode interfacial layers [61]. Devices with CrO_x exhibit higher PCEs and stability than those without CrO_x, showing improved stability 100 times better than those of devices without CrO_x or with LiF. It is likely attributed to the function of CrO_x as an electronic tunneling layer for electron collection and a protective layer for minimizing the damages caused by evaporating Al and also blocking diffusion of oxygen and water.

Insertion of an interfacial layer such as CrO_x and CuO_x is to effectively prevent diffusion of Al into the organic layer and thus to eliminate formation of the insulating layer that makes the device degrade. It is noted that diffusion of Cu atoms into the organic layer may also occur. However, the oxidation of Cu leads to

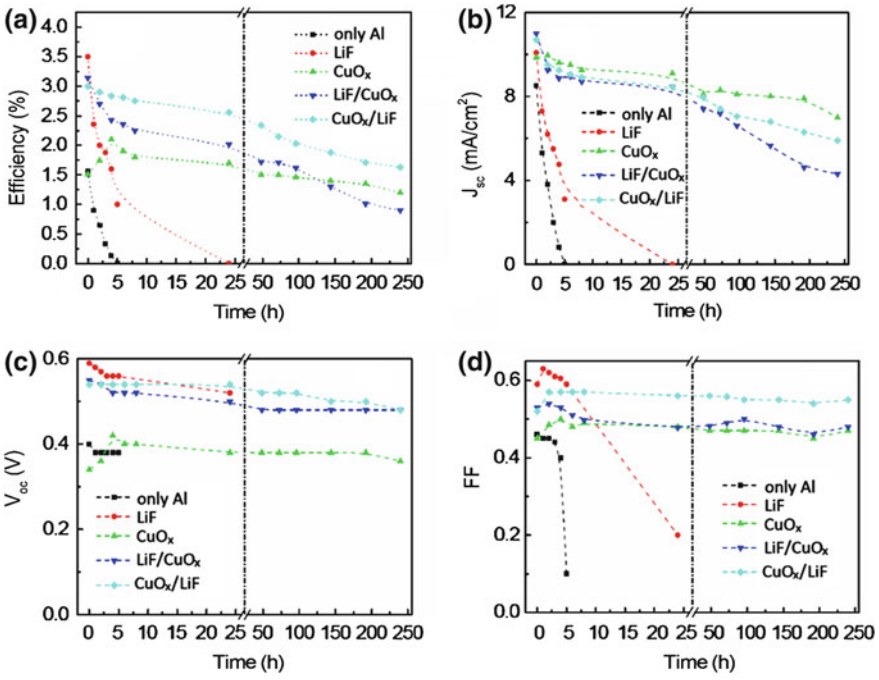

Fig. 6.9 Comparison of the **a** PCE, **b** (J_{sc}), **c** (V_{oc}), and **d** FF as a function of storage time for polymer solar cells without interfacial layer (only Al), with interfacial layer of LiF, CuO_x, CuO_x/LiF, LiF/CuO_x. Note that the device characteristics are monitored with increasing storage time for the same device [60]. (Reprinted with permission from Ref. [60]. Copyright [2011], American Institute of Physics)

a less insulating material as compared to Al_2O_3, likely explaining the slow degradation of the devices in air [60, 61].

Kim et al. produced a TiO_x layer by sol–gel procedure to modify the interface of P3HT:PCBM and Al cathode [62]. This TiO_x layer plays multiple functions as electron-transporting layer, hole- and exciton-blocking layer, optical spacer, and protecting layer during metal deposition. TiO_x layer serves to passivate the devices against intrusion of water vapor and oxygen, leading to remarkable enhancement of operation lifetimes [63, 64]. Moreover, the mechanism is proposed to be ascribed to oxygen deficiencies in the TiO_x film allowing adsorption sites for O_2 [62, 65]. Lee et al. investigated the correlation between TiO_x layer as optical spacer and the processing additive 1,8-octanedithiol [66]. The results indicate that the processing additive causes relatively rough surface of P3HT:PC_{60}BM film and reduces the effect as an optical spacer. Therefore, the dependence of processing additive on surface roughness also influences the interface stability.

Li et al. reported a study of the stability of OPV under air and UV irradiation, which consists of P3HT:PCBM as the active layer and 20 nm TiO_x as the protection layer prepared by partial hydrolysis of Ti-alkoxide in air [35], as shown in Fig. 6.10. It is stated that TiO_x as the protection layer could make significant improvement of device stability under air and UV exposure, implying a faster decay due to UV exposure compared to air.

Figure 6.11 shows the dependence of main parameters of OPVs on UV exposure time. It is clearly seen that the major loss in device efficiency under UV irradiation is induced by the decrease in the J_{sc} and the FF. Meanwhile, the V_{oc} remains essentially constant. Similar results happen to the air-exposure conditions. The measurements by transmission IR, UV spectroscopy, and ERS spectroscopy, indicate that the sol–gel derived TiO_x serves as an effective passivation film to prevent oxygen when exposed to light due to the photo-oxidation of the bound organic moieties causing oxygen gas scavenging [35]. The improvement mechanism behind by using TiO_x can be explained as [35]: the photochemical activity of a TiO_x film covers both Ti–OR functionalities and Ti–OH groups. From the results of IR spectroscopy, it is found that the residual Ti–OR functionalities bound into the sol–gel film are photo-oxidized, consuming O_2 (gas) and producing CO_2 (gas)

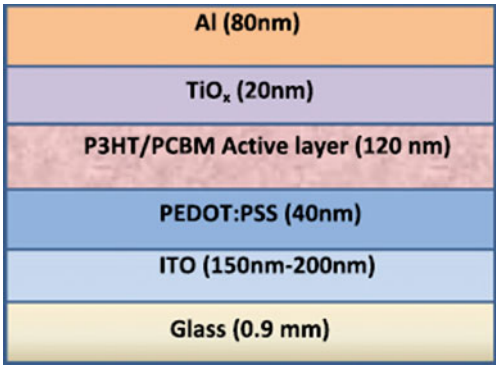

Fig. 6.10 OPV device structure [35]. (Reprinted from [35], with permission from Elsevier) (http://www.sciencedirect.com/science/journal/09270248)

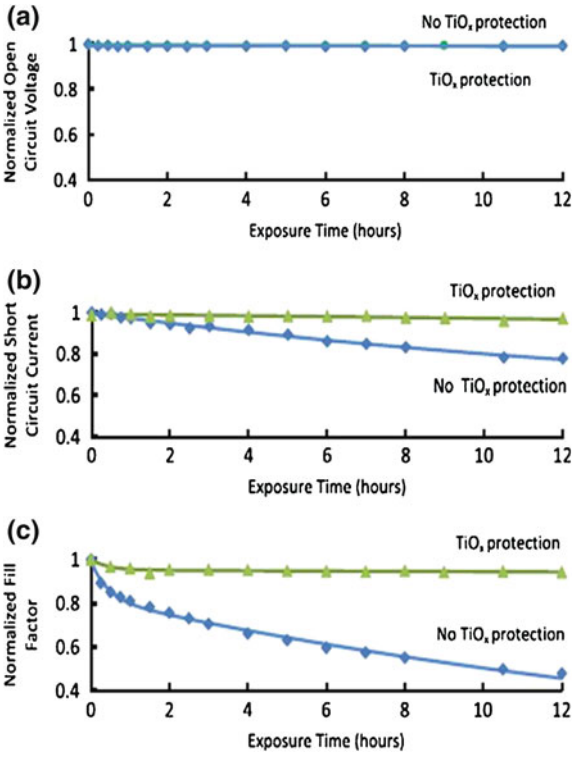

Fig. 6.11 Variance of **a** Voc, **b** Jsc, **c** FF with UV exposure time when sample was surrounded by nitrogen atmosphere (UV power density = 10 mW/cm2) [35]. (Reprinted from [35], with permission from Elsevier) (http://www.sciencedirect.com/science/journal/09270248)

and H_2O (gas), as well as bound format [HCOO–], H_2O, and Ti–OH moieties. The photoactivation of these films leads to O_2 scavenging and forms the basis for thin films, which removes oxygen upon exposed to light, thereby protecting an underlying surface from oxygen gas.

It is worth mentioning that the TiO_x film has a capacity of the order of 10^4–10^5 times the quantity of O_2 needed to seriously influence the organic active layer. Additionally, the TiO_x film will act as a diffusion barrier for oxygen, thus further slowing down the oxygen interaction with the active layer.

6.4.1.2 Anode Buffer Layer

Carter et al. shown polyaniline and polyethylenedioxythiophene based polymer transparent electrodes as hole-injecting anodes by replacing ITO in polymer OLEDs [25]. By varying the dopants of anodes, improved device performance was found independent of film conductivity, morphology, and type of conducting polymer. The results demonstrated that polymer anodes (1) create a clean repeatable surface without oxidation or water, facilitating the adhesion to polymer MEH–PPV; (2) partially dope the interface, forming Ohmic contacts and good

hole injection into electroluminescent polymer. These devices without ITO show a remarkably slower degradation.

Since PEDOT:PSS is a water-based solution with slight acidic nature, it is easy to cause interface instability associated with the etching of ITO and the diffusion to photoactive layer upon water adsorption. *p*-type like or transition metal oxides, such as MoO_3, V_2O_5, and WO_3, are becoming the most promising replacement of PEDOT:PSS as anode buffer layer to overcome the interface instability. Shrotriya et al. demonstrated transition metal oxides MoO_3 and V_2O_5 to replace PEDOT:PSS, forming Ohmic contact between active layer and ITO and improving device efficiency [67]. Recently, many investigations have involved transition metal oxides to enhance the hole transport/collection and extend the lifetime of device operation [68–71].

Sun et al. combined both benefits of anode and cathode interfacial layers MoO_x and TiO_x to obtain efficient and air-stable BHJ OPVs based on PCDTBT:PC_{70}BM [72], as shown in Fig. 6.12 (left). Figure 6.12 (right) shows the comparison of the air stability of PCDTBT:PC_{70}BM devices fabricated with a 9 nm MoO_x and PEDOT:PSS as a function of storage time in air under ambient conditions. The MoO_x based BHJ solar cells without encapsulation exhibit better air stability than PEDOT:PSS based ones. MoO_x based devices retain about 50 % of its original PCE after storage in air for 720 h, on the contrary, PEDOT:PSS based devices keep about 10 % of its original PCE after storage in air for 480 h, indicating that the former ones (MoO_x) have a slower degradation than the latter ones (PEDOT:PSS). The improvement of device stability is explained by the hygroscopic and acidic PSS, a source of interface instability due to the diffusion of PSS to other layers and reaction with other components. The replacement of PEDOT:PSS with MoO_x overcomes interface instability and yields significant improvement in air stability.

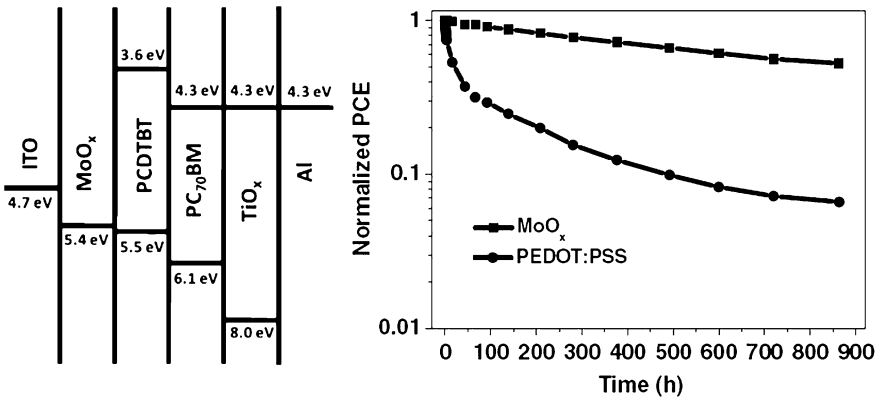

Fig. 6.12 (*left*) The device structure; (*right*) Normalized PCEs as a function of storage time for PCDTBT:PC_{70}BM solar cells fabricated with PEDOT:PSS and MoO_x in air under ambient conditions (no encapsulation) [72]. (Copyright John Wiley and Sons. Reproduced with permission)

6.4.2 Device Structures

6.4.2.1 Normal Structure

In normal structure, interface engineering can be concluded to improve the interface stability as discussed in Sect. 6.4.1.

6.4.2.2 Inverted Structure

A typical normal structure of OPV device is ITO/PEDOT:PSS/photoactive layer/LWF metal. LWF metal as cathode is a primary limit to the interface stability of devices since LWF metals (Li, Ca, and Al) are prone to be oxidized, resulting in the increase of series resistance at the organic/electrode interface and degrading device performance. In addition, oxygen preferably diffuses into the photoactive layer through pinholes and grain boundaries through the cathode, degrading the active layer and making the device instable in air [4]. On the other hand, the ITO/PEDOT:PSS interface is also instable due to likely indium diffusion into the photoactive layer and the ITO etching by acidic PEDOT:PSS adsorbing water [6, 51]. The reaction between PSS and water induces a faster degradation of the ITO/PEDOT:PSS interface [6].

To overcome the instability issue in normal structure device, one feasible approach is to construct an inverted configuration [73], where ITO serves as the cathode and a high work-function (HWF) metal as the anode, as shown in Fig. 6.13. It should be pointed out that only modified ITO can serve as the cathode for electron extraction. The functional layers for modifying ITO mainly focus on metal oxides such as TiO_2 [74] and ZnO [75, 76], and alkali-metal compound like

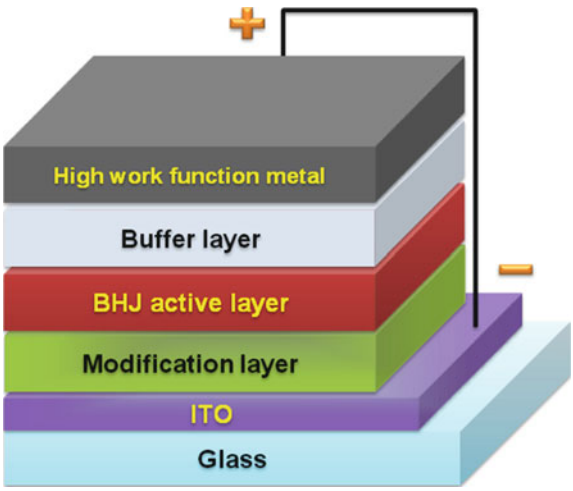

Fig. 6.13 A typical inverted device structure

Cs_2CO_3 [77, 78]. Large-area inverted devices with ZnO can also be realized by roll-to-roll processing of each layer [21, 79–81].

In principal, the inverted structure offers higher air stability than the normal one due to relatively stable HWF metal as top anode. Sahin et al. demonstrated a more air-stable inverted device with a structure of ITO/Perylene/MEH-PPV:PCBM/CuPc/Au than a normal device [82]. The inverted device shows a PCE of 0.14 % under 74.5 mW/cm^2 illumination in the first day. Although oxygen and humidity are present, the PCE is decreased by 27 % of the initial value after 2 weeks. On the contrary, the normal device with LiF/Al as top cathode has a PCE of 1.3 % under 100 mW/cm^2 illumination; however, the efficiency decreases by 91 % after only 1 day during storage in oxygen and diminishes thoroughly after a few days in air.

Hau et al. conducted the air-stability study of inverted devices employing ZnO nanoparticles (NP) as an electron-transporting layer and PEDOT:PSS/Ag as a hole-transporting layer and top anode [83]. The shelf lifetime is defined as the time when the PCE drops to half of its initial value. Figure 6.14a shows the *J–V* curves of a normal device of ITO/PEDOT:PSS/P3HT:PCBM/LiF/Al over variable periods from 0 to 4 days. The results show that the shelf lifetime is only 1 day, and a complete degradation is followed after 4 days. A large reduction of dark current at 2 V is observed after 4 days, as shown in the inset of Fig. 6.14a, suggesting the increased series resistance to be part of the degradation mechanism. On the other hand, the inverted device with a structure of ITO/ZnO NP/P3HT:PCBM/PEDOT:PSS/Ag without encapsulation exhibits a relatively stable performance despite being kept in air for a long time. A 20 % decrease of PCE is shown in Fig. 6.14b after 40 days. It is interesting that the decrease of dark current after a long-time storage does not occur.

Similarly, Liu et al. reported the stability improvement of inverted small-molecule OPVs with a structure of ITO/ZnO/CuPc:C_{60}/CuPc/PEDOT:PSS/Ag [84]. The authors compare two measurements for device stability: one is to test

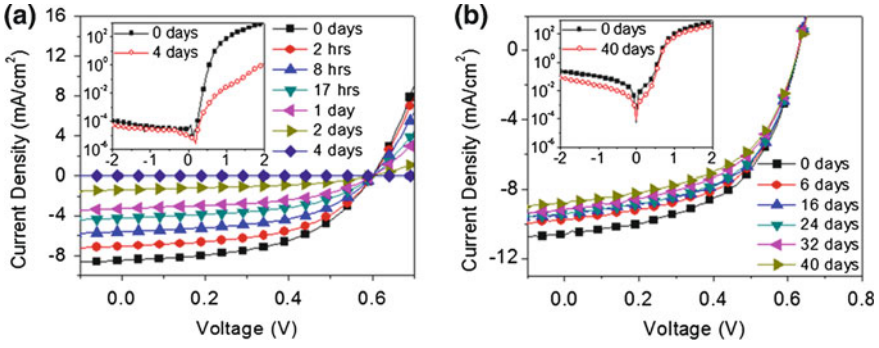

Fig. 6.14 *J–V* characteristics of unencapsulated **a** normal device over a period of 4 days and **b** inverted device over a period of 40 days in air under ambient conditions. Inset: dark *J–V* characteristics of the respective devices [83]. (Reprinted with permission from Ref. [83]. Copyright [2008], American Institute of Physics)

shelf lifetime (devices are kept in the dark), which is 912 h for inverted devices and 256 h for normal ones; meanwhile the other one is that the devices are kept under 100 mW/cm^2, exhibiting a negligible degradation for inverted devices and a faster degradation for normal devices due to continuous illumination. The stability tests imply that the degradation rate for inverted devices is slower than that for normal devices.

Such stability improvement could also be achieved by using TiO_x as the modification layer for ITO. Kuwabara et al. compared the stability of P3HT:PCBM-based inverted and normal devices with a structure of ITO/TiO_x/P3HT:PCBM/PEDOT:PSS/Au and ITO/PEDOT:PSS/P3HT:PCBM/Al, respectively. The devices were measured in ambient atmosphere under 100 mW/cm^2 [85]. As shown in Fig. 6.15, the PCE of the normal device drops to 50 % of its initial value after continuous illumination for 10 h, and the inverted device without encapsulation keeps its initial efficiency for 20 h under continuous illumination, indicating good stability either in ambient environment or under continuous illumination for inverted devices.

As an alternative, modifying ITO by a LWF metal would be an effective and simple approach to lower the work function of ITO. On the other hand, the contact between anode and active layer should be significantly improved by a buffer layer such as PEDOT:PSS [86], V_2O_5 [67, 73], and WO_3 [87] in order to reduce the exciton quenching and then increase the charge collection efficiency. Except for the roles of hole transport and extraction, such an anode buffer layer also acts as an optical spacer, adjusting the effective optical field distribution [88]. More importantly, the interface stability could be enhanced due to the prevention of oxygen and moisture from diffusing to active layer by using transition metal oxides (MoO_3 and V_2O_5).

Zimmermann et al. [89] systematically investigated the long-term stability of P3HT:PCBM-based OPVs with an inverted structure, as shown in Fig. 6.16, where

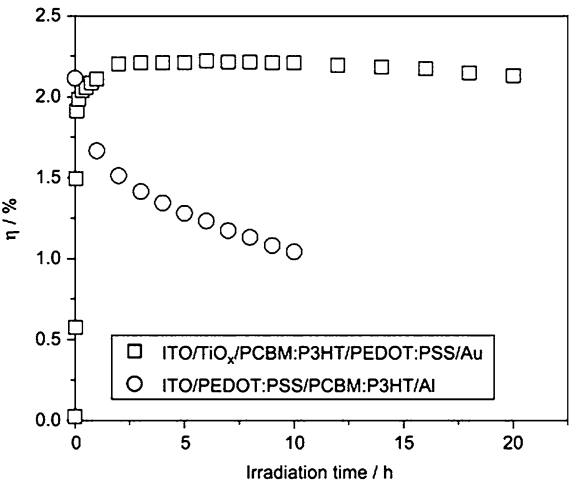

Fig. 6.15 The variation in η (PCE) of inverted device (ITO/TiOx/P3HT:PCBM/PEDOT:PSS/Au) and conventional device (ITO/PEDOT:PSS/P3HT:PCBM/LiF/Al) with irradiation time [85]. (Reprinted from [85], with permission from Elsevier) (http://www.sciencedirect.com/science/journal/09270248)

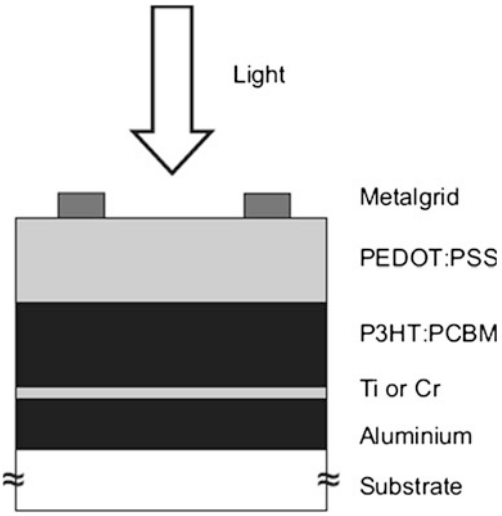

Fig. 6.16 Schematic structure of the inverted device. The first layer deposited on the substrate is the metallic electron contact, followed by the P3HT:PCBM blend and the PEDOT:PSS hole contact. The current is collected by a metal grid [89]. (Reprinted from [89], with permission from Elsevier) (http://www.sciencedirect.com/science/journal/09270248)

the devices consist of two different electron contact materials, titanium (Ti) and chromium (Cr), and two different thicknesses of P3HT:PCBM layers. In order to get the information of chemical composition distribution at the interface of active layer and metallic electron contact, Auger electron spectroscopy (AES) has been employed to show that electron contact is partially oxidized during the fabrication of inverted devices. It is concluded that oxygen is chemically bound at the organic/metal interface as well for Ti as for Cr as a contact layer. Moreover, both electrode material and active layer thickness have influences on the long-term stability of P3HT:PCBM BHJ inverted OPVs, and their results indicate that the devices with Cr as electrode are much more stable than those with Ti as electrode and a thinner active layer also has a positive effect. Two possibilities are to explain the effect of the layer thickness: one is that lower photocurrent caused by thinner active layers induces lower voltage drop due to the increase in series resistance caused by the decreased conductivity of PEDOT:PSS during aging [89, 90]; the other one is that defects in active layer affect and reduce the FF, especially for thick layers [89, 91]. After 1500 h of continuous illumination under a sulfur plasma lamp (100 mW/cm^2) at 50 °C, the most stable devices maintain 90 of their initial efficiency of more than 2.5 %. The results indicate that inverted structure is beneficial to the device stability.

We have presented inverted OPVs with LWF metals as interfacial layer modifying ITO as cathode [92–94]. First, we have investigated the impact of an ultrathin Ca deposited by thermal evaporation in inverted cell using a structure of ITO/Ca/P3HT:PCBM/MoO_3/Ag (Fig. 6.17 (left)) [94]. With the use of Ca lowering the work function of ITO and MoO_3 modifying the Ag anode, the efficiency of inverted devices is significantly improved compared with those without either of these two interfacial layers. Since Ca modifying the ITO is easily oxidized, we fabricated a CaO modified ITO on purpose to check if the corresponding device

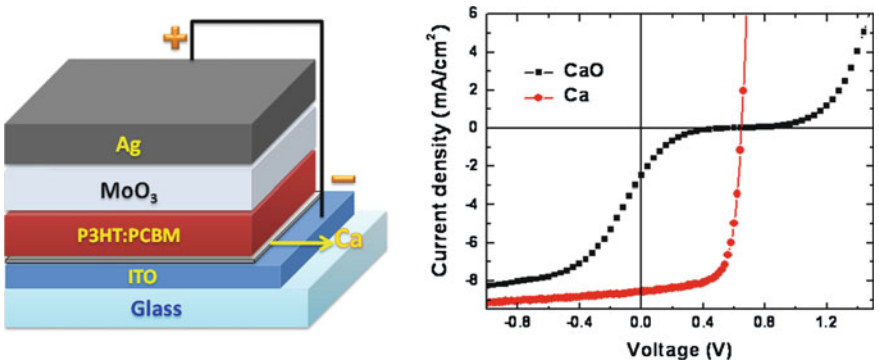

Fig. 6.17 (*left*) Device structure of an inverted OPV; (*right*) I–V characteristics of the devices with CaO and Ca as the electron-transporting layers under 100 mW/cm^2 illumination [92]. (Reprinted from [92], with permission from Elsevier) (http://www.sciencedirect.com/science/journal/09270248)

can still work properly. The CaO layer was obtained by purposely oxidizing the Ca deposited (expose the Ca to dry air). All the other layers are exactly the same. Figure 6.17 (right) shows the comparison of the *I–V* characteristics of two devices with the structures of ITO/Ca/P3HT:PCBM/MoO_3/Ag and ITO/CaO/P3HT:PCBM/MoO_3/Ag under 100 mW/cm^2. It is obvious that the device with CaO exhibits rather poor performance compared to that with Ca. In this way, we can indirectly confirm that Ca is not oxidized (at least not fully oxidized). Therefore, it can be concluded that the Ca still primarily remains in its metallic state.

Moreover, we have compared the effect of various metals (Ca, Mg, Al, and Ag) on electron collection. The results indicate that Ca and Mg give comparable photovoltaic effect. By comparison of inverted and normal devices, the improvement of the efficiency for inverted devices is explained by the possible origin from the favored vertical composition gradient of the P3HT:PCBM layer for the inverted device. It was reported that the active layer of P3HT:PCBM fabricated by spin-coating and post-annealing process usually has a composition with a higher PCBM (electron acceptor) content close to the substrate and a higher P3HT (electron donor) content close to the free (air) surface [73, 95]. This vertical composition gradient has an adverse effect on the photovoltaic performance of a normal forward device using glass/ITO/PEDOT:PSS as the bottom anode. However, this composition gradient is favorable to our inverted device because a P3HT-rich donor phase on the hole collecting side (MoO_3/Au) and a PCBM-rich acceptor phase on the electron collecting side (ITO/Ca) would reduce the charge recombination at the electrodes [96]. In addition, the possible metal penetration or damage to the active layer, caused by the deposition of the top metal contact [97], can be prevented in the inverted structure due to the protection of MoO_3 layer.

It is worth mentioning that all devices were not encapsulated for the measurement of air stability. The air stability of the inverted device is significantly

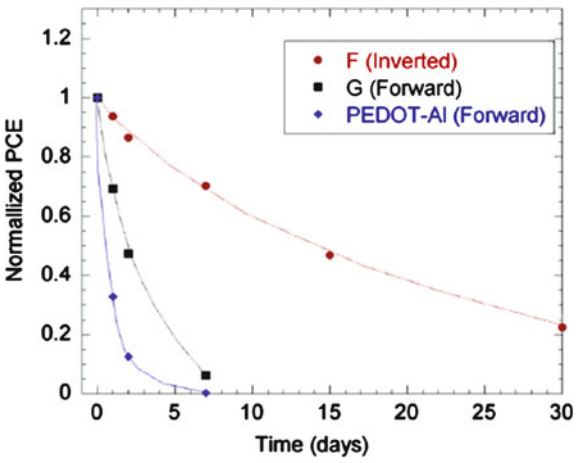

Fig. 6.18 Air-stability of the inverted and forward cells [93]. (Reprinted from [93], with permission from Elsevier) (http://www.sciencedirect.com/science/journal/09270248)

improved as compared with that of the normal device [93]. Figure 6.18 shows the change in the normalized PCE against the air-exposure time for inverted and normal OPVs. It is observed clearly that the shelf lifetime of the inverted device F is ~15 days, however the shelf lifetime of the normal cell G is only ~2 days. The explanation for the improvement of air stability for the inverted cell can be as follows. In the normal device G (ITO/MoO_3(10 nm)/P3HT:PCBM/Ca(10 nm)/Ag), the LWF metal (Ca) cathode on top of the active layer would easily react with the water and oxygen in air although a layer of Ag is deposited on top of the Ca layer. On the contrary, in the inverted device F (ITO/Ca(1 nm)/P3HT:PCBM/MoO_3(10 nm)/Au), air-stable Au is used as the top anode, however the reactive Ca incorporated between ITO and P3HT:PCBM layer has been prevented from its direct contact with air, resulting in the improvement of air stability. Figure 6.18 also shows the degradation of a normal PEDOT-Al device (ITO/PEDOT/P3HT:PCBM/Al) with time for comparison, which presents the poorest air stability with a short shelf lifetime of ~0.5 day. The rapid degradation of the PEDOT-Al cell can be ascribed to the degradations of both organic/Al and ITO/PEDOT interfaces [28, 98]. Therefore, the results reveal that LWF metals are also suitable to be adopted as electron selective interfacial layer for inverted cell and good for stability improvement.

6.4.3 Device Encapsulation

As discussed before, OLEDs suffer from different modes of degradations as (i) dark-spot degradation, (ii) catastrophic failure, and (iii) intrinsic degradation. The first two modes of degradation could be effectively controlled by means of proper device encapsulation and adequate control over device fabrication conditions; meanwhile, the intrinsic degradation mode has been far more challenging and continues to be an issue for OLED commercialization [20, 31, 32].

In OPV devices, PPV and its derivatives have been used, however, these polymers based devices exhibit low stability under illumination in air. Hence, an alternative is to use the polythiophenes, such as P3HT, which has given a PCE of 5 % or higher [99–101]. At the same time, the lifetime is reported in the range of 1000 h [102]. Very long-lifetime devices based on P3HT have also been presented with accelerated lifetime testing for 4000 h or even more than 1 year [103, 104]. It is thought that accelerated testing for 1 year corresponds to an operational lifetime of 3–10 years [37, 104].

Such a long lifetime would bring the technology into an expectation that this should be commercialized in the near future. However, one of the significant concerns or big challenges about commercialization is the stable encapsulation scheme for OPV devices. It is known that OPVs exhibit a rather poor property of air stability due to the chemical and physical and even mechanical degradations, primarily resulting from the oxygen and moisture in the atmosphere. Except for the stability improvements in essential materials and device structures, it is necessary and important to develop the technology and approaches of the device encapsulation benefiting to the long lifetime of OPV operation. Therefore, adequate encapsulation from ambient oxygen and water is an essential requirement for the commercial viability of OPV cells. The encapsulating layer in turn should be thin, defect-free, light weight, and offer ease of processing [105].

In this section, we will discuss a few methods on encapsulation techniques and their effect on the device stability.

Krebs et al. presented P3HT:PCBM-based device with an operational stability for more than a year after an efficient and proper method for the encapsulation, exhibiting a decrease in the efficiency to 65 % compared to the initial value [104]. This method follows the process of (1) device preparation on glass substrates; (2) sealing by using glass fiber reinforced thermosetting epoxy against a back plate. Such an encapsulation makes it possible to transport oxygen and moisture sensitive OPV devices outside a glove box. The author emphasized that once the substrates, backplate, prepreg, and jig are available in laboratory, this fast and simple sealing procedure requires only 10 min of work besides the thermosetting time of 12 h.

Atomic layer deposition (ALD) is a chemical vapor deposition technique involving the cycling of alternate precursor gasses into a chamber to react on the surface of samples and grow high-quality and conformal films [106, 107]. Ultrathin barrier layers have become promising candidates for device encapsulation [105, 107, 108], which are deposited by ALD at low temperature, particularly suitable for organic and flexible electronics as passivation layers with excellent film conformity [105].

Chang et al. presented a thin-film encapsulation of Al_2O_3/HfO_2 for OPVs by using ALD [108], in which 26 nm Al_2O_3/HfO_2 nanolaminated films consist of 52 pairs of alternating 2 Al_2O_3 and 3 HfO_2 layers, and the deposition temperature is 140 or 150 °C, and the chamber pressure is 0.1 Torr. Encapsulating the devices with ALD films brings three problems of ALD films: (1) poor nucleation on the surface of P3HT:PCBM layer exposed at the device edges, resulting in incomplete coverage of the ALD films (Fig. 6.19b); (2) rapid hydrolysis in air, causing the

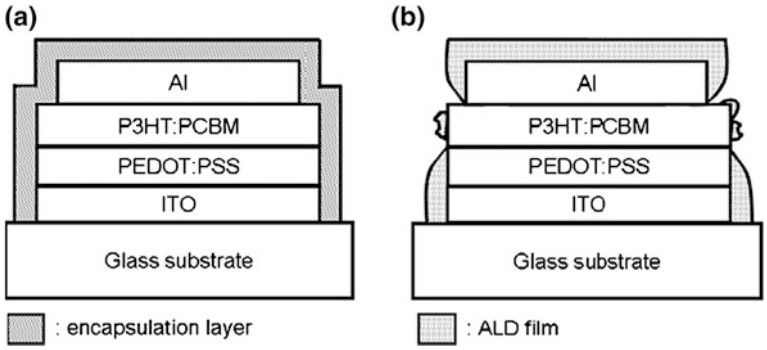

Fig. 6.19 Schematics of the cross-section of the PV devices: **a** Encapsulated by a barrier film with complete coverage over all device surface and **b** Encapsulated by a barrier film that has poor surface coverage over the P3HT/PCBM layer [108]. (Reprinted from [108], with permission from Elsevier) (http://www.sciencedirect.com/science/journal/15661199)

encapsulating films to disintegrate as the devices aged; (3) susceptibility to mechanical damages during device characterization and handling. The Al_2O_3/HfO_2 nanolaminated structure can overcome the issue of hydrolysis-induced aging for only Al_2O_3 films, owing to the hydrophobicity of the HfO_2 layers. However, a UV-curable epoxy resin film as a capping layer is required for the Al_2O_3/HfO_2 encapsulation of the devices in order to reach the control of the degradation profile. The aims to use this capping layer are (1) to reduce the accidental damages during characterization and handling due to its thin thickness and also to enhance the mechanical protection; (2) to diminish the small defects in the ALD film due to the hydrophobicity of the P3HT:PCBM surface. This technique can prevent device degradation induced by ambient atmosphere and also play a role in annealing step beneficial to the increase of the initial efficiency. Figure 6.19 shows the comparison of two devices encapsulated by a barrier film with complete coverage over all device surface and poor coverage over the P3HT:PCBM layer, indicating the importance of complete coverage surface for stability improvement. When the ALD temperature is fixed at 140 °C and the deposition time is 1 h, the devices achieve a PCE of 3.66 % due to optimal annealing during encapsulation.

As shown in Fig. 6.20, Potscavage et al. developed a 200 nm Al_2O_3 barrier layer grown by ALD as the encapsulation layer in pentacene/C_{60} based small-molecule OPVs [107]. The encapsulated device maintains a stable efficiency when exposed to ambient atmosphere for over 6000 h, much longer than those without encapsulation having a fast degradation upon exposure to air for 10 h. Moreover, the thermal annealing during ALD deposition improves the V_{oc} and then the overall PCE of the devices.

Figure 6.21 compares the change of main parameters of OPVs with various encapsulations from the initial values after exposure to ambient atmosphere, i.e., no encapsulation, UV epoxy, Al_2O_3, and Al_2O_3/UV epoxy. The device with no encapsulation degrades very fast, whose J_{sc} drops to <20 % of its initial value.

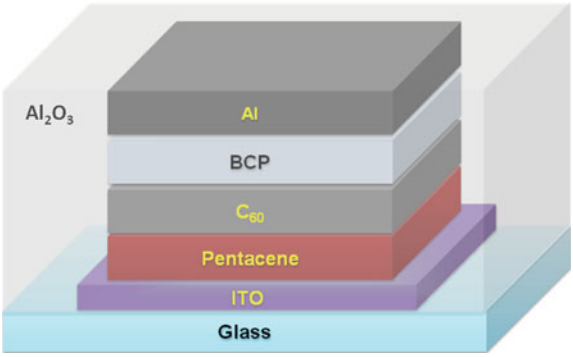

Fig. 6.20 Schematic of device structure [107]

The device encapsulated with only UV epoxy degrades by a slower rate, whose performance decreases to 50 % of the initial value after 100 h and to 25 % after almost 250 h upon exposure to ambient atmosphere due to a short-term protection of epoxy. The devices with Al_2O_3 by ALD and with or without UV epoxy layer have PCE and J_{sc} within 6 % of their initial values after 6,145 h of exposure to ambient atmosphere.

Moreover, Sarkar et al. did not use the UV-curable epoxy and developed improved ultrathin Al_2O_3 layers, grown by using ALD, as primary barrier layers for encapsulation of OPV devices [105], as shown in Fig. 6.22. The encapsulation characteristics of this barrier layer can be improved by replacing H_2O with O_3 as the ALD oxidant, exhibiting superior device encapsulation to the barrier layer grown by using H_2O. This Al_2O_3 barrier layer was done without any additional UV-curable epoxy resin film as a sealant for protecting the devices from ambient moisture and oxygen. Through optimization, the optimal thickness of Al_2O_3 is 18 nm to function well, and thus 210 cycles of O_3–Al_2O_3 give the best device encapsulation exhibiting 80 % of its initial efficiency over a period of 500 h. The authors have compared two different ALD temperatures functioning as an annealing step beneficial to the formation of phase separation in the active layer.

Additionally, Luo et al. presented a thin layer of MnO inserted in between photoactive layer and metal cathode to improve the device efficiency and air stability [109]. The results indicate that MnO can serve as electron-transporting layer and protection layer from damages caused by moisture and oxygen. The OPV device with 3 nm MnO layer retains a PCE of 28.42 % of its initial value after 2 weeks while the device without MnO layer has only 6.03 % of initial PCE just after 2 days without encapsulation. It is promising to use such a MnO layer to enhance both device efficiency and operation stability.

The most common technique to obtain an ultra-high barrier layer is to use alternating organic–inorganic multilayer, i.e., inserting inorganic barriers between polymer buffers to reduce the number of pinholes [110], resulting in smoothly coated surface, decreased mechanical damage, and increased thermal stability [18]. On the other hand, stacked structure is produced by repeating the alternating process, allowing organic layers to “decouple” the defects from neighboring inorganic layers. Madakasira et al. reported the conformal deposition of parylene

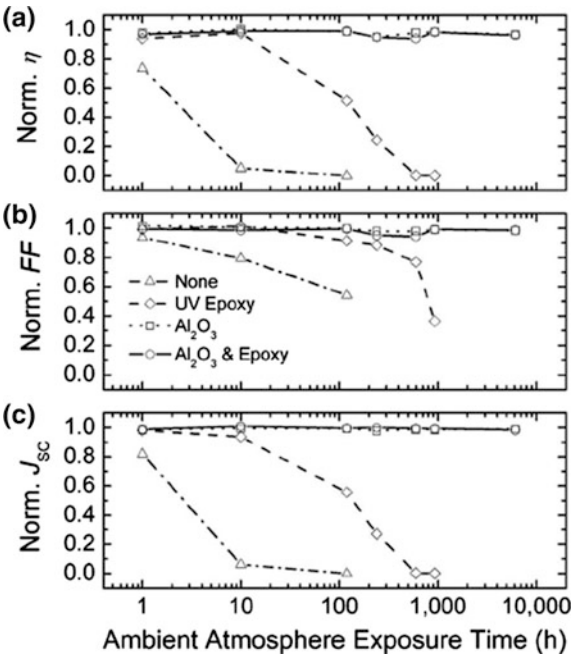

Fig. 6.21 Relative change in **a** η, **b** FF, and **c** J_{sc} of solar cells with various types of encapsulation from the initial values after exposure to ambient atmosphere. Four devices are shown with the following types of encapsulation: no encapsulation (dash-dotted line, *triangle*); UV epoxy (*dashed line*, *diamond*); Al_2O_3 (*dotted line*, *square*); and Al_2O_3 and UV epoxy (*solid line*, *circle*). The values for each device are normalized to the initial value for that device [107]. (Reprinted with permission from Ref. [107]. Copyright [2007], American Institute of Physics)

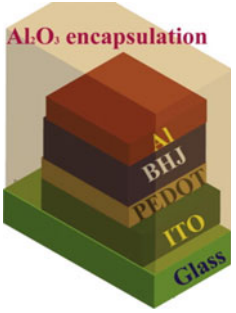

Fig. 6.22 Schematics of the device structure encapsulated with Al_2O_3. BHJ is P3HT:PCBM [105]. (Reprinted from [105], with permission from Elsevier) (http://www.sciencedirect.com/science/journal/15661199)

on polymer OPVs [111]. The results show that single parylene coating layer is not efficient to protect the degradation of P3HT:PCBM-based devices due to its photochemical reactions caused by oxygen. More importantly, the authors develop multilayer barriers consisting of parylene and Al_2O_3 to implement the full protection of the devices from degrading even under illumination.

It is promising that Dennler et al. firstly studied the shelf lifetime of MDMO-PPV:PCBM-based OPVs encapsulated by flexible and transparent ultra-high barrier poly(ethylene naphthalate) (PEN) grown by plasma enhanced chemical vapor deposition (PECVD) [19]. Figure 6.23 shows the cross-sectional view of OPV device and a photo of a bent device. Such an encapsulation could improve the shelf lifetime of OPV device with 30×57 mm^2 from a few hours to the range beyond 3000 h.

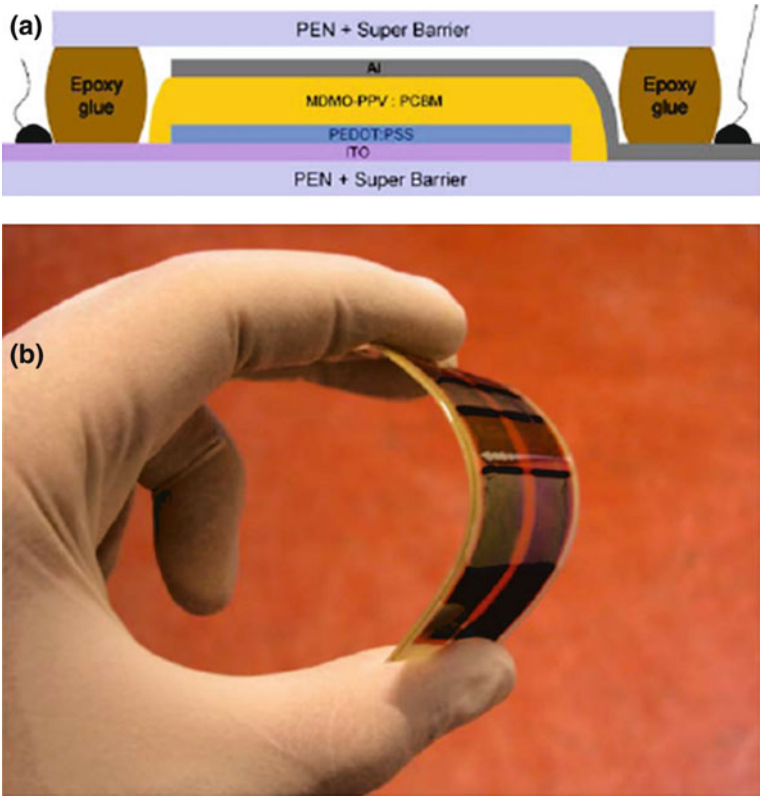

Fig. 6.23 **a** Cross-sectional view of the OPV device; **b** Picture of a bent device [19]. (Reprinted from [19], with permission from Elsevier) (http://www.sciencedirect.com/science/journal/00406090)

6.5 Conclusion and Outlook

6.5.1 Conclusion

With the rapid progress predominantly in the achievements of material science, the efficiency of OPVs has boosted significantly to the aim of industrial products. Low cost and long lifetime are also initially required by the market.

The degradation mechanisms of interface stability in OPVs have been presented, which are closely correlated with electrodes materials and interfacial layers modifying the electrode/organic interface due to the diffusion of oxygen and water into these layers and also their intrinsic properties.

In order to well understand the mechanisms, highly effective characterization techniques are of great significance to monitor and analyze the origins of interface instability and the degree of their influence. These characterization techniques, in

view of optical and electrical properties, provide various information of the changes of electronic/chemical structure, energy level, and energy/charge transfer at the interface.

All efforts on analyzing interface degradation mechanism and exploiting characterization techniques are serving as pathways toward further optimization and improvement of interface stability and device stability, such as essential materials used, device design and structure, and encapsulation, significantly crucial for the technological applications.

6.5.2 Outlook

If organic semiconducting and metallic materials and device design were further developed, it is much promising that efficiencies of 10 would be obtained in a relatively short term since 8 % efficiency has already been achieved by many companies so far. The future of renewable and green OPV technology turns out to be bright.

Another important factor is economical, i.e., to address the balance of product cost, which demands the progress of technology such as new electrodes' alternative to current ITO and metals, cost-reduced synthesis process of photoactive materials, low-cost encapsulation against oxygen and moisture diffusion, and fabrication process of flexible cells and flexible integrated power supply.

The last requirement for commercial technology of OPVs is lifetime or stability. High sensitivity to moisture, oxygen, UV light, and temperature results in serious degradations of organic materials and entire devices. In order to diminish the instability and extend the device lifetime, deep understanding and investigation on degradation of each component and interface via chemical and physical ways are necessary, followed by improvement techniques. Therefore, study of degradation is suggested as follows:

6.5.2.1 Electrodes

ITO as highly conductive and transparent anode faces problems of lack of indium reserves in nature and damage of indium to organic layer via diffusion. PEDOT:PSS as anode buffer layer exhibits slight acid property after adsorbing water, leading to the etched ITO. Thus, an alternative to ITO is gallium doped ZnO (GZO) which has a proper work function as anode and air stability. A replacement of hydrophilic and acidic PEDOT:PSS with metal oxides is viable since metal oxides with hole-transporting behavior as anode buffer layer exhibit appropriate work functions and stability against air. However, most of metal oxides are grown under high vacuum, which raises the process cost and hinders the large area. Therefore, solution-processed metal oxides as buffer layers could provide many opportunities and important insights on commercial OPVs.

LWF metals as cathode are easily oxidized, causing dark spots and degrading devices very fast. One way is to use inverted structure as mentioned before. The other way is to develop advanced encapsulation technology to protect the devices from moisture and oxygen.

6.5.2.2 Photoactive Materials

Organic semiconductors are easily oxidized by oxygen, especially under illumination. However, OPVs must be exposed to solar light during operation. Therefore, it is challenging to synthesize and develop air-stable organic materials with deep HOMO levels and low band gaps.

6.5.2.3 Device Design

BHJ structure offers an interpenetrating network for charge transport, which is controlled by annealing, solvents, additives, etc. The morphology is changeable by varying the annealing temperature and processing time, i.e., not at the thermodynamic equilibrium. Thus, it is necessary to exploit an effective and stable morphology beneficial to both efficiency and stability, providing bi-continuous pathways for charge transport in their individual phase. More importantly, it should be temperature and light stable, especially under illumination when the device is heated up.

On the other hand, inverted structure facilitates the stability improvement due to the reverse of anode and cathode, where HWF metal as anode at top could sustain the oxidization.

6.5.2.4 Encapsulation

Low-cost encapsulation technology leads to limited protection against oxygen and water. Therefore, a proper and powerful encapsulation is necessary to further improve the device stability. Encapsulation of alternating inorganic–organic multilayer actually serves as a high barrier, fulfilling the requirements for flexible OPVs. The encapsulating layer should be possessed with easy process, light weight, no defects, and flexibility.

In summary, all the factors influencing device stability should be emphasized in order to prolong device lifetime and achieve commercial products. Taking various interface parameters and factors into account, a much more comprehensive model should be established by improving previous models mentioned before. Deep insight and knowledge into degradation mechanism, which could disclose the relationship between degradation mechanisms and material design, preparation technique, heat effect during operation, annealing treatment, and encapsulation, are significantly beneficial to optimization of organic material design and device stability.

References

1. Konarka Technologies I http://www.konarka.com/
2. Heliatek G http://www.heliatek.com/
3. Solarmer Energy I http://www.solarmer.com/
4. Cai WZ, Gong X, Cao Y (2010) Polymer solar cells: recent development and possible routes for improvement in the performance. Sol Energy Mater Sol Cells 94:114–127
5. Helgesen M, Sondergaard R, Krebs FC (2010) Advanced materials and processes for polymer solar cell devices. J Mater Chem 20:36–60
6. Liang YY, Xu Z, Xia JB et al (2010) For the bright future-bulk heterojunction polymer solar cells with power conversion efficiency of 7.4 %. Adv Mater 22:E135–E138
7. Dennler G, Scharber MC, Brabec CJ (2009) Polymer-fullerene bulk-heterojunction solar cells. Adv Mater 21:1323–1338
8. Jorgensen M, Norrman K, Krebs FC (2008) Stability/degradation of polymer solar cells. Sol Energy Mater Sol Cells 92:686–714
9. Shrotriya V http://www.slideshare.net/vshrotriya/organic-solar-cells
10. Padinger F, Fromherz T, Denk P et al (2001) Degradation of bulk heterojunction solar cells operated in an inert gas atmosphere: a systematic study. Synth Met 121:1605–1606
11. Neugebauer H, Brabec C, Hummelen JC et al (2000) Stability and photodegradation mechanisms of conjugated polymer/fullerene plastic solar cells. Sol Energy Mater Sol Cells 61:35–42
12. Jeranko T, Tributsch H, Sariciftci NS et al (2004) Patterns of efficiency and degradation of composite polymer solar cells. Sol Energy Matter Sol Cells 83:247–262
13. Kroon JM, Wienk MM, Verhees WJH et al (2002) Accurate efficiency determination and stability studies of conjugated polymer/fullerene solar cells. Thin Solid Films 403:223–228
14. Krebs FC, Alstrup J, Spanggaard H et al (2004) Production of large-area polymer solar cells by industrial silk screen printing, lifetime considerations and lamination with polyethyleneterephthalate. Sol Energy Matter Sol Cells 83:293–300
15. Krebs FC, Carle JE, Cruys-Bagger N et al (2005) Lifetimes of organic photovoltaics: photochemistry, atmosphere effects and barrier layers in ITO-MEHPPV: PCBM-aluminium devices. Sol Energy Matter Sol Cells 86:499–516
16. Brabec CJ, Hauch JA, Schilinsky P et al (2005) Production aspects of organic photovoltaics and their impact on the commercialization of devices. MRS Bull 30:50–52
17. Holdcroft S (1991) Photochain scission of the soluble electronically conducting polymer—Poly(3-Hexylthiophene). Macromolecules 24:2119–2121
18. Lewis JS, Weaver MS (2004) Thin-film permeation-barrier technology for flexible organic light-emitting devices. IEEE J Sel Top Quantum Electron 10:45–57
19. Dennler G, Lungenschmied C, Neugebauer H et al (2006) A new encapsulation solution for flexible organic solar cells. Thin Solid Films 511:349–353
20. Aziz H, Popovic ZD (2004) Degradation phenomena in small-molecule organic light-emitting devices. Chem Mater 16:4522–4532
21. Krebs FC, Gevorgyan SA, Alstrup J (2009) A roll-to-roll process to flexible polymer solar cells: model studies, manufacture and operational stability studies. J Mater Chem 19: 5442–5451
22. Norrman K, Gevorgyan SA, Krebs FC (2009) Water-induced degradation of polymer solar cells studied by (H2O)-O-18 labeling. Acs Appl Mater Interfaces 1:102–112
23. Norrman K, Madsen MV, Gevorgyan SA et al (2010) Degradation patterns in water and oxygen of an inverted polymer solar cell. J Am Chem Soc 132:16883–16892
24. Scott JC, Kaufman JH, Brock PJ et al (1996) Degradation and failure of MEH-PPV light-emitting diodes. J Appl Phys 79:2745–2751
25. Carter SA, Angelopoulos M, Karg S et al (1997) Polymeric anodes for improved polymer light-emitting diode performance. Appl Phys Lett 70:2067–2069

26. Krebs FC, Norrman K (2007) Analysis of the failure mechanism for a stable organic photovoltaic during 10000 h of testing. Prog Photovolt Res Appl 15:697–712
27. Brabec C, Dyakonov V, Parisi J, et al (2003) Organic photovoltaics: concepts and realization, p 60
28. de Jong MP, van Ijzendoorn LJ, de Voigt MJA (2000) Stability of the interface between indium-tin-oxide and poly(3,4-ethylenedioxythiophene)/poly(styrenesulfonate) in polymer light-emitting diodes. Appl Phys Lett 77:2255–2257
29. Girtan M, Rusu M (2010) Role of ITO and PEDOT:PSS in stability/degradation of polymer: fullerene bulk heterojunctions solar cells. Sol Energy Matter Sol Cells 94:446–450
30. Kawano K, Pacios R, Poplavskyy D et al (2006) Degradation of organic solar cells due to air exposure. Sol Energy Matter Sol Cells 90:3520–3530
31. Aziz H, Xu G (1996) A degradation mechanism of organic light-emitting devices. Synth Met 80:7–10
32. Aziz H, Popovic ZD, Hu NX et al (1999) Degradation mechanism of small molecule-based organic light-emitting devices. Science 283:1900–1902
33. Reese MO, Morfa AJ, White MS et al (2008) Pathways for the degradation of organic photovoltaic P3HT : PCBM based devices. Sol Energy Matter Sol Cells 92:746–752
34. Reese MO, Morfa AJ, White MS et al (2008) Short-term metal/organic interface stability investigations of organic photovoltaic devices. Pvsc: 2008 33rd IEEE photovoltaic specialists conference. vols 1–4:1491–1493
35. Li JG, Kim S, Edington S et al (2011) A study of stabilization of P3HT/PCBM organic solar cells by photochemical active TiOx layer. Sol Energy Matter Sol Cells 95:1123–1130
36. Fery C, Racine B, Vaufrey D et al (2005) Physical mechanism responsible for the stretched exponential decay behavior of aging organic light-emitting diodes. Appl Phys Lett 87:213502
37. Schuller S, Schilinsky P, Hauch J et al (2004) Determination of the degradation constant of bulk heterojunction solar cells by accelerated lifetime measurements. Appl Phys A Mater Sci Process 79:37–40
38. Logdlund M, Bredas JL (1994) Theoretical-studies of the interaction between aluminum and poly(P-phenylenevinylene) and derivatives. J Chem Phys 101:4357–4364
39. Karst N, Bernede JC (2006) On the improvement of the open circuit voltage of plastic solar cells by the presence of a thin aluminium oxide layer at the interface organic/aluminium. Phys Status Solidi A-Appl Mat 203:R70–R72
40. Melzer C, Krasnikov VV, Hadziioannou G (2003) Organic donor/acceptor photovoltaics: the role of C-60/metal interfaces. Appl Phys Lett 82:3101–3103
41. Vogel M, Doka S, Breyer C et al (2006) On the function of a bathocuproine buffer layer in organic photovoltaic cells. Appl Phys Lett 89:163501
42. Zhang ST, Zhou YC, Zhao JM et al (2006) Role of hole playing in improving performance of organic light-emitting devices with an Al2O3 layer inserted at the cathode-organic interface. Appl Phys Lett 89:043502
43. Hung LS, Tang CW, Mason MG (1997) Enhanced electron injection in organic electroluminescence devices using an Al/LiF electrode. Appl Phys Lett 70:152–154
44. Brabec CJ, Shaheen SE, Winder C et al (2002) Effect of LiF/metal electrodes on the performance of plastic solar cells. Appl Phys Lett 80:1288–1290
45. van Gennip WJH, van Duren JKJ, Thune PC et al (2002) The interfaces of poly(p-phenylene vinylene) and fullerene derivatives with Al, LiF, and Al/LiF studied by secondary ion mass spectroscopy and x-ray photoelectron spectroscopy: formation of AlF3 disproved. J Chem Phys 117:5031–5035
46. McNeill CR, Fell CJR, Holdsworth JL et al (2005) Screening for artifacts in near-field scanning photocurrent microscopy images of polymer solar cells. Synth Met 153:85–88
47. Renaud G, Lazzari R, Leroy F (2009) Probing surface and interface morphology with grazing incidence small angle X-ray scattering. Surf Sci Rep 64:255–380
48. Caminiti R, Albertini VR (1999) The kinetics of phase transitions observed by energy-dispersive X-ray diffraction. Int Rev Phys Chem 18:263–299

49. Orita K, Morimura T, Horiuchi T et al (1997) In situ energy-dispersive X-ray reflectivity measurements of structural changes in thin films for organic electroluminescent devices. Synth Met 91:155–158
50. Paci B, Generosi A, Albertini VR et al (2005) In situ energy dispersive x-ray reflectometry measurements on organic solar cells upon working. Appl Phys Lett 87:194110
51. Paci B, Generosi A, Albertini VR et al (2006) Controlling photoinduced degradation in plastic photovoltaic cells: a time-resolved energy dispersive x-ray reflectometry study. Appl Phys Lett 89:043507
52. Andreasen JW, Gevorgyan SA, Schleputz CM et al (2008) Applicability of X-ray reflectometry to studies of polymer solar cell degradation. Sol Energy Matter Sol Cells 92:793–798
53. Garcia-Belmonte G, Munar A, Barea EM et al (2008) Charge carrier mobility and lifetime of organic bulk heterojunctions analyzed by impedance spectroscopy. Org Electron 9: 847–851
54. Bisquert J (2002) Theory of the impedance of electron diffusion and recombination in a thin layer. J Phys Chem B 106:325–333
55. Fabregat-Santiago F, Garcia-Belmonte G, Mora-Sero I et al (2011) Characterization of nanostructured hybrid and organic solar cells by impedance spectroscopy. Phys Chem Chem Phys 13:9083–9118
56. Garcia-Belmonte G, Boix PP, Bisquert J et al (2010) Simultaneous determination of carrier lifetime and electron density-of-states in P3HT:PCBM organic solar cells under illumination by impedance spectroscopy. Sol Energy Matter Sol Cells 94:366–375
57. Bisquert J, Fabregat-Santiago F, Mora-Sero I et al (2009) Electron lifetime in dye-sensitized solar cells: theory and interpretation of measurements. J Phys Chem C 113:17278–17290
58. Glatthaar M, Mingirulli N, Zimmermann B et al (2005) Impedance spectroscopy on organic bulk-heterojunction solar cells. Phys Status Solidi A-Appl Mat 202:R125–R127
59. Glatthaar M, Riede M, Keegan N et al (2007) Efficiency limiting factors of organic bulk heterojunction solar cells identified by electrical impedance spectroscopy. Sol Energy Mater Sol Cells 91:390–393
60. Wang MD, Xie FY, Xie WG et al (2011) Device lifetime improvement of polymer-based bulk heterojunction solar cells by incorporating copper oxide layer at Al cathode. Appl Phys Lett 98:183304
61. Wang MD, Tang Q, An J et al (2010) Performance and stability improvement of P3HT:PCBM-based solar cells by thermally evaporated chromium oxide (CrOx) interfacial layer. ACS Appl Mater Interfaces 2:2699–2702
62. Kim JY, Kim SH, Lee HH et al (2006) New architecture for high-efficiency polymer photovoltaic cells using solution-based titanium oxide as an optical spacer. Adv Mater 18:572–576
63. Kim JY, Lee K, Coates NE et al (2007) Efficient tandem polymer solar cells fabricated by all-solution processing. Science 317:222–225
64. Lee K, Kim JY, Park SH et al (2007) Air-stable polymer electronic devices. Adv Mater 19:2445–2449
65. Cho S, Lee K, Heeger AJ (2009) Extended lifetime of organic field-effect transistors encapsulated with titanium sub-oxide as an 'Active' passivation/barrier layer. Adv Mater 21:1941–1944
66. Lee JK, Coates NE, Cho S et al (2008) Efficacy of TiOx optical spacer in bulk-heterojunction solar cells processed with 1,8-octanedithiol. Appl Phys Lett 92:243308
67. Shrotriya V, Li G, Yao Y et al (2006) Transition metal oxides as the buffer layer for polymer photovoltaic cells. Appl Phys Lett 88:073508
68. Zhao DW, Sun XW, Jiang CY et al (2008) Efficient tandem organic solar cells with an Al/MoO3 intermediate layer. Appl Phys Lett 93:083305
69. Zhang F, Zhao D, Zhuo Z et al (2010) Inverted small molecule organic solar cells with Ca modified ITO as cathode and MoO3 modified. Sol Energy Matter Sol Cells 94:2416–2421

70. Zhang FJ, Sun FY, Shi YZ et al (2010) Effect of an ultra-thin molybdenum trioxide layer and illumination intensity on the performance of organic photovoltaic devices. Energy Fuels 24:3739–3742
71. Wang FX, Qiao XF, Xiong T et al (2008) The role of molybdenum oxide as anode interfacial modification in the improvement of efficiency and stability in organic light-emitting diodes. Org Electron 9:985–993
72. Sun Y, Takacs CJ, Cowan SR et al (2011) Efficient, air-stable bulk heterojunction polymer solar cells using moox as the anode interfacial layer. Adv Mater 23:2226–2230
73. Chen LM, Hong ZR, Li G et al (2009) Recent progress in polymer solar cells: manipulation of polymer: fullerene morphology and the formation of efficient inverted polymer solar cells. Adv Mater 21:1434–1449
74. Tao C, Ruan SP, Zhang XD et al (2008) Performance improvement of inverted polymer solar cells with different top electrodes by introducing a MoO3 buffer layer. Appl Phys Lett 93:193307
75. Hau SK, Yip HL, Ma H et al (2008) High performance ambient processed inverted polymer solar cells through interfacial modification with a fullerene self-assembled monolayer. Appl Phys Lett 93:233304
76. Kyaw AKK, Sun XW, Jiang CY et al (2008) An inverted organic solar cell employing a sol-gel derived ZnO electron selective layer and thermal evaporated MoO3 hole selective layer. Appl Phys Lett 93:221107
77. Li G, Chu CW, Shrotriya V et al (2006) Efficient inverted polymer solar cells. Appl Phys Lett 88:253503
78. Liao HH, Chen LM, Xu Z et al (2008) Highly efficient inverted polymer solar cell by low temperature annealing of Cs2CO3 interlayer. Appl Phys Lett 92:173303
79. Krebs FC (2009) All solution roll-to-roll processed polymer solar cells free from indium-tin-oxide and vacuum coating steps. Org Electron 10:761–768
80. Krebs FC (2009) Polymer solar cell modules prepared using roll-to-roll methods: Knife-over-edge coating, slot-die coating and screen printing. Sol Energy Mater Sol Cells 93:465–475
81. Krebs FC, Jorgensen M, Norrman K et al (2009) A complete process for production of flexible large area polymer solar cells entirely using screen printing-First public demonstration. Sol Energy Mater Sol Cells 93:422–441
82. Sahin Y, Alem S, de Bettignies R et al (2005) Development of air stable polymer solar cells using an inverted gold on top anode structure. Thin Solid Films 476:340–343
83. Hau SK, Yip HL, Baek NS et al (2008) Air-stable inverted flexible polymer solar cells using zinc oxide nanoparticles as an electron selective layer. Appl Phys Lett 92:253301
84. Liu JP, Wang SS, Bian ZQ et al (2009) Inverted photovoltaic device based on ZnO and organic small molecule heterojunction. Chem Phys Lett 470:103–106
85. Kuwabara T, Nakayama T, Uozumi K et al (2008) Highly durable inverted-type organic solar cell using amorphous titanium oxide as electron collection electrode inserted between ITO and organic layer. Sol Energy Mater Sol Cells 92:1476–1482
86. Steim R, Choulis SA, Schilinsky P et al (2008) Interface modification for highly efficient organic photovoltaics. Appl Phys Lett 92:093303
87. Tao C, Ruan SP, Xie GH et al (2009) Role of tungsten oxide in inverted polymer solar cells. Appl Phys Lett 94:043311
88. Ameri T, Dennler G, Waldauf C et al (2008) Realization, characterization, and optical modeling of inverted bulk-heterojunction organic solar cells. J Appl Phys 103:084506
89. Zimmermann B, Wurfel U, Niggemann M (2009) Longterm stability of efficient inverted P3HT:PCBM solar cells. Sol Energy Matter Sol Cells 93:491–496
90. Lee JK, Cho JM, Shin WS et al (2008) The stability of PEDOT: PSS films monitored by electron spin resonance. J Korean Phys Soc 52:621–626
91. Chang YM, Su WF, Wang L (2008) Influence of photo-induced degradation on the optoelectronic properties of regioegular poly(3-hexylthiophene). Sol Energy Matter Sol Cells 92:761–765

92. Zhao DW, Tan ST, Ke L et al (2010) Optimization of an inverted organic solar cell. Sol Energy Mater Sol Cells 94:985–991
93. Jiang CY, Sun XW, Zhao DW et al (2010) Low work function metal modified ITO as cathode for inverted polymer solar cells. Sol Energy Mater Sol Cells 94:1618–1621
94. Zhao DW, Liu P, Sun XW et al (2009) An inverted organic solar cell with an ultrathin Ca electron-transporting layer and MoO3 hole-transporting layer. Appl Phys Lett 95:153304
95. Campoy-Quiles M, Ferenczi T, Agostinelli T et al (2008) Morphology evolution via self-organization and lateral and vertical diffusion in polymer: fullerene solar cell blends. Nat Mater 7:158–164
96. Gunes S, Neugebauer H, Sariciftci NS (2007) Conjugated polymer-based organic solar cells. Chem Rev 107:1324–1338
97. Peumans P, Yakimov A, Forrest SR (2003) Small molecular weight organic thin-film photodetectors and solar cells. J Appl Phys 93:3693–3723
98. Wang EG, Wang L, Lan LF et al (2008) High-performance polymer heterojunction solar cells of a polysilafluorene derivative. Appl Phys Lett 92:033307
99. Li G, Shrotriya V, Huang JS et al (2005) High-efficiency solution processable polymer photovoltaic cells by self-organization of polymer blends. Nat Mater 4:864–868
100. Kim K, Liu J, Namboothiry MAG et al (2007) Roles of donor and acceptor nanodomains in 6% efficient thermally annealed polymer photovoltaics. Appl Phys Lett 90:163511
101. Reyes-Reyes M, Kim K, Carroll DL (2005) High-efficiency photovoltaic devices based on annealed poly(3-hexylthiophene) and 1-(3-methoxycarbonyl)-propyl-1-phenyl-(6,6)C-61 blends. Appl Phys Lett 87:083506
102. Yang XN, Loos J, Veenstra SC et al (2005) Nanoscale morphology of high-performance polymer solar cells. Nano Lett 5:579–583
103. Krebs FC, Spanggaard H (2005) Significant improvement of polymer solar cell stability. Chem Mat 17:5235–5237
104. Krebs FC (2006) Encapsulation of polymer photovoltaic prototypes. Sol Energy Mater Sol Cells 90:3633–3643
105. Sarkar S, Culp JH, Whyland JT et al (2010) Encapsulation of organic solar cells with ultrathin barrier layers deposited by ozone-based atomic layer deposition. Org Electron 11:1896–1900
106. Puurunen RL (2005) Surface chemistry of atomic layer deposition: a case study for the trimethylaluminum/water process. J Appl Phys 97:121301
107. Potscavage WJ, Yoo S, Domercq B et al (2007) Encapsulation of pentacene/C-60 organic solar cells with Al2O3 deposited by atomic layer deposition. Appl Phys Lett 90:253511
108. Chang CY, Chou CT, Lee YJ et al (2009) Thin-film encapsulation of polymer-based bulk-heterojunction photovoltaic cells by atomic layer deposition. Org Electron 10:1300–1306
109. Luo JX, Xiao LX, Chen ZJ et al (2010) Insulator MnO: highly efficient and air-stable n-type doping layer for organic photovoltaic cells. Org Electron 11:664–669
110. Affinito JD, Gross ME, Coronado CA et al (1996) A new method for fabricating transparent barrier layers. Thin Solid Films 290:63–67
111. Madakasira P, Inoue K, Ulbricht R et al (2005) Multilayer encapsulation of plastic photovoltaic devices. Synth Met 155:332–335

Chapter 7
Theoretical Studies of Plasmonic Effects in Organic Solar Cells

Wei E. I. Sha, Wallace C. H. Choy and Weng Cho Chew

Abstract The book chapter provides a systematic study on plasmonic effects in organic solar cells (OSCs). We first introduce the concepts, significance, and recent progress of OSCs incorporating plasmonic nanostructures. On the basis of unique features of OSCs, we exploit versatile resonance mechanisms acting on the absorption enhancement of OSCs; for example, Fabry-Pérot mode, quasi-guided mode, and plasmonic mode. Next, we present rigorous theoretical models to characterize optical properties of OSCs. The key physical quantities, as well as the pros and cons of different models, are described in detail. After that, we show some theoretical results to unveil the fundamental and device physics of plasmonic effects in typical OSC structures. Finally, we conclude the chapter and identify future opportunities in this field.

W. E. I. Sha (✉) · W. C. H. Choy · W. C. Chew
Department of Electrical and Electronic Engineering, The University of Hong Kong, Pokfulam Road, Hong Kong, People's Republic of China
e-mail: wsha@eee.hku.hk

W. C. H. Choy
e-mail: chchoy@eee.hku.hk

W. C. Chew
e-mail: wcchew@hku.hk

W. C. Chew
Department of Electrical and Computer Engineering, University of Illinois, Urbana-Champaign, USA

W. C. H. Choy (ed.), *Organic Solar Cells*, Green Energy and Technology,
DOI: 10.1007/978-1-4471-4823-4_7,

7.1 Introduction

Organic solar cells (OSCs) [1–3] have drawn much attentions in recent years, due to their interesting properties in terms of light incoupling and photocurrent generation, as well as the prospect of large-area production and low-cost processing. Many organic semiconductors exhibit very high absorption coefficients, making them promising for photovoltaic devices. However, short lifetime and diffusion length of exciton result in ultrathin-active-layer configuration in OSCs with a typical thickness of a few hundreds nanometers. The configuration limits the light absorption efficiency, and thereby the power conversion efficiency of OSCs. Having unique features of tunable resonance and unprecedented near-field concentration, plasmon is an enabling technique for light manipulation and management [4–6]. By altering the metallic nanostructure, the properties of plasmons, in particular their interactions with light, can be tailored, which offers the potential for developing new types of optoelectronic devices. Meanwhile, the use of metallic materials with negative permittivity is one of the most feasible ways of circumventing the fundamental (half-wavelength) limit and achieving localization of electromagnetic energy (at optical frequencies) into nanoscale. Breaking the half-wavelength limit has a fundamental significance for the optical design of thin-film OSCs.

Plasmonic effects allow us to significantly improve the optical absorption of thin-film OSCs [7] and promote emerging solar cell technology meeting clean energy demands. So far, plasmonic nanostructures can offer three principles to enhance the optical absorption of OSCs. The first one is surface plasmon resonance by metallic gratings fabricated on the top or bottom of the active layer [8–17]. The second one is local plasmon resonance by metallic nanoparticles incorporated into or near the active layer [18–30]. The third one is plasmon coupling and hybridization, such as surface plasmon resonance coupled with local plasmon resonance or plasmon resonance coupled with photonic resonance [31–33].

7.2 Resonance Mechanisms

Critically different from the thin-film polycrystalline or amorphous silicon SCs with active layer thickness of a few microns [34], the active polymer layer of thin-film OSCs only has a few hundreds nanometers or even thinner thickness due to an extreme short exciton diffusion length [1]. Such thin active layer with low refractive index induces not only the weak optical absorption of OSCs but also fundamental (half-wavelength) limit of the optical design. On the one hand, the strong Fabry-Pérot mode (or waveguide mode) cannot be expected in the ultrathin active layer. On the other hand, the physical mechanism of near-field concentration (not far-field scattering) should be taken into account in the design. Taking full advantage of versatile resonance mechanics is essential to enhance the optical

absorption of OSCs. Noting that the obscure and disparate glossaries describing the same resonance mechanism, we will focus more on their physical understandings and unique features.

Fabry-Pérot mode. The planar multilayer device can support the Fabry–Pérot mode whose spectrum has symmetric Lorentzian line shape. Considering the plane-wave excitation in OSC problems, the eigenmode of the multilayer device cannot be excited due to the momentum or phase mismatch ($\beta > k_0$). The Fabry-Pérot mode can be understood by the mode coupling between the excitation solution and the eigenmode. The fundamental limit in the optical design of OSCs forbids the Fabry-Pérot mode bouncing in a single active layer but possibly in several layers. Compared to thicker amorphous silicon SCs, OSCs support weaker Fabry-Pérot mode. The nonplanar device structure can also support the Fabry-Pérot mode if the nonplanar structure can be approximately decomposed as multiple planar structures [15].

Quasi-guided mode. The space harmonics in periodic nanostructure provide additional momentum, so that the eigenmode or guided mode can be excited with the momentum matching condition of $\pm\mathrm{Re}(\beta) = k_0 \sin\theta + \frac{2\pi}{P} m,\ m = 0, \pm 1, \pm 2, \ldots$. Here, we consider a 1-dimensional periodic structure with a periodicity P and an incident angle θ. The complex propagation constant β implies that the excited guided mode cannot be perfectly trapped in the grating layer but giving rise to a leaky wave. Arising from the constructive and destructive interference of a narrow discrete guided mode with a broad continuum (incident light), the quasi-guided mode [35] with an asymmetric and narrow Fano line shape has extraordinary transmittance and reflectance called Wood's anomaly [36–38]. The pronounced quasi-guided mode enhances the absorption of OSCs; however, its performance is limited by the narrow bandwidth.

Plasmonic mode. The excitation of plasmons by light is denoted as a surface plasmon resonance (SPR) for planar surfaces or localized plasmon resonance (LPR) for nanometer-sized metallic structures [39–41]. SPRs are electromagnetic excitations propagating at the interface between a dielectric and a metal, evanescently confined in the perpendicular direction. Using light to excite the SPR, the momentum matching condition can be satisfied by using a periodic structure with space harmonics or a subscatterer producing evanescent waves. LPRs are nonpropagating excitations of the conduction electrons of metallic nanostructures coupled to the electromagnetic field. The curved surface of the particle exerts an effective restoring force on the driven electrons, so that a resonance can arise at a specific wavelength independent of wave vector. The half-wavelength limit in the optical design of OSCs compels researchers to pay more attenuation on the physical mechanism of near-field concentration (not far-field scattering). Hence, plasmonic mode, which has unique features of near-field enhancement, is one of the best candidates to boost the optical absorption of OSCs. The resonance peaks of plasmonic mode strongly depend on the material, geometry, and surrounding environment and can be highly tunable and manipulated.

Mode hybridization. The superradiant plasmonic mode oscillating in-phase can be realized by the mode coupling and hybridization mechanisms [42, 43], which occur in the close-packed metallic nanostructures. For example, longitudinal modes in the metallic nanosphere chain or symmetric modes in two coupled metallic plates can increase the optical absorption of OSCs by several folds [30, 33]. Likewise, the LPR by a metallic nanosphere interacted with the SPR by a metallic plate leads to coherent near-field enhancement [33]. Moreover, the plasmonic mode can couple to the Fabry-Pérot mode through carefully optimizing both device and metallic structures [31, 32]. Mode coupling and hybridization open up a more effective and hopeful way in the optical design of OSCs.

Intrinsic limit and beyond. The intrinsic limit of plasmonic effects is the bad spectral overlap between the absorption of active materials and plasmonic resonances. In other words, strong plasmonic resonances only appear in the weak absorption region of active materials. For example, the absorption peak of the active material P3HT:PCBM is around 500 nm; however, the embedded into P3HT:PCBM are respectively at 600 and 650 nm. There are two potential schemes to go beyond the limit. One is to employ large and lossless dielectric concentrators [44–46]. Nevertheless, embedding too large dielectric scatterers seems not to be practical in fabricating thin-film OSCs. Exploring the mode hybridization mechanism is an alternative way to overcome the difficulty. By tuning the thicknesses of active and spacer layers, plasmon-coupled Fabry-Pérot mode can overlap with the absorption peak of active materials [16]. Symmetry breaking and retardation effects allow us to excite the dark modes or high-order modes in the vicinity of metallic structures with broadband and strong resonances [47].

7.3 Theoretical Model

7.3.1 Comparisons of Various Models

Computational electromagnetics [48], which are used for modeling the interaction of electromagnetic fields with physical objects and surrounding environment, play an important role in characterizing and optimizing the optical design of OSCs. A rigorous, fast, and efficient solution to Maxwell's equations facilitates understanding the underlying device physics, reducing the experimental cost, and accelerating the research and development period. With the aid of state-of-the-art methods, the critical physical quantities in the optical design of OSCs, such as optical absorption of active material, can be illustrated for observation and analyzed for optimization. It is highly desirable to know the strengths and weaknesses of various theoretical methods in modeling the optical properties of OSCs.

Time-domain methods versus frequency-domain methods. Most optical materials are dispersive, therefore, a recursive convolution method [49] or a piecewise linear recursive convolution method [50] must be adopted for time-domain

methods. For noble metals with plasmonic effects in the visible light range, such as silver and gold, the complex refractive index has to be described by a large number of summation terms in the Lorentz-Drude model [51] leading to longer calculation time. However, for frequency-domain methods, one can directly employ an experimentally tabulated refractive index of the dispersive materials. Another difficulty in time-domain methods is to treat the periodic boundary condition particularly for the oblique incidence caused by the anticausal property of the Floquet theorem. In most places, unless a solar panel is mounted on an expensive tracking system, most of the time, light is incident on the array obliquely. Hence, the ability of frequency-domain methods to handle the case of oblique incidence is clearly an important advantage over time-domain methods [52]. Moreover, time-domain methods suffer from numerical dispersion and stability problems in contrast to frequency-domain methods [53, 54]. This drawback becomes more serious if a 3-dimensional large-scale SC structure is investigated. A significant merit associated with time-domain method is a broadband simulation in the solar spectrum of interest. The frequency-domain method can employ the parallel computing technique to circumvent the problem.

Integral equation methods versus differential equation methods. Differential equation methods involving finite-difference and finite-element algorithms [54, 55] can treat a variety of inhomogeneous boundary conditions conveniently. The methods have a powerful ability to model the complex device structure of OSCs incorporating the metallic gratings or nanoparticles. The produced matrix by the differential equation methods is sparse due to the "local" differential operators of Maxwell's equations or wave equations. The method consumes memory cost of $O(N)$ and complexity of $O(N)$ per matrix–vector multiplication in Krylov subspace iteration algorithm [55, 56]. Moreover, multifrontal or multigrid methods [57, 58] can speed up the solution process of the differential equations. To simulate the interaction between light and OSCs, an efficient absorption boundary condition, as well as additional volume grids enclosing the OSC device, has to be adopted.

In comparison with differential equation methods, integral equation methods [56, 59] connect field components to equivalent currents by using "global" integral operators represented with the dyadic Green's functions. As a result, integral equation methods always guarantee higher accuracy but lead to full dense matrix. Fortunately, matrix-free fast algorithms [60], such as fast Fourier transform (FFT) [61, 62] and fast multipole methods [63, 64], can significantly reduce the computer resources occupied by the dense matrix. Thanks to the Green's tensor, the integral equation methods automatically satisfy the radiation boundary condition but need singularity treatments. In particular, the surface integral equation method having a unique feature of surface triangulation produces much smaller unknowns. However, the method can only be employed to analyze a homogenous or piecewise-homogenous structure. For an arbitrary inhomogeneity or complex environment encountered in plasmonic nanodevices, the near-field calculation by the SIE method is hard to implement.

Mode-matching methods. Mode-matching method [59, 65] is a commonly used technique for the formulation of optical problems, especially for structures

consisting of two or more separated regions. It is based on expanding the fields and matching them at the boundaries of different regions, and thus lends itself naturally to the analysis of multilayer optical devices. The most representative of mode-matching methods involves rigorous coupled-wave analysis [66], scattering-matrix method [67], and plane wave expansion method [68]. Using cheap computer resources, these methods are specially useful in characterizing the optical response of periodic OSC devices. The zero-order and high-order transmittance and reflectance can be easily obtained with a program. However, it is not well suited for characterizing plasmonic effects, because a large quantity of modes are required to describe the plasmon coupling and hybridization. For mode-matching methods, computing the optical absorption of active materials for the metal-incorporated OSCs is nontrivial. The trivial absorbance cannot truly represents the optical absorption of OSCs, and electric fields should be postprocessed for excluding the metallic absorption. Additionally, cascading many layer media with repeated matrix multiplications will cause the stability and accuracy issues, which always happens in OSC modeling with the curved geometries.

7.3.2 Finite-Difference Frequency-Domain Method

Considering a 2-dimensional OSC structure, the Maxwell's equations can be decoupled into a TE and TM modes. The wave equations for TE and TM modes are respectively formulated as [59]

$$\frac{1}{\varepsilon_r}\frac{\partial}{\partial x}\left(\frac{1}{\mu_r}\frac{\partial E_z}{\partial x}\right)+\frac{1}{\varepsilon_r}\frac{\partial}{\partial y}\left(\frac{1}{\mu_r}\frac{\partial E_z}{\partial y}\right)+k_0^2E_z=0 \tag{7.1}$$

$$\frac{1}{\mu_r}\frac{\partial}{\partial x}\left(\frac{1}{\varepsilon_r}\frac{\partial H_z}{\partial x}\right)+\frac{1}{\mu_r}\frac{\partial}{\partial y}\left(\frac{1}{\varepsilon_r}\frac{\partial H_z}{\partial y}\right)+k_0^2H_z=0 \tag{7.2}$$

where k_0 is the wave number of incident light, and ε_r and μ_r are the relative permittivities and permeabilities, respectively. Regarding nonmagnetic optical materials, $\mu_r=1$, $\varepsilon_r=n_c^2$, and n_c is the complex refractive index of optical materials.

With the Yee lattice [69], the 2D finite-difference frequency-domain (FDFD) method is utilized to characterize the optical properties of OSCs. As shown in Fig. 7.1, the five-point stencil is adopted for the FDFD method. The discretized forms for the TE and TM wave equations are respectively of the form

$$2\left(\frac{1}{\Delta_x^2}+\frac{1}{\Delta_y^2}\right)\frac{\Phi_0}{\bar{\varepsilon}}-k_0^2\Phi_0-\frac{\Phi_1+\Phi_3}{\bar{\varepsilon}\Delta_x^2}-\frac{\Phi_2+\Phi_4}{\bar{\varepsilon}\Delta_y^2}=0,\quad \Phi=E_z \tag{7.3}$$

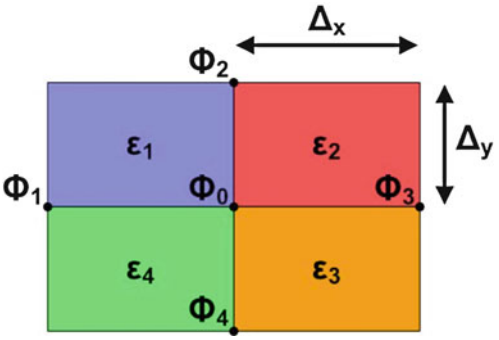

Fig. 7.1 The five-point stencil for the FDFD method. Δ_x and Δ_y are respectively the spatial steps along the x and y directions. $\Phi = E_z$ for the TE polarization and $\Phi = H_z$ for the TM polarization. Here, $\varepsilon = n_c^2$ is the relative permittivity in the discretized region and n_c is the complex refractive index of the optical material

$$2\left(\frac{1}{\Delta_x^2}+\frac{1}{\Delta_y^2}\right)\frac{\Phi_0}{\bar{\varepsilon}} - k_0^2\Phi_0 - \frac{\varepsilon_1^{-1}+\varepsilon_4^{-1}}{2\Delta_x^2}\Phi_1 - \frac{\varepsilon_2^{-1}+\varepsilon_3^{-1}}{2\Delta_x^2}\Phi_3 - \frac{\varepsilon_1^{-1}+\varepsilon_2^{-1}}{2\Delta_y^2}\Phi_2 - \frac{\varepsilon_3^{-1}+\varepsilon_4^{-1}}{2\Delta_y^2}\Phi_4 = 0, \quad \Phi = H_z \tag{7.4}$$

$$\bar{\varepsilon} = \begin{cases} \dfrac{\varepsilon_1+\varepsilon_2+\varepsilon_3+\varepsilon_4}{4}, & \Phi = E_z \\ 4(\varepsilon_1^{-1}+\varepsilon_2^{-1}+\varepsilon_3^{-1}+\varepsilon_4^{-1})^{-1}, & \Phi = H_z \end{cases} \tag{7.5}$$

Although Eqs. (7.3) and (7.4) can in principle treat the dielectric–dielectric and dielectric–metal interfaces, they will lose some accuracy at the interfaces and cannot well reproduce the features of exponentially decayed surface plasmon waves. Thus, a one-sided difference scheme is developed to rectify the problem. For the horizontal interface $(y = y_h)$ between the media 1 and 2, the flexible and high-order accurate one-sided difference reads

$$\begin{aligned} \frac{\partial}{\partial y}\Phi^1\Big|_{x=i\Delta_x} &\approx \frac{1.5\Phi^1(i,j) - 2\Phi^1(i,j-1) + 0.5\Phi^1(i,j-2)}{\Delta_y} \\ \frac{\partial}{\partial y}\Phi^2\Big|_{x=i\Delta_x} &\approx \frac{-1.5\Phi^2(i,j) + 2\Phi^2(i,j+1) - 0.5\Phi^2(i,j+2)}{\Delta_y} \end{aligned} \tag{7.6}$$

For the vertical interfaces, one can also use the scheme.

The incident Sunlight reflected by OSC devices converts to outgoing waves propagating into infinite air (or free space) region. A perfectly matched layer (PML) [70] absorbs the outgoing waves without spurious reflections and "perfectly" simulates unbounded wave propagations. The wave equation with the complex coordinate stretched PML is given by [71]

$$\frac{1}{s_r(x)}\frac{\partial}{\partial x}\left(\frac{1}{s_r(x)}\frac{\partial\Phi}{\partial x}\right) + \frac{1}{s_r(y)}\frac{\partial}{\partial y}\left(\frac{1}{s_r(y)}\frac{\partial\Phi}{\partial y}\right) + k_0^2\Phi = 0 \tag{7.7}$$

where $s_r = 1 + i_0\sigma/\omega\varepsilon_0$, i_0 is the imaginary unit, ε_0 is the permittivity of free space, and the conductivities $\sigma(x)$ and $\sigma(y)$ are nonzeros only within PML layers normal to the x- and y-axes, respectively. The optimized conductivities are chosen as

$$\begin{aligned}\sigma_i &= \frac{0.02}{\Delta}\left(\frac{2i-1}{16}\right)^{3.7}, \quad i = 1,\ldots,8\\ \sigma_{i+0.5} &= \frac{0.02}{\Delta}\left(\frac{2i}{16}\right)^{3.7}, \quad i = 0,\ldots,8\end{aligned} \tag{7.8}$$

where $\Delta = \Delta_x$ or $\Delta = \Delta_y$ for the PML layers normal to the x- or y-axis, and i is the grid index of the eight-layer PML.

At the outermost boundary of the PML, a Mur ABC [72] replacing the traditional perfectly electric conductor truncation boundary is employed to further reduce the spurious numerical reflections. Taking the top plane $y = 0$ as an example, the second-order Mur ABC can be written as

$$\left[\frac{\partial}{\partial y} + i_0\left(k_0 + \frac{1}{2k_0}\frac{\partial^2}{\partial x^2}\right)\right]\Phi\Big|_{y=0} = 0 \tag{7.9}$$

and its discretized form is

$$f_1\Phi(i,j) + f_2\Phi(i-1,j) + f_3\Phi(i+1,j) + f_4\Phi(i,j+1) = 0 \tag{7.10}$$

where

$$\begin{aligned}f_1 &= 2\exp(-i_0k_0\Delta_y) - 2k_0^2\Delta_x^2\exp(-i_0k_0\Delta_y) - 2\\ f_2 &= f_3 = 1 - \exp(-i_0k_0\Delta_y)\\ f_4 &= 2k_0^2\Delta_x^2\end{aligned} \tag{7.11}$$

Regarding a periodic OSC device, the periodic boundary conditions need to be implemented. According to the Floquet or Bloch theorem, we have

$$\begin{aligned}\Phi(x+P,y) &= \Phi(x,y)\exp(i_0k_0\sin\theta\cdot P)\\ \Phi(x,y) &= \Phi(x+P,y)\exp(-i_0k_0\sin\theta\cdot P)\end{aligned} \tag{7.12}$$

where P is the periodicity and θ is the incident angle with respect to the y-axis.

It should be noted that the FDFD equations of (7.1) and (7.2) are specially for total field. The scattered field equations to be solved can be derived by using the relations

$$H_z = H_z^i + H_z^s \tag{7.13}$$

and

$$E_z = E_z^i + E_z^s \tag{7.14}$$

where E_z^i (H_z^i) is the incident electric-field (magnetic-field), and E_z^s (H_z^s) is the scattered electric-field (magnetic-field).

7.3.3 Volume Integral Equation Method

As a rigorous solution to Maxwell's equations, a volume integral equation (VIE) method [59] is developed to characterize the optical properties of 3D OSCs. Considering nonmagnetic optical materials with an arbitrary inhomogeneity profile, the VIE can be written as

$$\mathbf{E}^i(\mathbf{r}) = \frac{\mathbf{J}(\mathbf{r})}{-i_0\omega(\varepsilon(\mathbf{r}) - \varepsilon_0)} - i_0\omega\mu_0 \int_v \overline{\mathbf{G}}(\mathbf{r}, \mathbf{r}') \cdot \mathbf{J}(\mathbf{r}')\mathrm{d}\mathbf{r}' \tag{7.15}$$

and

$$\mathbf{J} = -i_0\omega\mathbf{P} = -i_0\omega(\varepsilon - \varepsilon_0)\mathbf{E} \tag{7.16}$$

where i_0 is the imaginary unit, $\mathbf{E}^i(\mathbf{r})$ is the incident electric field of the light, $\varepsilon(\mathbf{r})$ is the position-dependent permittivity of the inhomogeneous materials, $\mathbf{J}$ is the volumetric polarization current to be solved, and $\overline{\mathbf{G}}(\mathbf{r}, \mathbf{r}')$ is the dyadic Green's tensor in free space. The widely adopted approach for solving the VIE is the discrete dipole approximation (DDA) method [73]. Due to the hypersingularity of the Green's tensor and spurious discontinuity of the tangential E-field induced by the scalar (piecewise constant) basis functions, the DDA method cannot accurately characterize the subwavelength plasmonic physics [74] and breaks down in the multilayered device structure with high-contrast metallic nanostructures. Here, we develop an alternate algorithm to bypass the difficulties. In our model, the polarization currents are expanded using the roof-top vector basis functions [75], and thus the continuity of normal current is naturally satisfied at the material interfaces. Furthermore, the hypersingular Green's tensor is smoothened by using the finite-difference approximation.

From the VIE (7.15), the scattered electric field generated by the volumetric polarization current $\mathbf{J}$ can be written as

$$\mathbf{E}^s(\mathbf{r}) = i_0\omega\mu_0 \int_v \overline{\mathbf{G}}(\mathbf{r}, \mathbf{r}') \cdot \mathbf{J}(\mathbf{r}')\mathrm{d}\mathbf{r}' \tag{7.17}$$

Considering the Cartesian coordinate system, we use the short notation (u_1, u_2, u_3) instead of (x, y, z), then we have

$$\begin{bmatrix} E_1^s \\ E_2^s \\ E_3^s \end{bmatrix} = \begin{bmatrix} L_{11} & L_{12} & L_{13} \\ L_{21} & L_{22} & L_{23} \\ L_{31} & L_{32} & L_{33} \end{bmatrix} \begin{bmatrix} J_1 \\ J_2 \\ J_3 \end{bmatrix} \tag{7.18}$$

where

$$L_{ij} = \begin{cases} L_{ii}^{\mathrm{c}} + L_{ii}^{\mathrm{q}}, \ i = j \\ L_{ij}^{\mathrm{q}}, \ i \neq j \end{cases} \tag{7.19}$$

$$L_{ii}^{\mathrm{c}} J_i = i_0 \omega \mu_0 \int\limits_v g(\mathbf{r}, \mathbf{r}') J_i(\mathbf{r}') \mathrm{d}\mathbf{r}' \tag{7.20}$$

$$L_{ij}^{\mathrm{q}} J_j = \frac{i_0}{\omega \varepsilon_0} \frac{\partial}{\partial u_i} \int\limits_v g(\mathbf{r}, \mathbf{r}') \frac{\partial J_j(\mathbf{r}')}{\partial u_j'} \mathrm{d}\mathbf{r}' \tag{7.21}$$

where $g(\mathbf{r}, \mathbf{r}')$ is the scalar Green's function, and $\overline{\mathbf{G}}(\mathbf{r}, \mathbf{r}') = \left[\overline{\mathbf{I}} + \frac{\nabla\nabla}{k_0^2}\right] g(\mathbf{r}, \mathbf{r}')$.

Using the roof-top basis functions to expand the unknown currents, we have

$$\mathbf{J}(\mathbf{r}) = \sum_{i=1}^{3} \mathbf{u}_i \sum_{k,m,n} J_i^D(k,m,n) T_{k,m,n}^i \tag{7.22}$$

where $T_{k,m,n}^1$, $T_{k,m,n}^2$, and $T_{k,m,n}^3$ are the volumetric roof-top functions given by

$$\begin{aligned} T_{k,m,n}^1 &= \Lambda_k(u_1) \Pi_m(u_2) \Pi_n(u_3) \\ T_{k,m,n}^2 &= \Pi_k(u_1) \Lambda_m(u_2) \Pi_n(u_3) \\ T_{k,m,n}^3 &= \Pi_k(u_1) \Pi_m(u_2) \Lambda_n(u_3) \end{aligned} \tag{7.23}$$

The functions $\Lambda_k(u_1)$ and $\Pi_m(u_2)$ are defined by

$$\begin{aligned} \Lambda_k(u_1) &= \begin{cases} 1 - \frac{|u_1 - k\Delta u_1|}{\Delta u_1}, & |u_1 - k\Delta u_1| \leq \Delta u_1 \\ 0, & \text{else} \end{cases} \\ \Pi_m(u_2) &= \begin{cases} 1, & \left|u_2 - \left(m - \frac{1}{2}\right)\Delta u_2\right| < \frac{\Delta u_2}{2} \\ 0, & \text{else} \end{cases} \end{aligned} \tag{7.24}$$

The cuboid cells are employed to discretize the structure to be modeled. Here, Δu_1 and Δu_2 are the grid sizes of each small cuboid along x and y directions, respectively. Other functions in (7.23) can be defined in the same way.

As a result, the discretized form for the operator L_{ii}^{c} in (7.20) can be written as

$$L_{ii}^{D,c} J_i^D = i_0 \omega \mu_0 g^D \otimes J_i^D \tag{7.25}$$

where $\otimes$ denotes the discrete convolution

$$g^D \otimes J_i^D = \sum_{k',m',n'} g^D(k-k', m-m', n-n') J_i^D(k', m', n') \tag{7.26}$$

and

$$g^D(k,m,n) = \int_0^{\Delta u_1} \int_0^{\Delta u_2} \int_0^{\Delta u_3} g(u_{1,k} - u_1', u_{2,m} - u_2', u_{3,n} - u_3') \mathrm{d}u_1' \mathrm{d}u_2' \mathrm{d}u_3' \tag{7.27}$$

Likewise, the operator L_{12}^q in (7.21) can be discretized as

$$\begin{aligned} L_{12}^{D,q} J_2^D &= \frac{i_0}{\omega \varepsilon_0 \Delta u_1 \Delta u_2} \left[g^D(k+1,m,n) - g^D(k,m,n) \right] \\ &\quad \otimes \left[J_2^D(k,m,n) - J_2^D(k,m-1,n) \right] \\ &= \frac{i_0}{\omega \varepsilon_0 \Delta u_1 \Delta u_2} \left\{ \left[g^D(k+1,m,n) - g^D(k,m,n) \right] \right. \\ &\quad \left. - \left[g^D(k+1,m-1,n) - g^D(k,m-1,n) \right] \right\} \otimes J_2^D(k,m,n) \end{aligned} \tag{7.28}$$

where the finite-difference method is used for the smooth approximation of the dyadic Green's function.

The computations of the discrete convolutions can be performed efficiently by means of cyclic convolutions and FFT [76], which is similar to the DDA method. As a traditional iterative solver of the resulting VIE matrix equation, the conjugate-gradient method [77] converges very slowly and will produce the nonphysical random errors in the calculation of optical absorption. To tackle the problem, we employ the fast and smoothly converging biconjugate gradient stabilized (BI-CGSTAB) method [78] (See Appendix). The FFT is adopted to accelerate the matrix–vector multiplications encountered in the BI-CGSTAB solver with computational complexity of $O(N \log N)$ and memory of $O(N)$.

7.3.4 Physical Quantities Extraction

Through the rigorous solutions to Maxwell's equations, we can access some important physical quantities to reveal the physical mechanism of plasmonic effects in OSCs and optimize device performances.

The absorption spectrum of OSCs is calculated by

$$S_{\mathrm{A}}(\lambda) = \int_v n_{\mathrm{r}}(\lambda) k_i(\lambda) \frac{2\pi c_0}{\lambda} \varepsilon_0 |\mathbf{E}|^2 \mathrm{d}V \tag{7.29}$$

where $n_c = n_r + i_0 k_i$ is the complex refractive index of the active material, λ is the incident wavelength, and c_0 is the speed of light in free space. It is worth mentioning that the absorption of metallic nanostructures should be precluded in the volume integral above. A spectral enhancement factor is the absorption spectrum of the OSC incorporating metallic nanostructures over that excluding the nanostructures.

Integrating with a standard solar irradiance spectrum (air mass 1.5 global), one can get the total absorption of OSCs

$$T_A = \int_{400\,\mathrm{nm}}^{800\,\mathrm{nm}} S_A(\lambda)\Gamma(\lambda)\mathrm{d}\lambda \tag{7.30}$$

where Γ is the solar irradiance spectrum. Likewise, a total enhancement factor is the total absorption of the OSC incorporating metallic nanostructures over that excluding the nanostructures. In addition, a total absorptivity is also an important physical quantity to evaluate the absorption performance of OSCs, i.e.

$$A = \frac{\int_{400\,\mathrm{nm}}^{800\,\mathrm{nm}} S_A(\lambda)\Gamma(\lambda)\mathrm{d}\lambda}{\int_{400\,\mathrm{nm}}^{800\,\mathrm{nm}} \Gamma(\lambda)\mathrm{d}\lambda} \tag{7.31}$$

The exciton generation rate, which determines the short current of OSCs, can be written as

$$G(\mathbf{r}) = \int_{400\,\mathrm{nm}}^{800\,\mathrm{nm}} \frac{2\pi}{h} n_r(\lambda) k_i(\lambda) \varepsilon_0 |\mathbf{E}(\mathbf{r})|^2 \Gamma(\lambda)\mathrm{d}\lambda \tag{7.32}$$

where h is the Planck constant.

Except for the above physical quantities essential to the performance of OSC, there are several quantities that can facilitate understanding the physics of plasmonic effects. The scattering cross-section, which can estimate the scattering strength of a metallic nanostructure, is defined by [79, 80]

$$\sigma_s = \frac{\int_s \mathrm{Re}\left[\frac{1}{2}\mathbf{E}^s \times \mathrm{conj}(\mathbf{H}^s)\right] \cdot \mathrm{d}\mathbf{S}}{|\mathbf{S}_i|} \tag{7.33}$$

where "conj" denotes the complex conjugation, S is an arbitrary surface enclosing the metallic nanostructure, $\mathbf{S}_i = \frac{1}{2}\left[\mathbf{E}^i \times \mathrm{conj}\left(\mathbf{H}^i\right)\right]$ is the incident energy flux, and $\mathbf{E}^s$ and $\mathbf{H}^s$ are the scattered electric and magnetic fields, respectively. Considering the total power absorbed by a metallic nanostructure, the absorption cross-section is of the form [79, 80]

$$\sigma_a = -\frac{\int_s \mathrm{Re}\left[\frac{1}{2}\mathbf{E} \times \mathrm{conj}(\mathbf{H})\right] \cdot \mathrm{d}\mathbf{S}}{|\mathbf{S}_i|} = \frac{\int_v k_0 \varepsilon_r''(\mathbf{r})|\mathbf{E}(\mathbf{r})|^2 \mathrm{d}V}{|\mathbf{E}^i|^2} \tag{7.34}$$

where ε_r'' is the imaginary part of relative permittivity. The extinction (total) cross-section describes the intrinsic losses of a plasmonic system including both absorption loss and scattering (or leaky) loss. Hence, the sum of the scattering and the absorption cross-section is the extinction cross-section. Moreover, we have another mathematical expression for the extinction cross-section by making use of the optical theorem at the far-field limit [80]

$$\sigma_e = \frac{4\pi}{k_0} \mathrm{Im}[\mathbf{e}^i \cdot \overline{\mathbf{F}} \cdot \mathbf{e}^i] \tag{7.35}$$

and

$$\mathbf{E}^s = \frac{\exp(i_0 k_0 r)}{r} \overline{\mathbf{F}} \cdot \mathbf{E}^i, \quad r \to \infty \tag{7.36}$$

where $\mathbf{e}_i$ is the polarization unit vector of the incident electric field $\mathbf{E}^i$.

To understand the mode hybridization for plasmon coupling, the polarization charge distribution on the surface of metallic nanostructure is given as follows

$$\rho_p = \nabla \cdot (\varepsilon_0 \mathbf{E}) = -\nabla \cdot \mathbf{P} \tag{7.37}$$

where $\mathbf{P} = (\varepsilon - \varepsilon_0)\mathbf{E}$ is the polarization density. Based on the divergence-free condition, the polarization charge is definitely zero except on the heterogeneous boundaries.

The Fabry-Pérot mode or quasi-guided mode can be characterized by analyzing the averaged power density of electromagnetic waves flowing within an active or a grating layer along the lateral direction of OSC devices, which is expressed in

$$P_x = \frac{1}{2} \mathrm{Re}\left[E_y H_z^\dagger - E_z H_y^\dagger\right] \tag{7.38}$$

where "†" is a notation of complex conjugation and the power density flows along the x direction.

7.4 Results and Discussions

We will review plasmonic effects of typical metallic nanostructures by involving their functionalities and performances in manipulating the optical properties of OSCs. The SPR, LPR, and their hybridization are investigated in the three following cases [16, 30, 33]. In modeling OSCs, the complex refractive indices of metals (Au, Ag, etc) and organic materials can be expressed by the Brendel-Bormann model [81] and measured from ellipsometry [82, 83], respectively. It is worth mentioning that standard solar irradiance spectrum (air mass 1.5 global) is taken into account in our theoretical models.

7.4.1 Periodic Back Nanostrips

We systematically study the angular response of a thin-film OSC with a periodic metal back nanostrips. The generalized equation of Lambert's cosine law for arbitrary periodic structure is formulated. We find that the periodic strip structure can achieve wide-angle absorption enhancement compared with the (planar) nonstrip structure for both the TE- and TM-polarized light. The quasi-guided modes supported by the periodic strip structure contribute to the enhancement for the TE-polarized light. The SPRs excited by the subwavelength Au nanostrips contribute to the enhancement for the TM-polarized light.

The energy conservation law in a periodic structure is given by

$$[1 - L(\theta)] \cdot \int \frac{-1}{2} \mathrm{Re}\left[\mathbf{E}^i \times \mathrm{conj}\left(\mathbf{H}^i\right)\right] \cdot \mathrm{d}\mathbf{S} = \int n_\mathrm{r} k_i \omega \varepsilon_0 |\mathbf{E}|^2 \mathrm{d}V \tag{7.39}$$

where $\mathbf{E}^i$ and $\mathbf{H}^i$ are the incident electric and magnetic fields, $\mathbf{S}$ is a virtual planar surface in front of a unit cell of the SC, $n_\mathrm{c} = n_\mathrm{r} + i_0 k_i$ are the complex refractive indices of the active materials, and $L(\theta)$ is an energy loss fraction. One part of the energy loss is the scattering loss, which can be characterized by the summation of the reflectance and transmittance of the periodic structure [66]. The scattering loss can be reduced by the light guiding, enhancement, and trapping schemes. Another part of the energy loss is the metallic absorption loss, which can be reduced by engineering the metal's size, material, and position. The irradiance of the Sun is the incident power per unit area of an electromagnetic radiation at the surface, i.e.

$$I = \frac{-1}{2} \mathrm{Re}\left[\mathbf{E}^i \times \mathrm{conj}\left(\mathbf{H}^i\right)\right] \cdot \mathbf{n} = \frac{\left|\mathbf{E}^i\right|^2}{2Z_0} \cos\theta \tag{7.40}$$

where $Z_0 = \sqrt{\mu_0/\varepsilon_0}$ is the wave impedance of free space and θ is the incident angle of the sunlight with respect to the normal direction of the surface $\mathbf{S}$. For the Lambertian bulk cells, which have an angle-independent energy loss fraction L, the absorption of the active layers represented by the right hand of Eq. (7.39) obeys Lambert's cosine law that the absorption is a cosine function of the incident angle θ. Eq. (7.39) is a generalized equation of Lambert's cosine law for any periodically structured SCs.

Figure 7.2a illustrates a typical structure of standard OSCs without any optimizations. The heterojunction active layer is composed of copper phthalocyanine (CuPc) and fullerene (C_{60}) as an electron donor and acceptor, respectively. The bathocuproine (BCP) layer is a spacer layer for extracting electrons. A metallic back nanopattern is made from an Au strips and Poly(3,4-ethylenedioxythiophene):poly(4-styrenesulfonic acid) (PEDOT:PSS; AI4083) that can collect holes. We use the FDFD method presented in Sect. 7.3.2 to calculate the angular response of the OSC. For the angular response simulation, a challenging problem lies at the wide angle (0°–90°) and broadband (400–800 nm) calculations. We employ the high-performance parallel computing technique to tackle the problem.

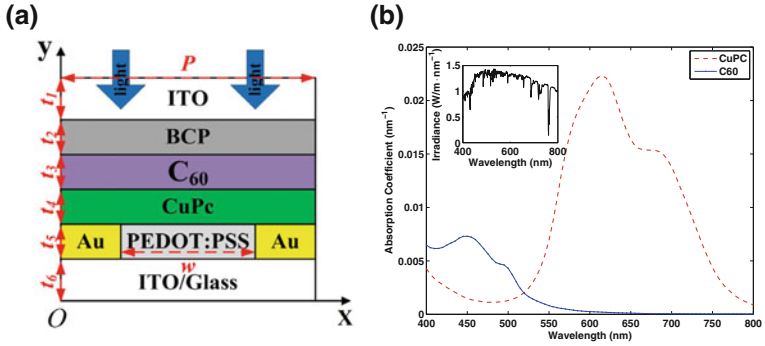

Fig. 7.2 **a** The schematic structure of a unit cell of the flat-heterojunction OSC. The structural parameters are $t_1 = 100$ nm, $t_2 = 10$ nm, $t_3 = 40$ nm, $t_4 = 30$ nm, $t_5 = 30$ nm, $t_6 = 100$ nm, $w = 100$ nm, and $P = 200$ nm; **b** the absorption coefficients of CuPc and C_{60}. The *inset* is the solar irradiance spectrum of an air mass 1.5 global. ©2011 OSA; Ref. [16]

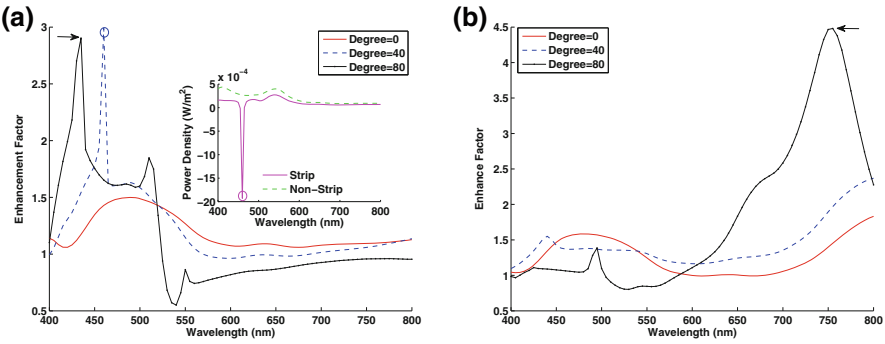

Fig. 7.3 The absorption of the periodic strip structure is compared to that of the nonstrip structure replacing the laterally periodic Au-PEDOT:PSS-Au pattern by the planar PEDOT:PSS layer. The near-field profiles of the absorption peaks pointed by the *arrows* are shown in Fig. 7.4. **a** The absorption enhancement factor for the TE polarization. The *inset* shows the averaged power density of the Au-PEDOT:PSS-Au pattern along the x direction calculated by Eq. (7.38). The negative power density peak due to the opposite propagation direction coincides with the absorption peak at $\theta = 40^\circ$ with the wavelength of 460 nm; **b** the absorption enhancement factor for the TM polarization. ©2011 OSA; Ref. [16]

Figure 7.2b shows the absorption coefficients of CuPc and C_{60}. The separated absorption peaks can improve the light absorption of OSCs, which can be realized by different enhancement mechanisms with respect to different materials. Compared with the absorption of the nonstrip structure making from the planar PEDOT:PSS layer, the enhancement factors of the absorption for the strip structure of the laterally periodic Au-PEDOT:PSS-Au pattern are shown in Fig. 7.3a, b for the TE and TM polarizations, respectively.

For the TE polarization, the absorption enhancement is obtained from 400 to 500 nm with the very strong absorption peaks, especially at the oblique angles.

The rapid and extraordinary variations in the absorption over narrow frequency bands imply the resonant Wood's anomalies with asymmetric Fano line shape [36, 37]. Figure 7.4a shows the E-field of the absorption peak pointed by the arrow in Fig. 7.3a for the Wood's anomalies. The intense E-field in the active layer is bounded between the periodic nanostrip pattern and the BCP layer. The E-field is related to the quasi-guided modes supported by the periodic strip structure with the phase-matching condition of $k_0 \sin\theta + 2\pi m/P = \pm\mathrm{Re}(\beta), m = 0, \pm 1, \pm 2, \ldots$, where P is the periodicity, k_0 is the incident wave number, and β is the complex propagation constant of the quasi-guided modes. The condition is easily satisfied in standard OSCs in view of the broadband and wide angle Sun illumination. For confirming the forced-resonance behavior of the Wood's anomalies, we calculate the averaged power density flowing in the x direction for the Au-PEDOT:PSS-Au pattern (strip structure) and PEDOT:PSS layer (nonstrip structure). For the strip structure, as shown in the inset of Fig. 7.3a, the negative (opposite direction) power density peak induced by the $n = -1$ space harmonics coincides with the absorption peak at $\theta = 40^\circ$ and 460 nm. In addition, the spectral overlap between the Wood's anomalies and the material absorption of C_{60} will be of a good help for short wavelength photon harvesting. Particularly, we can observe the sharp oscillations of the enhancement factor at $\theta = 80^\circ$ from 510 to 550 nm. The sharp oscillations result from the overlap between the Fabry-Pérot mode in the nonstrip structure and the quasi-guided mode in the strip structure. It should be noted that the quasi-guided mode is an eigenmode of Maxwell's equations for arbitrary periodic structure and cannot be excited in the planar nonstrip structure by the plane wave due to the momentum mismatch ($\beta > k_0$). However, the Fabry-Pérot mode can be found in the planar structure, and can be understood by the mode coupling between the excitation solution and the eigenmode.

For the TM polarization, a broadband absorption enhancement is obtained from 650 to 800 nm, especially at the oblique angles. Figure 7.4b shows the H-field of the absorption peak pointed by the arrow in Fig. 7.3b. The concentrated H-field at the interface between Au and CuPc layers is due to the SPRs excited by the evanescent waves produced by the subwavelength nanostrips. Regarding the absorption peaks around 750–800 nm in Fig. 7.3b, they are blue shifted as the incident angle increases due to the blue shift of the plasmon-coupled Fabry-Pérot mode. By studying the SPR spectrum (Fig. 7.3b; black straight-dotted line) and the absorption spectrum of CuPc (Fig. 7.2b; red dashed line) together, it is observed that the SPR peak at 675 nm is weaker than that at 755 nm because of the stronger absorption of CuPc at 675 nm.

Figure 7.5a, b shows the total absorptivity defined in Eq. (7.31) as a function of the incident angle, respectively, for the TE and TM polarizations. The ideal total absorptivity governed by the generalized Lambert's cosine law is calculated by $A_0 \cos\theta$, where A_0 is the total absorptivity under the vertical incidence condition. The total absorptivity of the strip structure is noticeably better than that of the nonstrip structure for both polarizations. The improvements are caused by the Wood's anomalies and the SPRs that have been explained previously. When the incident angle increases, the total absorptivity for the TM polarization decays

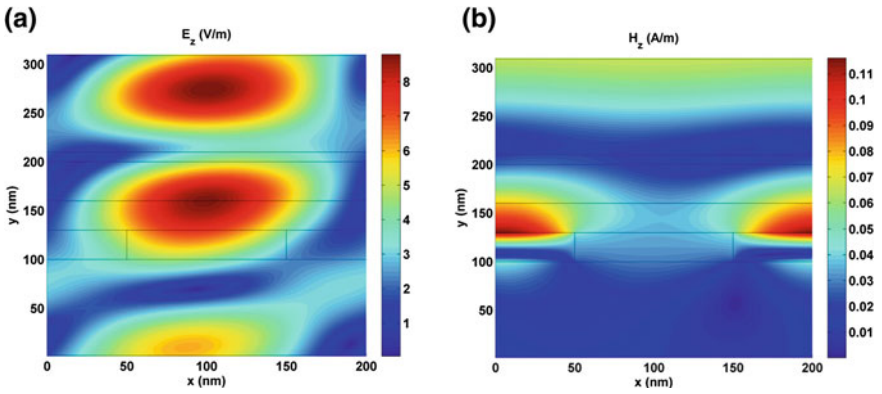

Fig. 7.4 **a** E_z field profile of the TE polarization at $\theta = 80°$ with the wavelength of 435 nm; **b** H_z field profile of the TM polarization at $\theta = 80°$ with the wavelength of 755 nm. ©2011 OSA; Ref. [16]

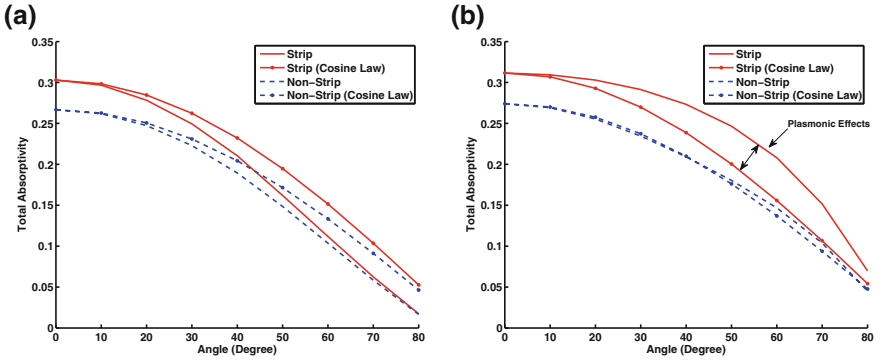

Fig. 7.5 The total absorptivity as a function of the incident angle θ. The generalized Lambert's cosine law (*straight-dotted* and *dash-dotted curves*) is calculated by $A_0 \cos\theta$, where A_0 is the total absorptivity under the vertical incidence condition. **a** TE polarization; **b** TM polarization. ©2011 OSA; Ref. [16]

slower than that for the TE polarization, which is independent of the structure. This feature may be understood by the fact that better light confinement can be achieved for the TM-polarized light where the *E*-field is not continuous across inhomogeneous material interfaces. For the TE polarization, the absorption of the strip structure becomes comparable to that of the nonstrip structure near grazing angles. The narrow absorption peaks due to the Wood's anomalies can improve the total absorption, but the improvement is smaller than that from the SPRs in the TM-polarized light. For the TM polarization, the plasmon-induced absorption enhancement strongly breaks the limit of the generalized Lambert's cosine law and shows the "super-Lambertian" absorption. The broadband and wide-angle

absorption enhancements by the SPRs will be of a great help for high-efficiency photovoltaic cells.

In conclusion, we have formulated the equation of the generalized Lambert's cosine law and comprehensively studied the Au nanostrip OSC structure for enhancing the TE- and TM-polarized light with the detailed explanations of the enhancements by the Wood's anomalies and SPRs.

7.4.2 Multiple Nanospheres

We studied in detail on the near-field multiple scattering effects of plasmonic nanospheres (NSPs) embedded into thin-film OSCs. The fundamental physics of the optical absorption shows remarkable differences between the NSPs embedded into a spacer and those embedded into an active layer. The direction-dependent features of near-field scattering from NSPs significantly affect the absorption enhancement when NSPs are embedded into the spacer. The interaction between longitudinal and transverse modes supported in the NSP chain plays a key role in the absorption enhancement when NSPs are embedded into the active layer. Through properly engineering the position and spacing of NSPs, our theoretical results show that the absorption enhancement can be improved by about 100 %. Moreover, we demonstrate the breakdown of the electrostatic scaling law that should be considered in the design of OSCs. The work provides the physical guidelines for plasmonic OSCs.

Figure 7.6a, b illustrates a schematic pattern of a bulk heterojunction OSC nanostructure [2, 3] to be investigated. The active layer is a typical blend polymer of P3HT (poly(3-hexylthiophene)) and PCBM (methanofullerene). A hole conduction layer is PEDOT:PSS chosen as a spacer between an electrode and the active layer. Figure 7.6c shows the absorption coefficient of the active material. With tunable size and spacing, a spherical chain comprising multiple silver (Ag) NSPs is embedded into the spacer or active layer as near-field concentrators. An incident light is propagated from the spacer to the active layer with a TM polarization ($H_z^i = 0$) at a vertical (0°) and an oblique (60°) incidences. In comparison with the TE polarization, the TM polarization supports much stronger dipole–dipole couplings between NSPs. Moreover, the absorption enhancement by a silver NSP array, which has a polarization-independent feature, can be regarded as a superposition of those by silver NSP chains with both the TM and TE polarizations. To unveil device-related multiple scattering mechanism of NSPs, we develop a rigorous VIE method presented in Sect. 7.3.3 to characterize the optical properties of the OSC. The coupling between multiple NSPs, as well as the interaction between NSPs and multilayer device structure, is fully taken into account in our model. It is worth mentioning that we only calculate the optical absorption of the active material excluding the metallic absorption of NSPs especially when NSPs are embedded into the active layer. Figures 7.7 and 7.8 show the spectral enhancement factors (defined

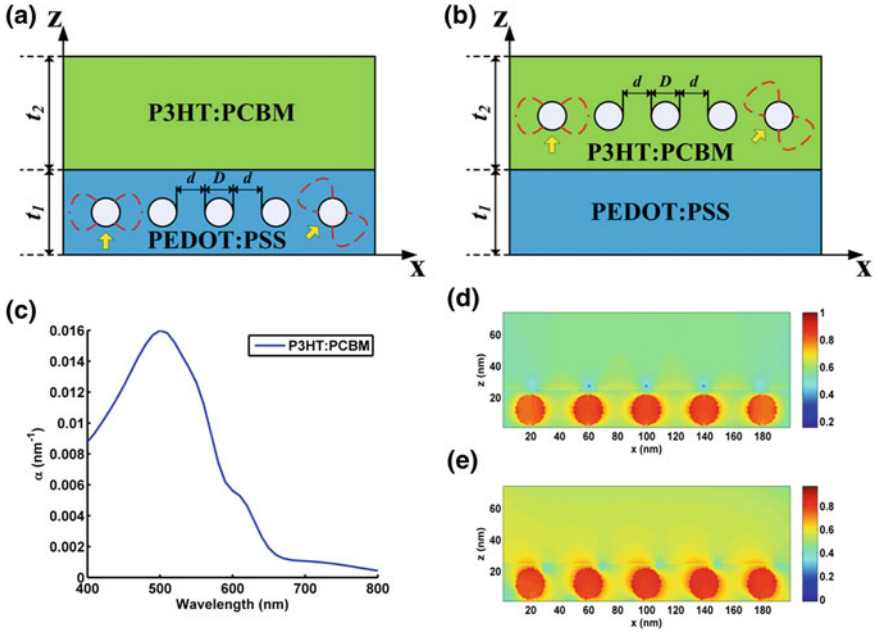

Fig. 7.6 **a**, **b** A schematic OSC nanostructure. To enhance the optical absorption of the OSC, a spherical chain comprising multiple NSPs is embedded into a spacer layer (PEDOT:PSS) or into an active layer (P3HT:PCBM). The geometric size is $t_1 = 1.25D$ and $t_2 = 2.5D$. The spacing between adjacent NSPs is $d = D$ or $d = 0.2D$ for the separated or close-packed ones, respectively. The diameter is $D = 20$ or $D = 40$ nm for the small or large NSPs, respectively. The *yellow arrows* represent the propagation direction of an incident light with a TM polarization ($H_z^i = 0$) and the *red dashed lines* denote corresponding near-field profiles of NSPs. **c** Absorption coefficient of the active material. **d**, **e** Near-field polarization current distributions of the OSC nanostructure at a vertical and an oblique incidences, respectively. ©2011 AIP; Ref. [30]

in Sect. 7.3.4). Table 7.1 lists the total enhancement factors (defined in Sect. 7.3.4) corresponding to Figs. 7.7 and 7.8.

When Ag NSPs are embedded into the spacer, as the incident angle increases, both the spectral and total enhancement factors increase independent of the NSP's size and spacing. The fundamental physics is that the near-field energy of a metal nanoparticle is mainly distributed along the polarization direction of incident *E*-field, which is critically different from the far-field scattering, where the energy scatters to the propagation direction of the incident light. As shown in Fig. 7.6a, d, the concentrated electric near field is distributed along the lateral direction at the vertical incidence, which deters the plasmonic resonance from enhancing the light absorption of the active material even though very strong near field is obtained. Hence, a careful design in introducing NSPs into a multilayer device structure is critical for enhancing the performances of plasmonic OSCs. Interestingly, absorption enhancement improves at the oblique incidence, because more energy transfers to the active layer having a significant directivity as depicted in Fig. 7.6e.

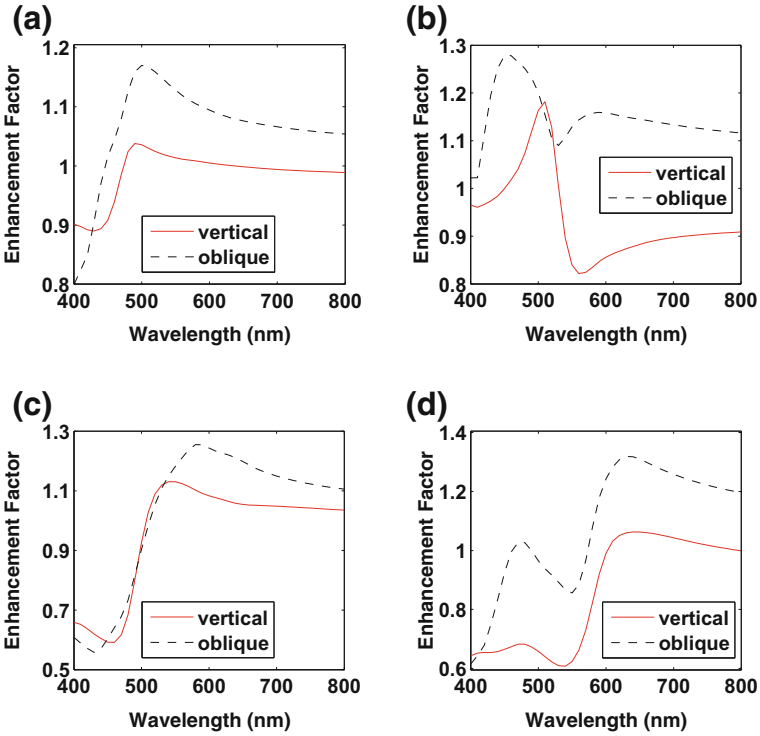

Fig. 7.7 The spectral enhancement factors of the OSC with NSPs are embedded into the spacer. The angular responses of the OSC for the vertical (0°) and oblique (60°) incidences are also shown: **a** separated small NSPs; **b** close-packed small NSPs; **c** separated large NSPs; **d** close-packed large NSPs. ©2011 AIP; Ref. [30]

It should be noticed that since the thickness of the active layer is thinner than one half of wavelength, near-field (not far field) physics plays a key role in the optical design of NSPs incorporated OSCs. Compared to the spectral enhancement factors for the separated NSPs, a deep dip can be observed for the close-packed ones as shown in Fig. 7.7b, d. The dips resulting from the metallic absorption of the NSPs correlate with the coupling resonance of the NSP chain. The close-packed NSPs, particularly for the large ones, block the light and absorb a large amount of sunlight energy. As a result, little energy penetrates into the active material. Due to the R^{-3} decay of electric near-field and the reflection by the interface between the spacer and active layer, the absorption enhancement is very small when NSPs are embedded into the spacer. Comparing Fig. 7.7d to Fig. 7.7b, the large close-packed NSPs with large scattering cross-section have more significant enhancement away from resonance but induce deeper dips near the resonance. Weighting the two effects, the large close-packed NSPs have smaller total enhancement factor as listed in Table 7.1.

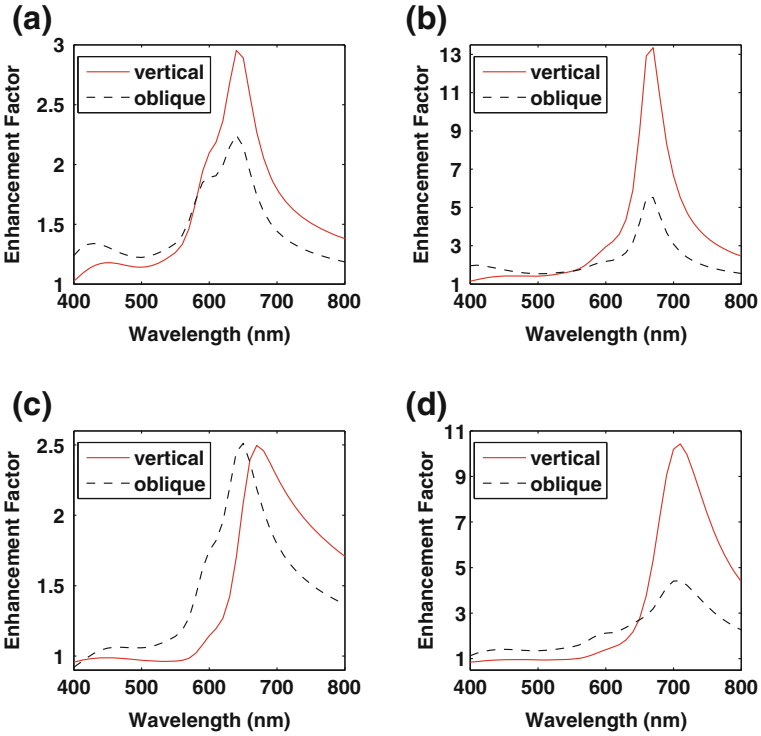

Fig. 7.8 The spectral enhancement factors of the OSC with NSPs are embedded into the active layer. The angular responses of the OSC for the vertical (0°) and oblique (60°) incidences are also shown: **a** separated small NSPs; **b** close-packed small NSPs; **c** separated large NSPs; **d** close-packed large NSPs. ©2011 AIP; Ref. [30]

Table 7.1 Total enhancement factors for the NSPs embedded into the spacer and active layer. ©2011 AIP; Ref. [30]

Spacer layer	Vertical incidence	Oblique incidence
Separated small	0.992	1.078
Close-packed small	0.989	1.174
Separated large	0.927	0.935
Close-packed large	0.725	0.960
Active layer	**Vertical incidence**	**Oblique incidence**
Separated small	1.366	1.374
Close-packed small	1.985	1.821
Separated large	1.118	1.216
Close-packed large	1.342	1.589

In contrast to the NSPs embedded into the spacer, our results show that the NSPs embedded into the active layer offer stronger optical absorption, which can be observed in Table 7.1. As seen in Fig. 7.6b, the scattering energy from the NSPs is directly and sufficiently absorbed by the contiguous active material uncorrelated with the directional property of the electric near field. Owing to the plasmon coupling and hybridization, the close-packed NSPs have more concentrated near-field distribution leading to larger enhancement (Table 7.1). Remarkably, the absorption of the OSC has about 2-fold increase by the small close-packed NSPs. For the large close-packed NSPs, the excessive red-shifted resonance reduces the spectral overlap between the resonance and the absorption peak of the active material as illustrated in Figs. 7.8d and 7.6c. At vertical incidence, the reduced spectral overlap gives a reason why the total enhancement factor by the large close-packed NSPs is smaller than that by the small ones. However, the total enhancement factor by the large close-packed NSPs increases at oblique incidence, which distinguishes from the close-packed small NSPs. The interplay between longitudinal and transverse modes [40, 84] supported by the NSP chain is a physical origin of the phenomenon. Having larger geometric size and stronger retardation effect, the large close-packed NSPs support more red-shifted longitudinal modes at the vertical incidence and more blue-shifted transverse modes at the oblique incidence (see Fig. 7.8b, d). In comparison with the red-shifted longitudinal modes, the blue-shifted transverse modes have a better spectral overlap with the absorption coefficient of the active material and can be further exploited or engineered in a future design of OSCs.

Regarding the electrostatic limit described by the Laplace equation, the near-field or far-field response of a subwavelength scatterer is independent of the scatterer's size and depends only on its shape [85]. Therefore, it may cause a misunderstanding that the same enhancement can be obtained if the scaling ratio of a device structure to a concentrator remains constant. However, using the same scaling ratio as shown in Fig. 7.6a, b, we find that the large NSPs and small ones have noticeable differences both in the spectral and total enhancement factors. The breakdown of the scaling law can be explained by the retarded and multiscale effects. The electromagnetic response of a single NSP is dominated by the electrostatic (nanocircuit) physics, but that of multiple NSPs is governed by the electrodynamic (wave) physics with nonnegligible retardation and long-range interplay between each NSPs. Furthermore, large-scale OSC nanostructure and small-scale NSPs strongly couple with each other, which makes the optical path very complicated; and the trapping confinement, together with leaky loss, must be considered quantitatively.

In conclusion, we study the near-field multiple scattering effects of plasmonic NSPs embedded into the thin-film OSC. The absorption enhancement of the OSC strongly depends on the directional property of near-field scattering from NSPs and the interplay between longitudinal and transverse modes supported for the NSPs embedded into the spacer and active layer, respectively. Moreover, the complex coupling between NSPs and device makes the scaling law in electrostatics inapplicable. The work provides the fundamental physical understanding and design guidelines for a typical class of plasmonic photovoltaics.

7.4.3 Hybrid Plasmonic System

We propose a novel optical design of OSC with a hybrid plasmonic system, which comprises a plasmonic cavity coupled with a dielectric core-metal shell (DC-MS) nanosphere. It has been investigated that optical absorption of the active polymer material has a 4-fold increase. With the help of rigorous VIE method presented in Sect. 7.3.3, we unveil the fundamental physics of the significant enhancement, which mainly attributes to the coupling of symmetric surface wave modes supported by the cavity resonator. We further demonstrate that the optical enhancement strongly depends on the decay length of surface plasmon waves penetrated into the active layer. Moreover, coherent interaction between the cavity and the DC-MS nanosphere is definitely confirmed by our theoretical model. A distribution of polarization charges on the surface of the cavity indicates a bonding and antibonding coupling modes [42] in the hybrid plasmonic system. The work introduces a new hybrid plasmonic cavity device structure to enhance the optical absorption of organic photovoltaics with detailed physical explanations.

Figure 7.9 shows the schematic pattern of a heterojunction OSC. A hybrid plasmonic system, which comprises a plasmonic cavity coupled with a dielectric core-metal shell nanosphere, is employed for improving the optical absorption of the active polymer material. A transparent spacer is inserted to avoid local shunt and extract carriers. The incident light is propagated from the spacer to the active layer at the vertical incident angle with an E-field polarized along the x direction. Figure 7.10a shows the real and imaginary parts of the refractive index of the active material.

First, various nanosphere concentrators (excluding the plasmonic cavity) are systematically and comparatively observed. These nanospheres include a dielectric sphere, a metal sphere, a metal core-dielectric shell (MC-DS) sphere, and a dielectric core-metal shell (DC-MS) sphere. The scattering cross-section (SCS) of the nanospheres can be obtained from the generalized reflection coefficients of the spherically layered media [59, 79, 80]

$$\sigma_s = \frac{2\pi}{K_3^2}\sum_{m=1}^{\infty}(2m+1)\left(\left|\tilde{R}_{3,2}^{\mathrm{TM}}(m)\right|^2+\left|\tilde{R}_{3,2}^{\mathrm{TE}}(m)\right|^2\right) \tag{7.41}$$

where 1, 2, and 3 denote the core, shell, and active layers as shown in Fig. 7.9, respectively, m is the order of the modified spherical Bessel (Hankel) functions, and $\tilde{R}_{3,2}^{\mathrm{TM}}$ and $\tilde{R}_{3,2}^{\mathrm{TE}}$ are the generalized reflection coefficients of the TM and TE spherical waves in the layer 3 reflected by the layer 2. For small spherical particles, the leading term ($m = 1$) of $\tilde{R}_{3,2}^{\mathrm{TM}}$ determines the value of the SCS. The generalized reflection coefficient can be written as a recursive equation

$$\tilde{R}_{i,i-1}^{\mathrm{TM}} = R_{i,i-1}^{\mathrm{TM}} + \frac{T_{i-1,i}^{\mathrm{TM}}\tilde{R}_{i-1,i-2}^{\mathrm{TM}}T_{i,i-1}^{\mathrm{TM}}}{1-R_{i-1,i}^{\mathrm{TM}}\tilde{R}_{i-1,i-2}^{\mathrm{TM}}} \tag{7.42}$$

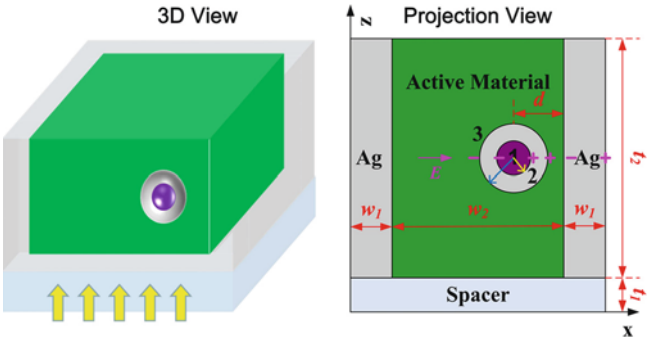

Fig. 7.9 The schematic pattern of a heterojunction OSC. A hybrid plasmonic system, which comprises a plasmonic cavity coupled with a dielectric core-metal shell nanosphere, is employed for improving the optical absorption of the active polymer material. A transparent spacer is inserted to avoid local shunt and extract carriers. The structural parameters are $t_1 = 20$ nm, $t_2 = 60$ nm, $w_1 = 30$ nm, $w_2 = 90$ nm, and $d = 21$ nm. The radius of the core layer (denoted by the *yellow arrow*) and that of the shell layer (denoted by the *blue arrow*) are set to $r_1 = 7.5$ nm and $r_2 = 15$ nm, respectively. For a bonding coupling mode in the hybrid system, the polarity of its polarization charge is also marked. ©2011 OSA; Ref. [33]

and

$$R_{i,i+1}^{\mathrm{TM}} = \frac{\sqrt{\varepsilon_{i+1}\mu_i}\hat{H}_m^{(1)}(K_{i+1}r_i)\hat{H}_m^{(1)'}(K_i r_i) - \sqrt{\varepsilon_i\mu_{i+1}}\hat{H}_m^{(1)'}(K_{i+1}r_i)\hat{H}_m^{(1)}(K_i r_i)}{\sqrt{\varepsilon_i\mu_{i+1}}\hat{J}_m(K_i r_i)\hat{H}_m^{(1)'}(K_{i+1}r_i) - \sqrt{\varepsilon_{i+1}\mu_i}\hat{H}_m^{(1)}(K_{i+1}r_i)\hat{J}'_m(K_i r_i)} \tag{7.43}$$

$$T_{i,i+1}^{\mathrm{TM}} = \frac{i_0\varepsilon_{i+1}\sqrt{\mu_{i+1}/\varepsilon_i}}{\sqrt{\varepsilon_i\mu_{i+1}}\hat{J}_m(K_i r_i)\hat{H}_m^{(1)'}(K_{i+1}r_i) - \sqrt{\varepsilon_{i+1}\mu_i}\hat{H}_m^{(1)}(K_{i+1}r_i)\hat{J}'_m(K_i r_i)} \tag{7.44}$$

$$R_{i,i-1}^{\mathrm{TM}} = \frac{\sqrt{\varepsilon_i\mu_{i-1}}\hat{J}_m(K_i r_{i-1})\hat{J}'_m(K_{i-1}r_{i-1}) - \sqrt{\varepsilon_{i-1}\mu_i}\hat{J}'_m(K_i r_{i-1})\hat{J}_m(K_{i-1}r_{i-1})}{\sqrt{\varepsilon_{i-1}\mu_i}\hat{J}_m(K_{i-1}r_{i-1})\hat{H}_m^{(1)'}(K_i r_{i-1}) - \sqrt{\varepsilon_i\mu_{i-1}}\hat{H}_m^{(1)}(K_i r_{i-1})\hat{J}'_m(K_{i-1}r_{i-1})} \tag{7.45}$$

$$T_{i,i-1}^{\mathrm{TM}} = \frac{i_0\varepsilon_{i-1}\sqrt{\mu_{i-1}/\varepsilon_i}}{\sqrt{\varepsilon_{i-1}\mu_i}\hat{J}_m(K_{i-1}r_{i-1})\hat{H}_m^{(1)'}(K_i r_{i-1}) - \sqrt{\varepsilon_i\mu_{i-1}}\hat{H}_m^{(1)}(K_i r_{i-1})\hat{J}'_m(K_{i-1}r_{i-1})} \tag{7.46}$$

where r_i, ε_i, μ_i, and K_i are the radius, permittivity, permeability, and wave number of the ith spherical layer, respectively. Figure 7.10b, c shows the spectral enhancement factors (defined in Sect. 7.3.4) and the SCS of the nanospheres,

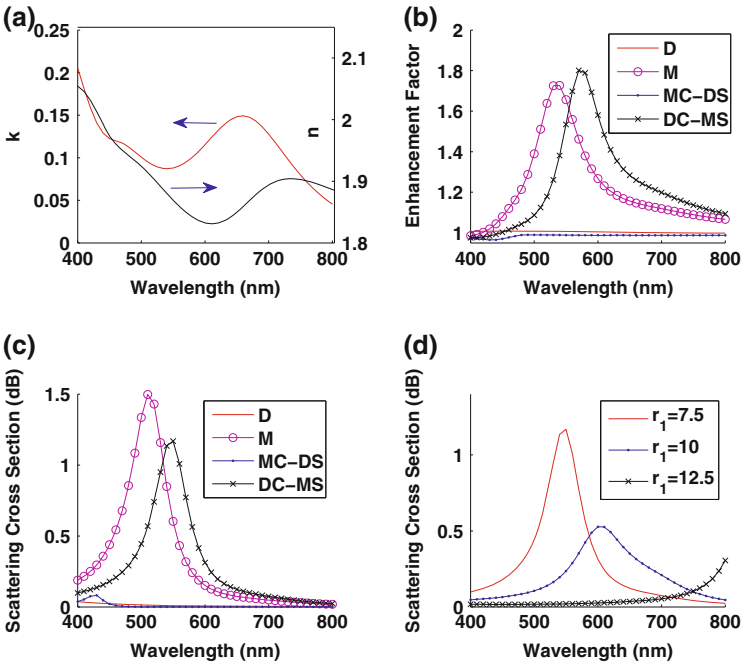

Fig. 7.10 **a** The real and imaginary parts of the refractive index of the active material; **b** the spectral enhancement factors for various nanospheres. D denotes the dielectric sphere ($n = 4$, $k = 0$), M denotes the metal silver sphere, MC-DS denotes the metal core-dielectric shell sphere, and DC-MS denotes the dielectric core-metal shell sphere. The SiO_2 and Ag as a dielectric and metal layers are adopted for the core–shell spheres; **c** the scattering cross-section (SCS) of the nanospheres; **d** the SCS of the DC-MS sphere as a function of the core radius (nm). ©2011 OSA; Ref. [33]

respectively. As seen in Fig. 7.10b, c, the peaks of the enhancement factors agree with those of the SCS well. The small dielectric nanosphere, although has no loss and large refractive index $(n = 4)$, is not a good concentrator for OSCs. The dielectric nanosphere with positive refractive index cannot produce strong dipole resonance compared to the metal nanosphere. Moreover, in contrast to the DC-MS sphere that has a metal layer adjacent to different materials (SiO_2 and polymer), the resonance of the MC-DS sphere is blue-shifted, because only one material SiO_2 with lower refractive index is adjacent to the metal layer. The near field of the MC-DS sphere confines to the shell layer and cannot sufficiently scatter to the active layer. As a result, the optical enhancement by the MC-DS sphere is very weak. Figure 7.10d shows a tunable plasmon resonance by engineering the geometry of the DC-MS sphere. The resonance is red shifted and becomes damped as the core radius increases.

Second, we investigate the plasmonic silver cavity structure enclosing the active polymer material. Here the nanosphere is excluded. Figure 7.11a shows the spectral enhancement factor by the plasmonic cavity. A broadband enhancement

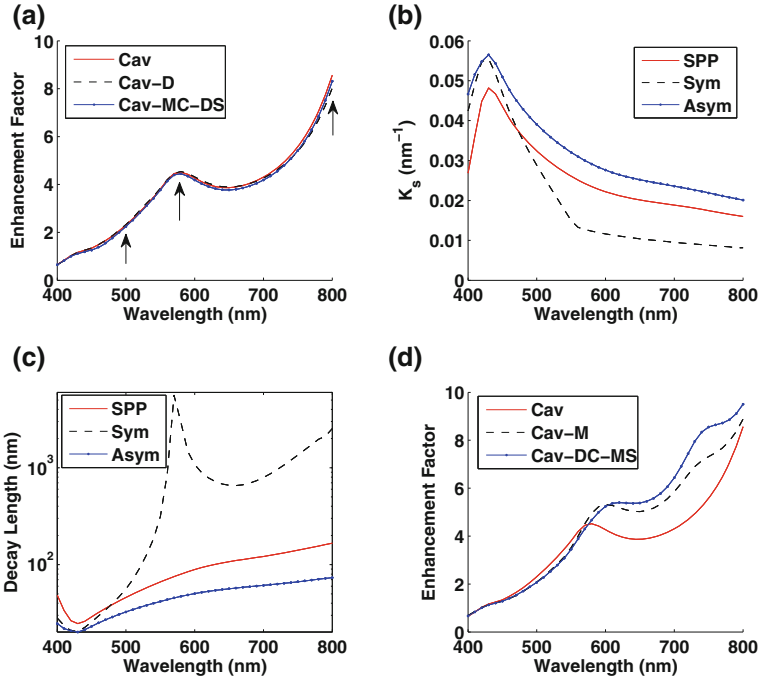

Fig. 7.11 **a** The spectral enhancement factors for the plasmonic cavity (Cav) and for that coupled with the dielectric (D) or the metal-core dielectric-shell (MC-DS) sphere; **b** the dispersion relations of surface plasmon polariton (SPP), and a symmetric (Sym) and asymmetric (Asym) surface wave modes. The surface plasmon polariton propagates at the interface between semi-infinite polymer and Ag half-spaces. The symmetric and asymmetric modes propagate in the active polymer layer bounded between the two metal claddings with finite thicknesses; **c** the decay lengths penetrated into the active material; **d** the spectral enhancement factors for the plasmonic cavity and for that coupled with the metal (M) or the dielectric-core metal-shell (DC-MS) sphere. ©2011 OSA; Ref. [33]

has a good overlap with the absorption spectrum of the active material as depicted in Fig. 7.10a. The dispersion relation of the cavity resonator plays a key role in unveiling the fundamental physics of the significant optical enhancement. Different from previous works assuming infinitely thick metal claddings [86], we take into account the finite-thickness effect of the metal claddings. The governing equation for the 1D eigenvalue problem of the Air/Ag/polymer/Ag/Air planar layered media is given by [59]

$$\left[p\frac{\mathrm{d}}{\mathrm{d}x}p^{-1}\frac{\mathrm{d}}{\mathrm{d}x}+K^2(x)\right]\phi(x)=K_z^2\phi(x) \tag{7.47}$$

where $p=\varepsilon$ and $\phi=H_y$ for TM wave, and $p=\mu$ and $\phi=E_y$ for TE wave. The eigenvalue equation (7.47) can be easily solved by the FDFD method with perfectly matched layer absorbing boundary conditions presented in Sect. 7.3.2. We

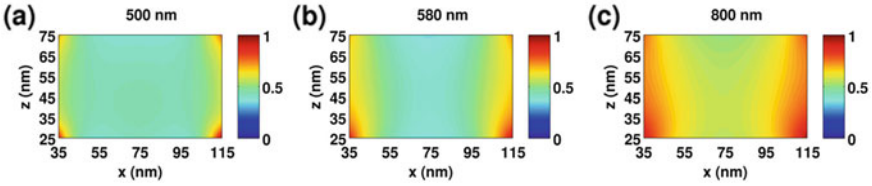

Fig. 7.12 The near-field distributions in the active polymer layer at the wavelengths denoted with the arrows of Fig. 7.11a: **a** 500 nm; **b** 580 nm; **c** 800 nm. ©2011 OSA; Ref. [33]

find two eigenvalues of the TM wave closest to the momentum of surface plasmon polariton (SPP). The SPP propagates at the interface between semi-infinite polymer and Ag half spaces and its dispersion relation is of the form

$$K_z = K_0 \sqrt{\frac{\varepsilon_{\mathrm{Ag}} \varepsilon_{\mathrm{pol}}}{\varepsilon_{\mathrm{Ag}} + \varepsilon_{\mathrm{pol}}}} \tag{7.48}$$

Particularly, the eigenvalue pair essentially corresponds to the symmetric and asymmetric surface wave modes supported by the Ag/polymer/Ag system [40, 86]. These modes are also associated with the guided-wave poles of the generalized reflection coefficient for the planar layered media [59]. Figure 7.11b shows the dispersion relations. At long wavelengths, the dispersion relation of the SPP is located between those of symmetric and asymmetric modes. Then we calculate the decay lengths of the surface plasmon waves penetrated into the active material as plotted in Fig. 7.11c. The peaks of the decay length of the symmetric mode strongly coincide with those of the spectral enhancement factor as shown in Fig. 7.11a. The incident light excites symmetric surface plasmon waves at the bottom corners of the cavity and the waves propagate in the active layer bounded between the metal claddings. A short decay length away from the metal claddings makes *E*-fields concentrate at the surfaces of the metals. Contrarily, a long decay length induces a concentrated *E*-field in the center of the active material. Figure 7.12 demonstrates the near-field distributions in the active layer at the wavelengths denoted with the arrows of Fig. 7.11a. At 800 nm, the slowly decaying near field away from the metal claddings leads to the most significant enhancement.

Third, we study the hybrid plasmonic system, which comprises a plasmonic cavity coupled with a nanosphere. The optical enhancement shows little improvements when the cavity is coupled with the dielectric or MC-DS sphere as illustrated in Fig. 7.11a. However, a significant enhancement can be achieved if the cavity is coupled with metal or DC-MS sphere as shown in Fig. 7.11d. Employing the cavity coupled with the DC-MS sphere, the optical absorption of the active polymer material has a 4-fold increase according to the obtained total enhancement factor (defined in Sect. 7.3.4). We calculate the algebraic summation of the spectral enhancement factor by the uncoupled single cavity and that by the uncoupled single DC-MS sphere. As shown in Fig. 7.13, the summation is

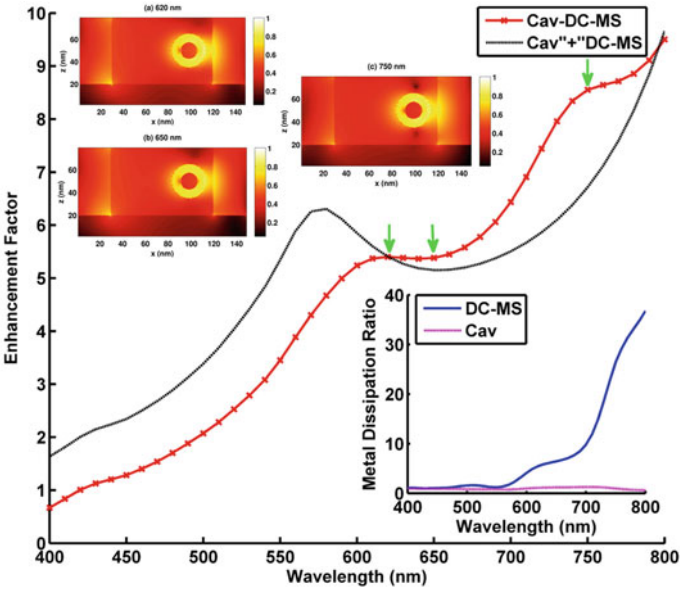

Fig. 7.13 The spectral enhancement factor comparisons. The enhancement factor by the cavity (Cav) coupled with the DC-MS sphere is drawn with *red straight line*. The algebraic summation of the enhancement factor by the uncoupled single cavity and that by the uncoupled single DC-MS sphere is plotted with *black dash line*. The near-field distributions at the wavelengths denoted with the *green arrows* are shown in the *inset*. The metal dissipation ratio of the cavity is defined as the metal loss of the coupled cavity over that of the uncoupled one. Likewise, the metal dissipation ratio of the DC-MS sphere is defined as the metal loss of the coupled DC-MS sphere over that of the uncoupled one. ©2011 OSA; Ref. [33]

observably smaller than the enhancement factor by the cavity coupled with the DC-MS sphere at long wavelengths ranging from 620 to 800 nm. The coherent interplay between the cavity and the DC-MS sphere is undoubtedly confirmed by the result. Then, we analyze the metal dissipation ratio defined as the metal loss of the coupled concentrator over that of the uncoupled one. The inset of Fig. 7.13 shows that the metal dissipation ratio of the DC-MS sphere is substantially larger than that of the cavity. The evanescent SPPs from the inner surface of metallic cavity sufficiently penetrate the DC-MS sphere inducing stronger local plasmon resonance as well as larger metallic loss. Thus, the DC-MS sphere becomes more effective concentrator when it is coupled with the cavity. Finally, we discuss the coupling modes in the hybrid plasmonic system. Calculated by Eq. (7.37), Fig. 7.14 depicts a polarization charge distribution on the surface of the cavity, indicating a bonding and antibonding coupling modes in the hybrid system. The bonding modes at 620 and 750 nm have a denser charge distribution if the distance between the cavity and the shell surfaces becomes closer. However, the anti-bonding mode at 650 nm reverses the polarity of the polarization charge when the face-to-face distance approaches the minimum. The near fields of the bonding

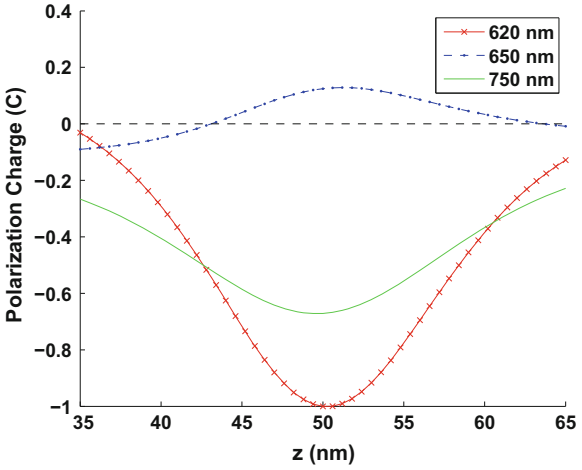

Fig. 7.14 The polarization charge distributions on the surface of the cavity at the wavelengths denoted with the *arrows* of Fig. 7.13. ©2011 OSA; Ref. [33]

modes show more concentrated field at the gap between the DC-MS sphere and the cavity, which can be seen in the inset of Fig. 7.13. For the bonding mode, the polarity of its polarization charge is marked in Fig. 7.9. Due to the in-phase plasmon oscillation and hybridization, the bonding mode is superradiant or strongly radiative, and provides a great help for the optical enhancement.

In conclusion, the hybrid plasmonic system, which comprises the plasmonic cavity coupled with the DC-MS nanosphere, can increase the optical absorption of the OSC by fourfold. The significant enhancement mainly results from the coupling of symmetric surface wave modes supported by the cavity resonator and strongly depends on the decay length of surface plasmon waves penetrated into the active layer. Furthermore, the coherent interplay between the cavity and the DC-MS nanosphere is strongly demonstrated by our theoretical model. The bonding coupling mode in the hybrid plasmonic system enhances the optical absorption further. The work provides detailed physical explanations for the hybrid plasmonic cavity device structure to enhance the optical absorption of organic photovoltaics.

7.5 Conclusion

In this book chapter, we have reviewed the basic concepts, physical mechanisms, and theoretical models for plasmonic effects in OSCs. Our results show that the absorption and performance of OSCs can be significantly enhanced by incorporating metallic nanostructures. The unparalleled near-field concentration inherent from plasmon resonances can break the half-wavelength limit in the optical design of thin-film OSCs, which is particularly useful for high-performance ultracompact photovoltaics.

We can explore new potentials and emerging functionalities of plasmonic effects in OSCs. On the one hand, the bad spectral overlap of plasmonic resonances with the absorption of active polymer materials could be improved by plasmonic hybridization or by combination with high-refractive-index materials. On the other hand, the electrical properties of plasmonic nanostructures and resulting effects can be investigated with multiphysics study.

Acknowledgments The authors acknowledge the support of the grants (Nos. 712010, 711609, and 711511) from the Research Grant Council (RGC) of Hong Kong, the grant (No. 10401466) from the University Grant Council (UGC) of the University of Hong Kong, and the Small Project Funding of the University of Hong Kong (No. 201109176133). This project is also supported by the UGC of Hong Kong (No. AoE/P-04/08), by The National Natural Science Foundation of China (No. 61201122), and in part by a Hong Kong UGC Special Equipment Grant (SEG HKU09).

Appendix—Biconjugate Gradient Stabilized Algorithm

The resulting VIE matrix equation can be expressed as

$$Ax = b$$

The procedure of the biconjugate gradient stabilized (BI-CGSTAB) algorithm is given as follows:

Give an initial guess x_0, we have

$$\begin{aligned} r_0 &= b - Ax_0,\ \hat{r}_0 = r_0 \\ \rho_0 &= \alpha = \omega_0 = 1 \\ v_0 &= p_0 = 0 \end{aligned}$$

Iterate for $i = 1, 2, \ldots, n$

$$\begin{aligned} \rho_i &= \langle \hat{r}_0, r_{i-1} \rangle \\ \beta &= (\rho_i / \rho_{i-1})(\alpha / \omega_{i-1}) \\ p_i &= r_{i-1} + \beta(p_{i-1} - \omega_{i-1} v_{i-1}) \\ v_i &= Ap_i \\ \alpha &= \rho_i / \langle \hat{r}_0, v_i \rangle \\ s &= r_{i-1} - \alpha v_i \\ t &= As \\ \omega_i &= \langle t, s \rangle / \langle t, t \rangle \\ x_i &= x_{i-1} + \alpha p_i + \omega_i s \\ r_i &= s - \omega_i t \end{aligned}$$

Terminate when

$$\frac{||r_i||_2}{||b||_2} < \eta$$

where η is the tolerance that specifies the desired accuracy of solution.

References

1. Hoppe H, Sariciftci NS (2004) Organic solar cells: an overview. J Mater Res 19:1924–1945
2. Brabec CJ, Gowrisanker S, Halls JJM, Laird D, Jia SJ, Williams SP (2010) Polymer-fullerene bulk-heterojunction solar cells. Adv Mater 22:3839–3856
3. Deibel C, Dyakonov V (2010) Polymer-fullerene bulk heterojunction solar cells. Rep Prog Phys 73:096401
4. Barnes WL, Dereux A, Ebbesen TW (2003) Surface plasmon subwavelength optics. Nature 424:824–830
5. Gramotnev DK, Bozhevolnyi SI (2010) Plasmonics beyond the diffraction limit. Nat Photonics 4:83–91
6. Schuller JA, Barnard ES, Cai WS, Jun YC, White JS, Brongersma ML (2010) Plasmonics for extreme light concentration and manipulation. Nat Mater 9:193–204
7. Atwater HA, Polman A (2010) Plasmonics for improved photovoltaic devices. Nat Mater 9:205–213
8. Tvingstedt K, Persson NK, Inganas O, Rahachou A, Zozoulenko IV (2007) Surface plasmon increase absorption in polymer photovoltaic cells. Appl Phys Lett 91:113514
9. Bai WL, Gan QQ, Bartoli F, Zhang J, Cai LK, Huang YD, Song GF (2009) Design of plasmonic back structures for efficiency enhancement of thin-film amorphous Si solar cells. Opt Lett 34:3725–3727
10. Bai WL, Gan QQ, Song GF, Chen LH, Kafafi Z, Bartoli F (2010) Broadband short-range surface plasmon structures for absorption enhancement in organic photovoltaics. Opt Express 18:A620–A630
11. Kang MG, Xu T, Park HJ, Luo XG, Guo LJ (2010) Efficiency enhancement of organic solar cells using transparent plasmonic Ag nanowire electrodes. Adv Mater 22:4378–4383
12. Min CJ, Li J, Veronis G, Lee JY, Fan SH, Peumans P (2010) Enhancement of optical absorption in thin-film organic solar cells through the excitation of plasmonic modes in metallic gratings. Appl Phys Lett 96:133302
13. Tsai SJ, Ballarotto M, Romero DB, Herman WN, Kan HC, Phaneuf RJ (2010) Effect of gold nanopillar arrays on the absorption spectrum of a bulk heterojunction organic solar cell. Opt Express 18:A528–A535
14. Wang W, Wu SM, Reinhardt K, Lu YL, Chen SC (2010) Broadband light absorption enhancement in thin-film silicon solar cells. Nano Lett 10:2012–2018
15. Sha WEI, Choy WCH, Chew WC (2010) A comprehensive study for the plasmonic thin-film solar cell with periodic structure. Opt Express 18:5993–6007
16. Sha WEI, Choy WCH, Chew WC (2011) Angular response of thin-film organic solar cells with periodic metal back nanostrips. Opt Lett 36:478–480
17. Sha WEI, Choy WCH, Wu Y, Chew WC (2012) Optical and electrical study of organic solar cells with a 2D grating anode. Opt Express 20:2572–2580
18. Catchpole KR, Polman A (2008) Plasmonic solar cells. Opt Express 16:21793–21800
19. Catchpole KR, Polman A (2008) Design principles for particle plasmon enhanced solar cells. Appl Phys Lett 93:191113

20. Morfa AJ, Rowlen KL, Reilly TH, Romero MJ, van de Lagemaat J (2008) Plasmon-enhanced solar energy conversion in organic bulk heterojunction photovoltaics. Appl Phys Lett 92:013504
21. Duche D, Torchio P, Escoubas L, Monestier F, Simon JJ, Flory F, Mathian G (2009) Improving light absorption in organic solar cells by plasmonic contribution. Sol Energy Mater Sol Cells 93:1377–1382
22. Mendes MJ, Luque A, Tobias I, Marti A (2009) Plasmonic light enhancement in the near-field of metallic nanospheroids for application in intermediate band solar cells. Appl Phys Lett 95:071105
23. Akimov YA, Koh WS, Ostrikov K (2009) Enhancement of optical absorption in thin-film solar cells through the excitation of higher-order nanoparticle plasmon modes. Opt Express 17:10195–10205
24. Akimov YA, Ostrikov K, Li EP (2009) Surface plasmon enhancement of optical absorption in thin-film silicon solar cells. Plasmonics 4:107–113
25. Mokkapati S, Beck FJ, Polman A, Catchpole KR (2009) Designing periodic arrays of metal nanoparticles for light-trapping applications in solar cells. Appl Phys Lett 95:053115
26. Lee JY, Peumans P (2010) The origin of enhanced optical absorption in solar cells with metal nanoparticles embedded in the active layer. Opt Express 18:10078–10087
27. Kulkarni AP, Noone KM, Munechika K, Guyer SR, Ginger DS (2010) Plasmon-enhanced charge carrier generation in organic photovoltaic films using silver nanoprisms. Nano Lett 10:1501–1505
28. Jung J, Sondergaard T, Pedersen TG, Pedersen K, Larsen AN, Nielsen BB (2011) Dyadic Green's functions of thin films: applications within plasmonic solar cells. Phys Rev B 83:085419
29. Diukman I, Tzabari L, Berkovitch N, Tessler N, Orenstein M (2011) Controlling absorption enhancement in organic photovoltaic cells by patterning Au nano disks within the active layer. Opt Express 19:A64–A71
30. Sha WEI, Choy WCH, Liu YG, Chew WC (2011) Near-field multiple scattering effects of plasmonic nanospheres embedded into thin-film organic solar cells. Appl Phys Lett 99:113304
31. Ferry VE, Sweatlock LA, Pacifici D, Atwater HA (2008) Plasmonic nanostructure design for efficient light coupling into solar cells. Nano Lett 8:4391–4397
32. Pala RA, White J, Barnard E, Liu J, Brongersma ML (2009) Design of plasmonic thin-film solar cells with broadband absorption enhancements. Adv Mater 21:3504–3509
33. Sha WEI, Choy WCH, Chen YP, Chew WC (2011) Optical design of organic solar cell with hybrid plasmonic system. Opt Express 19:15908–15918
34. Chopra KL, Paulson PD, Dutta V (2004) Thin-film solar cells: an overview. Prog Photovoltaics 12:69–92
35. Tikhodeev SG, Yablonskii AL, Muljarov EA, Gippius NA, Ishihara T (2002) Quasiguided modes and optical properties of photonic crystal slabs. Phys Rev B 66:045102
36. Hessel A, Oliner AA (1965) A new theory of Wood's anomalies on optical gratings. Appl Optics 4:1275–1297
37. Luk'yanchuk B, Zheludev NI, Maier SA, Halas NJ, Nordlander P, Giessen H, Chong CT (2010) The Fano resonance in plasmonic nanostructures and metamaterials. Nat Mater 9:707–715
38. Miroshnichenko AE, Flach S, Kivshar YS (2010) Fano resonances in nanoscale structures. Rev Mod Phys 82:2257–2298
39. Raether H (1988) Surface plasmons on smooth and rough surfaces and on gratings. Springer, Berlin
40. Maier SA (2007) Plasmonics: fundamentals and applications. Springer, New York
41. Kawata S, Shalaev VM (2007) Nanophotonics with surface plasmons. Elsevier, Amsterdam
42. Prodan E, Radloff C, Halas NJ, Nordlander P (2003) A hybridization model for the plasmon response of complex nanostructures. Science 302:419–422

43. Nordlander P, Oubre C, Prodan E, Li K, Stockman MI (2004) Plasmon hybridization in nanoparticle dimers. Nano Lett 4:899–903
44. Matheu P, Lim SH, Derkacs D, McPheeters C, Yu ET (2008) Metal and dielectric nanoparticle scattering for improved optical absorption in photovoltaic devices. Appl Phys Lett 93:113108
45. Akimov YA, Koh WS, Sian SY, Ren S (2010) Nanoparticle-enhanced thin film solar cells: metallic or dielectric nanoparticles? Appl Phys Lett 96:073111
46. Grandidier J, Callahan DM, Munday JN, Atwater HA (2011) Light absorption enhancement in thin-film solar cells using whispering gallery modes in dielectric nanospheres. Adv Mater 23:1272–1276
47. Giannini V, Fernandez-Dominguez AI, Sonnefraud Y, Roschuk T, Fernandez-Garcia R, Maier SA (2010) Controlling light localization and light-matter interactions with nanoplasmonics. Small 6:2498–2507
48. Chew WC, Jin J-M, Michielssen E, Song J (2001) Fast and efficient algorithms in computational electromagnetics. Artech House Publishers, Boston
49. Luebbers R, Hunsberger FP, Kunz KS, Standler RB, Schneider M (1990) A frequency-dependent finite-difference time-domain formulation for dispersive materials. IEEE Trans Electromagn Compat 32:222–227
50. Kelley DF, Luebbers RJ (1996) Piecewise linear recursive convolution for dispersive media using FDTD. IEEE Trans Antennas Propag 44:792–797
51. Veronis G, Fan S (2007) Overview of simulation techniques for plasmonic devices. In: Brongersma ML, Kik PG (eds) Surface plasmon nanophotonics. Springer, Dordrecht
52. Veysoglu ME, Shin RT, Kong JA (1993) A finite-difference time-domain analysis of wave scattering from periodic surfaces-oblique-incidence case. J Electromagn Waves Appl 7:1595–1607
53. Sullivan DM (2000) Electromagnetic simulation using the FDTD method. Wiley-IEEE Press, New York
54. Taflove A, Hagness SC (2005) Computational electrodynamics: the finite-difference time-domain method, 3rd edn. Artech House, Boston
55. Jin J-M (2002) The finite element method in electromagnetics, 2nd edn. Wiley-IEEE Press, New York
56. Chew WC, Tong MS, Hu B (2008) Integral equation methods for electromagnetic and elastic waves. Morgan and Claypool Publishers, San Rafael
57. Brandt A (1982) Guide to multigrid development. Lecture notes in mathematics, vol 960, pp 220–312
58. Davis TA, Duff IS (1997) An unsymmetric-pattern multifrontal method for sparse LU factorization. SIAM J Matrix Anal Appl 18:140–158
59. Chew WC (1995) Waves and fields in inhomogenous media. Wiley-IEEE Press, New York
60. Chew WC, Jin JM, Lu CC, Michielssen E, Song JMM (1997) Fast solution methods in electromagnetics. IEEE Trans Antennas Propag 45:533–543
61. Brandt A (1991) Multilevel computations of integral-transforms and particle interactions with oscillatory kernels. Comput Phys Commun 65:24–38
62. Phillips JR, White JK (1997) A precorrected-FFT method for electrostatic analysis of complicated 3-D structures. IEEE Trans Comput-Aided Des Integr Circuits Syst 16:1059–1072
63. Greengard L, Rokhlin V (1987) A fast algorithm for particle simulations. J Comput Phys 73:325–348
64. Song JM, Lu CC, Chew WC (1997) Multilevel fast multipole algorithm for electromagnetic scattering by large complex objects. IEEE Trans Antennas Propag 45:1488–1493
65. Bienstman P, Baets R (2001) Optical modelling of photonic crystals and VCSELs using eigenmode expansion and perfectly matched layers. Opt Quantum Electron 33:327–341
66. Moharam MG, Grann EB, Pommet DA, Gaylord TK (1995) Formulation for stable and efficient implementation of the rigorous coupled-wave analysis of binary gratings. J Opt Soc Am A 12:1068–1076

67. Yonekura J, Ikeda M, Baba T (1999) Analysis of finite 2-D photonic crystals of columns and lightwave devices using the scattering matrix method. J Lightwave Technol 17:1500–1508
68. Johnson SG, Joannopoulos JD (2001) Block-iterative frequency-domain methods for Maxwell's equations in a planewave basis. Opt Express 8:173–190
69. Yee KS (1966) Numerical solution of initial boundary value problems involving Maxwell's equations in isotropic media. IEEE Trans Antennas Propag 14:302–307
70. Berenger JP (1994) A perfectly matched layer for the absorption of electromagnetic-waves. J Comput Phys 114:185–200
71. Chew WC, Weedon WH (1994) A 3-D perfectly matched medium from modified Maxwell's equations with stretched coordinates. Microw Opt Technol Lett 7:599–604
72. Mur G (1981) Absorbing boundary-conditions for the finite-difference approximation of the time-domain electromagnetic-field equations. IEEE Trans Electromagn Compat 23:377–382
73. Draine BT, Flatau PJ (1994) Discrete-dipole approximation for scattering calculations. J Opt Soc Am A 11:1491–1499
74. Kern AM, Martin OJF (2009) Surface integral formulation for 3D simulations of plasmonic and high permittivity nanostructures. J Opt Soc Am A 26:732–740
75. Glisson AW, Wilton DR (1980) Simple and efficient numerical methods for problems of electromagnetic radiation and scattering from surfaces. IEEE Trans Antennas Propag 28:593–603
76. Catedra MF, Gago E, Nuno L (1989) A numerical scheme to obtain the RCS of three-dimensional bodies of resonant size using the conjugate gradient method and the fast Fourier transform. IEEE Trans Antennas Propag 37:528–537
77. Hestenes MR, Stiefel E (1952) Methods of conjugate gradients for solving linear systems. J Res Nat Bur Stand 49:409–436
78. Vandervorst HA (1992) Bi-CGSTAB: a fast and smoothly converging variant of Bi-CG for the solution of nonsymmetric linear systems. SIAM J Sci Stat Comput 13:631–644
79. Bohren CF, Huffman DR (1998) Absorption and scattering of light by small particles. Wiley-Interscience, New York
80. Tsang L, Kong JA, Ding KH (2000) Scattering of electromagnetic waves: theories and applications. Wiley, New York
81. Rakic AD, Djurisic AB, Elazar JM, Majewski ML (1998) Optical properties of metallic films for vertical-cavity optoelectronic devices. Appl Optics 37:5271–5283
82. Palik ED (1998) Handbook of optical constants of solids. Academic Press, London
83. Choy WCH, Fong HH (2008) Comprehensive investigation of absolute optical properties of organic materials. J Phys D Appl Phys 41:155109
84. Wei QH, Su KH, Durant S, Zhang X (2004) Plasmon resonance of finite one-dimensional Au nanoparticle chains. Nano Lett 4:1067–1071
85. Jain PK, El-Sayed MA (2007) Universal scaling of plasmon coupling in metal nanostructures: extension from particle pairs to nanoshells. Nano Lett 7:2854–2858
86. Prade B, Vinet JY, Mysyrowicz A (1991) Guided optical waves in planar heterostructures with negative dielectric-constant. Phys Rev B 44:13556–13572

Chapter 8
Experimental Studies of Plasmonic Nanoparticle Effects on Organic Solar Cells

Dixon D. S. Fung and Wallace C. H. Choy

Abstract The incorporation of plasmonic nanoparticles (NPs) into different layers of organic solar cells (OSCs) is studied in this chapter. First, we incorporate NPs into the hole collection layer of OSCs. The resulting improvements in Power Conversion Efficiency (PCE) are found to originate mainly from improvement in hole collection efficiency, while Localized Surface Plasmon Resonance (LSPR) effects are found to have negligible effect on active layer absorption. Next, we incorporate NPs into the active layer of OSCs. In this case, the absorption of the active layer improves, but we also showed that consideration of electrical properties including carrier mobility, exciton dissociation efficiency, and active layer morphology is required to account for the PCE trend. In both studies, we theoretically show that the very strong near field of NPs is found to distribute laterally along the layer in which the NPs are incorporated in, and hence leading to active layer absorption improvements only when NPs are incorporated into the active layer. Lastly, we incorporated NPs into both active layer and hole collection layer in which the accumulated effects of NPs in the different layers achieved ~ 22 % improvement in PCE as compared to the optimized control OSCs using poly (3-hexylthiophene): phenyl-C61-butyric acid methyl ester (P3HT:PCBM) as the active layer.

D. D. S. Fung · W. C. H. Choy (✉)
Department of Electrical and Electronic Engineering, The University of Hong Kong, Pokfulam, Hong Kong
e-mail: chchoy@eee.hku.hk

W. C. H. Choy (ed.), *Organic Solar Cells*, Green Energy and Technology,
DOI: 10.1007/978-1-4471-4823-4_8,

8.1 Introduction

Plasmonics has been proposed for various interesting applications including biosensing [1], waveguides [2], optical cloaking [3], and quantum computing [4]. Recently, the ability of plasmonic structures to greatly enhance electric fields has attracted attention in the field of organic solar cells (OSCs), in which material absorption is a crucial factor that has to be improved.

Incorporation of plasmonic structures on solar cells could potentially improve its efficiency through three possible optical effects [5]. First, metallic nanoparticles (NPs) can scatter the incident light into waveguide modes in the active layer of the solar cell, increasing the optical path distance and improving absorption. Second, by utilizing the Localized Surface Plasmon Resonance (LSPR) effect, the NPs can be mixed into the OSC during fabrication and act as antennas, creating a very strong near field around the NPs and enhancing absorption of the active layer. Third, using a nanostructured metallic electrode such as a grating, surface plasmon resonance (SPR) can be excited and increase the field near the dielectric/metal interface, thus improving absorption in the solar cell.

There has been great interest in the applications of plasmonic structures on OSCs to improve power conversion efficiency (PCE) in recent years. By conveniently mixing NPs into the hole collection layer of OSCs, reports have claimed that LSPR effects improved the absorption hence the efficiency of OSCs. [6–9] On the other hand, Heeger et al. have incorporated Au NPs into the active layer of solar cells and showed the wide-band improvement of absorption in poly(3-hexylthiophene): phenyl-C61-butyric acid methyl ester (P3HT:PCBM) is due to scattering of NPs instead of LSPR effects [10]. Ag NPs and nanowires were also demonstrated to improve absorption and PCE by addition into the active layer [11, 12]. Evaporation of a very thin layer of Au or Ag forms small clusters of metals which also exhibit LSPR effects and are used in solar cells [8]. On the other hand, various other nanostructures have also been used to improve absorption and PCE [13, 14].

On the electrical properties of NP-doped solar cells, an early report of NPs incorporated into solar cells has stated that the increase of solar cell performance may be due to the introduction of dopant states which increases the electrical conductivity of the active layer [15]. Incorporation of Ag nanowires into the active layer of OSCs has been shown to increase both hole and electron mobility, but the detailed physics was not investigated in depth [11]. There have also been reports on changes in open circuit voltage (V_{OC}) when NPs are incorporated into OSCs [10]. On the other hand, Wu et al. have reported an increase in exciton dissociation probability of OSCs incorporated with NPs and claimed that this increase is due to interactions between plasmons and photogenerated excitons [7].

In the mentioned reports, PCE improvements in OSCs incorporating NPs have been well demonstrated but the investigations in device mechanisms have been lacking in depth. In particular, the actual role of LSPR effects has not been well clarified and questions could still be raised about whether LSPR is actually improving device performances. On the other hand, as plasmonic nanostructures

are commonly incorporated in-side an OSC, their effects on the electrical properties of OSCs are likely equally important as optical properties. Previous reports have studied optical effects of the NPs, while the impact of NPs on the electrical properties of OSCs is still unclear. The understanding on the electrical properties of OSCs is important for optimizing the plasmonic OSCs and open new applications of plasmonic nanostructures.

In this chapter, detailed studies in the device mechanisms of OSCs will be described when NPs are incorporated into various positions through experiment and theoretical simulations. The objectives are (1) clarify the extent that LSPR improves absorption in active layer; (2) describe the difference in the role of LSPR effects when NPs are incorporated into the hole collection layer or active layer; (3) study the device mechanisms, apart from optical effects, that will be changed when NPs are incorporated; and (4) describe the large efficiency improvements in OSCs by incorporation of NPs in all organic layers.

8.2 Electrical and Optical Properties of Organic Solar Cells with Au Nanoparticles Doped into the PEDOT:PSS Layer

Considering the origin of performance improvement after addition of NPs, the effects of doping the poly(3,4-ethylenedioxythiophene) poly(styrenesulfonate) (PEDOT:PSS) layer of a OSC with Au NPs have been reported [36]. In the report, monofunctional poly(ethylene glycol) (PEG)-capped Au NPs with average diameter of 18 nm are doped into the PEDOT:PSS hole collection layer of an optimized OSC with P3HT:PCBM as the active layer, leading to $\sim$13 % peak PCE improvement. The effect of PEG capping on Au NPs has also been investigated from a device fabrication perspective. Together with theoretical simulations which are discussed in Chap. 7 [16], the effects of Au NPs on the optical and electrical properties of OSCs have been studied. The results show that the competition between improved hole collection at the PEDOT:PSS/active layer interface and reduced exciton quenching, at donor/acceptor junctions, instead of the LSPR effect, are major contributors to the measured PCE variation.

8.2.1 Performances of the Au NP Devices

The current density (J) versus voltage (V) characteristics of devices with structure ITO/PEDOT:PSS(with PEG-capped Au NPs)/P3HT:PCBM/LiF(1 nm)/Al(100 nm) incorporating various Au NP concentrations in PEDOT:PSS layer is shown in Fig. 8.1 and the device characteristics are summarized in Table 8.1.

It is shown that increasing Au NPs concentration in PEDOT:PSS improves PCE of our OSCs, peaking at 0.32 wt% with PCE of 3.51 % which corresponds to

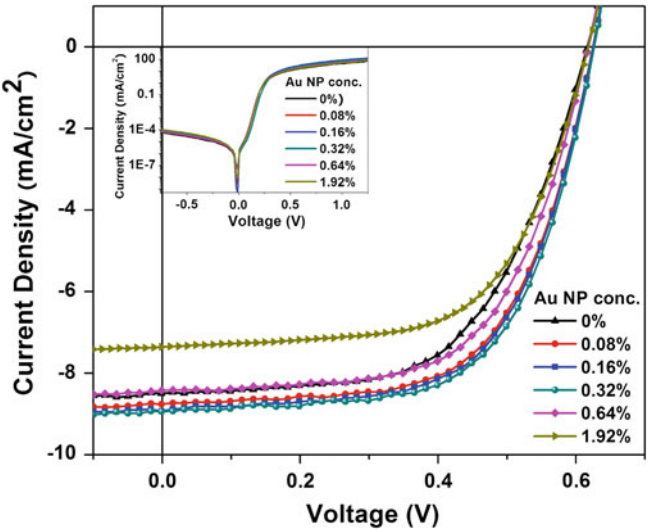

Fig. 8.1 *J–V* characteristics of solar cells with structures ITO/PEDOT:PSS (with PEG-capped Au NPs)/P3HT:PCBM/LiF (1 nm)/Al(100 nm), incorporated with different NP concentrations under AM 1.5G illumination at 100 mW/cm^2. *Inset Dark J–V* characteristics of the solar cells [18]

Table 8.1 Device performances for solar cells with structure ITO/PEDOT:PSS(with PEG-capped Au NPs)/P3HT:PCBM/LiF(1 nm)/Al(100 nm), incorporated with different NP concentrations [18]

NP conc. (wt %)	J_{sc} (mA/cm2)	V_{OC} (V)	FF (%)	PCE (%)
0	8.5 ± 0.19	0.62 ± 0.01	58 ± 1.3	3.10 ± 0.10
0.08	8.77 ± 0.23	0.63 ± 0.01	61 ± 1.0	3.40 ± 0.11
0.16	8.93 ± 0.19	0.63 ± 0.01	61 ± 1.1	3.46 ± 0.10
0.32	8.94 ± 0.15	0.63 ± 0.01	62 ± 1.0	3.51 ± 0.09
0.64	8.56 ± 0.11	0.62 ± 0.01	61 ± 1.2	3.21 ± 0.10
1.92	7.36 ± 0.2	0.62 ± 0.01	61 ± 0.5	2.80 ± 0.13

$\sim$13 % improvement. Improvements originate from increases in FF and J_{sc}, from 0.58 to 0.62 and 8.5–8.94 mA/cm^2, respectively. Further, increasing the concentration of NPs has detrimental effect on device performances, with PCE dropping to 2.80 % at 1.92 wt% Au NPs concentration. From the dark *J–V* characteristics in the inset of Fig. 8.1, no significant change in leakage current is observed after incorporation of Au NPs. The underlying physics of the PCE trend can be explored by studying the optical and electrical properties as described the following sections.

8.2.2 Au NP Properties and the Effects of PEG

The absorption spectrum of Au NPs without PEG in water is shown in Fig. 8.2. The absorption peak at ~520 nm corresponds to the excitation of LSPR. Coating PEG onto Au NPs has no discernable effect on the peak position of optical absorption. The average diameter of Au NPs is approximately 18 nm, based on TEM measurements, as shown in the inset of Fig. 8.2.

Regarding the effects of Au NPs with or without PEG coating on device performances, for the same concentration (0.32 wt%) of Au NPs, PCE of the device with Au NP (PEG) improves from 3.1 (control device without Au NPs) to 3.51 %, while devices with Au NP (no PEG) show no performance improvement for the same device structure of ITO/PEDOT:PSS:Au NPs/P3HT:PCBM/LiF(1 nm)/Al(100 nm) was fabricated to investigate the device performance. The origin of this effect can be further elaborated from SEM images taken on PEDOT:PSS:Au NP films. As shown in Fig. 8.3a, Au NPs with PEG are well dispersed in a PEDOT:PSS:Au NP film with no clear aggregation, while Au NPs without PEG aggregate into clumps of NPs in a film (Fig. 8.3b). This can be explained by the positive surface charge [17] of the Au NPs generated in the synthesis process [18], while PSS molecules are anionic in nature [19]. When Au NPs are added to PEDOT:PSS solution, the adsorption of anionic PSS molecules on positively charged Au NPs leads to the aggregation of Au NPs. On the other hand, the PEG capping layer has a shielding effect on Au NPs, leading to reduce interaction of NPs with the surrounding medium. Meanwhile, PEG itself does not have any effect other than the prevention of Au NP aggregation [20], this is confirmed from the devices with and without PEG (2 mg/ml) dissolved into the PEDOT:PSS layer and

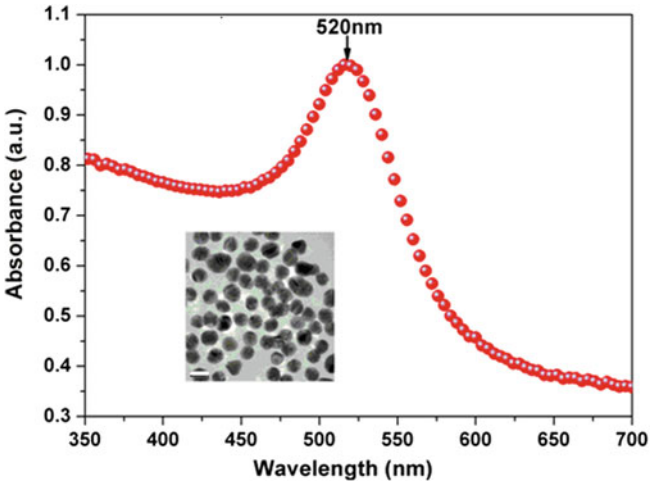

Fig. 8.2 Absorption spectrum of Au NPs in water. *Inset* is the TEM image of the NPs. The *white bar* is approximately 20 nm long [18]

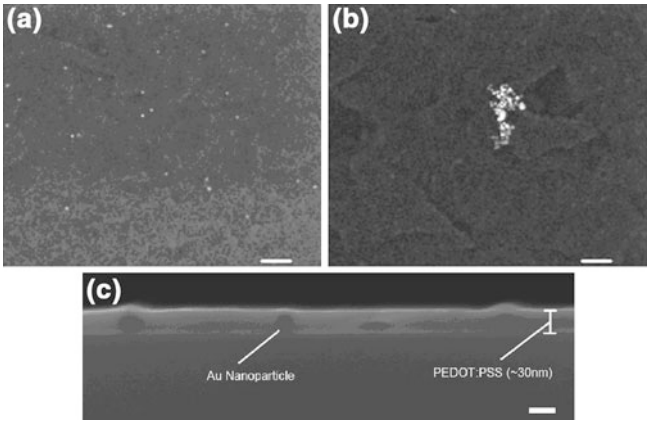

Fig. 8.3 SEM images of the surface of PEDOT:PSS:Au NPs films with **a** Au NPs capped with PEG, **b** Au NPs not capped with PEG. The *white bars* in (**a**) and (**b**) are approximately 200 nm long. **c** SEM image of the cross-section of a PEDOT:PSS:Au NPs film, with Au NPs capped with PEG. The *white bar* in (**c**) is approximately 30 nm long. Note that the image is focused on the cross-section surface of PEDOT:PSS and the Au NPs might be out of focus [18]

observed no discernible difference in the performance. Therefore, PEG itself does not exert any significant effects on our device performances. The contribution of PEG is to prevent formation of aggregation sites and allow the uniform dispersion of Au NPs. In the following discussion, the effects of PEG capped Au NPs on OSCs will be described.

The positioning of Au NPs along with the vertical profile of the PEDOT:PSS film is shown in Fig. 8.3c. It can be seen that the majority of the bulk of individual NPs are located within the PEDOT:PSS layer. At the locations of Au NPs, bumps are created on the surface of PEDOT:PSS. However, the Au NPs at the bumps are covered by a layer of PEDOT:PSS and no bare Au NP protrusions are reported in measurements.

8.2.3 Plasmonic Effects

The LSPR effects can be investigated from the absorption spectrum of the PEDOT:PSS/P3HT:PCBM films, with or without Au NPs in PEDOT:PSS as shown in Fig. 8.4a. Interestingly, no significant difference is observed in absorption between the samples with and without Au NPs. Theoretical studies [16] have also been conducted to understand plasmonic effects of Au NPs in the devices [18]. The theoretical enhancement factor (i.e., the ratio of the active layer light absorption of the PEDOT:PSS:Au NPs device over that of the conventional PEDOT:PSS one) shows no clear absorption enhancement, with a value around 1 as shown in the inset of Fig. 8.4a which agrees well with the experimental results.

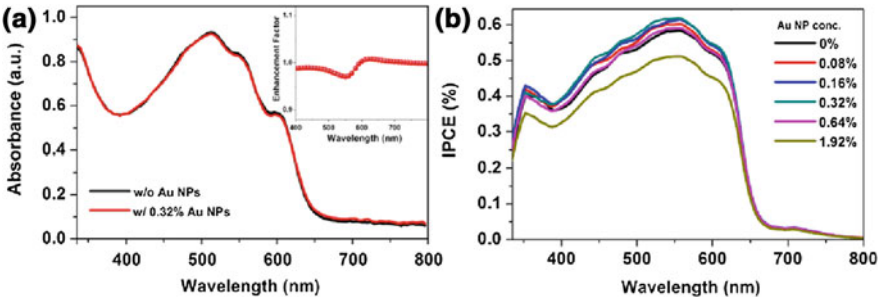

Fig. 8.4 **a** Absorbance of PEDOT:PSS/P3HT:PCBM film with or without Au NPs incorporation (0.32 wt%); *inset* of (**a**): theoretical absorption enhancement factor (detailed model shown in Appendix A); **b** IPCE of the solar cells with various Au NP concentrations in PEDOT:PSS [18]

LSPR is at about 580 nm, although the enhancement is weak. The theoretical results and reflectance measurements also show that the Al electrode does not obviously affect the LSPR effect on the absorption enhancement as the Al electrode is situated far (220 nm) from the PEDOT:PSS layer.

The reason for the small optical enhancement is that when light is incident in normal into the device through ITO, the very strong near field around Au NPs due to LSPR mainly distributes laterally along the PEDOT:PSS layer rather than vertically into the adjacent active layer as shown in Fig. 8.5. As a result, no clear light absorption enhancement can be obtained in the active layer of P3HT:PCBM. Importantly, the understanding can also be applied to other cases with the metallic NPs (such as Ag, Pt etc.) incorporated into the buffer layer adjacent to the active layer of typical organic thin-film solar cells due to the lateral distribution feature of the strong near-field. Meanwhile, the work suggests that near-field physics needs to be accounted for in the optical design of photovoltaics, and some traditional physical quantities, such as scattering cross-section, are not enough to fully characterize the optical properties of OSCs. For instance, typically, scattering cross-section is very useful to locate the plasmonic resonance region and determine the strength of scattering [21, 22]. However, it cannot provide the directional properties of electric field, and thus the direction dependence of absorption enhancement.

Although there is no obvious enhancement in the light absorption of the active layer, IPCE of our PEDOT:PSS:Au NPs devices increases with Au NP concentration and the 0.32 wt% device shows the highest IPCE, with ~64 % at 550 nm as shown in Fig. 8.4b. For higher Au NP concentrations, IPCE decreases. This is in good agreement with the trend of J_{sc}. The apparent discrepancy between light absorption and IPCE can be explained by the fact that IPCE measures the percentage of incident photons that eventually results in free charges being collected through the OSC electrodes. Factors beyond light absorption, such as the resistance of electrodes, exciton dissociation rate, and charge collection efficiencies will also affect the magnitude of IPCE. However, such nonoptical effects are likely to be not wavelength sensitive and are represented by vertical shifts of the entire

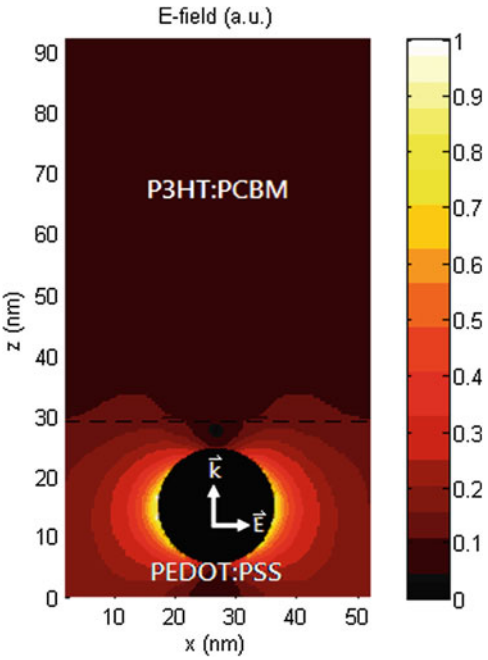

Fig. 8.5 Theoretical electric field profile in the PEDOT:PSS:Au NPs/ P3HT:PCBM OSCs [18]

IPCE spectrum. Comparing devices with or without Au NPs in Fig. 8.4b, it can be observed that the IPCE shows a wideband improvement from ~400 to 650 nm. It therefore can be concluded that plasmonic effects does not play a major role in improving PCE and electrical effects have to be accounted for.

It should be noted that in the measurement of light absorption shown in Fig. 8.4a, the absorption of the PEDOT:PSS layer (with or without Au NPs) has been deduced as they will absorb light. Therefore, the absorption spectrum represents light harvesting within the active layer only, which is important for understanding the plasmonic effects on device performances. The insignificant change in absorption spectra is a direct evidence that light absorption in P3HT:PCBM is unaffected by the incorporation of Au NPs.

8.2.4 Effects of Au NPs on PEDOT:PSS

The morphology changes of the PEDOT:PSS:Au NP layer can be observed from AFM images on a PEDOT:PSS:Au NP film for different NP concentrations as shown in Fig. 8.6. Upon increasing Au NP concentration, an obvious change can be observed in surface morphology of the PEDOT:PSS film, with an increase in roughness of ~5 and ~40 % for 0.32 and 0.64 wt% Au NPs, respectively. It has been reported that increasing anode surface roughness will increase the interface area between the anode and active layer, providing shorter routes for holes to

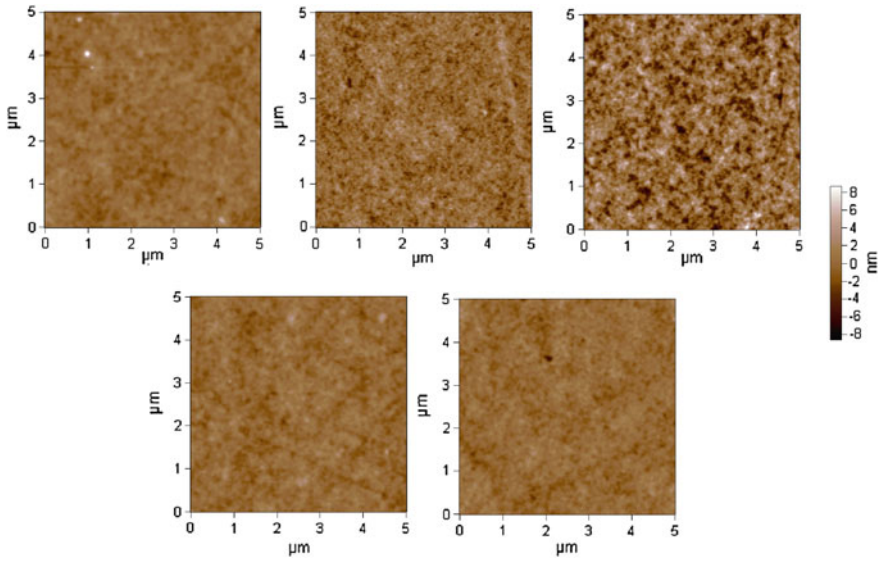

Fig. 8.6 AFM height images for different Au NP concentrations in PEDOT:PSS—0 % (*top left*), 0.32 % (*top center*), 0.64 % (*top right*). After spin-coating an extra layer of PEDOT:PSS on *top* of the PEDOT:PSS:Au NPs layer, the AFM images show a smoothened surface for 0.32 % (*bottom left*) and 0.64 % (*bottom right*) [18]

travel to the anode and enhancing hole collection at the anode [23]. The increased interfacial area between PEDOT:PSS and P3HT:PCBM allows the collection of a larger number of holes in the P3HT:PCBM layer, thus increasing J_{sc} of our devices. In addition, the reduced mean distance of between generated holes and the PEDOT:PSS interface diminishes the dependence of holes on the external electric field for collection at the anode, explaining the improvement in FF of our devices. Besides, it has been suggested that a rough P3HT:PCBM surface creates defect sites that assist exciton dissociation [24]. These effects together account for the improvements in J_{sc} and FF in our devices. The improved forward bias injection upon addition of Au NPs in our devices further support the claim that the increased PEDOT:PSS roughness increases PEDOT:PSS/P3HT:PCBM interfacial area. Considering the optical effects of a rough PEDOT:PSS surface, the transmission of PEDOT:PSS with or without Au NPs has been studied and observed no discernible difference. In addition, the refractive index difference between PEDOT:PSS and P3HT:PCBM is not large and the roughness is nanoscale. Hence, the rough PEDOT:PSS surface does not contribute to scatter light significantly.

To further elucidate this effect, an approach has been implemented to remove the surface roughness of the PEDOT:PSS layer while retaining Au NPs inside the PEDOT:PSS film. The approach is to spin-coat an extra PEDOT:PSS layer on top of the PEDOT:PSS:Au NP layer. From AFM images in Fig. 8.6, this extra layer smoothens the surface of the PEDOT:PSS to a morphology similar to a regular PEDOT:PSS layer. Devices are fabricated with the structure ITO/PEDOT:PSS:Au

NPs/PEDOT:PSS/P3HT:PCBM/LiF(1 nm)/Al (100 nm). After the insertion of the pristine PEDOT:PSS layer, the presence of Au NPs in these devices provides no improvements in device performance. Meanwhile, since optical effects have been proven to be unlikely to be a major contributor to performance improvement, one cannot argue that positive LSPR effects are diminished by the alteration of optical interference profile inside the OSC due to the addition of an extra layer of PEDOT:PSS. As a result, the main effect of the extra PEDOT:PSS layer is to smoothen the rough surface of the PEDOT:PSS:Au NPs layer. Consequently, the results indicate that the rough PEDOT:PSS: Au NPs layer surface positively contributes to device performances.

The resistance of PEDOT:PSS from resistive devices with the structure ITO/PEDOT:PSS:Au NPs/Al(80 nm) has also been reported [36]. *J–V* measurements from these devices indicate a slight reduction in PEDOT:PSS resistance from 1.33 (No NPs) to 0.97 Ω (0.32 wt%). Although reduction in PEDOT:PSS resistance reduces the series resistance of OSCs, the small decrease in PEDOT:PSS resistance can only provide minor contributions to device performance improvement. On the whole, it can be concluded that the improved hole collection at the roughened interface between PEDOT:PSS and P3HT:PCBM enhance device performances, while a slight reduction in PEDOT:PSS resistance by the incorporation of Au NPs can also provide minor contribution to performance improvements.

8.2.5 Effects of Au NPs on Exciton Quenching

A missing picture is the origin of device performance degradation at high NP concentrations. To investigate this effect, the photoluminescence (PL) spectrum of PEDOT:PSS:AuNPs/P3HT:PCBM films has been investigated (see Fig. 8.7). The PL spectra show increasing PL intensity upon increasing concentrations of Au NPs, with a maximum of $\sim$10 % increase at $\sim$647 nm.

PL intensity changes can be caused by three main reasons: changes in optical absorption, exciton quenching at metal/organic interfaces [25–27], and exciton quenching at donor/acceptor (D/A) interfaces [28, 29]. The possibility of changes in optical absorption is eliminated, as we have experimentally and theoretically shown previously that light absorption of OSCs do not change significantly after the incorporation of Au NPs. Considering the second reason, exciton quenching at metal/organic interfaces, it has been reported that capping an insulating layer on Au NPs can prevent direct contact between the metal and organic layer, hence preventing exciton quenching on the NP surface [30]. Furthermore, as shown in Fig. 8.3c, Au NPs located near the surface of PEDOT:PSS are well covered by PEDOT:PSS. Hence, it is expected that the Au NPs are not in direct contact with the P3HT:PCBM layer and the effect of exciton quenching by Au NPs is negligible.

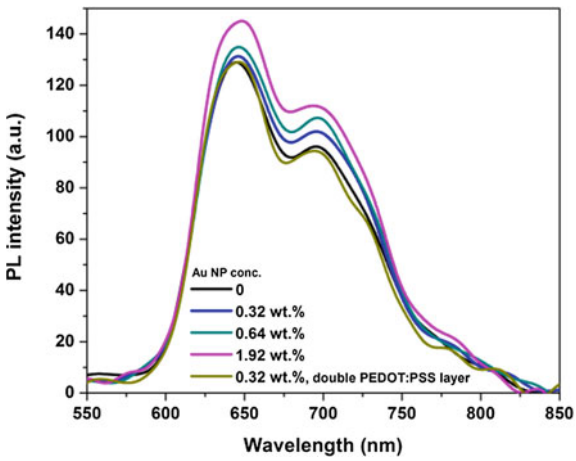

Fig. 8.7 Photoluminescence spectra of P3HT:PCBM for different Au NP concentrations in PEDOT:PSS [18]

For the third reason, the reduction in exciton quenching at D/A junctions indicates reduced D/A interface area, and hence a change in the morphology of the active layer [31]. It should be noted that studies have shown that PL increase can be a result of an increase in crystallinity of P3HT in the P3HT:PCBM blend, causing an increase in hole mobility and PCE [28, 32, 33], which apparently cannot address our results. However, it should be noted that the increase in crystallinity of P3HT has also been associated with an enhancement of absorption of P3HT:PCBM in the red region, which is not observed in the results of Ref. [18]. Hence, the increase in PL is attributed to changes in phase separation in the P3HT:PCBM blend leading to reduced D/A junction interfacial area, instead of changes in crystallinity of P3HT. The reduced D/A junction area causes exciton dissociation efficiency to decrease and reduce PCE. In addition, the AFM images of the top surface of the P3HT:PCBM film show no significant change in top surface morphology. This implies that the rough PEDOT:PSS surface, caused by the incorporation of NPs, could only cause a change in internal networking of the subsequently spin-coated P3HT:PCBM film near the PEDOT:PSS side.

Further evidence of the roughness effects on the change of phase separation can be found from the PL spectrum of PEDOT:PSS:Au NPs/PEDOT:PSS/P3HT:PCBM film (see Fig. 8.7) that no significant difference in PL intensity between the samples with single PEDOT:PSS layer (without Au NPs) and double PEDOT:PSS layer (with Au NPs in first layer) is observed. In this case, no clear PL intensity change is observed as the smoothened PEDOT:PSS surface, caused by the addition of an extra PEDOT:PSS layer, does not alter the internal networking of the active layer. Therefore, it can be concluded that incorporation of Au NPs modifies PEDOT:PSS surface morphology and leads to the reduced exciton quenching, which can be explained by alterations in the internal networking of the P3HT:PCBM film near the PEDOT:PSS side.

In terms of the impact on device performances, on the one hand, the reduction in exciton quenching after addition of Au NPs implies a reduction in free carrier

generation, leading to a lower J_{sc} and FF. On the other hand, the previously investigated hole collection improvement is advantageous to J_{sc} and FF. The competition between the two effects contributes to the trend in PCE variation as shown Table 8.1: as Au NPs are added to PEDOT:PSS, the surface roughness increases, creating a larger PEDOT:PSS/P3HT:PCBM interface area. Therefore, more holes can be collected at the anode, leading to enhancements in J_{sc}, FF and PCE. However, the increased roughness also affects P3HT:PCBM networking and reduces exciton quenching. When the Au NPs concentration increases further from 0.32 toward 1.92 %, the negative effects of reduced exciton quenching outweigh the positive effects of improved hole collection, resulting in the reduction of PCE as shown in Table 8.1 and thus PCE peaks at 0.32 wt%.

8.2.6 Section Summary

The incorporation of Au NPs into the PEDOT:PSS layer of an OSCs offers ~13 % improvement in PCE in robust material system of P3HT:PCBM, mainly due to improvements in J_{sc} and FF. The experimental and theoretical studies showed that absorption enhancements are minimal, and this is explained by the lateral distribution of the strong near field of NPs. The study of PEDOT:PSS morphology reveals that Au NP incorporation will cause the surface roughness of PEDOT:PSS to increase, leading to more efficient hole collection. Also, the resistance of PEDOT:PSS reduces upon incorporation of NPs. On the other hand, PL measurements indicate that exciton quenching is reduced due to the change in internal networking of the active layer. The combination of these electrical effects explains the trend of PCE reported in the work [18].

8.3 Electrical and Optical Properties of Organic Solar Cells with Au Nanoparticles Doped into the Active Layer

With our previous section showing that performance improvement of OSCs incorporated with Au NPs in the PEDOT:PSS layer is not due to LSPR effects, we would like to discuss the OSC performance improvement mechanisms when NPs are doped in a different layer and understanding the conditions in which LSPR effects can be utilized in OSCs. We noticed that previous studies have commonly used the metallic NPs as an interfacial layer on ITO coated glass substrates or a dopant of buffer layers such as PEDOT:PSS [6–9]. OSCs with the incorporation of metallic NPs into the active layer, however, have received limited detailed investigation. [12, 15, 34] Therefore, the study for further understanding both optical and electrical properties is highly desirable for OSCs with metallic NPs incorporated into the active layer.

In this section, the impact of the incorporation of monofunctional PEG-capped Au NPs into the active layer of polymer blend will be discussed [35]. The polymer donor used in the active layer of the OSCs is poly[2,7-(9,9-dioctylfluorene)-*alt*-2-((4-(diphenylamino) phenyl)thiophen-2-yl)malononitrile] (PFSDCN) [36]. The improvement of V_{OC}, J_{sc}, *FF* is reported with an appropriate amount of Au NPs incorporated into the active layer. As a result, after optimization, the improvement of PCE by ~32 % can be achieved [35]. The theoretical and experimental studies of effects of LSPR introduced by Au NPs on the optical and electrical properties of OSCs, particularly the OSC active layer will be discussed in this section.

8.3.1 Overall Device Performances

The absorption spectrum of PFSDCN film is shown in Fig. 8.8 and has two absorption peaks at around 374 and 518 nm. The chemical structure of PFSDCN is shown in the inset of Fig. 8.8. The optical bandgap and oxidation potential of PFSDCN are 2.05 eV and 0.91 V, respectively. The HOMO is –5.32 eV as measured by cyclic voltammetry (CV) method and the LUMO is −3.27 eV calculated from HOMO level and optical bandgap. The absorption spectrum of Au NPs in chloroform/chlorobenzene (1:1 v/v ratio) is shown in Fig. 8.9 with the peak at ~520 nm. The average diameter of Au NPs is ~18 nm determined from TEM measurement (inset of Fig. 8.9).

The *J*–*V* characteristics are shown in Fig. 8.10a. The effects of Au NPs concentration on performances including V_{OC}, J_{sc}, FF, and PCE of OSCs with structure of ITO/PEDOT:PSS (30 nm)/PFSdCN:PCBM (1:4 wt%; 2 mg/ml:8 mg/ml dissolved in chloroform/chlorobenzene (1:1, v/v ratio)): Au NPs/LiF (1 nm)/Al(100 nm) are shown in Fig. 8.10b (i)–(iv), respectively. It should be noted that the fabrication conditions such as the ratio of PFSDCN to PCBM, spin-coating

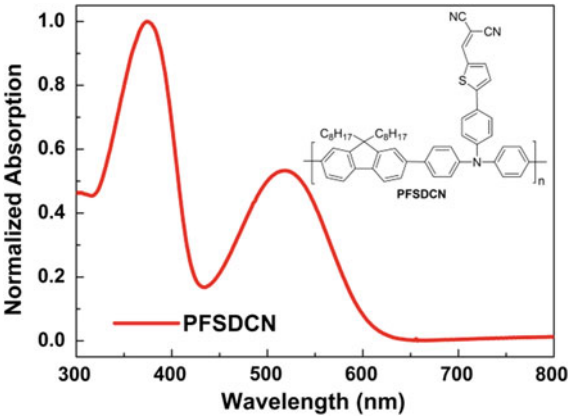

Fig. 8.8 The normalized absorption spectrum and chemical structure of PFSDCN [35]

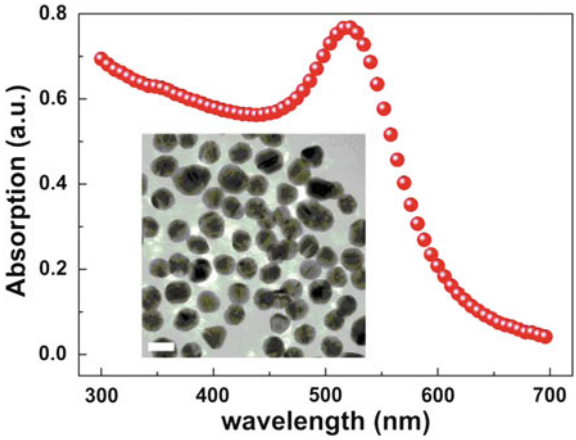

Fig. 8.9 The absorption spectrum of Au NPs in chloroform/chlorobenzene (1:1 volume ratio) with the peak at ~520 nm. *Inset* is the TEM image of Au NPs. The *white color bar* is 20 nm long [35]

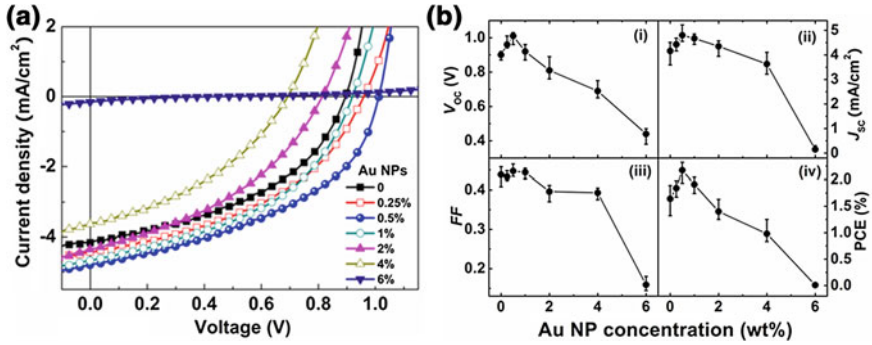

Fig. 8.10 **a** The current–voltage characteristics of the representative OSCs incorporated with different NP concentration under AM 1.5G illumination at 100 mW/cm^2. **b** Electrical parameters of NP incorporated OSCs: (i) V_{OC}; (ii) J_{SC}; (iii) *FF*; (iv) PCE [35]

speed and time, annealing temperature, and duration have been optimized for the control devices before the addition of Au NPs.

It is observed that Au NPs with a low concentration of 0.5 wt% improve V_{OC} and J_{sc}. However, both V_{OC} and J_{sc} reduce when Au NPs concentration increases further. *FF* increases slightly and then decreases as Au NPs concentration increases. From the dark *J*–*V* characteristic, it can be observed that the electrical conductivity improves by adding Au NPs, which is in good agreement with other reports [15]. However, the electrical conductivity reduces with the further increase of Au NPs concentration >2 wt%. Consequently, PCE is improved by ~32 % from 1.64 (without Au NPs) to 2.17 % (with 0.5 wt% Au NPs), and then

decreases. When Au NPs concentration reaches 6 wt%, almost no photovoltaic effect is observed (PCE $\sim$0.01 %).

It should be noted that in the study [35], Au NPs have been capped with PEG. In order to investigate the effects of PEG on device performances, the PEG-only OSCs were fabricated in which only PEG was incorporated into the polymer blend. PEG concentration in the mixed solution is $\sim$0.08 mg/ml which equals that of the PEG in 0.5 wt% Au NPs mixed with polymer blend solution. The PEG-only OSC shows similar *J*–*V* characteristics and PCE ($\sim$1.67 %) to that of the device without PEG incorporation (PCE $\sim$1.64 %). Therefore, PEG itself is not likely to have pronounced effects on device performances.

8.3.2 LSPR Effects

The degree of contributions of LSPR effect can be observed from the absorption spectrum of the active layer incorporated with various Au NPs concentrations, while the physical understanding can be obtained from theoretical analyzing the absorption of OSCs as shown in Fig. 8.11. The theoretical near-field profile of electric field (Fig. 8.11b) shows very strong field strength laterally distributed along the active layer which can enhance the light absorption by the polymer blend for generating carriers. It is noteworthy that when Au NPs incorporated into PEDOT:PSS layer (i.e., the layer adjacent to the active layer), the light absorption in the active layer is not clearly enhanced due to the lateral distribution feature of the strong LSPR near field along the PEDOT:PSS layer rather than a vertical distribution into the active layer as described in our another work [18].

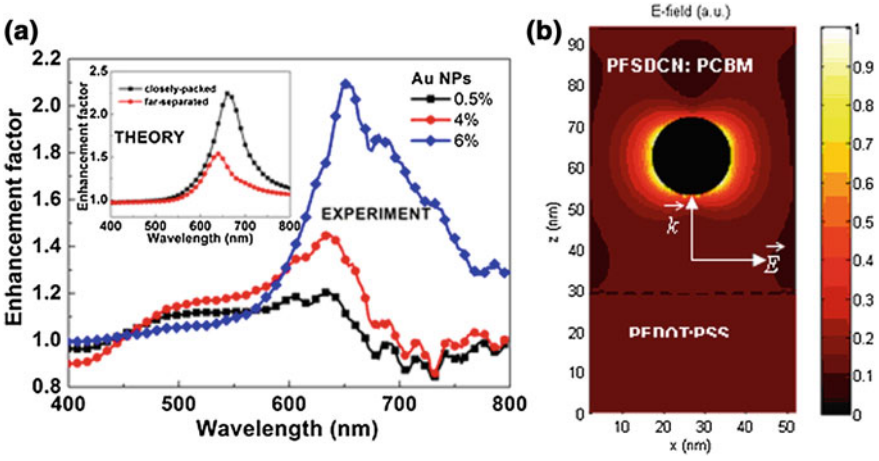

Fig. 8.11 **a** Experimental and theoretical (*inset*) absorbance enhancement factor of the active layer with different amount of Au NPs. **b** Theoretical near-field distribution around an Au NP in the active layer [35]

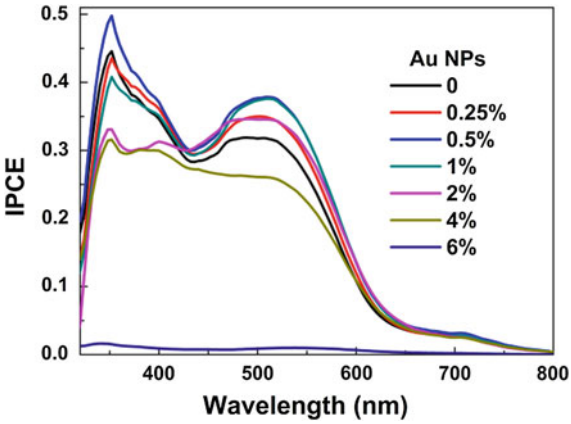

Fig. 8.12 IPCE of OSCs incorporated with different concentrations of Au NPs [35]

The theoretical and experimental absorption enhancement of the active layer (PFSDCN:PCBM) indicates that LSPR for the case of low Au NPs concentration mixed active layer exists at around 650 nm which is different from that of Au NPs ($\sim$520 nm) in chloroform/chlorobenzene (1:1 v/v ratio) due to the change of the surrounding optical environment. Moreover, when the spacing between Au NPs reduces (i.e., higher Au NPs concentration), the theoretical and experimental results show that the resonance strength increases and slightly red shifts. Consequently, the theoretical results are in agreement with the experimental results. The results demonstrate and explain the features of LSPR excited by Au NPs incorporated into OSCs active layer.

The light absorption can be enhanced experimentally by over 100 % at the resonance region when Au NPs concentration increases to 6 wt% as shown in Fig. 8.11a. However, the effects of LSPR alone cannot completely interpret the overall observed phenomena of OSCs. For example, low Au NPs concentration can benefit OSC performances. Continuously enhanced light absorption is obtained with the increase of Au NPs concentration due to the stronger LSPR. However, when Au NPs concentration >0.5 wt%, deterioration of device performances is obtained, which is quite unexpected in the viewpoint of LSPR effects. This can be further illustrated from IPCE characteristics as shown in Fig. 8.12. When the Au NPs concentration reaches 6 wt%, a large absorption enhancement factor is obtained (Fig. 8.11a), but IPCE decreases to almost zero. Therefore, besides LSPR effects, the effects of Au NPs on OSC electrical properties need to be investigated for understanding the results.

8.3.3 Effects on Carrier Mobility

Generally, electron and hole mobilities are the important factors and should be high enough to guarantee large carrier hopping rate, to avoid carrier recombination

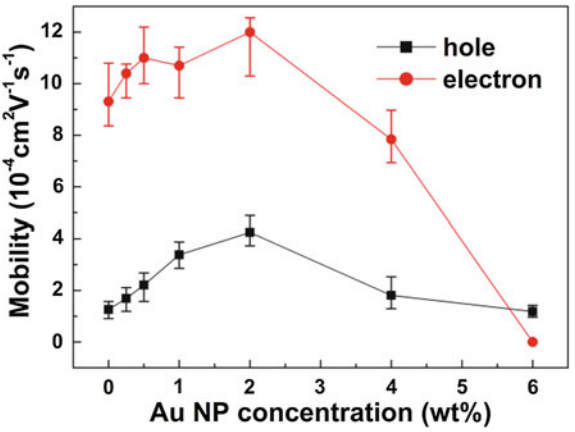

Fig. 8.13 Effects of Au NP concentration on the hole and electron mobilities in the active layer [35]

and to prevent the build-up of space charge. [37, 38] For Au NPs incorporated OSCs, the hole and electron mobilities have been determined from hole-only and electron-only devices, respectively, by fitting from the dark *J*–*V* curves using the space-charge limited current (SCLC) model. [39] Hole-only devices have structures of ITO/PEDOT:PSS/polymer blend: Au NPs/Au (20 nm)/Al (80 nm). It has been reported that the work function of ITO can be effectively modified for electron collection in inverted OSCs by evaporating 1 nm of Ca [40, 41]. For our electron-only devices, the structure of ITO/Ca (2 nm)/polymer blend: Au NPs/LiF(1 nm)/Al(100 nm) has been investigated. The mobility of holes and electrons is shown in Fig. 8.13 and the detailed experimental data and fitting curves are shown in Fig. 8.14. The hole mobility (1.18–4.25 $\times$ 10^{-4} $cm^2V^{-1}s^{-1}$) is about one order less than electron mobility (0.78–1.2 $\times$ 10^{-3} cm^2 $V^{-1}s^{-1}$) except for that of OSC with 6 wt% Au NPs. Hence, the charge transport of the devices is dominantly limited by the hole transport property, which agrees well with the fact that the transport process in the organic materials is dominated by the slow charge carriers [42].

The effects of Au NPs on the carrier mobility are manifold. On the one hand, Au NPs can introduce dopant states within the bandgap of polymer which can provide hopping sites for holes, and thus enhance the mobility [15]. In fact, the metallic NP-induced energy levels for holes have also been reported previously in a hybrid Ag NPs/organic resonant tunneling diode [43]. On the other hand, the incorporated Au NPs will modify the nanoscale morphology of the polymer/fullerene blend, especially with high NPs concentration, which can be evidenced by the AFM image as shown in Fig. 8.15. The root mean square (RMS) roughness of the active layer increases significantly from $\sim$0.617 (without Au NPs) to $\sim$8.062 nm (6 wt% Au NPs) and an obvious different surface morphology is observed. In addition, the phase image shows a much larger contrast for the active layer film with 6 wt% Au NPs, indicating a nanoscale morphology change of the blends. [44, 45] Such NPs-induced nanoscale morphology change may not favor charge transport, and thus degrades the carrier mobility. The two factors will

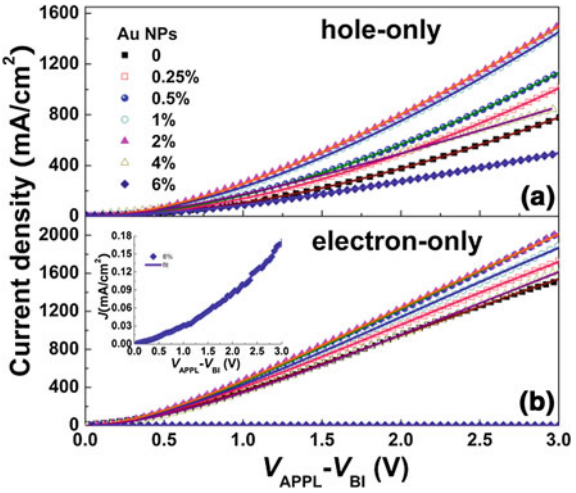

Fig. 8.14 Experimental data (*symbols*) and fitted *J*–*V* curves (*solid lines*) of **a** hole-only devices **b** electron-only devices. The electrical conductivity of electron-only device with 6 wt% Au NP concentration is rather low, and thus is shown in the *inset* of (**b**) [35]

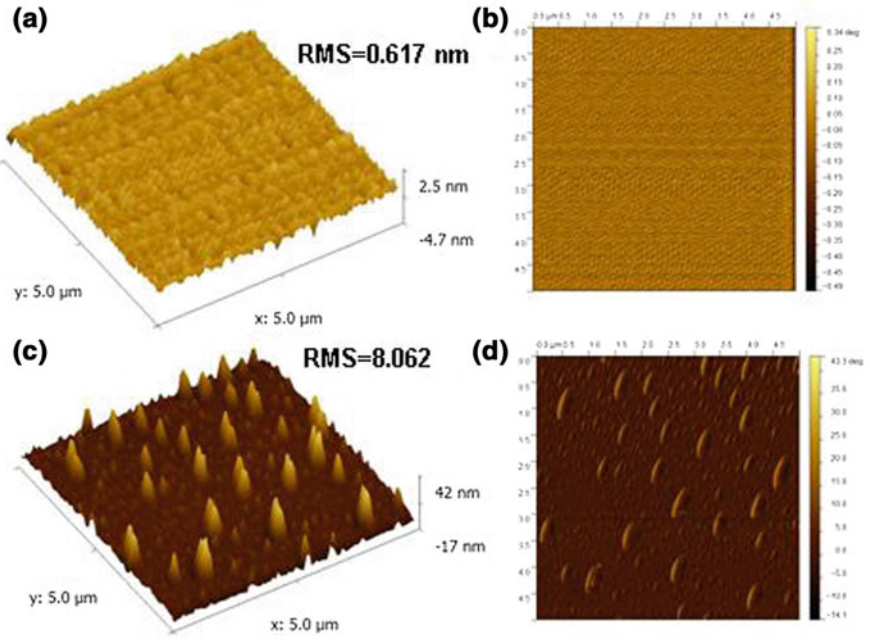

Fig. 8.15 AFM images of the active layer **a** height image, RMS = 0.617 nm and **b** phase image of active layer film without Au NPs; **c** height image, RMS = 8.062 nm and **d** phase image of active layer film with Au NPs: 6 wt% [35]

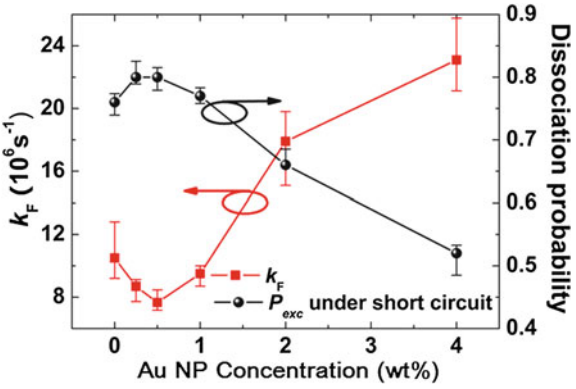

Fig. 8.16 Effects of Au NP concentration on the decay rate of bound electron–hole pair (k_F) (*square*) and exciton dissociation probability (P_{exc}) under short-circuit condition (*circle*) [35]

therefore compete with each other in our devices. At low Au NPs concentration, the blend morphology does not have clear changes from our AFM results (i.e., rms. roughness only increases to ~1.204 nm for 1 wt% Au NP incorporation, and therefore only plays a less important role in modifying carrier mobility. As a result, with low Au NPs concentration, the increases of carrier mobility should be explained by the introduction of hopping sites for holes. These hopping sites are expected to have greater influence on hole mobility than electron mobility, which agrees well with the experimental results. Compared with the control devices (without Au NPs), incorporation with 2 wt% Au NPs contributes to an improvement of hole mobility by ~237 % (from 1.26×10^{-4} to 4.25×10^{-4} $cm^2V^{-1}s^{-1}$), and an improvement of electron mobility only by ~28 % (from 0.93×10^{-3} to 1.2×10^{-3} $cm^2V^{-1}s^{-1}$). With high Au NPs concentration, the NP-induced morphology change dominates the charge transport process, and thus both the hole and electron mobility are expected to degrade, which is well consistent with the experimental results as shown in Fig. 8.16. Therefore, the enhanced carrier mobilities with the proper amount of Au NPs can partly account for the improved photocurrent generation and *FF* due to the improved carrier collection and the reduced bulk resistance. However, when the carrier mobility maintains increment until Au NPs concentration reaching 2 wt%, device performances, i.e., J_{sc} and PCE decrease when Au NPs concentration ≥1 wt%. This indicates that besides the carrier mobility, Au NPs should affect other operation processes of OSCs. One process likely to be affected is the dissociation of excitons to free carriers as described below.

8.3.4 Effects on Exciton Dissociation

The efficiency of exciton dissociation can be investigated by fitting photocurrent (J_{ph}) as a function of effective voltage (V_{EFF}) as reported in Mihailetchi et al. [46]. The maximal generation rate of excitons (G_{max}) for all the devices with different

Au NPs concentration [35] is on the order of 5×10^{27} m^{-3} s^{-1}. The exciton decay rate (k_F) and exciton dissociation probability (P_{exc}) under short-circuit condition are shown in Fig. 8.16. It can be observed that Au NPs indeed affects the exciton dissociation. Low Au NPs concentration makes k_F reduce and P_{exc} increase slightly from ~76 to ~80 %. While Au NPs concentration further increases, P_{exc} reduces.

The slight enhancement of P_{exc} at low Au NPs concentration can be attributed to the excitation of LSPR [47] and the enhanced hole mobility which reduces the carrier back-transfer induced recombination. [37, 42] The degradation of exciton dissociation efficiency at high NPs concentration can be attributed to the morphology change of the active layer and the reduced V_{OC}. As indicated from the surface image of the active layer in Fig. 8.15, the nanoscale morphology change inside the active layer is significant especially at high NPs concentration. Such NP-induced morphology change may make the polymer blend less favorable for exciton dissociation. On the other hand, the reduction of V_{OC} means a decrease of built-in electric field in the active layer, which will make the exciton dissociation process less efficient since the exciton dissociation is very field-dependent [48].

8.3.5 V_{oc}

As Au NPs concentration increases, V_{OC} first increases from ~0.90 (without Au NPs) to ~1.01 V (Au NPs: 0.5 wt%) and then decreases. When Au NPs concentration increases to 6 wt%, V_{OC} reduces significantly to 0.44 V. In BHJ OSCs, charge recombination is commonly regarded as one important loss mechanism limiting V_{OC}. [49, 50]. With a proper amount of Au NPs (≤0.5 %), the reduced recombination due to the enhanced carrier mobility and exciton dissociation is expected to improve V_{OC}. Theoretical studies built based on the fundamental equations describing carrier transports in semiconductors following Koster et al. [42] have been conducted to understand the contribution of recombination reduction on V_{OC}. Details of the model can be found in Appendix A. In modeling, the device parameters for OSCs with various Au NPs such as carrier mobilities and k_F are obtained by experiment and modeling in the previous sections, while other parameters are remained constant. The results show that V_{OC} has almost no change, suggesting that the reduced recombination due to increased carrier mobilities does not contribute to the V_{OC} improvement. An alternative explanation for the V_{OC} improvement with Au NPs incorporation (≤0.5 wt%) is the downwards shift of the donor HOMO level due to reduced polarization energy [51, 52]. Downwards shift of donor HOMO level by 0.1 eV is best fitted as shown in Appendix A: Fig. 8.17, for the increase of the measured V_{OC} by ~0.1 V for 0.5 wt% Au NP case.

The degradation of V_{OC} at high Au NPs concentration is due to several factors. At high concentration, large amount of Au NPs may modify the interfacial charge states at the cathode and even breakdown the Fermi level pinning between the

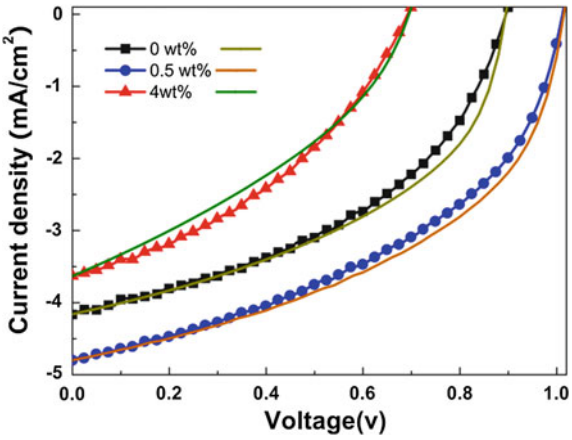

Fig. 8.17 *J–V* characteristics of the OSCs with different Au NPs concentration under AM 1.5G illumination at 100 mW/cm^2. The *symbols* denote experimental data (*squares*: without Au NPs; *circles*: Au NPs 0.5 wt%; *triangles*: Au NPs 4 wt%). The *solid lines* denote theoretical results [35]

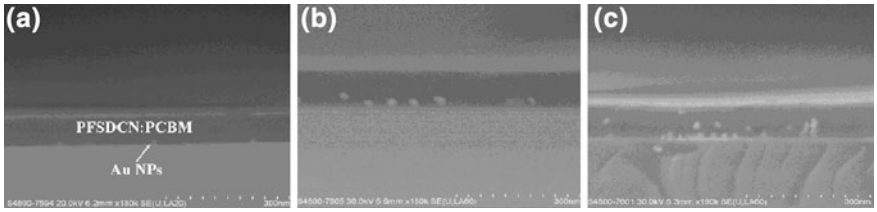

Fig. 8.18 SEM cross-section image of the active layer embedding with Au NPs **a** 0.5 wt%, **b** 2 wt% and **c** 6 wt% [35]

cathode metal and the fullerene reduction potential, which can downward shift the cathode work function and lead to remarkable V_{OC} reduction. This can be further revealed by the SEM cross-section images of the active layer in Fig. 8.18. With low concentration of Au NPs (0.5 and 2 wt%), the Au NPs are mostly located near the bottom of PFSDCN:PCBM (near to the interface with PEDOT:PSS). When embedding high concentration Au NPs (6 wt%, Fig. 8.18c), aggregation of NPs is observed and some are located at the surface of the active layer, which induce a significant morphology change and V_{OC} reduction. The theoretical results show that the change of work function of the cathode causes the reduction of V_{OC}. When the cathode work function is downward shifting by 0.56 eV, V_{OC} reduces to 0.69 V for OSCs with 4 wt% of Au NPs concentration. The other subordinate factor resulting in V_{OC} reduction is that more shunt paths are induced by the Au NPs, which can be well indicated from the increased reverse current for the OSCs as the concentration of Au NPs increases. The shunt paths formed directly from anode to cathode are believed to reduce the V_{OC} [53, 54].

8.3.6 Section Summary

The effects of Au NPs incorporated into the active layer PFSDCN:PCBM of OSCs have been described in this section. Theoretical simulations indicated that the near field of NPs distribute laterally along the active layer, leading to the absorption improvement which is also experimentally observed. On the other hand, electrical properties of these OSCs are also described. The carrier mobility is found to increase upon incorporation of NPs. In particular, hole mobility increased to a larger extent than electron mobility, leading to reduced carrier transport imbalance. Exciton dissociation efficiency is found to increase then decrease as NP concentration is increased. The active layer morphology is also altered after NP incorporation. These factors together lead to the observed PCE trend.

8.4 Efficiency Improvement of Polymer Solar Cells by Incorporating Au Nanoparticles into All Polymer Layers

Although PCE of OSCs has been shown to improve by incorporating metallic NPs in either the buffer layer such as PEDOT:PSS or the active layer [6, 7, 9–11, 47, 55], we have shown in Sects. 8.2 and 8.3 that in fact, the contribution of LSPR effects to PCE improvements varies when NPs are doped in different layers. Electrical properties such as carrier mobility, exciton dissociation probability, and the morphology of the organic layer incorporated with NPs are affected by NPs, and are major contributors to the PCE changes as NP concentration increases. With the experience of incorporating NPs individually in the hole collection layer or active layer, we noticed that there are very limited studies on incorporating metallic NPs in more than one organic layer. The study of incorporation of NPs in all organic layers has two objectives: (1) Achieving high efficiency OSCs by incorporating NPs within all possible layers of a OSC; (2) Investigating their effects on the optical and electrical properties, in particular, observing the presence of interaction between the NPs in different layers, if any. Achieving these two objectives will enhance our understanding in device mechanisms and is essential for designing high efficiency NP-incorporated OSCs.

In this work, monofunctional PEG-capped Au NPs of sizes 18 and 35 nm are doped in the PEDOT:PSS and P3HT:PCBM layers, respectively, leading to an improvement of PCE by $\sim$22 % compared to the optimized control device. We will first identify the impact of NPs in each polymer layer on OSC characteristics by doping Au NPs in either the PEDOT:PSS or P3HT:PCBM layer. Then, we will investigate the impact of Au NPs incorporated in all polymer layers. We demonstrate that the accumulated benefits of incorporating Au NPs in all organic layers of OSCs can achieve larger improvements in OSC performances.

8.4.1 Performances of Au NP Devices

Four device structures have been investigated [56] as follows:

Device A: (control): ITO/PEDOT:PSS/P3HT:PCBM/LiF (1 nm)/Al (100 nm)
Device B: ITO/PEDOT:PSS + Au NPs/P3HT:PCBM/LiF (1 nm)/Al (100 nm)
Device C: ITO/PEDOT:PSS/P3HT:PCBM + Au NPs/LiF (1 nm)/Al (100 nm)
Device D: ITO/PEDOT:PSS + AuNPs/P3HT:PCBM + Au NPs/LiF (1 nm)/Al (100 nm)

J–V characteristics of the four OSC device structures with Au NPs incorporated into different organic layers are shown in Fig. 8.19, and the photovoltaic parameters are listed in Table 8.2.

We observe that the incorporation of Au NPs into either the PEDOT:PSS layer (Device B) or the active layer (Device C) or improves PCE from 3.16 (control Device A) to 3.61 and 3.44 %, respectively. Interestingly, the simultaneous incorporation of Au NPs into both layers results in a further improvement of average PCE to 3.85 %, which corresponds to ~22 % increment from the control Device A. In all cases, the increases in PCE are results of improvements in J_{sc} and *FF*, while the V_{OC} is unchanged. Notably, when incorporating Au NPs into both PEDOT:PSS and active layer simultaneously, the series resistance (R_S) reduces obviously from 3.05 (Device A) to 1.93 $\Omega \cdot cm^2$ (Device D), contributing to a remarkable increase of *FF* from 61.92 to 65.00 %. To study the origins of PCE improvement, we first separately study the effects of NPs when incorporated into either the PEDOT:PSS or P3HT:PCBM layer, which is followed by discussions on PCE improvement when NPs are incorporated in all polymer layers.

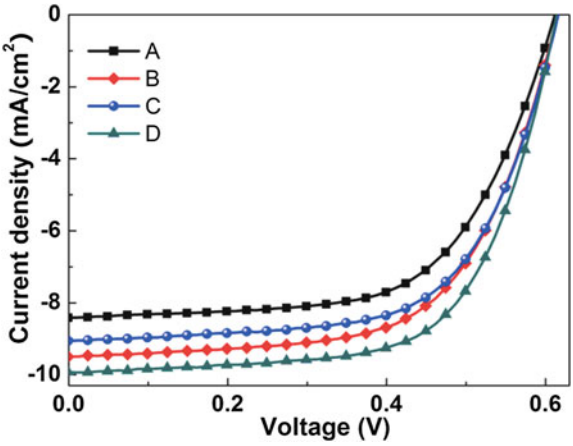

Fig. 8.19 **a** *J–V* characteristics of the OSCs with NPs incorporated into different layers under AM 1.5G illumination at 100 mW/cm^2 [35]

Table 8.2 Photovoltaic parameters of the PSCs with NPs incorporated in different layers under AM 1.5G illumination at 100 mW/cm^2. R_S is derived from the slope of the current–voltage (J–V) curves under dark at 2 V [56]

Device	V_{OC} (V)	J_{sc} (mA/cm^2)	FF (%)	PCE (%)	R_S (Ω.cm^2)
A	0.61 ± 0.00	8.35 ± 0.09	61.92 ± 0.33	3.16 ± 0.04	3.05 ± 0.03
B	0.61 ± 0.01	9.41 ± 0.28	62.52 ± 0.66	3.61 ± 0.08	2.11 ± 0.06
C	0.61 ± 0.00	8.85 ± 0.27	63.56 ± 0.53	3.41 ± 0.11	2.92 ± 0.13
D	0.61 ± 0.01	9.74 ± 0.57	65.00 ± 1.02	3.85 ± 0.20	1.93 ± 0.04

8.4.2 *Effects of Au NPs Incorporated in the PEDOT:PSS Layer Only*

For the case of Au NPs doped into the PEDOT:PSS layer only (Device B), a study of the physics been conducted in Sect. 8.2 [18]. In this set of experiment, the absorption spectrum of the active layer does not show any clear change from the control Device A as shown in Fig. 8.20.

This is in good agreement with previous report [18], which can be explained by the finding that the strong near field around Au NPs due to the LSPR distributes laterally along the PEDOT:PSS layer instead of vertically penetrating into the active layer. Meanwhile, from the hole mobilities of Devices A and B derived from the hole-only devices, there is no obvious changes (see Fig. 8.21), indicating that charge transport in the bulk of the active layer is unaffected by NPs incorporated in PEDOT:PSS. The surface morphology of the PEDOT:PSS + Au NPs layer showed an obvious increase in surface roughness with the RMS roughness increasing from 0.97 to 1.55 nm. Therefore, the incorporation of Au NPs only in PEDOT:PSS increases the interfacial contact area between the active layer (P3HT:PCBM) and PEDOT:PSS, allowing more efficient hole collection at the anode, and hence increases J_{sc} and FF [23, 57]. Furthermore, from resistive

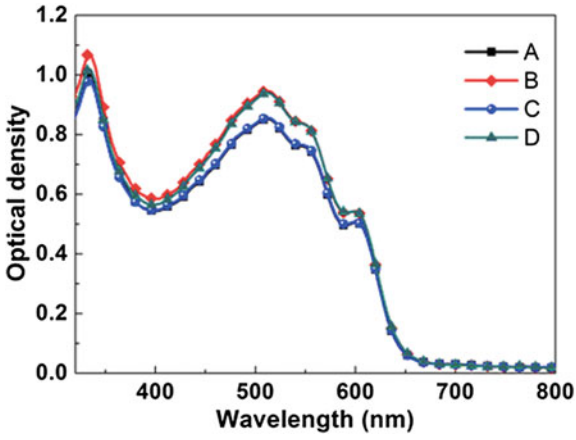

Fig. 8.20 Absorbance of the active layer for different NP doping structures [56]

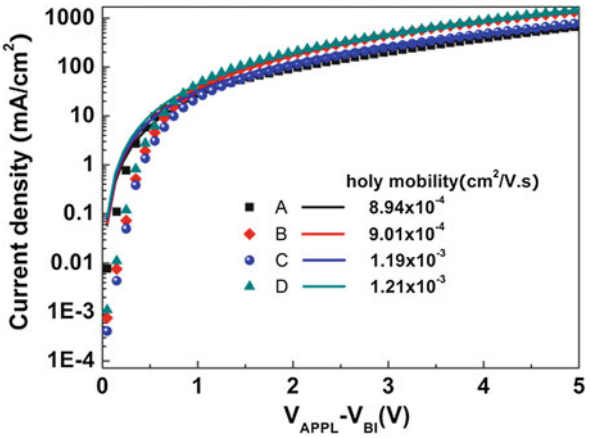

Fig. 8.21 The *J–V* characteristics of hole-only devices with Au NPs incorporated into different layers with the structure of ITO/PEDOT:PSS (with or without Au NPs)/ P3HT:PCBM (with or without Au NPs)/Au (20 nm)/ Al (100 nm). The *symbols* are experimental data while the *lines* are fitting curves. Fitting is done according to the space-charge limited current model [56]

devices of structure ITO/PEDOT:PSS (with or without Au NPs)/Al, it is found that the resistance of PEDOT:PSS reduces upon addition of NPs. Both the increased interfacial contact area and conductivity of PEDOT:PSS contributes to the reduction of the series resistance of OSCs from 3.05 to 2.11 $\Omega \cdot cm^2$, and improvement of *FF* and PCE.

8.4.3 Effects of Au NPs Incorporated into P3HT:PCBM

Although electrical effects dominantly address the performance improvement when incorporating Au NPs only in PEDOT:PSS, the mechanism for PCE improvement is found to be different when NPs are incorporated into the active layer. In contrast to Sect. 8.3, a different active layer material, P3HT:PCBM is used instead of PFSDCN:PCBM and the device characteristics are investigated here. As shown in Fig. 8.20, when NPs are incorporated into the active layer only (Device C), absorption of the active layer increases over a wide wavelength range.

From the theoretical studies [56], it is found that the absorption enhancement can be explained by LSPRs in the Au NPs excited by the TE polarized light. The dipoles generated in the Au NPs and the strong near field by LSPRs by Au NPs in the active layer are shown in Fig. 8.22. It can be observed that the strong near field distributes into the active layer and directly enhance the light absorption by the blended polymers of the active layer.

As a result of the strong near field of NPs which overlaps with the active layer, the amount of photogenerated excitons is increased, and hence increases the J_{sc} of OSCs. Regarding electrical properties, *J–V* measurements and fitting on hole-only devices indicate that the hole mobility of the active layer increases from 8.94×10^{-4} to 1.19×10^{-3} $cm^2/V \cdot s$. Studies have shown that in P3HT:PCBM, electron mobility is higher than hole mobility and this carrier imbalance is

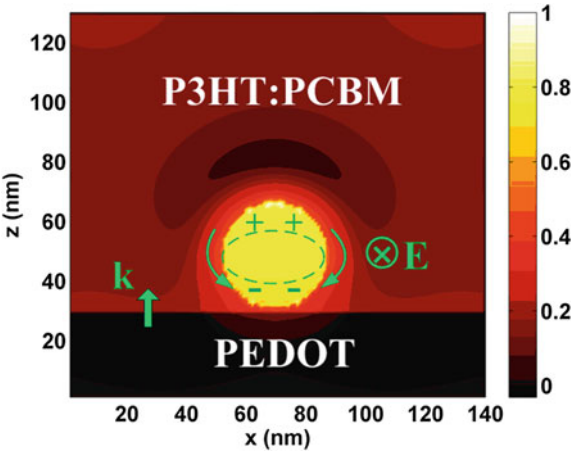

Fig. 8.22 The schematic pattern for the plasmon resonance and charge distribution of an Au NP, as well as the near-field distributions for the vertically incident light with TE polarization in P3HT:PCBM [56]

detrimental to the photovoltaic performance [29]. The increase in hole mobility allows more balanced charge transport in the active layer, thus improving the J_{sc} and *FF* of the device.

8.4.4 Effects of Au NPs Incorporated in All Polymer Layers

When Au NPs are doped into both PEDOT:PSS and the active layer, the PCE of our OSCs further increases to 3.85 %. From hole-only devices, the hole mobility of P3HT:PCBM is determined to be $\sim 1.21 \times 10^{-3}$ cm^2/V.s, which is similar to the case when NP is doped in the active layer only (1.19×10^{-3} cm^2/V.s). From the cross-section SEM images are shown in Fig. 8.23, Au NPs doped in the active layer are mostly located at the bottom of P3HT:PCBM (near to the interface with PEDOT:PSS), while the Au NPs doped to PEDOT:PSS are well embedded in the PEDOT:PSS layer. However, despite the fact that the active layer is adjacent to the PEDOT:PSS layer, the highly similar absorption spectra of Devices C (Au NPs in P3HT:PCBM only) and D (Au NPs in both P3HT:PCBM and PEDOT:PSS) shown in Fig. 8.20 show that there is no clear interaction between the Au NPs in the active layer and those in the PEDOT:PSS layer. From the principle of optics, the absence of couplings between Au NPs in PEDOT and Au NPs in P3HT:PCBM is reasonable, because the polarization direction of the electric field of vertically incident light is parallel to each device layer. Furthermore, we have shown that the improvement mechanisms when incorporating NPs in PEDOT:PSS mainly originates from PEDOT:PSS/P3HT:PCBM interfacial effects, while incorporating NPs in the active layer mainly improves optical absorption and charge transport in the bulk of the active layer. As interfacial and bulk effects are two individual effects and optical coupling between NPs is not observed, we expect that the improvement of PCE from 3.16 to 3.85 % is the accumulated improvements of addition of NPs into the individual layers.

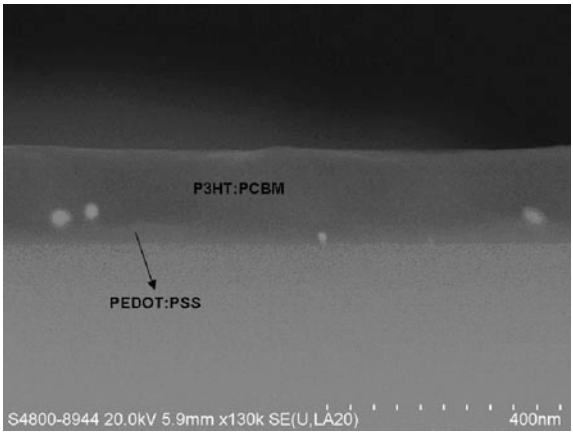

Fig. 8.23 Representative cross-section SEM image of the film structure PEDOT:PSS + Au NPs/ P3HT:PCBM + Au NPs [35]

8.4.5 Section Summary

In conclusion, by incorporating Au NPs into all organic layers in the OSCs, the efficiency can be improved by 22 %. The improvement is attributed to the accumulated enhancements in device performance due to addition of NPs into individual layers. NPs doped into PEDOT:PSS mainly contributes to more efficient hole collection due to increased PEDOT:PSS/P3HT:PCBM interfacial area, while NPs doped into the active layer improves optical absorption by LSPR effects and improves the hole mobility of the active layer. No optical coupling was observed between NPs in PEDOT:PSS and P3HT:PCBM. As the effects of NPs in PEDOT:PSS or P3HT:PCBM are separated, the PCE improvement was attributed to the accumulated benefits of NPs in the individual organic layers. Although the NPs in different layer did not interact to achieve extra improvements in PCE, this study shows that the advantages of incorporating NPs in individual layers can be utilized together to achieve larger increases of OSC performance and the role of NPs play when incorporated into OSCs has been further clarified, which is highly useful in designing high efficiency OSCs in the future.

8.5 Conclusions

We have discussed in detail that the effect of incorporation of NPs into various layers of an OSC. In Sect. 8.2, it has been reported [36] that about 13 % improvement in PCE for PSCs incorporating PEG-capped Au NPs in PEDOT:PSS, with enhancements mainly originating from J_{sc} and FF. A peak in PCE performance is obtained at an Au NP concentration of 0.32 wt% [35]. The contribution of LSPR effect to performance improvement has been theoretically and experimentally described. Both theoretical and experimental results show that absorption

enhancement due to incorporation of Au NPs is insignificant and provides only minor contribution to PCE improvement. It is found that the reason is due to the lateral distribution feature of the strong near-field of plasmonic resonance around the metallic NPs. Importantly, the finding can also be applied to other cases with metallic NPs (such as Ag and Pt) incorporated into the buffer layer adjacent to active layers of typical organic thin film solar cells. These studies [35, 58], that the optical properties of OSCs such as the direction dependence of absorption enhancement cannot but fully described by traditional physical quantities, such as scattering cross-section. It is highly necessary to account for near-field physics in order to provide a full picture for the effective optical design of photovoltaics.

Considering electrical characteristics, it is found [18] that the incorporation of an appropriate amount of Au NPs reduces the resistance of PEDOT:PSS layer. AFM images of NP incorporated PEDOT:PSS show that there is an increase in the interfacial roughness between P3HT:PCBM and PEDOT:PSS after incorporation of Au NPs. The roughened interface contributes to the improvement of hole collection efficiency and leads to J_{sc} and FF enhancements. PL measurements show that incorporation of Au NPs lead to reduced exciton quenching at D/A junctions at high NP concentrations due to change in internal networking of the active layer. The report indicates [18] that the competition between the effects of hole collection improvements and reduced exciton quenching, instead of LSPR effects, lead to the performance peak at 0.32 wt%.

In Sect. 8.3, the effects of PEG-capped Au NPs (0.5 wt%) on OSCs have been theoretically and experimentally discussed by introducing the Au NPs into a blend of a newly synthesized polymer of PFSDCN and PCBM [35]. The results show that due to the interesting feature of the strong lateral distribution of LSPR near field along the active layer, light absorption is enhanced by incorporating Au NPs into the active layer. This is in stark contrast with the case of NPs incorporated into PEDOT:PSS where LSPR cannot contribute to absorption enhancement.

Meanwhile, our discussion shows that electrical properties are also strongly affected by the NPs. Carrier mobility was found to increase which is beneficial to device performance. In particular, hole mobility increases at a quicker rate than electron mobility which may contribute to reducing carrier mobility imbalance. Exciton dissociation probability is also found to increase slightly then decrease rapidly upon increasing NP concentration. The morphology of the active layer is also strongly altered by high concentrations of Au NPs. The interplay of these various factors showed that enhancement in electrical properties can initially improve OSC performance at low NP concentrations. At higher concentrations, electrical effects can counter-diminish the optical enhancement from LSPR which reduces the overall performance improvement. Hence, it is very important that both optical and electrical properties need to be studied and optimized simultaneously. After optimization, power conversion efficiency can be improved by $\sim$32 % [35].

The studies in Sects. 8.2 and 8.3 have provided us with insights into the device mechanisms of OSCs. The role of LSPR is found to be not as important as many studies claimed to be in improving PCE of solar cells. In particular, only NPs

incorporated in the active layer can utilize LSPR to improve active layer absorption. On the other hand, electrical properties are found to play significant roles in improving PCE. Our studies highlight the important point that both electrical and optical characteristics have to be investigated in OSCs, and our findings are highly useful in the design of NP-incorporated solar cells.

In Sect. 8.4, Au NPs incorporated into both the hole collection layer and the active layer have been discussed. A large increase in PCE ($\sim$22 %) has been reported [56] which is attributed to the stacked improvements of NPs incorporating in the hole collection layer and the active layer. Coupling is not observed between NPs in the different layers, but this study shows that NPs can be incorporated in all layers to achieve large improvements in efficiency.

Appendix A

The electrical properties of OSCs with Au NPs in the active layer of PFSDCN: PCBM [35] have been theoretically studied by solving the organic semiconductor equations involving Poisson, drift–diffusion, and continuity equations [42, 46, 59]. The field-dependent mobility uses the Frenkel-Poole form $\mu = \mu_0 \cdot \exp(F/F_0)$. The Braun-Onsager model is employed for the exciton dissociation. The boundary conditions for ohmic or schottky contacts are also taken into account.

Due to the very thin active layer ($\sim$65 nm), it can be assumed the generation rate of bound electron–hole pairs (G_{max}) is uniform. G_{max} can be obtained from the measured absorption spectra. The electron and hole mobilities can be obtained by fitting the *J–V* curves of the measured electron- and hole-only devices following the SCLC model. The HOMO is -5.32 eV as measured by cyclic voltammetry (CV) method and the LUMO is -3.27 eV calculated from HOMO level and optical bandgap. The exciton decay rate (k_F) of exciton and charge separation distance (a) can be fitted to make our theoretical *J-V* curves best fit to the experimental *J-V* curves

References

1. Anker JN, Hall WP, Lyandres O, Shah NC, Zhao J, Van Duyne RP (2008) Biosensing with plasmonic nanosensors. Nat Mater 7(6):442–453
2. Stockman MI (2004) Nanofocusing of optical energy in tapered plasmonic waveguides. Phys Rev Lett 93(13):137404
3. Shalaev VM (2007) Optical negative-index metamaterials. Nat Photon 1(1):41–48
4. Chang DE, Sorensen AS, Demler EA, Lukin MD (2007) A single-photon transistor using nanoscale surface plasmons. Nat Phys 3(11):807–812
5. Atwater HA, Polman A (2010) Plasmonics for improved photovoltaic devices. Nat Mater 9(3):205–213

6. Chen F-C, Wu J-L, Lee C-L, Hong Y, Kuo C-H, Huang MH (2009) Plasmonic-enhanced polymer photovoltaic devices incorporating solution-processable metal nanoparticles. Appl Phys Lett 95(1):013305
7. Wu J-L, Chen F-C, Hsiao Y-S, Chien F-C, Chen P, Kuo C-H, Huang MH, Hsu C-S (2011) Surface plasmonic effects of metallic nanoparticles on the performance of polymer bulk heterojunction solar cells. ACS Nano 5(2):959–967. doi:10.1021/nn102295p
8. Morfa AJ (2008) Plasmon-enhanced solar energy conversion in organic bulk heterojunction photovoltaics. Appl Phys Lett 92(1):013504
9. Kim S (2008) Plasmon enhanced performance of organic solar cells using electrodeposited Ag nanoparticles. Appl Phys Lett 93(7):073307
10. Wang DH, Kim DY, Choi KW, Seo JH, Im SH, Park JH, Park OO, Heeger AJ (2011) Enhancement of donor–acceptor polymer bulk Heterojunction solar cell power conversion efficiencies by addition of Au nanoparticles. Angew Chem Int Ed 50(24):5519–5523. doi:10.1002/anie.201101021
11. Kim C-H, Cha S-H, Kim SC, Song M, Lee J, Shin WS, Moon S-J, Bahng JH, Kotov NA, Jin S-H (2011) Silver nanowire embedded in P3HT:PCBM for high-efficiency hybrid photovoltaic device applications. ACS Nano 5(4):3319–3325. doi:10.1021/nn200469d
12. Naidu BVK, Park JS, Kim SC, Park S-M, Lee E-J, Yoon K-J, Joon Lee S, Wook Lee J, Gal Y-S, Jin S-H (2008) Novel hybrid polymer photovoltaics made by generating silver nanoparticles in polymer: fullerene bulk-heterojunction structures. Sol Energy Mater Sol Cells 92(4):397–401. doi:10.1016/j.solmat.2007.09.017
13. Min C (2010) Enhancement of optical absorption in thin-film organic solar cells through the excitation of plasmonic modes in metallic gratings. Appl Phys Lett 96(13):133302
14. Kang M-G, Xu T, Park HJ, Luo X, Guo LJ (2010) Efficiency enhancement of organic solar cells using transparent plasmonic Ag nanowire electrodes. Adv Mater 22(39):4378–4383. doi:10.1002/adma.201001395
15. Kim K, Carroll DL (2005) Roles of Au and Ag nanoparticles in efficiency enhancement of poly(3-octylthiophene)/C[sub 60] bulk heterojunction photovoltaic devices. Appl Phys Lett 87(20):203113
16. Sha WEI, Choy WCH, Liu YG, Cho Chew W (2011) Near-field multiple scattering effects of plasmonic nanospheres embedded into thin-film organic solar cells. Appl Phys Lett 99(11):113304
17. Enüstün BV, Turkevich J (1963) Coagulation of colloidal gold. J Am Chem Soc 85(21):3317–3328. doi:10.1021/ja00904a001
18. Fung DDS, Qiao L, Choy WCH, Wang C, Sha WEI, Xie F, He S (2011) Optical and electrical properties of efficiency enhanced polymer solar cells with Au nanoparticles in a PEDOT-PSS layer. J Mater Chem 21(41):16349–16356
19. Bouyer F, Robben A, Yu WL, Borkovec M (2001) Aggregation of colloidal particles in the presence of oppositely charged polyelectrolytes: effect of surface charge heterogeneities. Langmuir 17(17):5225–5231. doi:10.1021/la010548z
20. Qian J, Jiang L, Cai F, Wang D, He S (2011) Fluorescence-surface enhanced Raman scattering co-functionalized gold nanorods as near-infrared probes for purely optical in vivo imaging. Biomaterials 32(6):1601–1610. doi:10.1016/j.biomaterials.2010.10.058
21. Catchpole KR, Polman A (2008) Design principles for particle plasmon enhanced solar cells. Appl Phys Lett 93(19):191113
22. Lee J-Y, Peumans P (2010) The origin of enhanced optical absorption in solar cells with metal nanoparticles embedded in the active layer. Opt Express 18(10):10078–10087
23. Hsu M-H, Yu P, Huang J-H, Chang C-H, Wu C-W, Cheng Y-C, Chu C-W (2011) Balanced carrier transport in organic solar cells employing embedded indium-tin-oxide nanoelectrodes. Appl Phys Lett 98(7):073308
24. Li G, Shrotriya V, Yao Y, Yang Y (2005) Investigation of annealing effects and film thickness dependence of polymer solar cells based on poly(3-hexylthiophene). J Appl Phys 98(4):043704

25. Chen L-M, Xu Z, Hong Z, Yang Y (2010) Interface investigation and engineering—achieving high performance polymer photovoltaic devices. J Mater Chem 20(13):2575–2598
26. Becker H, Burns SE, Friend RH (1997) Effect of metal films on the photoluminescence and electroluminescence of conjugated polymers. Phys Rev B 56(4):1893
27. Markov DE, Blom PWM (2005) Migration-assisted energy transfer at conjugated polymer/metal interfaces. Phys Rev B 72(16):161401
28. Zhokhavets U, Erb T, Hoppe H, Gobsch G, Serdar Sariciftci N (2006) Effect of annealing of poly(3-hexylthiophene)/fullerene bulk heterojunction composites on structural and optical properties. Thin Solid Films 496(2):679–682. doi:10.1016/j.tsf.2005.09.093
29. Li G, Shrotriya V, Yao Y, Huang J, Yang Y (2007) Manipulating regioregular poly(3-hexylthiophene): [6]-phenyl-C61-butyric acid methyl ester blends-route towards high efficiency polymer solar cells. J Mater Chem 17(30):3126–3140
30. Shen H, Bienstman P, Maes B (2009) Plasmonic absorption enhancement in organic solar cells with thin active layers. J Appl Phys 106(7):073109
31. Drees M, Hoppe H, Winder C, Neugebauer H, Sariciftci NS, Schwinger W, Schaffler F, Topf C, Scharber MC, Zhu Z, Gaudiana R (2005) Stabilization of the nanomorphology of polymer-fullerene "bulk heterojunction" blends using a novel polymerizable fullerene derivative. J Mater Chem 15(48):5158–5163
32. Kim Y, Cook S, Tuladhar SM, Choulis SA, Nelson J, Durrant JR, Bradley DDC, Giles M, McCulloch I, Ha C-S, Ree M (2006) A strong regioregularity effect in self-organizing conjugated polymer films and high-efficiency polythiophene: fullerene solar cells. Nat Mater 5(3):197–203
33. Kim H, So W-W, Moon S-J (2007) The importance of post-annealing process in the device performance of poly(3-hexylthiophene): Methanofullerene polymer solar cell. Sol Energy Mater Sol Cells 91(7):581–587. doi:10.1016/j.solmat.2006.11.010
34. Topp K, Borchert H, Johnen F, Tunc AV, Knipper M, von Hauff E, Parisi J, Al-Shamery K (2009) Impact of the incorporation of Au nanoparticles into polymer/fullerene solar cells†. J Phys Chem A 114(11):3981–3989. doi:10.1021/jp910227x
35. Wang CCD, Choy WCH, Duan C, Fung DDS, Sha WEI, Xie F-X, Huang F, Cao Y (2012) Optical and electrical effects of gold nanoparticles in the active layer of polymer solar cells. J Mater Chem 22(3):1206–1211
36. Duan CH, Wang CD, Liu SJ, Huang F, Choy CHW, Cao Y (2011) Two-dimensional like conjugated copolymers for high efficiency bulk-heterojunction solar cell application: band gap and energy level engineering. Sci China Chem 54(4):685–694
37. Mayer AC, Scully SR, Hardin BE, Rowell MW, McGehee MD (2007) Polymer-based solar cells. Mater Today 10:28–33
38. Mandoc MM (2007) Optimum charge carrier mobility in organic solar cells. Appl Phys Lett 90(13):133504
39. Mihailetchi VD, van Duren JKJ, Blom PWM, Hummelen JC, Janssen RAJ, Kroon JM, Rispens MT, Verhees WJH, Wienk MM (2003) Electron transport in a methanofullerene. Adv Funct Mater 13(1):43–46. doi:10.1002/adfm.200390004
40. Zhao DW (2009) An inverted organic solar cell with an ultrathin Ca electron-transporting layer and MoO3 hole-transporting layer. Appl Phys Lett 95(15):153304
41. Jiang CY, Sun XW, Zhao DW, Kyaw AKK, Li YN (2010) Low work function metal modified ITO as cathode for inverted polymer solar cells. Sol Energy Mater Sol Cells 94(10):1618–1621. doi:10.1016/j.solmat.2010.04.082
42. Koster LJA, Smits ECP, Mihailetchi VD, Blom PWM (2005) Device model for the operation of polymer/fullerene bulk heterojunction solar cells. Phys Rev B 72(8):085205
43. Zheng T, Choy WCH, Sun Y (2009) Hybrid nanoparticle/organic devices with strong resonant tunneling behaviors. Adv Funct Mater 19(16):2648–2653. doi:10.1002/adfm.200900308
44. Chen H-Y, Hou J, Zhang S, Liang Y, Yang G, Yang Y, Yu L, Wu Y, Li G (2009) Polymer solar cells with enhanced open-circuit voltage and efficiency. Nat Photon 3(11):649–653

45. Xu Z, Chen L-M, Yang G, Huang C-H, Hou J, Wu Y, Li G, Hsu C-S, Yang Y (2009) Vertical phase separation in poly(3-hexylthiophene): fullerene derivative blends and its advantage for inverted structure solar cells. Adv Funct Mater 19(8):1227–1234. doi:10.1002/adfm.200801286
46. Mihailetchi VD, Koster LJA, Hummelen JC, Blom PWM (2004) Photocurrent generation in polymer-fullerene bulk heterojunctions. Phys Rev Lett 93(21):216601
47. Chen F-C, Wu J-L, Lee C-L, Hong Y, Kuo C-H, Huang MH (2009) Plasmonic-enhanced polymer photovoltaic devices incorporating solution-processable metal nanoparticles. Appl Phys Lett 95(1):013305
48. Blom PWM, Mihailetchi VD, Koster LJA, Markov DE (2007) Device physics of polymer: fullerene bulk heterojunction solar cells. Adv Mater 19(12):1551–1566. doi:10.1002/adma.200601093
49. Brabec CJ, Cravino A, Meissner D, Sariciftci NS, Fromherz T, Rispens MT, Sanchez L, Hummelen JC (2001) Origin of the open circuit voltage of plastic solar cells. Adv Funct Mater 11(5):374–380. doi:10.1002/1616-3028(200110)11:5<374:aid-adfm374>3.0.co;2-w
50. Vandewal K, Tvingstedt K, Gadisa A, Inganas O, Manca JV (2009) On the origin of the open-circuit voltage of polymer-fullerene solar cells. Nat Mater 8(11):904–909
51. Tress W, Leo K, Riede M (2011) Influence of hole-transport layers and donor materials on open-circuit voltage and shape of I-V curves of organic solar cells. Adv Funct Mater 21(11):2140–2149. doi:10.1002/adfm.201002669
52. Akaike K, Kanai K, Ouchi Y, Seki K (2010) Impact of ground-state charge transfer and polarization energy change on energy band offsets at donor/acceptor interface in organic photovoltaics. Adv Funct Mater 20(5):715–721. doi:10.1002/adfm.200901585
53. Sun B (2005) Vertically segregated hybrid blends for photovoltaic devices with improved efficiency. J Appl Phys 97(1):014914
54. Snaith HJ, Greenham NC, Friend RH (2004) The origin of collected charge and open-circuit voltage in blended polyfluorene photovoltaic devices. Adv Mater 16(18):1640–1645. doi:10.1002/adma.200305766
55. Kim K, Carroll DL (2005) Roles of Au and Ag nanoparticles in efficiency enhancement of poly(3-octylthiophene)/C_{60} bulk heterojunction photovoltaic devices. Appl Phys Lett 87(20):203113. doi:10.1063/1.2128062
56. Xie FX, Choy WCH, Wang CCD, Wei E, Fung DDS (2011) Improving the efficiency of polymer solar cells by incorporating gold nanoparticles into all polymer layers. Appl Phys Lett 99:153304
57. Peng B, Guo X, Cui C, Zou Y, Pan C, Li Y (2011) Performance improvement of polymer solar cells by using a solvent-treated poly(3,4-ethylenedioxythiophene): poly(styrenesulfonate) buffer layer. Appl Phys Lett 98(24):243308
58. Xie F, Choy WCH, Zhu X, Li X, Li Z, Liang C (2011) Improving polymer solar cell performances by manipulating the self-organization of polymer. Appl Phys Lett 98:243302
59. Sievers DW, Shrotriya V, Yang Y (2006) Modeling optical effects and thickness dependent current in polymer bulk-heterojunction solar cells. J Appl Phys 100:114509

Chapter 9
Hybrid Solar Cells with Polymer and Inorganic Nanocrystals

Qidong Tai and Feng Yan

Abstract In this chapter, we aim to present an overview of the development of the polymer/inorganic hybrid solar cells. In the first section, we introduce the basic concepts of hybrid solar cells including the device architecture and operation mechanism. Then we summarize the recent progress in this area classified by the nanomorphology of inorganic nanocrystals, including nanoparticles, nanorods, nanowires, and vertically aligned nanoarrays. The nanoscale morphology of the inorganic crystal could play a decisive role in determining the conversion efficiencies of the hybrid solar cells. Finally, we focus on the interface modifications involved in hybrid solar cells. It is noteworthy that an appropriate interface modification could not only facilitate the exciton dissociation but also suppress the backward recombination of carriers and therefore significantly boost the device performance.

9.1 Introduction

To meet the urgent needs for cheap and clean energy, great efforts have been done on the development of the third generation of photovoltaics, including dye-sensitized solar cells (DSSCs) [1] and bulk heterojunction (BHJ) solar cells [2–4], which have the advantages of low cost, promising power conversion efficiency (PCE), facile fabrication by contact printing [5] or roll-to-roll process [6, 7] for large area devices, and so on. State-of-the-art BHJ solar cells are composed of conjugated

Q. Tai · F. Yan (✉)
Department of Applied Physics, The Hong Kong Polytechnic University, Kowloon, Hong Kong, China
e-mail: apafyan@polyu.edu.hk

W. C. H. Choy (ed.), *Organic Solar Cells*, Green Energy and Technology,
DOI: 10.1007/978-1-4471-4823-4_9,

polymers and fullerene derivatives, which are all organics, therefore, such devices are also called BHJ organic solar cells (OSCs). When the fullerene derivatives are replaced by their inorganic counterparts such as CdSe [8–12], CdS [13–15], TiO_2 [16–22], ZnO [23–31], SnO_2 [32], $CuInS_2$ [33] etc., the devices are then named hybrid solar cells (HSCs). Those inorganic materials have the advantages of high dielectric constant, high electron mobility and affinity, and good thermal stability and their optoelectronic properties can be tuned by changing their sizes and shapes, which could facilitate the design of high performance HSCs [34–38].

HSCs have been developed for years and insights of the underlying physics were gradually disclosed. Various inorganic nanocrystals with different morphologies, such as nanoparticle, nanorods, nanowires, and vertically aligned nanorod-, nanowire-, nanotube arrays, have been used together with many conjugated polymers. Both the materials and the nanofabrication techniques are critical issues to the HSCs, which have been developed by many research groups recently. Although the current PCEs of the HSCs are still much lower than the OSCs and DSSCs, higher PCEs are expected in the future when the device physics is further understood and new breakthroughs in synthesis of materials and device fabrication are achieved.

In this chapter, an overview of device structure and operation principle will be first introduced. Then, the developments of HSCs will be reviewed in view of the morphologies of the inorganic nanomaterials. Finally, the interface modification that would help to improve the device performance will be discussed. As there are hundreds of papers have been published in this area, we will not go through all of them but give a glance at the most representative and interesting results.

9.2 Device Physics and Device Structure

The HSCs work in the same way as OSCs, where the conjugated polymers serve as light absorber and electron donor (D), the inorganic nanocrystals serve as electron acceptor (A). Figure 9.1 gives the schematic illustration of the energy level alignment and the photocurrent generation mechanism in HSCs. Upon illumination, the photocurrent is generated via the following processes [36, 38]:

(1) *Photo absorption and exciton generation*. The conjugated polymers mainly account for the light absorption in HSCs. In some cases, the inorganic nanocrystals could also absorb light, but the majority of the light absorption are attributed to the conjugated polymers. The light harvesting efficiency (η_{LHE}) is determined by the bandgap (E_g) and the absorption coefficient of the polymers. After absorbing the incident photons, electrons will be excited from the highest occupied molecular orbit (HOMO) to the lowest unoccupied molecular orbit (LUMO). Due to the low dielectric constant of the polymers, the electrons in LUMO and the holes in HOMO are not free charges but excitons with strong Coulomb interaction. The exciton binding energy (E_b) is typically

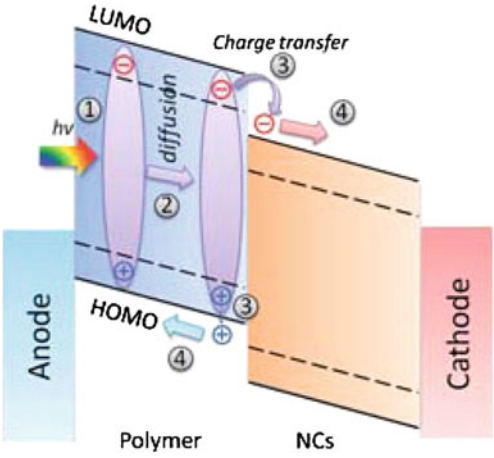

Fig. 9.1 Schematic illustration of the energy levels alignment and photocurrent generation mechanism in hybrid solar cells. Reproduced with permission from Ref. [36]

0.2–0.5 eV. Therefore, the exciton generation efficiency (η_g), which is regarded as the possibility of generating one exciton by one photon, is critical to the device performance. In addition, the excitons have a good chance to recombine [38].

(2) *Exciton diffusion*. Before separating into free charges, the excitons have to diffuse to the D/A interfaces. The exciton diffusion efficiency (η_{diff}) depends on how much the excitons could successfully diffuse to the D/A interface before recombination takes place. Noted that the exciton diffusion length is 4–20 nm for most conjugated polymers [36–38], the D/A domains in HSCs should also be in this range for high exciton diffusion efficiency.

(3) *Exciton dissociation*. Once reaching the D/A interface, excitons could be dissociated into free electrons and holes if the energy offset between the LUMO of the polymer and the conduction band (CB) of the inorganic nanocrystals overcomes the binding energy of the excitons; therefore, the relative positions of the LUMO of the Donors and the CB level of the inorganic acceptors determine the exciton dissociation efficiency (η_d).

(4) *Charge transfer and collection*. After the exciton dissociation, the free electrons and holes need to transfer through the inorganic nanocrystals and conjugated polymers until they are collected at the electrodes. The charge transfer efficiency (η_{tr}) is related to the intrinsic properties of the materials, e.g., the carrier mobility, the crystallinity and the purity, and so on. Besides, continuous pathways are also needed for efficient charge transfer. While the charge collection efficiency (η_{cc}) mainly depends on the energy level alignments of the active layer and the electrodes as well as the contact between them.

Therefore, the external quantum efficiency (EQE) of a HSC could be calculated through the following equation [38]:

$$EQE = \eta_{LHE} * \eta_g * \eta_{diff} * \eta_d * \eta_{tr} * \eta_{cc} \tag{9.1}$$

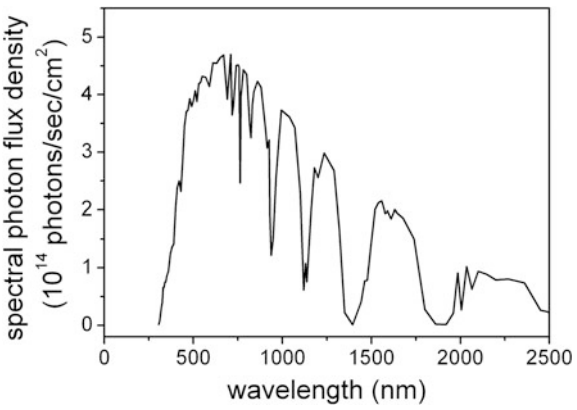

Fig. 9.2 Spectral photon flux density of the AM 1.5 G solar irradiation

Then the short circuit current (J_{sc}) could be obtained as [39]:

$$J_{sc} = q \int_{\lambda_{min}}^{\lambda_{max}} \Phi(\lambda) EQE(\lambda) d\lambda \tag{9.2}$$

The $\Phi(\lambda)$ is spectral photon flux (see Fig. 9.2).

The theoretical maximum open circuit voltage ($V_{oc,max}$) is determined by the energy level difference between the CB of the inorganic acceptor and the HOMO of the polymer donor, i.e., [38]

$$\begin{aligned} eV_{oc,max} &= \left|E_{HOMO,D}\right| - \left|E_{CB,A}\right| \\ &= E_g + \left|E_{LUMO,D}\right| - \left|E_{CB,A}\right| \end{aligned} \tag{9.3}$$

For a given inorganic material with fixed conduction band, the photovoltaic performance of HSC is mainly determined by the E_g and LUMO of the conjugated polymer and this could be understood from the views of J_{sc} and V_{oc}. On one hand, the polymer bandgap (E_g) should be as narrow as possible to absorb as much light as it can to generate more photocurrent and the LUMO of the polymer should lies at least E_b higher than the CB of the inorganic acceptor for efficient exciton dissociation. On the other hand, the energy difference between the CB of the inorganic crystal and the HOMO of the polymer should be as large as possible for high V_{oc} as described in Eq. 9.3. Due to the two contradictory requirements for high J_{sc} and V_{oc}, the E_g and the LUMO level of the conjugated polymer should be balanced in a real HSC for optimized device performance.

Usually, the HSCs show a similar structure with OSCs, i.e., an active layer consisting of conjugated polymers and inorganic nanocrystals sandwiched by two electrodes with different work functions. According to the different morphologies of the active layer, the architectures of HSCs can be classified as the following three types: (1) bilayer heterojunction, (2) bulk heterojunction, and (3) ordered heterojunction, as shown in Fig. 9.3.

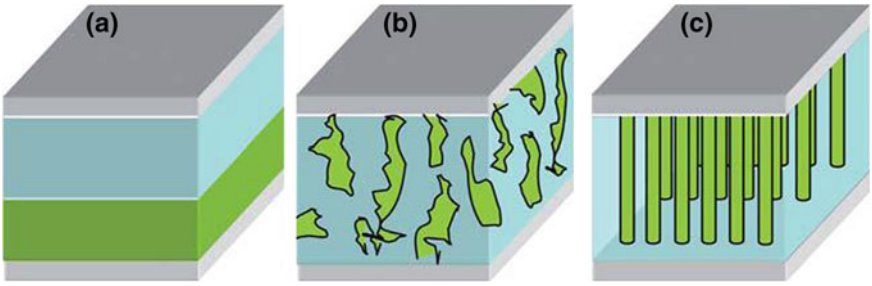

Fig. 9.3 Three types of device configuration of hybrid solar cells: **a** bilayer heterojunction, **b** bulk heterojunction, **c** ordered heterojunction. Reproduced with permission from Ref. [38]

The bilayer heterojunction HSCs can be easily fabricated by consecutive depositing the acceptor and donor layers on the substrate; however, the efficiencies of bilayer heterojunction HSCs are typically much lower than that of BHJ HSCs [40, 41], due to the reduced D/A interface area and the dilemma of efficient light harvesting and exciton diffusion [42].

Similar problems have also been encountered by the organic bilayer heterojunction solar cells and well solved by the design of bulk heterojunction, which is a three dimensional interpenetrating network of the donor and acceptor materials. Learning from that, the concept of BHJ could also be applied into HSCs for improving their performance. The BHJ HSCs can be fabricated through: (1) infiltrating of polymers into inorganic network, (2) simultaneous deposition of the blend of polymer and inorganic nanocrystals, and (3) in situ growth of one material into another.

If the BHJ is formed in ordered inorganic nanostructures, e.g., ordered nanorod, nanowire, and nanotube arrays, it is also called ordered heterojunction. It is believed to be the ideal morphology for HSCs, for the direct charge passway and tunable D/A domain size, both of which are crucial for efficient charge dissociation and transport [37].

9.3 Progress in Hybrid Solar Cells

HSCs have been extensively studied for many years. Although the conjugated polymers could play a crucial role in determining the efficiencies of HSCs, much of the research interests have been paid to the development of the inorganic nanocrystals. Although some new polymers with robust light harvesting properties and photovoltaic performances have been developed for organic solar cells [43–46], few have yet been used into HSCs [47]. By now, most of the HSCs are based on polythiophene and poly(p-phenylene vinylene) and their derivatives are shown in Fig. 9.4. Herein, we will not discuss much about the conjugated polymers but focus on the proceedings in inorganic nanocrystals from the point of view of their

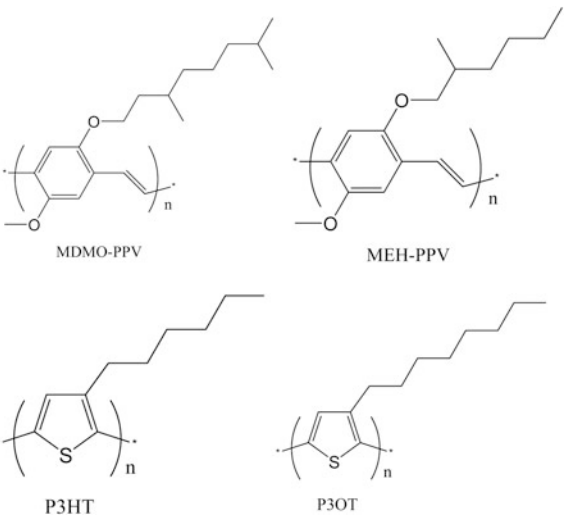

Fig. 9.4 Molecule structures of the four common used conjugated polymers in hybrid solar cells

micromorphologies, i.e., nanoparticles, nanorods and nanorod-, nanowire-, and nanowire arrays. The micromorphologies of inorganic nanocrystals may have profound effect on the performance of HSCs [9, 48].

9.3.1 Nanoparticles

The charge separation and transport in the conjugated polymer/semiconductor nanocrystals composites were first studied by Greenham et al. in 1996 [8]. A HSC with ITO/MEH:PPV-CdSe/Al structure was fabricated, after incorporating 90 wt% of CdSe into the polymer matrix the device gave a 0.6 % PCE and a 12 % quantum efficiency at 514 nm, while the PCE could only approached 0.1 % under 80 mW/cm^2 white light. After the breakthrough in control the shape of CdSe nanocrystals, CdSe quantum dots (QDs), nanorods, and tetrapods have been extensively studied [49–51]. Compared to the earlier CdSe QDs based HSCs, the PCEs have been improved by an order of magnitude, through the modification of CdSe QDs and the use of new polymers [52–54], however, the elongated CdSe nanocrystals were found to have better charge transport properties than nanoparticles, consequently drew more attention [9, 10, 12, 48].

Triggered by the research on CdSe nanocrystals, charge transport properties in TiO_2/polymer heterojunction were also studied and photoinduced charger transfer from conjugated polymers to TiO_2 was confirmed to be possible [55–57]. Mesoporous TiO_2 film with a uniform pore distribution was prepared with the block polymer template (Fig. 9.5) and used for preparing HSCs by infiltrating P3HT into the pores, a monochromatic PCE of 1.5 % was obtained at 33 mW/cm^2 514 nm illumination and an efficiency of 0.45 % was estimated under AM 1.5 condition [16, 17]. Besides, many

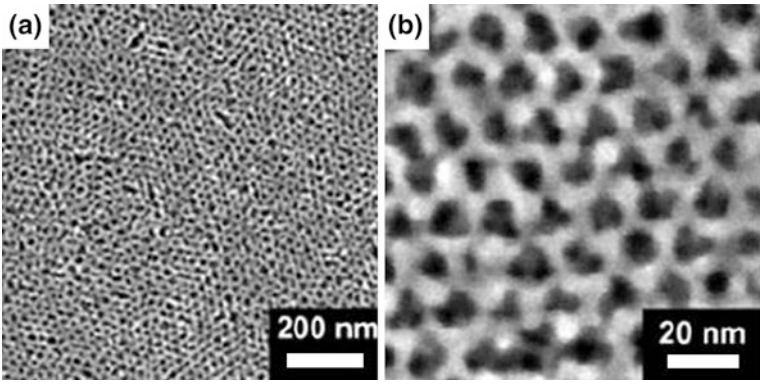

Fig. 9.5 SEM images of the self-assembled porous TiO_2 film, **a** lower magnification, **b** higher magnification. Reproduced with permission from Ref. [16]

other efforts have also been done to prepare HSCs based on porous TiO_2 film [18, 58–60]; however, the PCEs are typically lower than 0.5 % except for the cases when interface modifications are applied [61, 62]. However, it is difficult to optimize the polymer/TiO_2 interface and the complete infiltration of polymers into TiO_2 network is also a challenge [63]. These problems could be overcome by simultaneous deposition of the blend of polymer and TiO_2 particles and a 0.42 % PCE has been achieved under AM 1 irradiation by Kwong et al. [20, 21], but there are also some disadvantages that could limit further improvement of the device performance, namely, for the different nature of the two distinct components which cannot be simply dissolved in the same solvent. Direct blending will cause unavoidable aggregation of TiO_2 particles resulting in poor organic–inorganic interface, and therefore low efficiency [34]. Capping TiO_2 nanocrystals with amphiphilic molecules, e.g., oleic acid or trioctylphosphine oxide could improve their solubility in organic solvents, but the long alkyl chain of these molecules might hinder the charge transfer process, sometimes ligand exchange is needed for better charge transfer, all of this will complicate the fabrication of such devices and it is still difficult to control the morphology and dispersion of TiO_2 particles in polymer matrix [64, 65].

The aforementioned problem could be avoided by using Ti precursor instead of TiO_2 particles; unfortunately, a new problem arose, i.e., the low crystallinity of TiO_2 due to the absence of high temperature sintering, which could also lead to poor device performance [19].

All these drawbacks might be overcome by using ZnO nanocrystals, since soluble ZnO nanoparticles could be synthesized without using any surfactant. Uniform ZnO/conjugated polymer composite films have been easily prepared [34] and ZnO-MDMO:PPV-based devices gave PCEs of about 1.6 % [23, 25, 66] while the ZnO:P3HT gave 0.9 % [26] under AM 1.5, 1 sun condition. Both devices show much higher efficiencies than that of TiO_2: polymer-based devices owing to the improved polymer/nanocrystal interface. Besides, crystallized ZnO nanoparticles could be prepared under low temperature by using a highly reactive ZnO precursor

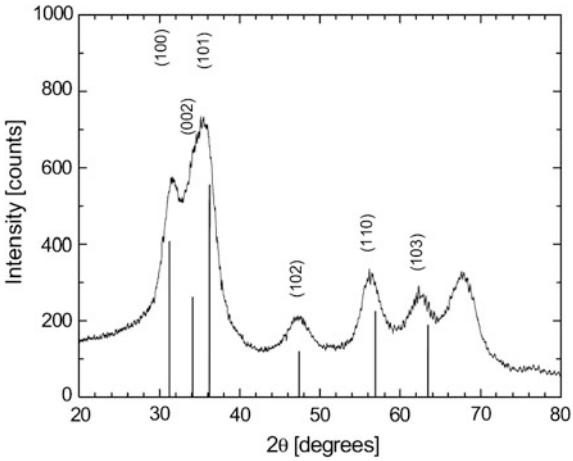

Fig. 9.6 XRD pattern of ZnO prepared from Diethylzinc under 110 °C in air. The appearance of the peaks shows that ZnO is crystallized. Reproduced with permission from Ref. [24]

(see Fig. 9.6); namely, Diethyl Zinc which has been used to fabricate HSCs with MDMO-PPV [24] and P3HT [27] and 1.1 % and 1.4 % conversion efficiencies had been achieved, respectively. Great breakthrough has been made in 2009, Oosterhout et al. [30] were able to study the 3D morphology of the device prepared from Diethyl Zinc and P3HT via electron tomography. The authors provided a detailed insight into the role of 3D morphology in charge generation and transporting. The hybrid device showed a PCE up to 2 % when the nanoscale morphology of the active layer was optimized, Fig. 9.7 shows the structure and *J–V* characteristics of the device.

9.3.2 Nanorods and Nanowires

An important achievement in the development of CdSe-based HSCs was reported by Huynh et al. in 2002 [9]. CdSe nanorods with aspect ratios ranging from 1 to 10 had been studied and the one with highest aspect ratio showed the most excellent charge transport property and gave the best performance with a milestone efficiency of 1.7 % under AM 1.5 global condition. After that, many efforts have been done toward the improvement of CdSe nanorods-based HSCs, Sun et al. [67] have studied the influences of solvents on the morphology and photovoltaic property of CdSe/P3HT blend film and a promising PCE of 2.6 % had been achieved by using a high boiling point solvent, 1,2,4-trichlorobenzene, for the enhanced hole transport of P3HT, similar PCE was also reported by using a post-treatment method called chemical vapor annealing [68]. The efficiency of HSCs was further improved to 3.2 % by using a new low band gap polymer, poly[2,6-(4,4-bis-(2-ethylhexyl)-4H-cyclopenta[2,1-b;3,4-b′] dithiophene)-alt-4,7-(2,1,3-benzothiadiazole)] (PCPDTBT) [47] (see Fig. 9.8). Except for CdSe, another Cadmium Chalcogenide, CdSe nanorods were also used to prepared HSCs with polymers

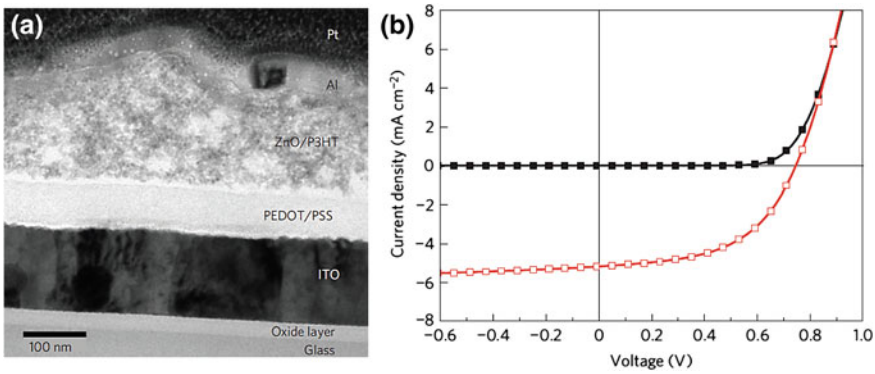

Fig. 9.7 **a** TEM image of the cross-section of a ZnO/P3HT device; **b** *J*–*V* characteristics of the best device obtained in dark (*black*) and under simulated illumination (*red*). Reproduced with permission from Ref. [30]

[14, 69], it is notable that when they were in situ synthesized in the presence of P3HT, a 2.9 % PCE was obtained [69].

Apart from Cadmium Chalcogenide nanorods, TiO_2 nanorods were also widely used for fabricating HSCs. As mentioned before, the synthesis of soluble TiO_2 nanorods requires the treatment of long chain surfactants which would act as insulating layers and reduce the device performance [64]. Chang et al. [70] were able to remove the insulating surfactant through ligand exchange technique and an improvement of the PCE from 0.4 to 1.14 % was achieved with P3HT as donor. Recently, the same group reported a respectable PCE of 2.2 % by modifying the surface of TiO_2 nanorods with interfacial modifiers [65]. In the case of ZnO, little papers focused on the blend of ZnO nanorods and conjugated polymers [71] while the ZnO nanorod arrays were most studied and we will discuss this issue in detail in the following section.

We have mentioned in the above section that the main challenges for porous film formed by nanoparticles are the efficient infiltration of polymers into the inorganic network and the optimization of polymer/nanocrystal interface. Except for using the blend of the two materials, another solution to these problems could be electrospinning, a technique that has been widely used for preparing high aspect-ratio nanowires and highly porous films [72–74]. The pore size, porosity and the film thickness could be easily tailored for polymer infiltration while the high aspect ratios of the nanowires guarantee the large interfacial area for efficient charge separation and the continuous charge transport paths. Admirable conversion efficiencies of the devices based on electrospun TiO_2 [22, 75, 76] or ZnO [31] nanofibrous networks and P3HT have been reported (see Fig. 9.9). This technique seems to be a promising way to prepare large area, low cost and efficient HSCs.

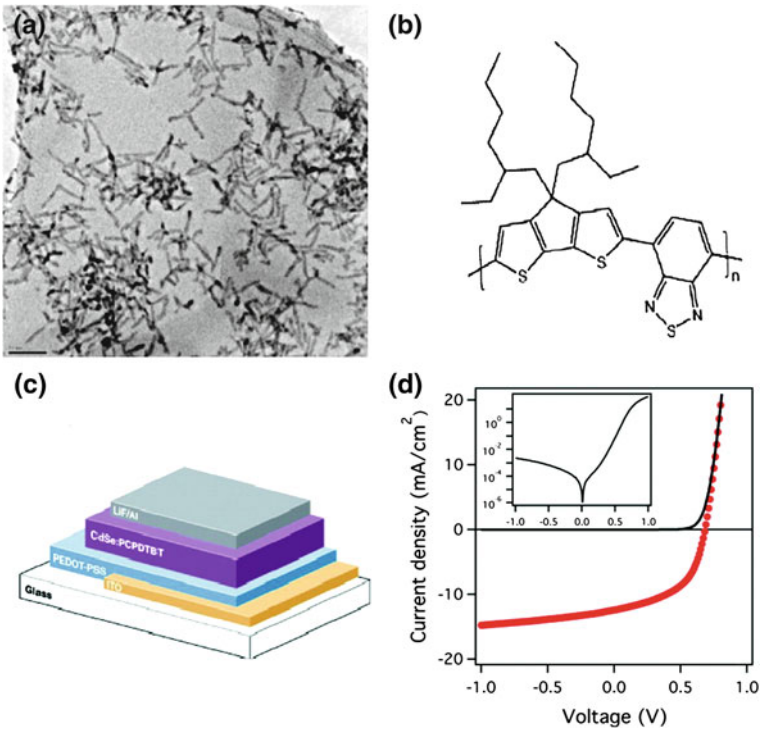

Fig. 9.8 **a** TEM image of CdSe tetrapods. Scale bar, 50 nm. **b** Molecular structure of PCPDTBT. **c** Structure of PCPDTBT-CdSe solar cell. **d** *J–V* characteristics measured under AM 1.5 irradiation. Reproduced with permission from Ref. [47]

9.3.3 Nanorod, Nanowire, and Nanotube Arrays

Compared to the bilayer devices, bulk heterojunction HSCs have much higher conversion efficiencies. However, they are still limited by the inefficient charge transport caused by the discontinuous percolation pathways as shown in Fig. 9.10a, b. Therefore, an ordered heterojunction which has direct charge transport pathways is generally regarded as an ideal structure for HSCs, as shown in Fig. 9.10c [77].

The ordered heterojunction can be formed by infiltrating conjugated polymers into the vertically aligned nanostructures of the inorganic nanocrystals, such as nanorod, nanowire, and nanotube arrays that can be prepared by a variety of physical or chemical methods including nanoimprint [41, 78], low temperature liquid phase deposition [79], template method [80], anodization [81], etching [82], and so on.

Cadmium Chalcogenide nanorod and nanowire arrays have been extensively studied for preparing high performance ordered heterojunction HSCs in the past years. Kang et al. [83] first reported such a device with an admirable PCE of 1 %

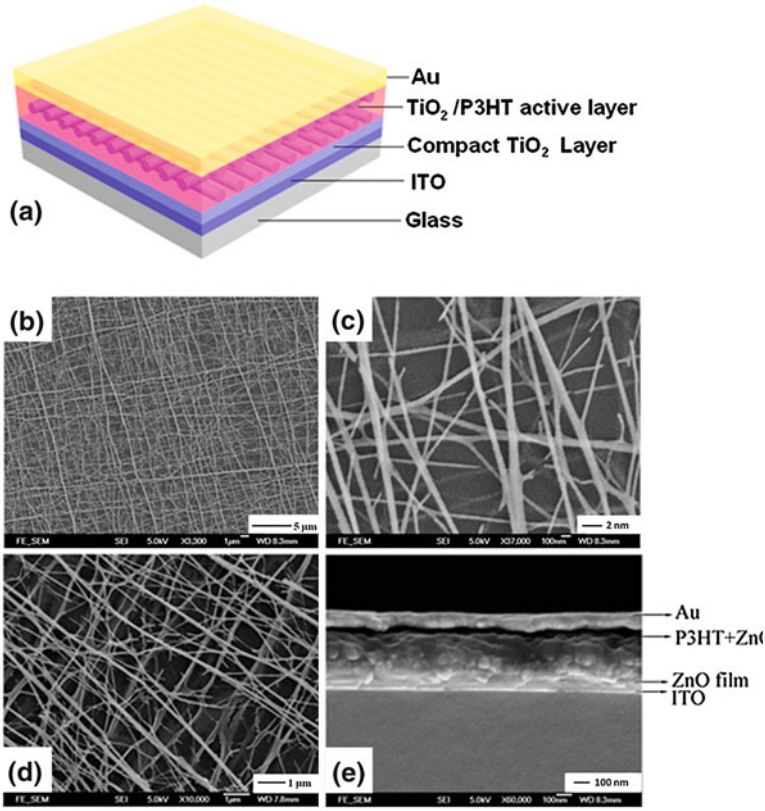

Fig. 9.9 **a** Schematic of the TiO_2 nanofiber/P3HT device. **b** low magnification, **c** high magnification, SEM images of the electrospun TiO_2 network. **d** SEM image of electrospun ZnO network. **e** SEM cross-section view of the ZnO nanofiber/P3HT device. **a**, **b**, **c** reproduced with permission from Ref. [22], **d**, **e** reproduced with permission from Ref. [31]

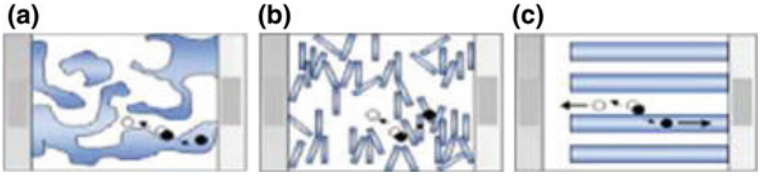

Fig. 9.10 Schematic illustrations of charge transport pathways in **a** polymer blend cell. **b** nanorod-polymer cell. **c** ordered heterojunction cell. Reproduced with permission from Ref. [77]

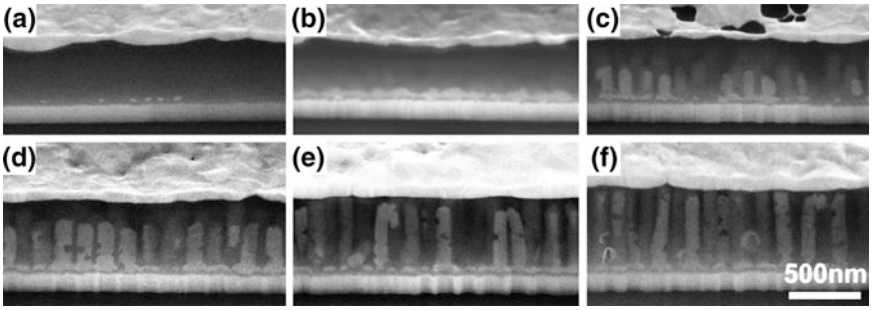

Fig. 9.11 Tilted SEM cross-section images of the CdSe nanorod/P3HT solar cells with different nanorod lengths: **a** nanorod free, **b** 58 ± 12 nm, **c** 280 ± 85 nm, **d** 368 ± 41 nm, **e** 612 ± 46 nm, **f** 721 ± 15 nm. Reproduced with permission from Ref. [85]

based on CdTe nanorod array and poly(3-octylthiophene) (P3OT), then the MEH-PPV/CdS nanorod array device was fabricated with an efficiency of about 0.6 % [13]. Schierhorn et al. [84] successfully synthesized vertically aligned CdSe nanorods on ITO glass and systematically investigated the influence of nanorod length on the device performance (see Fig. 9.11), As shown in Fig. 9.12, the J_{sc} increased linearly with nanorod length and the device based on 612 ± 46 nm long nanorod gave the highest efficiency of 1.38 % [85].

Shankar et al. [86] demonstrated a single heterojunction solid-state solar cell by sensitizing the anodic TiO_2 nanotube array with a P3HT derivative. However, the device exhibited poor performance due to the bad contact between the active layer and electrode. When they infiltrated both P3HT and PCBM into TiO_2 nanotube arrays to form double heterojunction solar cells, a 1 % PCE was achieved. Vertically aligned TiO_2 nanorods were used to fabricate HSC with P3HT by Kuo et al. [87], but only a 0.12 % PCE was obtained. Higher efficiency could be realized by the control of the dimensions of the nanorods and/or sizes of the D/A domains. Tepavcevic et al. [88] found that, when the polymer was in situ polymerized in the TiO_2 nanotube arrays, the device showed a much stronger ($>10^3$) photocurrent density than that of device fabricated with ex-situ synthesized polymer. However, the white light efficiency was not reported by the authors. Mor et al. [89] successfully demonstrated an efficient TiO_2 nanotube arrays/dye/P3HT device structure (see Fig. 9.13), where the dye accounted for the absorption of the red and near-infrared portion of the solar spectrum while P3HT absorbed the higher energy photons and served as a hole transport material. Such a device that combined the advantages of both solid-state DSSC and BHJ solar cell showed an average PCE as high as 3.2 %. Recently, highly oriented TiO_2 nanotubes were synthesized with ZnO nanorod template and a 3.32 % efficiency was reported for the HSC fabricated by infiltrating P3HT/PCBM into the TiO_2 matrix [90].

Vertically aligned ZnO nanorods and nanowires that could be easily prepared were also extensively studied for preparing high performance HSCs. Figure 9.14 presents the typical morphology of ZnO nanorods array. The charge recombination

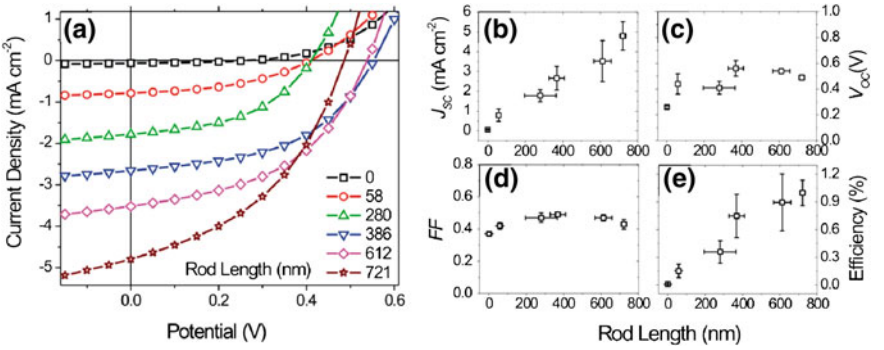

Fig. 9.12 *J–V* Characteristics and the device parameters versus nanorod lengths. Reproduced with permission from Ref. [85]

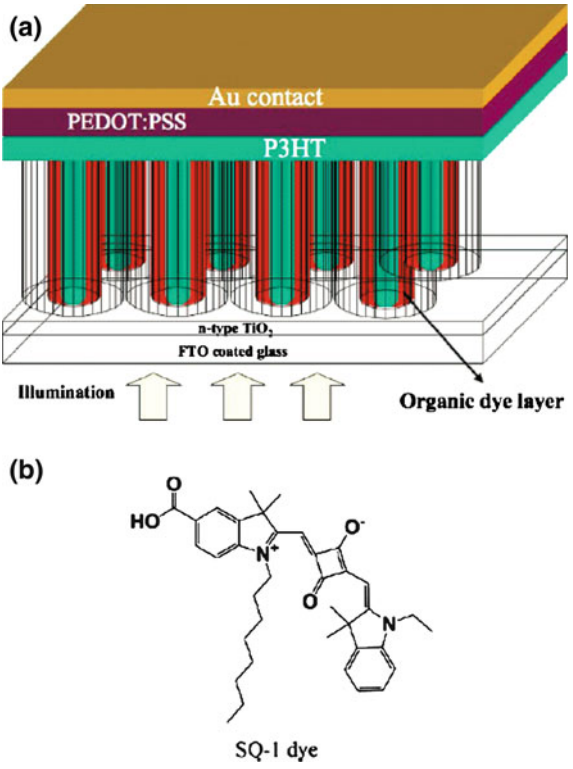

Fig. 9.13 **a** Schematic of the hybrid device, **b** molecular structure of the organic dye. Reproduced with permission from Ref. [89]

rate in ZnO nanorods array-based device was found to be over two orders of magnitude slower than that of device based on ZnO nanoparticles [91]. Although many efforts have been done to optimize the morphologies of the active layers for the ZnO nanorod and nanowire arrays based HSCs [92–97], the PCEs of such devices were still very low, typically lower than 1 %. Similar to TiO_2 nanotube

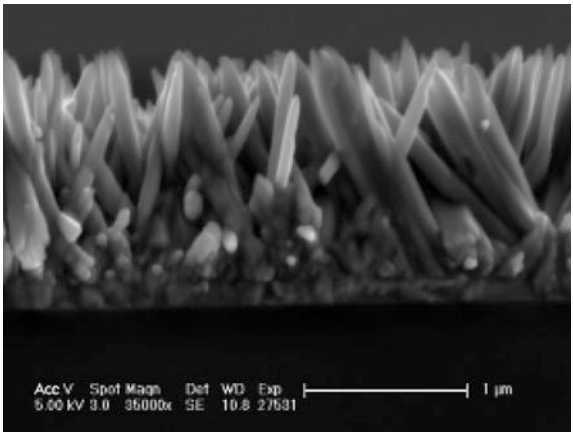

Fig. 9.14 SEM images of the vertically aligned ZnO nanorods. Reproduced with permission from Ref. [91]

arrays [88], higher efficiencies could be achieved by infiltrating the blend of P3HT and PCBM into the ZnO nanorods array [98, 99], but the reported efficiencies were still lower than that of state-of-the-art BHJ organic solar cells.

Besides the above mentioned materials, Si [100, 101], InP [102] and CuO [103] nanowire arrays were also used for fabricating hybrid solar cells with conjugated polymers with the efficiencies normally lower than 2 %.

9.4 Interface Modification for Enhanced Photovoltaic Performance

There are two important interfaces in HSCs, i.e., the polymer/inorganic nanocrystal interface where the charge separation takes place and the active layer/electrode interface where the free charges are collected. Therefore, their properties are crucial to the device performance. Efficient interface modification could not only facilitate the charge transport but also retard the backward recombination and remarkably improve the conversion efficiencies of the solar cells [61, 62, 65, 104–119].

One of the most important work on interface modification was reported by Goh et al. in 2007 [105], who systematically studied the effect of interface modification in TiO_2/P3HT-based HSCs using different types of modifiers as shown in Fig. 9.15, and the corresponding device physics was also provided by the authors. They concluded that there were two kinds of dipoles existed at the TiO_2/P3HT interface when the interface modifiers were introduced; namely, the molecular dipole and the interfacial dipole that generated by the interaction between the carboxylic group and TiO_2. They both could lead to the TiO_2 band edge shift, and thus affect the V_{oc} of the device. A nearly 2-fold improvement of the PCE was achieved by using Ruthenium dye which could mediate the interface charge transfer and slow down the recombination kinetics.

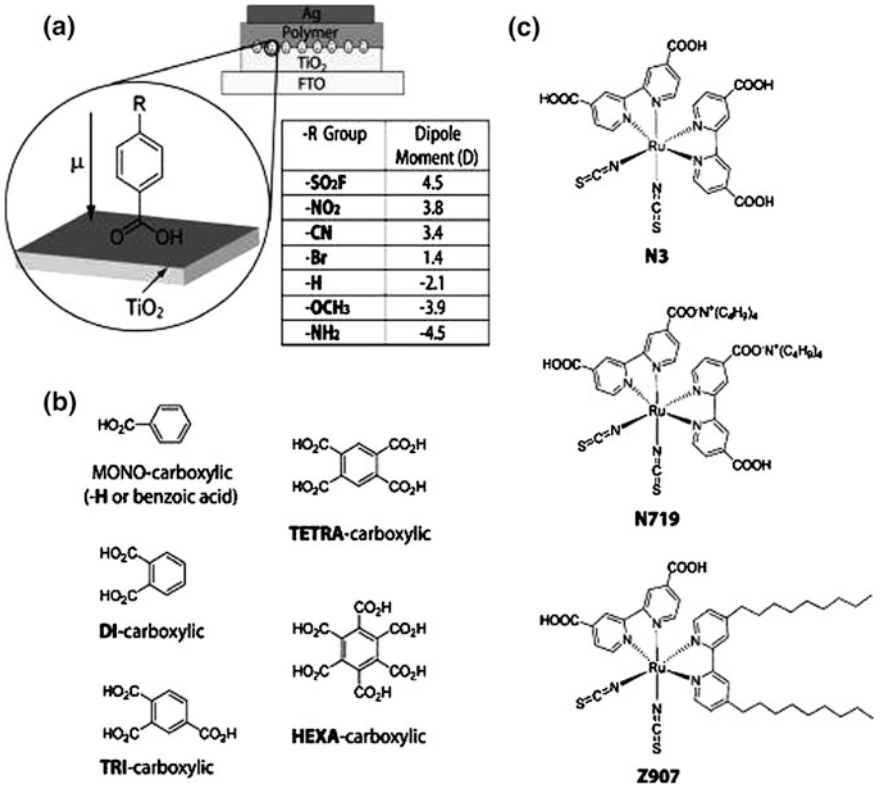

Fig. 9.15 **a** Schematic of the interface modification of the bilayer TiO2/polymer solar cell. The table lists the calculated dipole of the benzoic acid with different R group. **b** molecular structures of benzene carboxylic molecules. **c** molecular structure of Ruthenium dyes. Reproduced with permission from Ref. [105]

Interface modification was also reported to affect the crystallinity of the interfacial P3HT layer in a bilayer ZnO/P3HT device. The crystallinity of P3HT was decreased when it was casted on ZnO surface as identified by the blue shift (50 nm) of its absorption peaks. Upon modification by alkanethiol, the crystallinity of P3HT was recovered and enhanced J_{sc} was observed since the more ordered P3HT has broader absorption spectrum and higher hole mobility [108]. Similar effects were also reported for the Ruthenium dye [22].

Ruthenium dyes are most commonly used interface modifiers. However, the surface of inorganic acceptors cannot be fully covered by single dye molecules due to their large molecular size. Tai et al. [22] were able to solve this problem by using a small molecule 3-phenylpropionic acid (PPA) as a co-modifier which could cover the voids that were inaccessible for Ruthenium dye (see Fig. 9.16) and improved performance was achieved for the co-modified device due to the better passivation of the backward recombination kinetics.

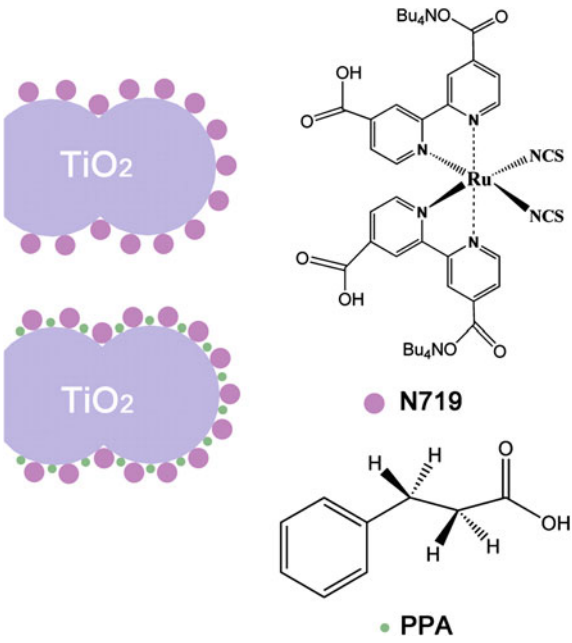

Fig. 9.16 Schematic illustration of the N719-modification and the N719-PPA co-modification of TiO2 surface. Reproduced with permission from Ref. [22]

It is now a standard procedure to introduce the electron blocking layer (dense TiO_2, ZnO, etc.) and/or hole blocking layer (typically PEDOT) in HSCs for more efficient charge collection, which both fall into the category of the interface modification (the active layer/electrode interface). Besides, Takanezawa et al. [99] used VOx as a buffer layer between active layer and Ag electrode to prevent the recombination at the organic/Ag interface and the photovoltaic performance of the device was greatly enhanced accordingly. Qian et al. [118] demonstrated the use of solution-processed ZnO nanoparticle buffer layer in HSCs based on the blend of CdSe quantum dots and P3HT. Upon ZnO modification, the PCEs of the devices were increased by 30–80 %. More interestingly, the stability of the device was also dramatically improved.

9.5 Conclusion

Polymer/inorganic HSC has grown to be an important member of the new generation of photovoltaics. An increasing attention has been paid to HSCs in the past years for their potential high efficiencies and low fabrication costs. Many efforts have been made toward the improvement of device performance, including the optimization of the device architecture and the active layer morphologies, interface engineering and design of new materials, etc. Although the current PCEs of HSCs are still lower than conventional silicon solar cells, DSSCs, and BHJ OSCs, if looking back upon the

history of the development of the HSCs, we could find that the PCEs of HSCs have increased all the way. Despite the slow increasing rate of PCE, the trend is obvious and much higher efficiencies are expected upon the further understanding of the device physics and the development of nanofabrication techniques.

References

1. Hagfeldt A, Boschloo G, Sun LC, Kloo L, Pettersson H (2010) Dye-sensitized solar cells. Chem Rev 110(11):6595–6663. doi:10.1021/Cr900356p
2. Thompson BC, Frechet JMJ (2008) Organic photovoltaics—polymer-fullerene composite solar cells. Angew Chem Int Edit 47(1):58–77. doi:10.1002/anie.200702506
3. Dennler G, Scharber MC, Brabec CJ (2009) Polymer-fullerene bulk-heterojunction solar cells. Adv Mater 21(13):1323–1338. doi:10.1002/adma.200801283
4. Brabec CJ, Gowrisanker S, Halls JJM, Laird D, Jia SJ, Williams SP (2010) Polymer-fullerene bulk-heterojunction solar cells. Adv Mater 22(34):3839–3856. doi:10.1002/adma.200903697
5. Ito S, Chen P, Comte P, Nazeeruddin MK, Liska P, Pechy P, Gratzel M (2007) Fabrication of screen-printing pastes from TiO2 powders for dye-sensitised solar cells. Prog Photovoltaics 15(7):603–612. doi:10.1002/Pip.768
6. Krebs FC, Gevorgyan SA, Alstrup J (2009) A roll-to-roll process to flexible polymer solar cells: model studies, manufacture and operational stability studies. J Mater Chem 19(30):5442–5451. doi:10.1039/B823001c
7. Krebs FC, Tromholt T, Jorgensen M (2010) Upscaling of polymer solar cell fabrication using full roll-to-roll processing. Nanoscale 2(6):873–886. doi:10.1039/B9nr00430k
8. Greenham NC, Peng X, Alivisatos AP (1996) Charge separation and transport in conjugated-polymer/semiconductor-nanocrystal composites studied by photoluminescence quenching and photoconductivity. Phys Rev B 54(24):17628
9. Huynh WU, Dittmer JJ, Alivisatos AP (2002) Hybrid nanorod-polymer solar cells. Science 295(5564):2425–2427
10. Sun BQ, Marx E, Greenham NC (2003) Photovoltaic devices using blends of branched CdSe nanoparticles and conjugated polymers. Nano Lett 3(7):961–963. doi:10.1021/Nl0342895
11. Liu JS, Tanaka T, Sivula K, Alivisatos AP, Frechet JMJ (2004) Employing end-functional polythiophene to control the morphology of nanocrystal-polymer composites in hybrid solar cells. J Am Chem Soc 126(21):6550–6551. doi:10.1021/Ja0489184
12. Gur I, Fromer NA, Chen CP, Kanaras AG, Alivisatos AP (2007) Hybrid solar cells with prescribed nanoscale morphologies based on hyperbranched semiconductor nanocrystals. Nano Lett 7(2):409–414. doi:10.1021/Nl062660t
13. Kang Y, Kim D (2006) Well-aligned CdS nanorod conjugated polymer solar cells. Sol Energy Mater Sol C 90(2):166–174. doi:10.1016/j.solmat.2005.03.001
14. Wang L, Liu YS, Jiang X, Qin DH, Cao Y (2007) Enhancement of photovoltaic characteristics using a suitable solvent in hybrid polymer/multiarmed CdS nanorods solar cells. J Phys Chem C 111(26):9538–9542. doi:10.1021/Jp0715777
15. Leventis HC, King SP, Sudlow A, Hill MS, Molloy KC, Haque SA (2010) Nanostructured hybrid polymer-inorganic solar cell active layers formed by controllable in situ growth of semiconducting sulfide networks. Nano Lett 10(4):1253–1258. doi:10.1021/Nl903787j
16. Coakley KM, Liu YX, McGehee MD, Frindell KL, Stucky GD (2003) Infiltrating semiconducting polymers into self-assembled mesoporous titania films for photovoltaic applications. Adv Funct Mater 13(4):301–306. doi:10.1002/adfm.200304361

17. Coakley KM, McGehee MD (2003) Photovoltaic cells made from conjugated polymers infiltrated into mesoporous titania. Appl Phys Lett 83(16):3380–3382. doi:10.1063/1.1616197
18. Huisman CL, Goossens A, Schoonman J (2003) Aerosol synthesis of anatase titanium dioxide nanoparticles for hybrid solar cells. Chem Mater 15(24):4617–4624
19. Slooff LH, Wienk MM, Kroon JM (2004) Hybrid TiO2: polymer photovoltaic cells made from a titanium oxide precursor. Thin Solid Films 451–52:634–638. doi:10.1016/j.tsf.2003.11.032
20. Kwong CY, Choy WCH, Djurisic AB, Chui PC, Cheng KW, Chan WK (2004) Poly(3-hexylthiophene): TiO2 nanocomposites for solar cell applications. Nanotechnology 15(9):1156–1161. doi:10.1088/0957-4484/15/9/008 Pii S0957-4484(04)74605-X
21. Kwong CY, Djurisic AB, Chui PC, Cheng KW, Chan WK (2004) Influence of solvent on film morphology and device performance of poly(3-hexylthiophene): TiO2 nanocomposite solar cells. Chem Phys Lett 384(4–6):372–375. doi:10.1016/j.cplett.2003.12.045
22. Tai QD, Zhao XZ, Yan F (2010) Hybrid solar cells based on poly(3-hexylthiophene) and electrospun TiO2 nanofibers with effective interface modification. J Mater Chem 20(35):7366–7371. doi:10.1039/C0jm01455a
23. Beek WJE, Wienk MM, Janssen RAJ (2004) Efficient hybrid solar cells from zinc oxide nanoparticles and a conjugated polymer. Adv Mater 16(12):1009–1013. doi: 10.1002/adma.200306659
24. Beek WJE, Slooff LH, Wienk MM, Kroon JM, Janssen RAJ (2005) Hybrid solar cells using a zinc oxide precursor and a conjugated polymer. Adv Funct Mater 15(10):1703–1707. doi:10.1002/adfm.200500201
25. Beek WJE, Wienk MM, Kemerink M, Yang XN, Janssen RAJ (2005) Hybrid zinc oxide conjugated polymer bulk heterojunction solar cells. J Phys Chem B 109(19):9505–9516. doi:10.1021/Jp050745x
26. Beek WJE, Wienk MM, Janssen RAJ (2006) Hybrid solar cells from regioregular polythiophene and ZnO nanoparticles. Adv Funct Mater 16(8):1112–1116. doi:10.1002/adfm.200500573
27. Moet DJD, Koster LJA, de Boer B, Blom PWM (2007) Hybrid polymer solar cells from highly reactive diethylzinc: MDMO-PPV versus P3HT. Chem Mater 19(24):5856–5861. doi:10.1021/Cmo70555u
28. Krebs FC, Thomann Y, Thomann R, Andreasen JW (2008) A simple nanostructured polymer/ZnO hybrid solar cell—preparation and operation in air. Nanotechnology 19(42):424013. doi: 10.1088/0957-4484/19/42/424013
29. Lloyd MT, Prasankumar RP, Sinclair MB, Mayer AC, Olson DC, Hsu JWP (2009) Impact of interfacial polymer morphology on photoexcitation dynamics and device performance in P3HT/ZnO heterojunctions. J Mater Chem 19(26):4609–4614. doi:10.1039/B903849c
30. Oosterhout SD, Wienk MM, van Bavel SS, Thiedmann R, Koster LJA, Gilot J, Loos J, Schmidt V, Janssen RAJ (2009) The effect of three-dimensional morphology on the efficiency of hybrid polymer solar cells. Nat Mater 8(10):818–824. doi:10.1038/Nmat2533
31. Wu SJ, Tai QD, Yan F (2010) Hybrid photovoltaic devices based on poly (3-hexylthiophene) and ordered electrospun ZnO nanofibers. J Phys Chem C 114(13):6197–6200. doi:10.1021/Jp910921a
32. Ayllon JA, Lira-Cantu M (2009) Application of MEH-PPV/SnO2 bilayer as hybrid solar cell. Appl Phys A Mater 95(1):249–255. doi:10.1007/s00339-008-5023-z
33. Arici E, Sariciftci NS, Meissner D (2003) Hybrid solar cells based on nanoparticles of CuInS2 in organic matrices. Adv Funct Mater 13(2):165–171
34. Beek WJE, Wienk MM, Janssen RAJ (2005) Hybrid polymer solar cells based on zinc oxide. J Mater Chem 15(29):2985–2988. doi:10.1039/B501979f
35. Sanchez C, Julian B, Belleville P, Popall M (2005) Applications of hybrid organic-inorganic nanocomposites. J Mater Chem 15(35–36):3559–3592. doi:10.1039/B509097k

36. Zhou YF, Eck M, Kruger M (2010) Bulk-heterojunction hybrid solar cells based on colloidal nanocrystals and conjugated polymers. Energy Environ Sci 3(12):1851–1864. doi:10.1039/C0ee00143k
37. Weickert J, Dunbar RB, Hesse HC, Wiedemann W, Schmidt-Mende L (2011) Nanostructured organic and hybrid solar cells. Adv Mater 23(16):1810–1828. doi:10.1002/adma.201003991
38. Xu T, Qiao Q (2011) Conjugated polymer-inorganic semiconductor hybrid solar cells. Energy Environ Sci 4(8):2700–2720. doi:10.1039/C0EE00632G
39. Halme J, Vahermaa P, Miettunen K, Lund P (2010) Device physics of dye solar cells. Adv Mater 22(35):E210–E234. doi:10.1002/adma.201000726
40. Boucle J, Ravirajan P, Nelson J (2007) Hybrid polymer-metal oxide thin films for photovoltaic applications. J Mater Chem 17(30):3141–3153. doi:10.1039/B706547g
41. McGehee MD (2009) Nanostructured organic-inorganic hybrid solar cells. MRS Bull 34(2):95–100
42. Notes: The diffusion length of excitons (L_d)in conjugated polymers is typcially around 10 nm, therefore the efficient exciton diffusion requires the film thickness, $L < L_d$. In the case of the light absortpion, the typcial absorption length of conjugated films (L_a) is around 50–100 nm, thus the film thickness, $L > L_a$ is required for efficient light harvesting which is inconsistent with the efficient exicton diffusion
43. Peet J, Kim JY, Coates NE, Ma WL, Moses D, Heeger AJ, Bazan GC (2007) Efficiency enhancement in low-bandgap polymer solar cells by processing with alkane dithiols. Nat Mater 6(7):497–500. doi:10.1038/Nmat1928
44. Park SH, Roy A, Beaupre S, Cho S, Coates N, Moon JS, Moses D, Leclerc M, Lee K, Heeger AJ (2009) Bulk heterojunction solar cells with internal quantum efficiency approaching 100 %. Nat Photonics 3(5):U297–U295. doi:10.1038/Nphoton.2009.69
45. Chen HY, Hou JH, Zhang SQ, Liang YY, Yang GW, Yang Y, Yu LP, Wu Y, Li G (2009) Polymer solar cells with enhanced open-circuit voltage and efficiency. Nat Photonics 3(11):649–653. doi:10.1038/Nphoton.2009.192
46. Liang YY, Xu Z, Xia JB, Tsai ST, Wu Y, Li G, Ray C, Yu LP (2010) For the bright future-bulk heterojunction polymer solar cells with power conversion efficiency of 7.4 %. Adv Mater 22(20):E135–E138. doi: 10.1002/adma.200903528
47. Dayal S, Kopidakis N, Olson DC, Ginley DS, Rumbles G (2010) Photovoltaic devices with a low band gap polymer and CdSe nanostructures exceeding 3 % efficiency. Nano Lett 10(1):239–242. doi:10.1021/Nl903406s
48. Dayal S, Reese MO, Ferguson AJ, Ginley DS, Rumbles G, Kopidakis N (2010) The effect of nanoparticle shape on the photocarrier dynamics and photovoltaic device performance of poly(3-hexylthiophene): CdSe nanoparticle bulk heterojunction solar cells. Adv Funct Mater 20(16):2629–2635. doi:10.1002/adfm.201000628
49. Peng XG, Manna L, Yang WD, Wickham J, Scher E, Kadavanich A, Alivisatos AP (2000) Shape control of CdSe nanocrystals. Nature 404(6773):59–61
50. Peng ZA, Peng XG (2001) Formation of high-quality CdTe, CdSe, and CdS nanocrystals using CdO as precursor. J Am Chem Soc 123(1):183–184
51. Peng ZA, Peng XG (2001) Mechanisms of the shape evolution of CdSe nanocrystals. J Am Chem Soc 123(7):1389–1395. doi:10.1021/Ja0027766
52. Han LL, Qin DH, Jiang X, Liu YS, Wang L, Chen JW, Cao Y (2006) Synthesis of high quality zinc-blende CdSe nanocrystals and their application in hybrid solar cells. Nanotechnology 17(18):4736–4742. doi:10.1088/0957-4484/17/18/035
53. Lokteva I, Radychev N, Witt F, Borchert H, Parisi J, Kolny-Olesiak J (2010) Surface treatment of CdSe nanoparticles for application in hybrid solar cells: the effect of multiple ligand exchange with pyridine. J Phys Chem C 114(29):12784–12791. doi:10.1021/Jp103300v

54. Zhou YF, Riehle FS, Yuan Y, Schleiermacher HF, Niggemann M, Urban GA, Kruger M (2010) Improved efficiency of hybrid solar cells based on non-ligand-exchanged CdSe quantum dots and poly(3-hexylthiophene). Appl Phys Lett 96(1):13304. doi: 10.1063/1.3280370
55. van Hal PA, Christiaans MPT, Wienk MM, Kroon JM, Janssen RAJ (1999) Photoinduced electron transfer from conjugated polymers to TiO2. J Phys Chem B 103(21):4352–4359
56. van Hal PA, Wienk MM, Kroon JM, Verhees WJH, Slooff LH, van Gennip WJH, Jonkheijm P, Janssen RAJ (2003) Photoinduced electron transfer and photovoltaic response of a MDMO-PPV : TiO2 bulk-heterojunction. Adv Mater 15(2):118–121
57. Lin YT, Zeng TW, Lai WZ, Chen CW, Lin YY, Chang YS, Su WF (2006) Efficient photoinduced charge transfer in TiO2 nanorod/conjugated polymer hybrid materials. Nanotechnology 17(23):5781–5785. doi:10.1088/0957-4484/17/23/012
58. Lancelle-Beltran E, Prene P, Boscher C, Belleville P, Buvat P, Lambert S, Guillet F, Boissiere C, Grosso D, Sanchez C (2006) Nanostructured hybrid solar cells based on self-assembled mesoporous titania thin films. Chem Mater 18(26):6152–6156. doi:10.1021/Cm060925z
59. Her HJ, Kim JM, Kang CJ, Kim YS (2008) Hybrid photovoltaic cell with well-ordered nanoporous titania-P3HT by nanoimprinting lithography. J Phys Chem Solids 69(5–6):1301–1304. doi:10.1016/j.jpcs.2007.10.121
60. Atienzar P, Ishwara T, Horie M, Durrant JR, Nelson J (2009) Hybrid polymer-metal oxide solar cells by in situ chemical polymerization. J Mater Chem 19(30):5377–5380. doi:10.1039/B902271f
61. Jiang KJ, Manseki K, Yu YH, Masaki N, Suzuki K, Song YL, Yanagida S (2009) Photovoltaics based on hybridization of effective dye-sensitized titanium oxide and hole-conductive polymer P3HT. Adv Funct Mater 19(15):2481–2485. doi:10.1002/adfm.200900283
62. Zhu R, Jiang CY, Liu B, Ramakrishna S (2009) Highly Efficient Nanoporous TiO2-Polythiophene Hybrid Solar Cells Based on Interfacial Modification Using a Metal-Free Organic Dye. Adv Mater 21(9):994–1000. doi: 10.1002/adma.200802388
63. Bartholomew GP, Heeger AJ (2005) Infiltration of regioregular poly[2,2'-(3-hexylthiopene)] into random nanocrystalline TiO2 networks. Adv Funct Mater 15(4):677–682. doi:10.1002/adfm.200400277
64. Boucle J, Chyla S, Shaffer MSP, Durrant JR, Bradley DDC, Nelson J (2008) Hybrid solar cells from a blend of poly(3-hexylthiophene) and ligand-capped TiO2 nanorods. Adv Funct Mater 18(4):622–633. doi:10.1002/adfm.200700280
65. Lin YY, Chu TH, Li SS, Chuang CH, Chang CH, Su WF, Chang CP, Chu MW, Chen CW (2009) Interfacial nanostructuring on the performance of polymer/TiO2 nanorod bulk heterojunction solar cells. J Am Chem Soc 131(10):3644–3649. doi:10.1021/Ja8079143
66. Koster LJA, van Strien WJ, Beek WJE, Blom PWM (2007) Device operation of conjugated polymer/zinc oxide bulk heterojunction solar cells. Adv Funct Mater 17(8):1297–1302. doi:10.1002/adfm.200600371
67. Sun BQ, Greenham NC (2006) Improved effciency of photovoltaics based on CdSe nanorods and poly(3-hexylthiophene) nanofibers. Phys Chem Chem Phys 8(30):3557–3560. doi:10.1039/B604734n
68. Wu Y, Zhang GQ (2010) Performance enhancement of hybrid solar cells through chemical vapor annealing. Nano Lett 10(5):1628–1631. doi:10.1021/Nl904095n
69. Liao HC, Chen SY, Liu DM (2009) In situ growing CdS single-crystal nanorods via P3HT polymer as a soft template, for enhancing photovoltaic performance. Macromolecules 42(17):6558–6563. doi:10.1021/Ma900924y
70. Chang CH, Huang TK, Lin YT, Lin YY, Chen CW, Chu TH, Su WF (2008) Improved charge separation and transport efficiency in poly(3-hexylthiophene)-TiO2 nanorod bulk heterojunction solar cells. J Mater Chem 18(19):2201–2207. doi:10.1039/B800071a
71. Said AJ, Poize G, Martini C, Ferry D, Marine W, Giorgio S, Fages F, Hocq J, Boucle J, Nelson J, Durrant JR, Ackermann J (2010) Hybrid bulk heterojunction solar cells based on

P3HT and porphyrin-modified ZnO nanorods. J Phys Chem C 114(25):11273–11278. doi:10.1021/Jp911125w
72. Li D, Xia YN (2004) Electrospinning of nanofibers: reinventing the wheel? Adv Mater 16(14):1151–1170. doi:10.1002/adma.200400719
73. Greiner A, Wendorff JH (2007) Electrospinning: a fascinating method for the preparation of ultrathin fibres. Angew Chem Int Edit 46(30):5670–5703. doi:10.1002/anie.200604646
74. Onozuka K, Ding B, Tsuge Y, Naka T, Yamazaki M, Sugi S, Ohno S, Yoshikawa M, Shiratori S (2006) Electrospinning processed nanofibrous TiO2 membranes for photovoltaic applications. Nanotechnology 17(4):1026–1031. doi:10.1088/0957-4484/17/4/030
75. Shim HS, Na SI, Nam SH, Ahn HJ, Kim HJ, Kim DY, Kim WB (2008) Efficient photovoltaic device fashioned of highly aligned multilayers of electrospun TiO2 nanowire array with conjugated polymer. Appl Phys Lett 92(18):183107. doi: 10.1063/1.2919800
76. Zhu R, Jiang CY, Liu XZ, Liu B, Kumar A, Ramakrishna S (2008) Improved adhesion of interconnected TiO2 nanofiber network on conductive substrate and its application in polymer photovoltaic devices. Appl Phys Lett 93(1):013102. doi: 10.1063/1.2907317
77. Hochbaum AI, Yang PD (2010) Semiconductor nanowires for energy conversion. Chem Rev 110(1):527–546. doi:10.1021/cr900075v
78. Williams SS, Hampton MJ, Gowrishankar V, Ding IK, Templeton JL, Samulski ET, DeSimone JM, McGehee MD (2008) Nanostructured titania-polymer photovoltaic devices made using PFPE-based nanomolding techniques. Chem Mater 20(16):5229–5234. doi:10.1021/Cm800729q
79. Greene LE, Law M, Tan DH, Montano M, Goldberger J, Somorjai G, Yang PD (2005) General route to vertical ZnO nanowire arrays using textured ZnO seeds. Nano Lett 5(7):1231–1236. doi:10.1021/Nl050788p
80. Cao G, Liu D (2008) Template-based synthesis of nanorod, nanowire, and nanotube arrays. Adv Colloid Interface 136(1–2):45–64
81. Mor GK, Shankar K, Paulose M, Varghese OK, Grimes CA (2006) Use of highly-ordered TiO2 nanotube arrays in dye-sensitized solar cells. Nano Lett 6(2):215–218. doi:10.1021/Nl052099j
82. Peng KQ, Hu JJ, Yan YJ, Wu Y, Fang H, Xu Y, Lee ST, Zhu J (2006) Fabrication of single-crystalline silicon nanowires by scratching a silicon surface with catalytic metal particles. Adv Funct Mater 16(3):387–394. doi:10.1002/adfm.200500392
83. Kang YM, Park NG, Kim D (2005) Hybrid solar cells with vertically aligned CdTe nanorods and a conjugated polymer. Appl Phys Lett 86(11):113101. doi: 10.1063/1.1883319
84. Schierhorn M, Boettcher SW, Kraemer S, Stucky GD, Moskovits M (2009) Photoelectrochemical performance of CdSe nanorod arrays grown on a transparent conducting substrate. Nano Lett 9(9):3262–3267. doi:10.1021/Nl901522b
85. Schierhorn M, Boettcher SW, Peet JH, Matioli E, Bazan GC, Stucky GD, Moskovits M (2010) CdSe nanorods dominate photocurrent of hybrid CdSe-P3HT photovoltaic cell. ACS Nano 4(10):6132–6136. doi:10.1021/Nn101742c
86. Shankar K, Mor GK, Prakasam HE, Varghese OK, Grimes CA (2007) Self-assembled hybrid polymer-TiO2 nanotube array heterojunction solar cells. Langmuir 23(24):12445–12449. doi:10.1021/La7020403
87. Kuo CY, Tang WC, Gau C, Guo TF, Jeng DZ (2008) Ordered bulk heterojunction solar cells with vertically aligned TiO2 nanorods embedded in a conjugated polymer. Appl Phys Lett 93(3):033307. doi: 10.1063/1.2937472
88. Tepavcevic S, Darling SB, Dimitrijevic NM, Rajh T, Sibener SJ (2009) Improved hybrid solar cells via in situ UV polymerization. Small 5(15):1776–1783. doi:10.1002/smll.200900093
89. Mor GK, Kim S, Paulose M, Varghese OK, Shankar K, Basham J, Grimes CA (2009) Visible to near-infrared light harvesting in TiO2 nanotube array-P3HT based heterojunction solar cells. Nano Lett 9(12):4250–4257. doi:10.1021/Nl9024853

90. Yodyingyong S, Zhou XY, Zhang QF, Triampo D, Xi JT, Park K, Limketkai B, Cao GZ (2010) Enhanced photovoltaic performance of nanostructured hybrid solar cell using highly oriented TiO2 nanotubes. J Phys Chem C 114(49):21851–21855. doi:10.1021/Jp1077888
91. Ravirajan P, Peiro AM, Nazeeruddin MK, Graetzel M, Bradley DDC, Durrant JR, Nelson J (2006) Hybrid polymer/zinc oxide photovoltaic devices with vertically oriented ZnO nanorods and an amphiphilic molecular interface layer. J Phys Chem B 110(15):7635–7639. doi:10.1021/Jp0571372
92. Peiro AM, Ravirajan P, Govender K, Boyle DS, O'Brien P, Bradley DDC, Nelson J, Durrant JR (2006) Hybrid polymer/metal oxide solar cells based on ZnO columnar structures. J Mater Chem 16(21):2088–2096. doi:10.1039/B602084d
93. Olson DC, Lee YJ, White MS, Kopidakis N, Shaheen SE, Ginley DS, Voigt JA, Hsu JWP (2007) Effect of polymer processing on the performance of poly(3-hexylthiophene)/ZnO nanorod photovoltaic devices. J Phys Chem C 111(44):16640–16645. doi:10.1021/Jp0757816
94. Lee YJ, Lloyd MT, Olson DC, Grubbs RK, Lu P, Davis RJ, Voigt JA, Hsu JWP (2009) Optimization of ZnO nanorod array morphology for hybrid photovoltaic devices. J Phys Chem C 113(35):15778–15782. doi:10.1021/Jp904387z
95. Olson DC, Piris J, Collins RT, Shaheen SE, Ginley DS (2006) Hybrid photovoltaic devices of polymer and ZnO nanofiber composites. Thin Solid Films 496(1):26–29. doi:10.1016/j.tsf.2005.08.179
96. Greene LE, Law M, Yuhas BD, Yang PD (2007) ZnO-TiO2 core-shell nanorod/P3HT solar cells. J Phys Chem C 111(50):18451–18456. doi:10.1021/Jp0775931
97. Hao YZ, Pei J, Wei Y, Cao YH, Jiao SH, Zhu F, Li JJ, Xu DH (2010) Efficient semiconductor-sensitized solar cells based on poly(3-hexylthiophene)@CdSe@ZnO core-shell nanorod arrays. J Phys Chem C 114(18):8622–8625. doi:10.1021/Jp911263d
98. Takanezawa K, Hirota K, Wei QS, Tajima K, Hashimoto K (2007) Efficient charge collection with ZnO nanorod array in hybrid photovoltaic devices. J Phys Chem C 111(19):7218–7223. doi:10.1021/Jp071418n
99. Takanezawa K, Tajima K, Hashimoto K (2008) Efficiency enhancement of polymer photovoltaic devices hybridized with ZnO nanorod arrays by the introduction of a vanadium oxide buffer layer. Appl Phys Lett 93(6):063308. doi: 10.1063/1.2972113
100. Kuo CY, Gau C (2009) Arrangement of band structure for organic-inorganic photovoltaics embedded with silicon nanowire arrays grown on indium tin oxide glass. Appl Phys Lett 95(5):053302–053304. doi: 10.1063/1.3189088
101. Peng KQ, Lee ST (2011) Silicon nanowires for photovoltaic solar energy conversion. Adv Mater 23(2):198–215. doi:10.1002/adma.201002410
102. Novotny CJ, Yu ET, Yu PKL (2008) InP nanowire/polymer hybrid photodiode. Nano Lett 8(3):775–779. doi:10.1021/Nl072372c
103. Wang P, Zhao X, Li B (2011) ZnO-coated CuO nanowire arrays: fabrications, optoelectronic properties, and photovoltaic applications. Opt Express 19(12):11271–11279
104. Ravirajan P, Haque SA, Durrant JR, Bradley DDC, Nelson J (2005) The effect of polymer optoelectronic properties on the performance of multilayer hybrid polymer/TiO2 solar cells. Adv Funct Mater 15(4):609–618. doi:10.1002/adfm.200400165
105. Goh C, Scully SR, McGehee MD (2007) Effects of molecular interface modification in hybrid organic-inorganic photovoltaic cells. J Appl Phys 101(11):114503. doi: 10.1063/1.2737977
106. Kudo N, Honda S, Shimazaki Y, Ohkita H, Ito S, Benten H (2007) Improvement of charge injection efficiency in organic-inorganic hybrid solar cells by chemical modification of metal oxides with organic molecules. Appl Phys Lett 90(18):183513. doi: 10.1063/1.2736192
107. Allen CG, Baker DJ, Albin JM, Oertli HE, Gillaspie DT, Olson DC, Furtak TE, Collins RT (2008) Surface modification of ZnO using triethoxysilane-based molecules. Langmuir 24(23):13393–13398. doi:10.1021/La802621n

108. Monson TC, Lloyd MT, Olson DC, Lee YJ, Hsu JWP (2008) Photocurrent Enhancement in Polythiophene- and Alkanethiol-Modified ZnO Solar Cells. Adv Mater 20(24):4755–4756. doi: 10.1002/adma.200801082
109. Qiao QQ, Xie Y, McLeskey JT (2008) Organic/inorganic polymer solar cells using a buffer layer from all-water-solution processing. J Phys Chem C 112(26):9912–9916. doi:10.1021/Jp7115615
110. Shen L, Zhu GH, Guo WB, Tao C, Zhang XD, Liu CX, Chen WY, Ruan SP, Zhong ZC (2008) Performance improvement of TiO2/P3HT solar cells using CuPc as a sensitizer. Appl Phys Lett 92(7):073307. doi: 10.1063/1.2884270
111. Seo J, Kim WJ, Kim SJ, Lee KS, Cartwright AN, Prasad PN (2009) Polymer nanocomposite photovoltaics utilizing CdSe nanocrystals capped with a thermally cleavable solubilizing ligand. Appl Phys Lett 94(13):133302. doi: 10.1063/1.3110969
112. Hsu CW, Wang LY, Su WF (2009) Effect of chemical structure of interface modifier of TiO2 on photovoltaic properties of poly(3-hexylthiophene)/TiO2 layered solar cells. J Colloid Interface Sci 329(1):182–187. doi:10.1016/j.jcis.2008.10.008
113. Lin YY, Lee YY, Chang LW, Wu JJ, Chen CW (2009) The influence of interface modifier on the performance of nanostructured ZnO/polymer hybrid solar cells. Appl Phys Lett 94(6):063308. doi: 10.1063/1.3080203
114. Spoerke ED, Lloyd MT, McCready EM, Olson DC, Lee YJ, Hsu JWP (2009) Improved performance of poly(3-hexylthiophene)/zinc oxide hybrid photovoltaics modified with interfacial nanocrystalline cadmium sulfide. Appl Phys Lett 95(21):213506. doi: 10.1063/1.3232231
115. Huang YC, Yen WC, Liao YC, Yu YC, Hsu CC, Ho ML, Chou PT, Su WF (2010) Band gap aligned conducting interface modifier enhances the performance of thermal stable polymer-TiO2 nanorod solar cell. Appl Phys Lett 96(12):123501. doi: 10.1063/1.3357425
116. Jiang XX, Chen F, Qiu WM, Yan QX, Nan YX, Xu H, Yang LG, Chen HZ (2010) Effects of molecular interface modification in CdS/polymer hybrid bulk heterojunction solar cells. Sol Energy Mater Sol C 94(12):2223–2229. doi:10.1016/j.solmat.2010.07.016
117. Huang YC, Hsu JH, Liao YC, Yen WC, Li SS, Lin ST, Chen CW, Su WF (2011) Employing an amphiphilic interfacial modifier to enhance the performance of a poly(3-hexyl thiophene)/TiO2 hybrid solar cell. J Mater Chem 21(12):4450–4456. doi:10.1039/C0jm03615c
118. Qian L, Yang JH, Zhou RJ, Tang AW, Zheng Y, Tseng TK, Bera D, Xue JG, Holloway PH (2011) Hybrid polymer-CdSe solar cells with a ZnO nanoparticle buffer layer for improved efficiency and lifetime. J Mater Chem 21(11):3814–3817. doi:10.1039/C0jm03799k
119. Shao SY, Liu FM, Fang G, Zhang BH, Xie ZY, Wang LX (2011) Enhanced performances of hybrid polymer solar cells with p-methoxybenzoic acid modified zinc oxide nanoparticles as an electron acceptor. Org Electron 12(4):641–647. doi:10.1016/j.orgel.2011.01.011